61 /4/2023

JOURNAL OF THEORETICAL AND APPLIED MECHANICS

WARSAW 2023, QUARTERLY, VOLUME 61, INDEX 365238, ISSN 1429-2955

POLISH SOCIETY OF THEORETICAL AND APPLIED MECHANICS

ptmts

POLISH SOCIETY OF THEORETICAL AND APPLIED MECHANICS

JOURNAL OF THEORETICAL AND APPLIED MECHANICS

No. 4 • Vol. 61

Quarterly

WARSAW, OCTOBER 2023

JOURNAL OF THEORETICAL AND APPLIED MECHANICS
(until 1997 Mechanika Teoretyczna i Stosowana, ISSN 0079-3701)

Beginning with Vol. 45, No. 1, 2007, *Journal of Theoretical and Applied Mechanics* (JTAM) has been selected for coverage in Thomson Reuters products and custom information services. Now it is indexed and abstracted in the following:

- **Science Citation Index Expanded** (also known as SciSearch®)
- **Journal Citation Reports/Science Edition**

* * * * *

Editorial Office

Al. Armii Ludowej 16, room 650; 00-637 Warsaw, Poland
phone (+48) 664 099 345, e-mail: biuro@ptmts.org.pl

www.jtam.pl

* * * * *

Rozwój kwartalnika naukowego *Journal of Theoretical and Applied Mechanics*, ISSN 1429-2955, jest dofinansowany ze środków Ministra Edukacji i Nauki przyznanych z pomocy *de minimis* w ramach programu „Rozwój czasopism naukowych", umowa RCN/SN/0056/2021/1.

JOURNAL OF THEORETICAL AND APPLIED MECHANICS
61, 4, pp. 647-658, Warsaw 2023
https://doi.org/10.15632/jtam-pl/170721

ANALYSIS OF AN AIRCRAFT DEPARTURE AND SPIN CHARACTERISTICS USING NASH EQUILIBRIUM THEORY

Chao Yan, Lianghui Tu, Yang Yang, Yuhao Wang
School of Aircraft Engineering, Nanchang Hangkong University, China
corresponding author Lianghui Tu, e-mail: 71016@nchu.edu.cn

The departure characteristics and steady-spin characteristics of a training aircraft are analyzed. The sideslip departure characteristics of the aircraft under the maximum weight and the minimum weight are obtained, respectively. When predicting the steady-spin, the equilibrium point of the spin is found by an analytic-graphic method based on "Nash equilibrium theory", and the steady-spin parameters of this aircraft are obtained under the conditions of maximum weight and minimum weight, left spin and right spin, neutral controls and pro--spin controls. The simulation results have good theoretical significance for the optimization and improvement of the aircraft in the preliminary design stage.

Keywords: departure characteristics, spin characteristics, spin equilibrium point

Nomenclature

m	–	Aircraft mass
b	–	Wing span
c	–	Mean aerodynamic chord
g	–	Gravitational acceleration
S	–	Wing area
V	–	Free-stream velocity
R	–	Radius of spin
F_c	–	Lateral force
C_D, C_L	–	Coefficient of lift and drag
$C_{n\beta D}$	–	Sideslip departure parameter
C_{ka}, C_{ki}	–	Moment coefficient of aerodynamic and inertia
$C_{l\beta}, C_{n\beta}$	–	Body-axis aerodynamic rolling and yawing moment due to sideslip
Ω	–	Aircraft conical rate
ΔH	–	Altitude lost in turn
Δt	–	Time in turn
ρ	–	Air density
α	–	Angle of attack, AOA
α_{sd}	–	Angle of attack at sideslip departure
β	–	Angle of sideslip
ψ	–	Euler yaw angles
$\delta_a, \delta_e, \delta_r$	–	Aileron, elevator, rudder deflection
τ	–	Non-dimensionalized wind-axis rotation rate, $\tau = \Omega b/2V$
$\omega_x, \omega_y, \omega_z$	–	Body-axis pitching, rolling and yawing rate
$\dot{\omega}_x, \dot{\omega}_y, \dot{\omega}_z$	–	Derivative of pitching, rolling and yawing rate
I_{xx}, I_{yy}, I_{zz}	–	Moment of inertia
I_{xy}, I_{yz}, I_{zx}	–	Products of inertia
M_x^A, M_y^A, M_z^A	–	Aerodynamic moment components about body axes

1. Introduction

The essence of spin is a curved flight state formed by strong interaction of longitudinal and lateral forces and moments. Despite the continuous development of the aviation industry, the complicated and dangerous spin has not disappeared. Frequent flight accidents caused by aircraft entering the spin in recent years have been made pilots, particularly civil pilots, fearful of the spin. Therefore, researchers should constantly dig deep into the spin mechanism, investigate the spin characteristics, and take preventive measures. The research on spin includes spin mechanism analysis (Bennett and Lawson, 2018; Collins and Sable, 2015), unsteady aerodynamic modeling at high angles of attack (Kou and Zhang, 2021; Mokhtari and Sabzehparvar, 2018), departure characteristics and spin sensitivity analysis (Stenfelt and Ringertz, 2013; Farcy *et al.*, 2020), spin characteristics prediction (Malik *et al.*, 2017), design of spinning control laws (Rogalski *et al.*, 2020), spin recovery and spin prevention measures (Figat and Goraj, 2016; Kapuscinski *et al.*, 2020), etc.

Wind tunnel data is the basis for predicting high angles of attack, stall and spin. Using wind tunnel test data, a differential equation model or neural network can be established to simulate the complicated and unsteady aerodynamic effect during spinning (Abramov *et al.*, 2004; Ignatyev and Khrabrov, 2015). From the high angle of attack to the stall and finally to the spin, the aerodynamic characteristics can be simulated based on the data of the high angle of attack static force test, forced oscillation test and rotary balance test in the low-speed wind tunnels. The dynamic motion characteristics of the spin in the unstable stage are analyzed using unsteady aerodynamic wind tunnel testing techniques such as rotary balance oscillatory coning motion tests and large-amplitude forced oscillation dynamic wind tunnel tests (Cummings *et al.*, 2018; Lee *et al.*, 2019).

There will be a divergent and large-scale non-command motion for the aircraft, that is, departure. When the aircraft enters departure, there exist dangerous actions such as wing swaying, nose pitching-down and shaking. If the recovery process takes too long, the aircraft will most likely enter a spin. Mature departure prediction criteria include the lateral control departure parameter $LCDP$, the sideslip departure parameter $C_{n\beta D}$, the "$\beta + \delta$" stability indication, Weissman ($LCDP - C_{n\beta D}$) and Kalviste criteria. The application scenarios of each criterion are different, e.g., when a yaw departure occurs, the sideslip departure parameter $C_{n\beta D}$ can be applied, and when pitching and yawing departures are coupled, the Kalviste criterion, a stability criterion considering longitudinal and lateral motion coupling effect and aerodynamic nonlinear characteristics, is applied.

At present, the commonly used spin prediction methods include the simplified six-degree-of--freedom equation of motion and nonlinear bifurcation analysis (Sibilski and Wróblewski, 2012). For different types of spins, their prediction methods are different. If the lateral angular velocity is constant, the rotation direction of the aircraft is constant, and the pilot does not clearly feel that the aircraft stops rotating, the aircraft is in a steady-spin. For the prediction of steady--spin, the relationship between the triaxial moment coefficient and is needed, and the solutions are mainly numerical analysis and the analytical graphic method (Bihrle and Barnhart, 1983). However, the disadvantages of the two methods are also clear. The numerical method necessitates a large initial value, which can result in an incorrect or missing solution. The graphic method is fast, but the accuracy of the equilibrium point is not high enough.

Based on the wind tunnel test data of a specific aircraft, including static force test data and rotary balance test data, the departure characteristics and steady-spin characteristics of the aircraft in the range of α from 0° to 90° are analyzed. Using the sideslip departure parameter $C_{n\beta D}$, the departure characteristics of the aircraft in the range of the positive AOA are obtained; when predicting the steady-spin, the equilibrium point of the spin is found by an analytic graphic

method based on "Nash equilibrium theory", and the steady-spin parameters of this aircraft under several different conditions are obtained.

2. Basic theories

2.1. Departure prediction

$C_{n\beta D}$ is used to predict whether the aircraft will have a high probability of yaw departure at high AOA, and its expression (Chambers, 1969) is

$$C_{n\beta D} = C_{n\beta}\cos\alpha - \frac{I_{zz}}{I_{xx}} C_{l\beta}\sin\alpha \tag{2.1}$$

At different AOAs, $C_{n\beta D}$ combines the static derivative of directional stability, the static derivative of lateral stability, and the moment of inertia, which can more realistically reflect the stability of the aircraft direction. The judgment criteria are:

$C_{n\beta D} > 0$, the directional stability is secured, and placed in steady region;
$C_{n\beta D} = 0$, the aircraft begins to lose directional stability, the sideslip departure will occur, and the corresponding AOA is α_{sd};
$C_{n\beta D} < 0$, there is no directional stability, placed in unsteady region, and yawing divergence occurs.

2.2. Prediction of steady-spin

When steady-spin occurs, the pitching, rolling and yawing moments in aerodynamics must balance their respective inertial moments at the same time. Since most of the mass of a modern aircraft is concentrated in the fuselage, the inertial pitching moment causes the nose to pitch up, which means that $q > 0$. The aircraft in steady-spin is in vertical rotation, and always produces a positive inertial pitching moment, so a negative aerodynamic pitching moment must exist in order to achieve the equilibrium. In order to keep the aircraft spinning, there must be an aerodynamic torque that can provide the drive. In the stalling and post-stalling AOA regions, the rolling moment is the dominant driving force for rotation around the velocity vector, but as the AOA increases to a flatter rotational attitude, the yawing moment becomes the dominant term.

In the steady-spin prediction, first the aerodynamic moment curves and the inertia moment curves are made, then the required equilibrium points are found from the intersections of the curves, and finally the complete steady-spin equilibrium solution is obtained by calculation.

3. Analytical graphic method based on Nash equilibrium theory

Game theory is a mathematical theory and method to describe a mathematical model containing contradictions, conflicts, confrontations and cooperation in the real world. It has penetrated into many aspects of social and scientific research and gradually formed an independent and complete theoretical system (Churkin *et al.*, 2021). It is the mutual game of the aerodynamic moment and the inertia moment in the steady-spin. When the strategies of both sides of the game are consistent, an equilibrium is reached.

Nash equilibrium is a typical form of non-cooperative game solution. Through the competitive selection process among all the players, the corresponding benefits of all the players are actively realized, and finally a systematic equilibrium can be achieved in the overall benefits. Nash's main idea is: in a multi-objective game $G = \{S_1, S_2, \ldots, S_m; F_1, F_2, \ldots, F_m\}$, the set

$(s_1^*, s_2^*, \ldots, s_m^*)$ composed of one strategy of each player, the strategy s_i^* of any player i is the best strategy compared with the other players $(s_1^*, \ldots, s_{i-1}^*, s_{i+1}^*, \ldots, s_m^*)$, then $(s_1^*, s_2^*, \ldots, s_m^*)$ is a Nash equilibrium of G.

Based on Nash equilibrium theory, the aerodynamic moment coefficient C_{ka} and inertia moment coefficient C_{ki} are taken as the game players ($k = l, m, n$, the same below), and the equilibrium solution of the coefficients is taken as the iterative strategy $\Delta S_k^w = (\Delta S_k^1, \ldots, \Delta S_k^w)$, and the variable group $(\alpha, \beta, \Omega, V)$ exists in the iterative strategy as the strategy space. More, define the payoff function as

$$\min f_u = |C_{ka} - C_{ki}| \qquad u = 1, 2, 3 \tag{3.1}$$

The specific steps are as follows:

a. Construct the initial iteration strategy group $\Delta S_m^w = (\Delta S_m^1, \ldots, \Delta S_m^w)$, the iteration strategy is taking α and β as an parameters, and τ as independent variable.
b. Execute the payoff function: $\min f_1 = |C_{ma} - C_{mi}|$, according to the strategy group.
c. Set a new iteration strategy group $\Delta S_l^w = (\Delta S_l^1, \ldots, \Delta S_l^w)$, the new iteration strategy is taking β as an independent variable and α as a parameter variable, and combined with τ, also the strategy space in the new strategy group is the variable group obtained by the previous payoff function
d. Execute the payoff function: $\min f_2 = |C_{la} - C_{li}|$, according to the strategy group.
e. Set a new iteration strategy group $\Delta S_n^w = (\Delta S_n^1, \ldots, \Delta S_n^w)$, and there is no new iteration strategy in this iteration group, and the strategy space in the new strategy group is the variable group obtained by the previous payoff function.
f. Execute the payoff function: $\min f_3 = |C_{na} - C_{ni}|$, according to the variable group.

Based on Nash equilibrium theory, it will be more direct to reflect the balance between the aerodynamic moment coefficient and inertia moment coefficient in the form of a payoff function. What is more, after modeling the state equation by this method, the system state and time--varying parameters are placed separately, which is convenient for subsequent program drawing.

4. Mathematical modelling

4.1. Equilibrium equations for forces and moments

After the aircraft entered a steady-spin, the average value of the rotation direction and the rotation angular rate remained unchanged, the aircraft descended rapidly along a small radius helical trajectory, and the spin axis almost coincided with the plumb line. A steady-spin is a dynamic equilibrium motion process, it can be expressed in Fig. 1. During this process, it can be assumed that (1) lateral force is equal to zero; (2) drag is equal to gravity; (3) lift is equal to the centrifugal force. It is assumed that the lateral force is zero in the calculation, which is because small lateral forces have negligible effects on the entire system relative to lift and drag. So that the force equilibrium equations of the aircraft are

$$D = \frac{1}{2}\rho S V^2 C_D = mg \qquad F_c = 0 \qquad L = \frac{1}{2}\rho S V^2 C_L = m\Omega^2 R \tag{4.1}$$

The three-axis moment equations about the body axis are

$$M_i = f(I_{ij}, \omega_i, \dot{\omega}_i) \tag{4.2}$$

where $i = x, y, z$, $j = x, y, z$.

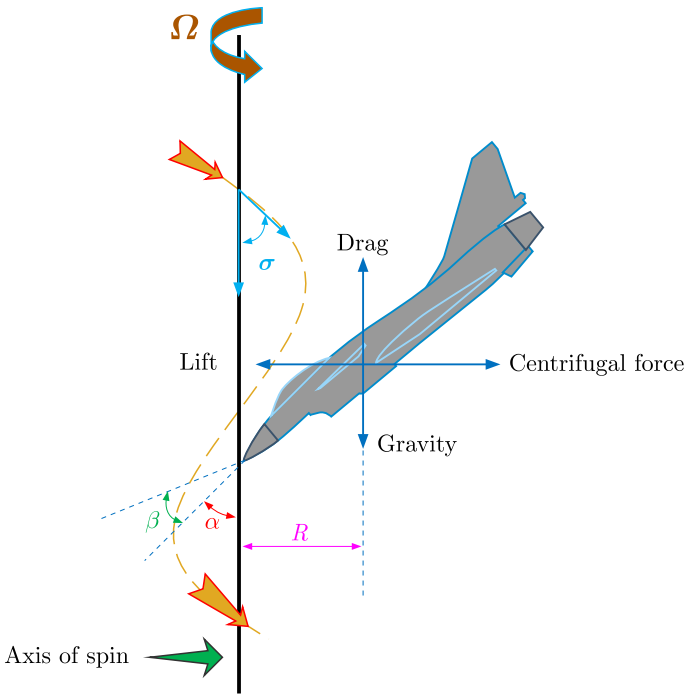

Fig. 1. Aircraft equilibrium of forces in the steady-spin

Because the longitudinal axis is the main axis of inertia in modern aircraft structures, and the cross inertial product of the symmetry plane satisfies $I_{xy} = I_{yz} = 0$, the complete body axis moment equilibrium equations can be expressed as

$$\begin{aligned} M_x^A &= I_{xx}\dot{\omega}_x + (I_{zz} - I_{yy})\omega_y\omega_z - I_{zx}(\omega_x\omega_y + \dot{\omega}_z) \\ M_y^A &= I_{yy}\dot{\omega}_y + (I_{xx} - I_{zz})\omega_x\omega_z + I_{zx}(\omega_x^2 - \omega_z^2) \\ M_z^A &= I_{zz}\dot{\omega}_z + (I_{yy} - I_{xx})\omega_x\omega_y + I_{zx}(\omega_y\omega_z - \dot{\omega}_x) \end{aligned} \tag{4.3}$$

4.2. Motion state equations

After the aircraft enters the steady-spin, the conical rate remains constant, so

$$\dot{\omega}_i = 0 \tag{4.4}$$

more

$$\omega_x = \Omega\cos\psi\cos\alpha \qquad \omega_y = \Omega\sin\psi \qquad \omega_z = \Omega\cos\psi\sin\alpha \tag{4.5}$$

where $\psi = -(\beta + \sigma)$, σ is the angle between the flight path and the vertical axis, and $\sigma = \arctan(R\Omega/V)$. The spin radius is generally very small when the aircraft is in the steady--spin, which makes $R \approx 0$, then $\psi \approx \beta$.

Although for the convenience of calculation, we assumed the aircraft with zero lateral force in the steady-spin, but the nose of the aircraft does not actually face the spin axis in the steady--spin. In this condition, the side slip still exists and comes from two aspects: one is that the aircraft does not face the spin axis, that β is generated; and the other is that the aircraft rotates around the spin axis and the airflow deflection produces a side slip. Although the side slip occurs, it is very small relative to the AOA, and the simulation results also confirmed this.

The general form of the moment coefficient in the steady-spin is

$$C_i = A_j F(\mathbf{q}, \mathbf{u}) \tag{4.6}$$

where $i = l, m, n$ $j = 1, 2$, then

$$A_1 = \frac{1}{\rho S b} \qquad A_2 = \frac{1}{\rho S c} \tag{4.7}$$

and

$$\mathbf{q} = \begin{bmatrix} I_{xx} & I_{yy} & I_{zz} & I_{zx} \end{bmatrix}^{\mathrm{T}} \tag{4.8}$$

The state model of the aerodynamic moment coefficient can be obtained as follows

$$\begin{bmatrix} C_l \\ C_m \\ C_n \end{bmatrix} = \begin{bmatrix} A_1 & 0 & 0 \\ 0 & A_2 & 0 \\ 0 & 0 & A_1 \end{bmatrix} \cdot (\mathbf{u} \cdot \mathbf{q}) \tag{4.9}$$

where

$$\mathbf{u} = \begin{bmatrix} 0 & \sin(2\alpha)\cos^2\Big(\beta\dfrac{\Omega^2}{V^2}\Big) & -\cos\alpha\sin\Big(2\beta\dfrac{\Omega^2}{V^2}\Big) \\ -\sin\alpha\sin\Big(2\beta\dfrac{\Omega^2}{V^2}\Big) & 0 & \cos\alpha\sin\Big(2\beta\dfrac{\Omega^2}{V^2}\Big) \\ \sin\alpha\sin\Big(2\beta\dfrac{\Omega^2}{V^2}\Big) & -\sin(2\alpha)\cos^2\Big(\beta\dfrac{\Omega^2}{V^2}\Big) & 0 \\ -\cos\alpha\sin\Big(2\beta\dfrac{\Omega^2}{V^2}\Big) & 2(\cos^2\alpha - \sin^2\alpha)\cos^2\Big(\beta\dfrac{\Omega^2}{V^2}\Big) & \sin\alpha\sin\Big(2\beta\dfrac{\Omega^2}{V^2}\Big) \end{bmatrix}^{\mathrm{T}} \tag{4.10}$$

5. Simulation and result analysis

5.1. Calculation conditions

In this paper, a training aircraft is taken as an example to simulate the departure characteristics and steady-spin. The data satisfy: $0^\circ \leqslant \alpha \leqslant 90^\circ$, positive τ signifies clockwise rotation of the aircraft to the outside observers, and the center of gravity is the front. The left spin ($\tau < 0$) is calculated separately from the right spin ($\tau > 0$) and two different control conditions, neutral control and pro-spin control, are considered:

— Neutral control, that means $\delta_a = \delta_e = \delta_r = 0^\circ$
— Pro-spin control, for the left spin, $\delta_e = -30^\circ$, $\delta_r = +30^\circ$, $\delta_a = -18^\circ$ - $+12^\circ$, and the same operations for the right spin. Positive δ_e and δ_a when the trailing-edge is down, positive δ_r when trailing-edge is left.

Also, it is calculated according to the maximum weight wt_{max} and the minimum weight wt_{min}, with the following conditions as shown in Table 1.

Table 1. Initial calculation conditions

Condition	Max-weight	Min-weight
m [kg]	3300	2800
I_{xx} [kg·m^2]	6200	3800
I_{yy} [kg·m^2]	15000	14500
I_{zz} [kg·m^2]	20000	17000

5.2. Simulation results and analysis

5.2.1. Departure characteristic

When predicting the departure characteristics, wt_{max} is calculated separately from wt_{min}, because the weight will cause a change of the moment of inertia. The curve of $C_{n\beta D}$-α is obtained, as shown in Fig. 2.

As can be seen from Fig. 2, $C_{n\beta D}$ in whole, positive AOA are in a steady region, whether in wt_{max} or wt_{min}, indicating that directional stability is present, and with increasing AOA, the value of $C_{n\beta D}$ increases and the directional stability is enhanced. In addition, it can also be seen that the rise of the wt_{min} curve is greater than that of wt_{max}, indicating that the directional stability under wt_{min} is better than that under wt_{max}. Therefore, it can be determined that the aircraft will not deviate from its course sharply after stalling.

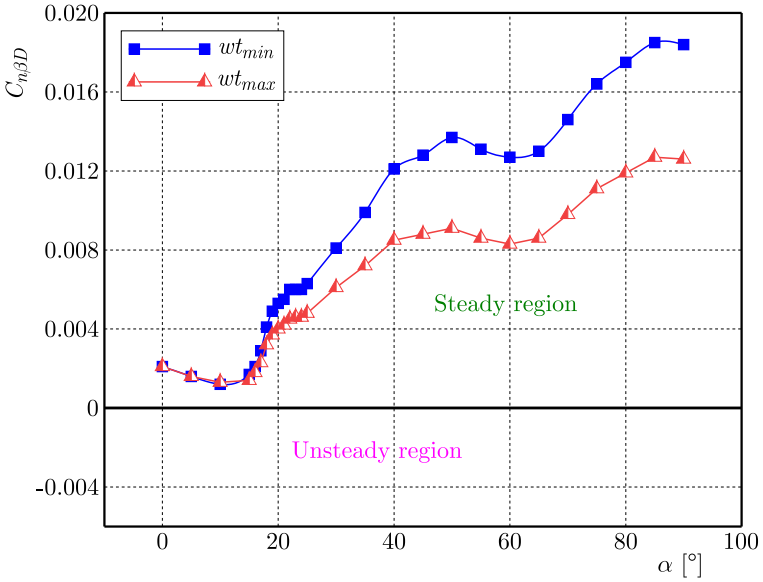

Fig. 2. $C_{n\beta D}$-α curves

5.2.2. Simulation of steady-spin characteristics

(A) Characteristics of steady-spin

After simulation, the yawing moment equilibrium curves C_{na}-C_{ni} and the corresponding curves of τ under several conditions in Section 5.1 are obtained, as shown in Fig. 3 and Fig. 4.

Figure 3 shows the yawing moment coefficient equilibrium curves and the corresponding τ for the four cases in the left spin $\tau < 0$, but not all of the curves have intersections. In Fig. 3a, the curves of the aerodynamic yawing moment and the inertial yawing moment have no intersection, but they are very close between AOA 45° and 55°, which proves that the aircraft is in a near--equilibrium state in this region. Except for this case, the curves in the other three states have intersections, especially in Fig. 3b, which has two intersections. But these two intersections may not be all that we need. The judgment of the equilibrium point will appear in the following (B).

By comparing Figs. 3a and 3b, we found that under neutral control, the curves of wt_{min} and wt_{max} are highly consistent, and the same conclusion can be drawn by comparing Figs. 3c and 3d. However, comparing Fig. 3a with Fig. 3c, the curves have changed significantly, as have Fig. 3b and 3d. In addition, the number of intersections at the curves is also changing in various ways. This is because the deflection has a great influence on the moment coefficient of the three axes, while the weight change has little effect in a small range. However, both of them will have an effect on the steady-spin characteristics.

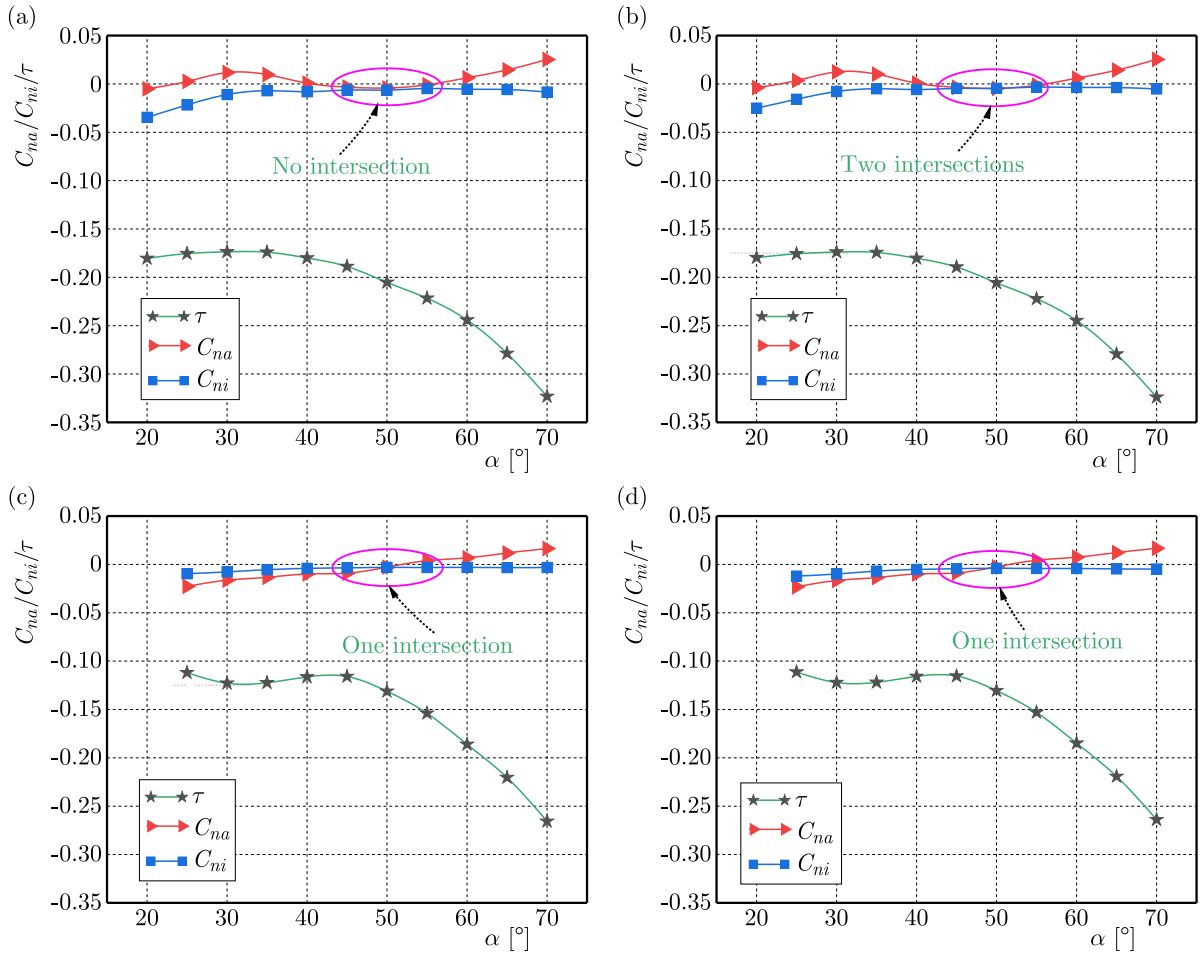

Fig. 3. The yawing moment equilibrium and τ vs α in the left spin: (a) wt_{min} and neutral control, (b) wt_{max} and neutral control, (c) wt_{min} and pro-spin control, (d) wt_{max} and pro-spin control

Similarly, as shown in Fig. 4, we obtained curves under the right spin ($\tau > 0$), with the same deflection control as the left spin. Like the left spin, the right spin also shows that the deflection has a greater influence on the moment coefficient than the weight. However, in the right spin, the curves only have two intersections (see Fig. 4c), and the curves are close to the equilibrium in other configurations between AOA 45° and 55°. Comparing Fig. 3 with Fig. 4, we can see that it is hard for the aircraft to enter the steady-spin in the right spin but easy in the left spin.

(B) Equilibrium criterion

The moment equilibrium and τ curves of the aircraft in the left and right spin were obtained in (A), and four cases of the configuration with intersections are shown in Fig. 5. Among the two intersections, there must be one intersection that we do not need, but even if there is a single intersection, it is not necessarily a solution, and the equilibrium criterion needs to be used for screening.

The criterion of steady-spin equilibrium requires that the slope of the aerodynamic moment coefficient curve at the intersection be different from the corresponding curve of τ. This occurs because the aircraft with longitudinal stability must obtain increased or decreased $|\tau|$ at a larger or smaller AOA than predicted, otherwise it will not be able to maintain pitching stability. The aerodynamic yawing moment coefficient, as a damping moment, should correspond to τ, which means that the slope of the aerodynamic yawing moment coefficient curve must be opposite to the τ curve in order to maintain stability. In the right spin, the slopes of the curves of τ at the

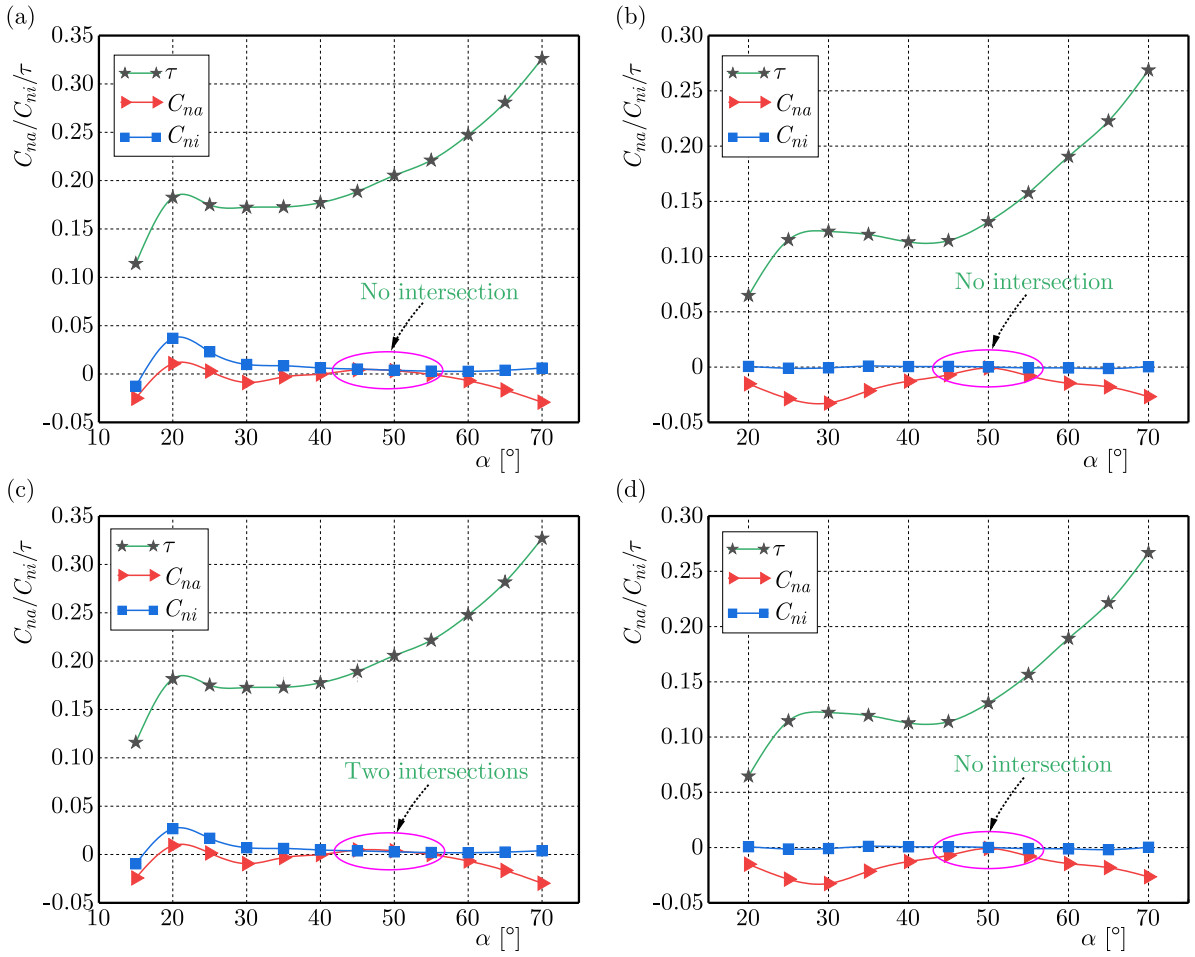

Fig. 4. The yawing moment equilibrium and τ vs α in the right spin: (a) wt_{min} and neutral control, (b) wt_{max} and pro-spin control (for the left spin), (c) wt_{max} and neutral control, (d) wt_{min} and pro-spin control (for the left spin)

intersection are all positive, so the slopes of the aerodynamic moment coefficient curves should be negative. The equilibrium point to be found in Fig. 5a is intersection II. Unlike the right spin, the slopes of the τ curves at the intersections in the left spin are negative, so the slopes of the aerodynamic moment coefficient curves should be positive. Therefore, in Fig. 5b, intersection IV meets the requirements, while the intersections in Fig. 5c and 5d both meet the criteria.

(C) Calculation of spin parameters

According to the equilibrium AOA, β and τ of steady-spin can be found out from the curves of moment equilibrium, as shown in Fig. 6. After α, β and τ are obtained, C_L and C_D in this state can be found from the test data of the rotary balance, and then V and R can be determined according to equation (4.1).

In the steady-spin, ΔH and Δt can be expressed as

$$\Delta H = \frac{\pi b}{\tau} \qquad \Delta t = \frac{\Delta H}{V} \tag{5.1}$$

Finally, all steady-spin equilibrium solutions can be obtained, which are shown in Table 2.

Although the aircraft is symmetrical, the characteristics of the left and right spin will be different. In this paper, this situation is mainly related to aerodynamic characteristics. When predicting the left and right spin of an aircraft in the steady-spin, the aerodynamic moment

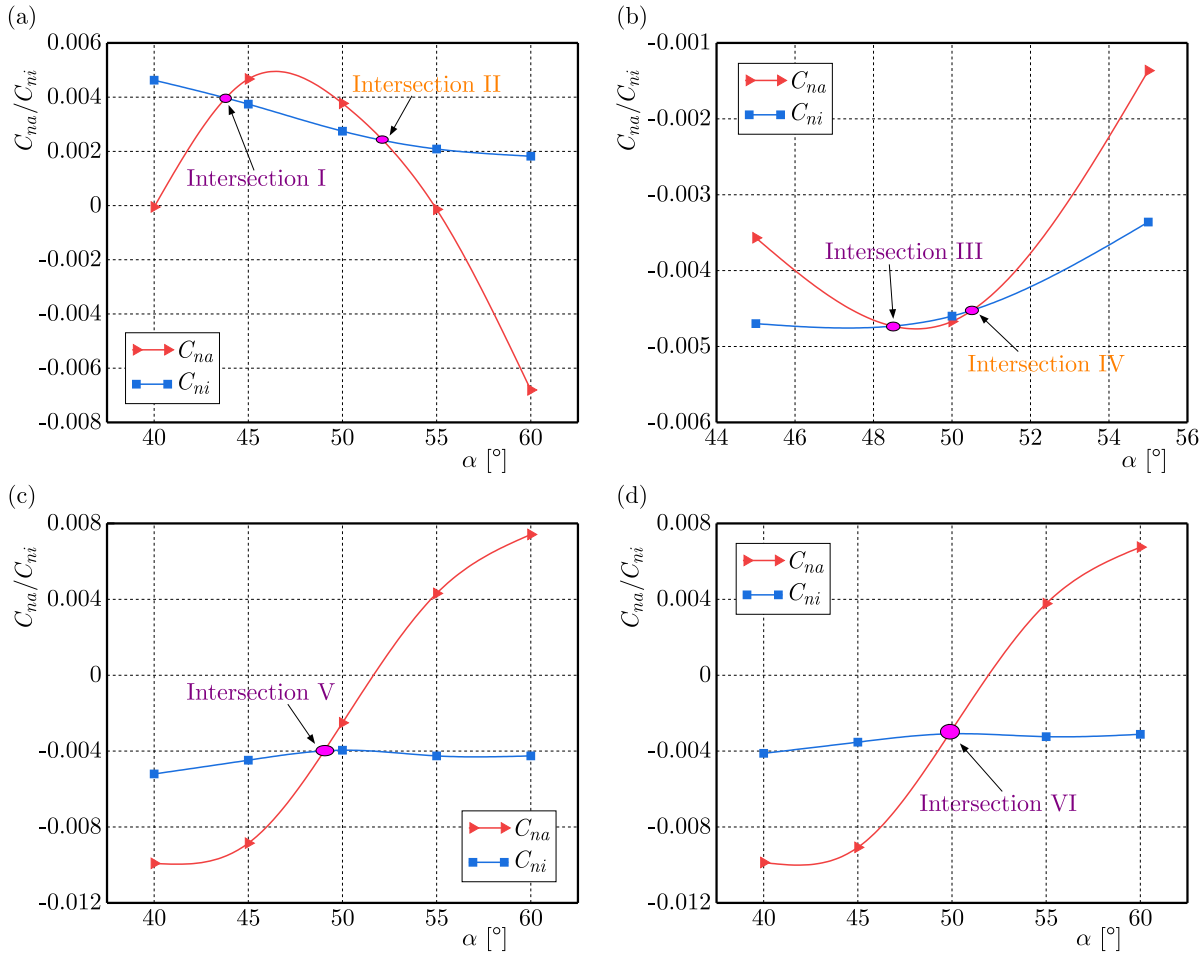

Fig. 5. Curves at the intersections: (a) wt_{max} and neutral control, in the right spin, (b) wt_{max} and neutral control, in the left spin, (c) wt_{min} and pro-spin control, in the left spin, (d) wt_{max} and pro-spin control, in the left spin

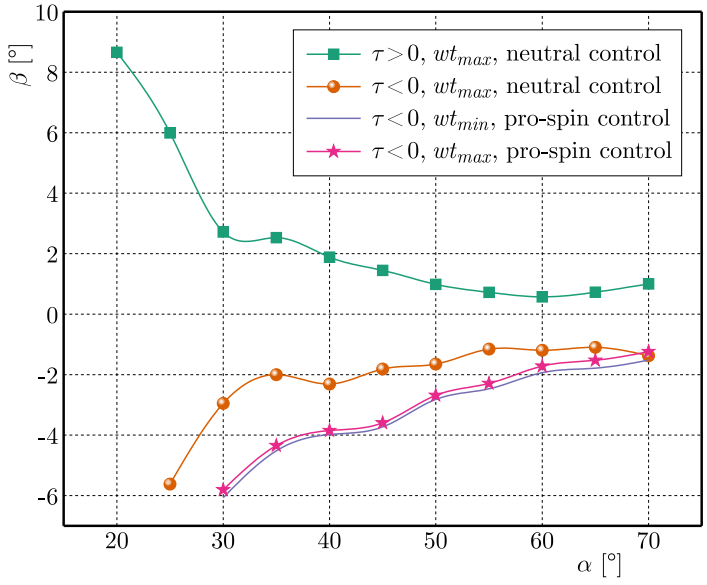

Fig. 6. β corresponding to the equilibrium points

Table 2. Complete steady-spin equilibrium solutions

	Intersection II	Intersection IV	Intersection V	Intersection VI
α [deg]	51.6	50.2	48.8	49.8
τ [–]	0.21	−0.21	−0.13	−0.13
β [deg]	0.9	−1.6	−3.0	−2.7
V [m/s]	68.5	69.8	64.7	70.2
R [m]	1.87	1.89	6.04	4.94
ΔH [m]	149	149	241	241
Δt [s]	2.2	2.1	3.7	3.4

coefficients needed are obtained from the wind tunnel test data of the rotary balance with positive and negative τ. However, under the same α, the aerodynamic moment coefficients corresponding to positive and negative τ are not necessarily symmetrical, especially at high α, which may be caused by the small asymmetry of the aircraft model, asymmetric vortex at high α, wind tunnel test equipment, and other factors.

6. Conclusion

In this paper, we can draw some conclusions:

- The departure characteristics and spin characteristics of the aircraft can be well analyzed using the wind tunnel test data; however, due to limitations of the analysis method, the simulation results will have large errors. There are many assumptions and preconditions, which will cause many subtle influencing factors to be ignored, so that the simulation results have large errors, which can only meet the initial stage of aircraft design and analysis.
- Through the static force test data at high AOA, the sideslip characteristics of the aircraft can be simulated. The obtained results show that the aircraft has good directional stability in the entire positive AOA range, and that it will improve as the AOA increases. At the same time, the directional stability of the aircraft under wt_{max} is weaker than wt_{min}.
- The influence of deflection on the steady-spin characteristics is greater than the moment of inertia, but in several different situations, the aircraft is in an equilibrium state or close to the equilibrium when AOA is about 50°.
- Among four equilibrium solutions, three appear in the left spin and only one appears in the right spin, which means that the probability of the aircraft having a steady spin in the left spin is greater than that in the right spin.
- The criterion of the steady-spin equilibrium point should be discussed according to whether the aircraft is in the left spin or the right spin. Some references have expressed that the criterion for the equilibrium point is that the slope of the aerodynamic moment curve is negative. But this situation is only for the right spin, since the slope of the τ curve for the right spin is positive, while the situation for the left spin is just opposite. It requires that the slope of the aerodynamic moment curve where the equilibrium point is located be positive in the left spin.
- The spin trajectories in different states are quite different. In intersections II and IV, $R \approx 1.8\,\mathrm{m}$, while it is 6 m in intersection V, and $\Delta H = 241\,\mathrm{m}$.

Acknowledgements

This research work was financially supported by the Special Funding for Postgraduate Innovation of Nanchang Hangkong University (No. YC2022060).

References

1. Abramov N., Goman M., Khrabrov A., 2004, Aircraft dynamics at high incidence flight with account of unsteady aerodynamic effects, *AIAA Atmospheric Flight Mechanics Conference and Exhibit*, **5274**
2. Bennett C.J., Lawson N.J., 2018, On the development of flight-test equipment in relation to the aircraft spin, *Progress in Aerospace Sciences*, **102**, 47-59
3. Bihrle Jr W., Barnhart B., 1983, Spin prediction techniques, *Journal of Aircraft*, **20**, 2, 97-101
4. Chambers J.R., 1969, Analysis of lateral-directional stability characteristics of a twin-jet fighter airplane at high angles of attack, *NASA TN D-5361*
5. Churkin A., Bialek J., Pozo D., Sauma E., Korgin N., 2021, Review of cooperative game theory applications in power system expansion planning, *Renewable and Sustainable Energy Reviews*, **145**, 111056
6. Collins J., Sable A., 2015, *Stall and Spin Accidents: Keep the Wings Flying*, AOPA Air Safety Institute
7. Cummings R.M., Liersch C., Schuette A., 2018, Multi-disciplinary design and performance assessment of effective, agile NATO air vehicles, *2018 Applied Aerodynamics Conference*, 2838
8. Farcy D., Khrabrov A.N., Sidoryuk M.E., 2020, Sensitivity of spin parameters to uncertainties of the aircraft aerodynamic model, *Journal of Aircraft*, **57**, 922-937
9. Figat M., Goraj Z., 2016, Analysis of stability derivatives important to recovery from spin, *Aviation*, **20**, 2, 48-52
10. Ignatyev D.I., Khrabrov A.N., 2015, Neural network modeling of unsteady aerodynamic characteristics at high angles of attack, *Aerospace Science and Technology*, **41**, 106-115
11. Kapuscinski T., Szczerba P., Rogalski T., Rzucidlo P., Szczerba Z., 2020, A vision-based method for determining aircraft state during spin recovery, *Sensors (Basel)*, **20**, 8, 2401
12. Kou J., Zhang W., 2021, Data-driven modeling for unsteady aerodynamics and aeroelasticity, *Progress in Aerospace Sciences*, **125**, 100725
13. Lee S., Choi Y., Chung H.S., 2019, Forced oscillation wind tunnel tests for dynamic characteristic of aircraft, *AIAA Aviation 2019 Forum*
14. Malik B., Akhtar S., Masood J., 2017, Influence of flight control law on spin dynamics of aerodynamically asymmetric aircraft, *Journal of Theoretical and Applied Mechanics*, **55**, 963-975
15. Mokhtari M.A., Sabzehparvar M., 2018, Identification of spin maneuver aerodynamic nonlinear model by applying ensemble empirical mode decomposition and extended multipoint modeling, *Proceedings of the Institution of Mechanical Engineers, Part G: Journal of Aerospace Engineering*, **233**, 1865-1878
16. Rogalski T., Rzucidło P., Prusik J., 2020, Unmanned aircraft automatic flight control algorithm in a spin maneuver, *Aircraft Engineering and Aerospace Technology*, **92**, 8, 1215-1224
17. Sibilski K., Wróblewski W., 2012, Prediction of aircraft spin characteristics by continuation and bifurcation methods, *AIAA Atmospheric Flight Mechanics Conference*, **4799**
18. Stenfelt G., Ringertz U., 2013, Yaw departure and recovery of a tailless aircraft configuration, *Journal of Aircraft*, **50**, 311-315

Manuscript received March 11, 2023; accepted for print June 16, 2023

JOURNAL OF THEORETICAL AND APPLIED MECHANICS
61, 4, pp. 659-672, Warsaw 2023
https://doi.org/10.15632/jtam-pl/170706

STABILITY ANALYSIS OF A SPINNING SHAFT IN THE CONCENTRIC CYLINDER FILLED WITH AN INCOMPRESSIBLE FLUID

Zhongkai Jiang, Guangding Wang

School of Engineering, Anhui Agricultural University, Hefei, China; and

Anhui Province Engineering Laboratory of Intelligent Agricultural Machinery and Equipment, Hefei, China

e-mail: ahau_evib@163.com; wgd_vib@yeah.net

Huiqun Yuan

Institute of Applied Mechanics, College of Science, Northeastern University, Shenyang, China

e-mail: hq_yuan@yeah.net

This paper deals with the stability of a spinning shaft in a concentric cylinder filled with an incompressible fluid. The steady-state momentum and continuity equations for the external fluid are established. Using Taylor expansion, the fluid forces exerted on the shaft are calculated. The shaft is in the Rayleigh model taking into account the rotary inertia and gyroscopic effects. Accordingly, the governing equation of the considered system is formulated analytically. The explicit characteristic frequency equation for the pinned-pinned spinning shaft system is then derived. Finally, the stability of the system is studied by means of characteristic value analysis.

Keywords: spinning shaft, external fluid, stability, critical spinning speed

1. Introduction

Spinning shafts have held wide applications in energy, aviation and automotive engineering. One class of spinning shafts works in an annular fluid medium, such as the spinning shaft of axial flow pumps. In the large pump unit, its hydraulic components are subject to various hydraulic unbalanced forces and other various excitation sources during the operation of the unit. As a result, vibration and instability of the structure occur, which will directly affect the reliable operation of the unit. In this study, a spinning shaft in a concentric cylinder filled with an incompressible fluid is considered. The focus is on the instability characteristics of the spinning shaft with external fluids.

The vibration and stability of spinning shafts are key concerns in engineering, which have attracted attention of many researchers. There are two analytical methods for such problems, one is the analytical study and the other is numerical calculation (Chen and Ku, 1990; Gross *et al.*, 1993). Sheu and Yang (2005) conducted an analytical study of vibration for a rotating Rayleigh beam with typical boundary conditions as well as an analysis of the unbalanced response. Using the Hamilton principle and multiple scales method, natural vibration of a nonlinear slender spinning shaft was investigated by Shahgholi *et al.* (2014). Zhang *et al.* (2020a) studied the frequency and mode of a flexible rotor system using Hamilton's principle and Euler's angle, and discussed the effect of centrifugal forces on the stability of the system. In recent years, researchers have been concerned with vibration of shafts under simultaneous effects of axial movement and rotational motion (Zhu and Chung, 2019; Ebrahimi-Mamaghani *et al.*, 2021; Yang *et al.*, 2021; Li *et al.*, 2018; Katz, 2001). For example, applying the Hamilton principle, Zhu and Chung (2019) derived the governing equation of motion for a simply supported Rayleigh beam with spinning and axial

motions. Using the Galerkin method, vibration and stability of the beam were studied. Ebrahimi-Mamaghani *et al.* (2021) considered the effects of spinning and axial motions and investigated stability of an axially functionally graded beam via the Laplace transform and Galerkin discretization. In summary, there is a great deal of literature reporting on the dynamics and stability of spinning shafts, and the study in this area has been relatively extensive (Aouadi and Lakrad, 2018; Arvin, 2019; Saeed, 2019; Manchi and Sujatha, 2021; Li, 2022; Li *et al.*, 2021; Zhu *et al.*, 2018).

Furthermore, there are many studies concerning fluid-structure coupled vibration of spinning shafts, such as liquid-filled rotors and spinning pipes conveying fluids. For the liquid-filled rotor, the flexural vibration governing equation of the rotor is established by the analytical calculation method, and the characteristic frequency equation of the system is derived by combining the corresponding support boundary conditions. Then, the stability of the rotor system is analyzed by the positive and negative signs of the characteristic roots (Tao and Zhang, 2002; Firouz-Abadi and Haddadpour, 2010; Kern and Jehle, 2016; Sahebnasagh *et al.*, 2018; Wang and Yuan, 2018; Wang and Yuan, 2019b; Wang and Chen, 2020; Wang *et al.*, 2021; Zhang *et al.*, 2020b; Wang and Yuan, 2021; Païdoussis and Issid, 1974). Commonly, the two-dimensional linearized Navier-Stokes equation is employed to calculate the fluid forces on the rotor (Tao and Zhang, 2002; Firouz-Abadi and Haddadpour, 2010; Wang and Chen, 2020). Wang and Yuan (2018) established three-dimensional equations of fluid motion in the rotor cavity and studied stability of the rotor system. In addition to the above-mentioned stability discrimination methods, Wang and Chen (2020; 2021) also applied the Andronov-Hopf bifurcation and wave resonance theory to investigate stability of the fluid-filled rotor system. On the other hand, many advanced papers have reported vibration and stability of spinning pipes conveying fluid in literature on the study (Abdollahi *et al.*, 2021; Dwivedi *et al.*, 2022; Michaelides and Feng, 2023; Wang and Yuan, 2019a; Oyelade and Oyediran, 2020). Basically, the spinning pipe is seen as a beam structure. The structural equations of motion are established based on the Euler-Bernoulli beam or Rayleigh beam theory (Païdoussis and Issid, 1974; Kheiri *et al.*, 2014). In terms of solution methods, numerical calculation methods are more frequently used, such as the transfer matrix method (Li *et al.*, 2014), Galerkin method (Bahaadini *et al.*, 2018; Liang *et al.*, 2018; Liang *et al.*, 2020), and the differential quadrature method (DQM) (Zhou *et al.*, 2018). There are also some studies reporting vibration of spinning pipes conveying fluid under external loads including additional mass (ElNajjar and Daneshmand, 2020), thermal effects (Qian *et al.*, 2009; Bahaadini and Saidi, 2018), etc. It can be found that the studies on the vibration of spinning pipes conveying fluid are basically consistent in terms of research methods. In general, theoretical studies on fluid-structure coupled vibration of spinning cylinders/pipes are common. However, there are few reports on vibration and stability of spinning shafts in an annular fluid medium.

In summary, most of the studies have investigated vibration of spinning shafts subjected to external loads. Also, some studies have reported instability of pipes conveying fluid. On the other hand, there was very little literature studying the vibration of shafts with external fluids. The present paper is aimed to investigate the instability of a spinning slender shaft in a concentric cylinder filled with an incompressible fluid. Accordingly, the rotary inertia and gyroscopic effects are considered in the modeling of the considered system. The steady-state governing equations of fluid motion are established, and the external fluid forces are obtained by means of Taylor expansion. Then the coupled-field governing equations of the shaft and external fluid are derived on the basis of the spinning Rayleigh beam theory. After that, the characteristic frequency equation of the system is determined and then used for stability analysis. Finally, the effects of the slenderness ratio and density ratio on the natural frequency, instability and critical spinning speed are studied numerically.

2. Fluid dynamics

2.1. Formulation for the external fluid

Consider a spinning shaft in a concentric cylinder filled with an incompressible fluid as shown in Fig. 1. It has rotational speed Ω, length of shaft L, radius of cylinder a, fluid density ρ_f, and b refers to the radius of the shaft. It is assumed that the shaft spins at a steady state. Since perturbations due to flexural deformation of the shaft occur, vibrational instability of the shaft will be generated as a result of the perturbed pressure P formed by the external fluid. In order to reveal the instability characteristics of the spinning shaft, this subsection will be devoted to the formulation of the external fluid force.

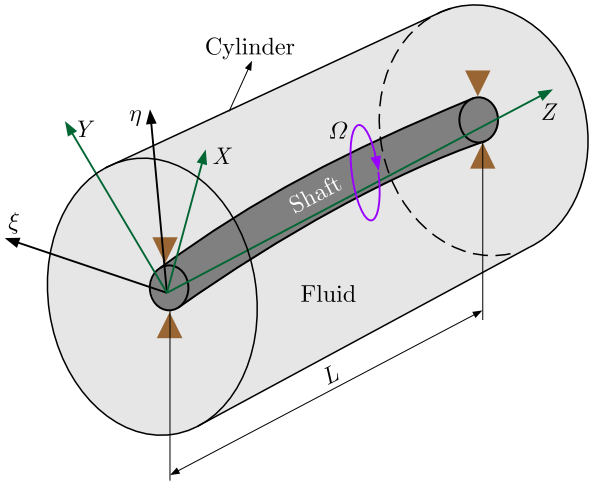

Fig. 1. Schematic of a spinning shaft in the concentric cylinder filled with an incompressible fluid

In the steady state, the two-dimensional Navier-Stokes equations and continuity equation of the external fluid in the rotating frame $\eta\xi$ can be written as

$$\begin{aligned} &-2\Omega v_\theta - r\Omega^2 + v_r\frac{\partial v_r}{\partial r} + \frac{v_\theta}{r}\frac{\partial v_r}{\partial \theta} - \frac{v_\theta^2}{r} = -\frac{1}{\rho_f}\frac{\partial P}{\partial r} + \nu\Big(\nabla^2 v_r - \frac{v_r}{r^2} - \frac{2}{r^2}\frac{\partial v_\theta}{\partial \theta}\Big) \\ &2\Omega v_r + v_r\frac{\partial v_\theta}{\partial r} + \frac{v_\theta}{r}\frac{\partial v_\theta}{\partial \theta} + \frac{v_r v_\theta}{r} = -\frac{1}{\rho_f r}\frac{\partial P}{\partial \theta} + \nu\Big(\nabla^2 v_\theta - \frac{v_\theta}{r^2} + \frac{2}{r^2}\frac{\partial v_r}{\partial \theta}\Big) \end{aligned} \tag{2.1}$$

and

$$\frac{\partial (r v_r)}{\partial r} + \frac{\partial v_\theta}{\partial \theta} = 0 \tag{2.2}$$

where v_r and v_θ denote the radial and tangential velocity components of fluid particles, respectively, and ν is kinematic viscosity. Also, ∇^2 is the Laplacian operator which is defined as

$$\nabla^2 = \frac{\partial^2}{\partial r^2} + \frac{1}{r}\frac{\partial}{\partial r} + \frac{1}{r^2}\frac{\partial^2}{\partial \theta^2} \tag{2.3}$$

The corresponding flow boundary conditions at $r = a, b$ are

$$\begin{aligned} &v_r\Big|_{r=b} = 0 \qquad v_\theta\Big|_{r=b} = b\Omega \\ &v_r\Big|_{r=a} = 0 \qquad v_\theta\Big|_{r=a} = 0 \end{aligned} \tag{2.4}$$

According to the proposed model, it is noticed that in this flow, the circumferential velocity is valued, but the derivative of all parameters along the circumference is equal to zero, i.e. $\partial/\partial\theta = 0$. Moreover, under the boundary conditions given in Eqs. (2.4), the continuity equation shown in Eq. (2.2) is solved to obtain the radial velocity component $v_r = 0$. By substituting these conditions into Eqs. (2.1), we get

$$2\Omega v_\theta - r\Omega^2 - \frac{v_\theta^2}{r} = -\frac{1}{\rho_f}\frac{\partial P}{\partial r} \qquad \frac{1}{r}\frac{\partial}{\partial r}\Big(r\frac{\partial v_\theta}{\partial r}\Big) - \frac{v_\theta}{r^2} = 0 \tag{2.5}$$

By solving Eq. $(2.5)_2$, the solution of the circumferential velocity component v_θ can be obtained as

$$v_\theta = Ar + \frac{B}{r} \tag{2.6}$$

where

$$A = \frac{\Omega}{1-\kappa^2} \qquad B = \frac{a^2\Omega}{\kappa^2 - 1} \tag{2.7}$$

in which κ is defined as

$$\kappa = \frac{a}{b} \tag{2.8}$$

Since v_θ is determined, the total pressure P can be calculated in terms of Eq. $(2.5)_1$ as

$$P = \rho_f\Omega^2\Big(\frac{1}{2}r^2 + \chi r^2 - \frac{a^4\chi^2}{2r^2} + \frac{1}{2}r^2\chi^2 - 2a^2\chi\ln r - 2a^2\chi^2\ln r\Big) + C \tag{2.9}$$

where

$$\chi = \frac{1}{1-\kappa^2} \tag{2.10}$$

Due to the influence of flexural deformation of the spinning shaft, the fluid particles on the surface of the shaft will undergo in a corresponding radial displacement. Assuming that the radial displacement is ζ, substituting into Eq. (2.9) yields

$$P\Big|_{b+\zeta} = \rho_f\Omega^2\Big[\frac{1}{2}(b+\zeta)^2 + \chi(b+\zeta)^2 - \frac{a^4\chi^2}{2(b+\zeta)^2} + \frac{1}{2}(b+\zeta)^2\chi^2 - 2a^2\chi\ln(b+\zeta) - 2a^2\chi^2\ln(b+\zeta)\Big] + C \tag{2.11}$$

As seen, Eq. (2.11) is a nonlinear expression. As a result, the Taylor expansion is employed to linearize this equation. The linearization expression for the pressure P can be expressed as

$$\begin{aligned} P = {} & \rho_f\Omega^2\Big[\frac{1}{2}b^2 + \chi b^2 - \frac{a^4\chi^2}{2b^2} + \frac{1}{2}b^2\chi^2 - 2a^2\chi\ln b - 2a^2\chi^2\ln b\Big] \\ & + \rho_f\Omega^2 b\zeta\Big[(1+\chi)^2 + \frac{a^4\chi^2}{b^4} - \frac{2a^2\chi}{b^2} - \frac{2a^2\chi^2}{b^2}\Big] + C \end{aligned} \tag{2.12}$$

It can be found that the part of Eq. (2.12) containing ζ is a perturbed term caused by deformation of the spinning shaft, which is the main source of the instability. In this study, only the perturbation pressure needs to be concerned. Therefore, Eq. (2.12) can be simplified as

$$P = \rho_f\Omega^2 b[(1+\chi) - \kappa^2\chi]^2\zeta \tag{2.13}$$

By substituting Eq. (2.10) into Eq. (2.13), the perturbed pressure acting on the surface of the spinning shaft can be determined as

$$P = 4\rho_f \Omega^2 b\zeta \tag{2.14}$$

in which the radial displacement ζ can be described by the flexural deformation of the shaft as

$$\zeta = u_\eta \cos\theta + u_\xi \sin\theta \tag{2.15}$$

where u_η and u_ξ are displacement components of the spinning shaft in the η and ξ directions, respectively.

Finally, the fluid forces exerted on the shaft can be calculated as

$$F_\eta = \int_0^{2\pi} P(b)\cos(\theta) b\, d\theta \qquad F_\xi = \int_0^{2\pi} P(b)\sin(\theta) b\, d\theta \tag{2.16}$$

After substituting Eqs. (2.14) and (2.15) into Eqs. (2.16), the analytical expressions for the fluid forces can be obtained as

$$F_\eta = 4\rho_f \pi b^2 \Omega^2 u_\eta \qquad F_\xi = 4\rho_f \pi b^2 \Omega^2 u_\xi \tag{2.17}$$

3. Structural dynamics

In this study, the rotary inertia and gyroscopic effects of the spinning shaft are both considered. Therefore, the Rayleigh model is adopted to formulate the governing equation of motion of the spinning shaft in the concentric cylinder filled with an incompressible fluid.

If adopting the Rayleigh beam theory, the basic governing differential equation for flexural vibration of the considered spinning shaft system reads

$$EI\frac{\partial^4 u}{\partial Z^4} + \rho A\frac{\partial^2 u}{\partial t^2} - \rho I\frac{\partial^4 u}{\partial t^2 \partial Z^2} + \mathrm{i}2\rho I\Omega\frac{\partial^3 u}{\partial t \partial Z^2} = F \tag{3.1}$$

where E, I, A and ρ are Young's modulus, mass moment of inertia, cross-sectional area and density of the shaft, respectively. Also, the fluid force F can be obtained by using Eqs. (2.17) as

$$F = 4\rho_f \pi b^2 \Omega^2 u \tag{3.2}$$

where flexural deformation u is defined as

$$u = u_\eta + \mathrm{i}u_\xi \tag{3.3}$$

After inserting Eq. (3.2) into Eq. (3.1), the governing equation can be rewritten as

$$EIu'''' + \rho A\ddot{u} - \rho I\ddot{u}'' + \mathrm{i}2\rho I\Omega\dot{u}'' = 4m_f\Omega^2 u \tag{3.4}$$

where m_f is defined as $m_f = \rho f \pi b^2$.

Since only harmonic vibrations are considered, $u(Z,t)$ may take the form as

$$u(Z,t) = U(Z)\mathrm{e}^{\mathrm{i}\omega t} \tag{3.5}$$

where ω is the circular frequency of vibration of the spinning shaft.

After using the above expression for u in Eq. (3.5) into Eq. (3.4), one gets

$$EIU'''' + (\rho I\omega^2 - 2\rho I\Omega\omega)U'' - (\rho A\omega^2 + 4m_f\Omega^2)U = 0 \tag{3.6}$$

To simplify the analysis, the following dimensionless quantities are introduced

$$\varsigma = \frac{Z}{l} \qquad W = \frac{U}{l} \qquad \gamma = \frac{l}{r} \qquad \omega_0^2 = \frac{EI}{\rho A l^4} \qquad g = \frac{\omega}{\omega_0} \qquad s = \frac{\Omega}{\omega_0} \tag{3.7}$$

Then, the dimensionless form of Eq. (3.6) can be written as

$$W'''' + \Big[\Big(\frac{1}{2\gamma}\Big)^2 g^2 - 2\Big(\frac{1}{2\gamma}\Big)^2 gs\Big]W'' - (g^2 + 4\mu s^2)W = 0 \tag{3.8}$$

where density ratio μ is given as

$$\mu = \frac{\rho_f}{\rho} \tag{3.9}$$

It is well known that the general form of the solution to Eq. (3.8) can be expressed as

$$W(\varsigma) = C_1 \sin(\alpha\varsigma) + C_2 \cos(\alpha\varsigma) + C_3 \sinh(\beta\varsigma) + C_4 \cosh(\beta\varsigma) \tag{3.10}$$

Considering that the two ends of the spinning shaft are hinged in this study, the corresponding dimensionless boundary conditions at $\varsigma = 0$ and 1 are

$$W\Big|_{\varsigma=0} = W\Big|_{\varsigma=1} = 0 \qquad W''\Big|_{\varsigma=0} = W''\Big|_{\varsigma=1} = 0 \tag{3.11}$$

Using Eq. (3.11), the characteristic frequency equation of the spinning shaft can be obtained as

$$\sin\alpha = \sin(n\pi) \tag{3.12}$$

where α can be determined by using Eqs. (3.8) and (3.10).

After expanding Eq. (3.12), the explicit expression of the dimensionless characteristic frequency equation is expressed as

$$n^4\pi^4 - n^2\pi^2(g^2 - 2gs)\Big(\frac{1}{2\gamma}\Big)^2 - (g^2 + 4\mu s^2) = 0 \tag{3.13}$$

It can be seen that the characteristic equation is an algebraic equation with respect to the dimensionless whirl frequency g. Solving this equation, the real and imaginary parts of the eigenvalues can be determined, i.e. $g = \lambda + \mathrm{i}\sigma$, where the real part represents the dimensionless natural frequency of the system and the imaginary part represents the dimensionless damping. Also, the stability of the system can be determined by the variation of the real and imaginary parts versus the dimensionless spinning frequency (Abdollahi *et al.*, 2021). In the present study, it is supposed that both ends of the shaft are pinned-pinned boundary conditions. Therefore, the other boundary conditions are not included in the mathematical formulation. However, the method described in this article is also applicable to examine stability of spinning shafts in the concentric fluid-filled cylinder with other boundary conditions.

Furthermore, by inserting $g = s$ into Eq. (3.13), the dimensionless critical spinning speed can be calculated as

$$s_n^c = n^2\pi^2 \sqrt{\frac{1}{1 + 4\mu - n^2\pi^2\Big(\frac{1}{2\gamma}\Big)^2}} \tag{3.14}$$

As seen, if supposing $\gamma = 0$, then the critical spinning speed can be reduced to

$$s_n^c = n^2\pi^2 \sqrt{\frac{1}{1 - n^2\pi^2\Big(\frac{1}{2\gamma}\Big)^2}} \tag{3.15}$$

which is identical to that for pinned-pinned spinning Rayleigh beams (Sheu and Yang, 2005).

4. Numerical results

In this Section, a numerical study is conducted to investigate the instability of the spinning shaft in the concentric cylinder filled with an incompressible fluid. In particular, the factors that affect the stability of the system are discussed in depth.

In order to validate the proposed model, the first four critical spinning speeds versus slenderness ratio for the spinning Rayleigh beams without the external fluid are obtained and compared with those reported by Sheu and Yang (2005), as shown in Fig. 2. It can be seen that the present results are in good agreement with those obtained in the literature. Furthermore, to clarify the effect of the external fluid, the critical spinning speeds of the spinning shaft with the external fluid are illustrated and compared with the spinning shaft without considering external fluid effects, as seen in Fig. 3. It can be observed that after considering the external fluid, the critical spinning speed for each order has become noticeably smaller.

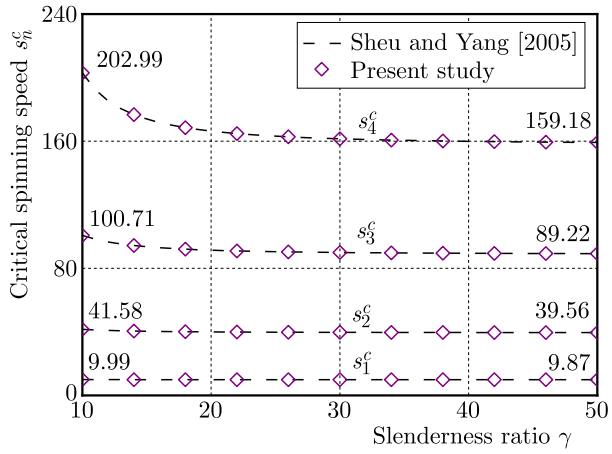

Fig. 2. Comparison of the first four critical spinning speeds versus slenderness ratio of the spinning shaft with Sheu and Yang (2005) at $\mu = 0$

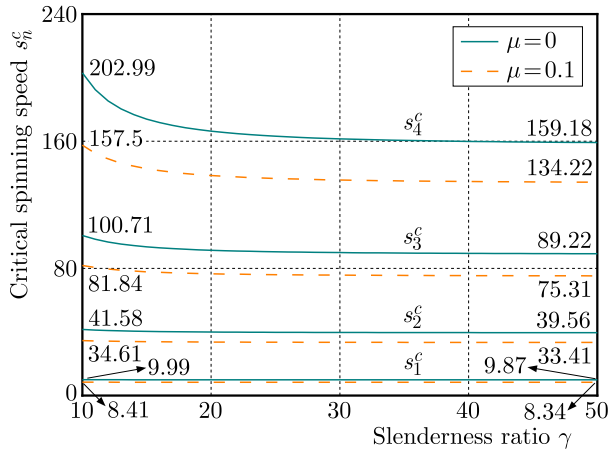

Fig. 3. The effects of external fluid on the critical spinning speed of the spinning shaft

Figure 4 shows the whirl speed map of the spinning shaft in the concentric cylinder filled with the incompressible fluid for $\mu = 0.13$, $\gamma = 5$ and different values of the mode number. Also, in order to clarify the influence of the external fluid on the spinning shaft, the whirl speed map of the spinning Rayleigh beam is plotted in the figure. It can be seen that the critical spinning speed of the system decreases significantly at each order due to the influence of the external fluid. In addition, the dimensionless whirl frequency of the system no longer increases with the

dimensionless spinning frequency, but the two characteristic frequencies are converged at a point, forming a closed arc-shaped region. It indicates that the characteristic equation has no real roots when the spinning speed is higher than the speed at the convergence point. This result shows that the external fluid has a strong influence on the whirl characteristics and stability of the spinning shaft.

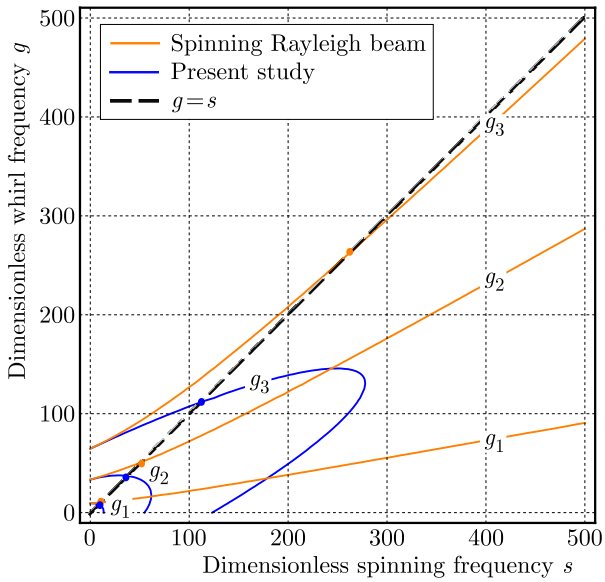

Fig. 4. Comparison of whirl speed maps of the spinning Rayleigh beam and the considered spinning shaft system

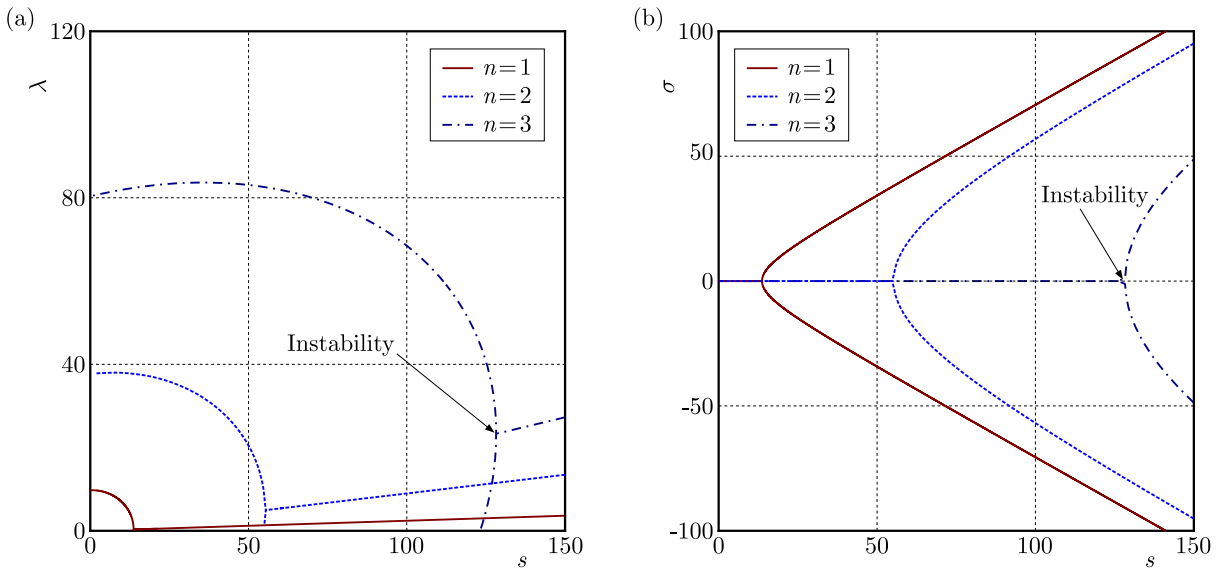

Fig. 5. Dimensionless natural frequency and damping of the spinning shaft versus the dimensionless spinning frequency with $\mu = 0.13$ and $\gamma = 10$ for different mode numbers: (a) dimensionless natural frequency, (b) dimensionless damping

Figures 5a and 5b, respectively, demonstrate the dimensionless natural frequency and damping of the system in terms of the dimensionless spinning frequency at $\mu = 0.13$ and $\gamma = 10$ for different mode numbers. It can be seen that as the spinning frequency increases, the natural frequency of the system for both modes decreases. The damping of the system bifurcates at a specific speed, which indicates that there is an inflow and outflow of energy and the system

becomes unstable. The speed corresponding to the bifurcation point is called the "instability critical spinning speed s_{cr}". Moreover, a comparative study is carried out to illustrate the effect of the external fluid on the stability of the considered system, as shown in Fig. 6. It can be found that the spinning Rayleigh beam is always stable as the rotational speed increases. However, when considering the external fluid, the system will lose its stability at a certain speed. This makes it clearer that external fluids are the main source of instability.

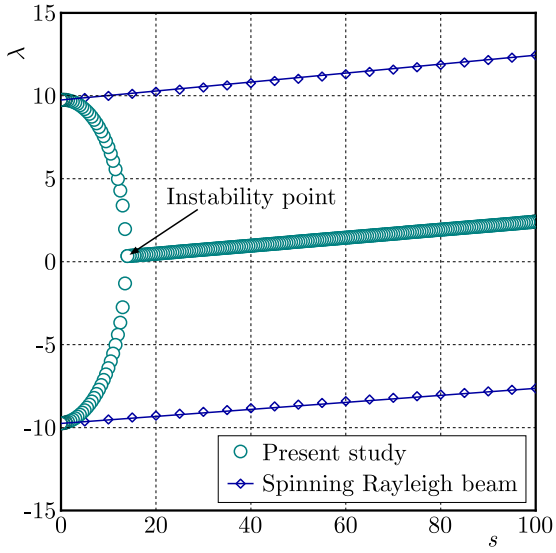

Fig. 6. Comparison of the dimensionless natural frequencies of the spinning shaft in the concentric cylinder filled with the incompressible fluid and spinning Rayleigh beams

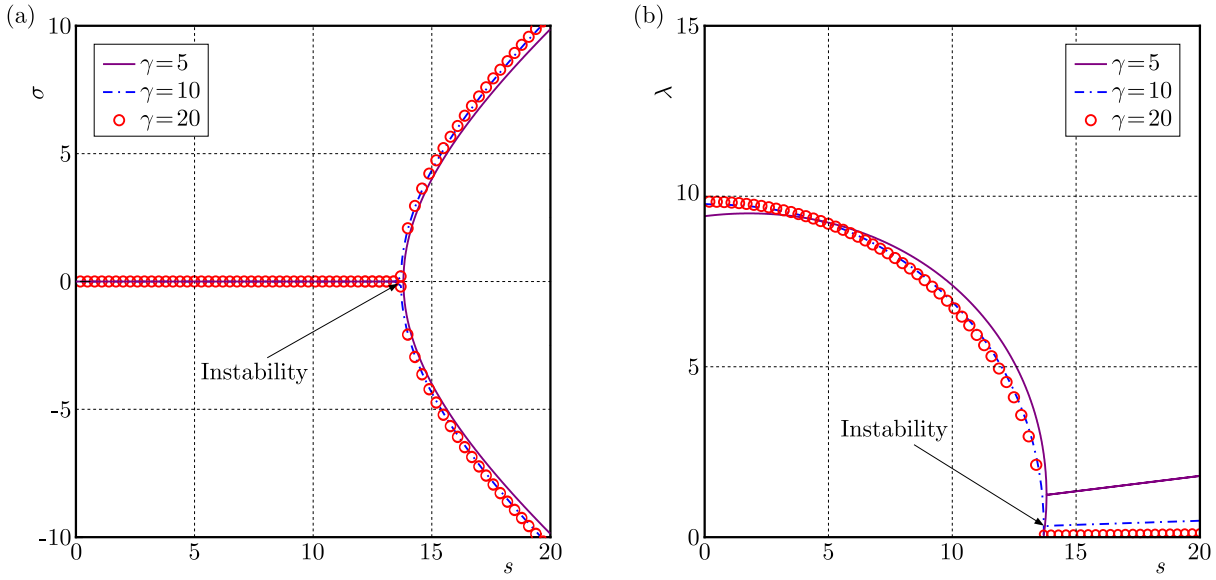

Fig. 7. Dimensionless natural frequency and damping for the spinning shaft versus the dimensionless spinning frequency with $n = 1$ and $\mu = 0.13$ for various values of the slenderness ratio: (a) dimensionless natural frequency, (b) dimensionless damping

Variations of the dimensionless natural frequency and damping of the system versus the dimensionless spinning speed at $n = 1$ and $\mu = 0.13$ for various values of the slenderness ratio are depicted in Fig. 7. It can be seen that for the first-order mode, the variation of the natural frequency of the system is not obvious with the increase of the slenderness ratio. Especially, when the value of the slenderness ratio is large ($\gamma \geqslant 10$), the natural frequency is generally

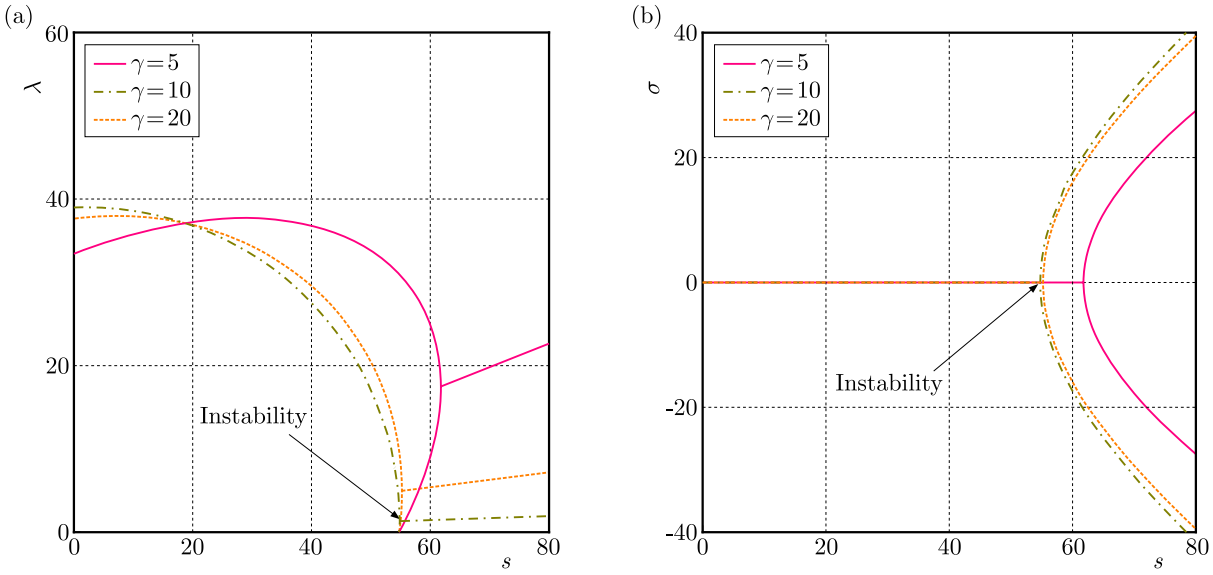

Fig. 8. Dimensionless natural frequency and damping of the spinning shaft versus the dimensionless spinning frequency with $n = 2$ and $\mu = 0.13$ for various values of the slenderness ratio: (a) dimensionless natural frequency, (b) dimensionless damping

consistent. It also can be seen in Fig. 7b that by increasing the slenderness ratio, the instability points are almost coincident. This means that the effect of slenderness ratio on the system instability can be negligible. However, it is interesting to note that for higher-order modes, the effect of the slenderness on the natural frequency and stability of the system is more pronounced. Figure 8 shows the dimensionless natural frequency and damping of the spinning shaft versus the dimensionless spinning frequency with $n = 2$ and $\mu = 0.13$ at different slenderness ratios. It can be found that as the slenderness ratio increases, the natural frequency of the system first increases and then decreases. At the same time, the instability critical spinning speed s_{cr} decreases. However, for large slenderness ratios ($\gamma \geqslant 10$), the variation of critical spinning speed is still not noticeable. This indicates that the smaller slenderness ratio leads to a greater effect on the stability of the system. Furthermore, the effects of the slenderness ratio on the unstable region of the considered spinning shaft system are reported in Fig. 9. Results show that the

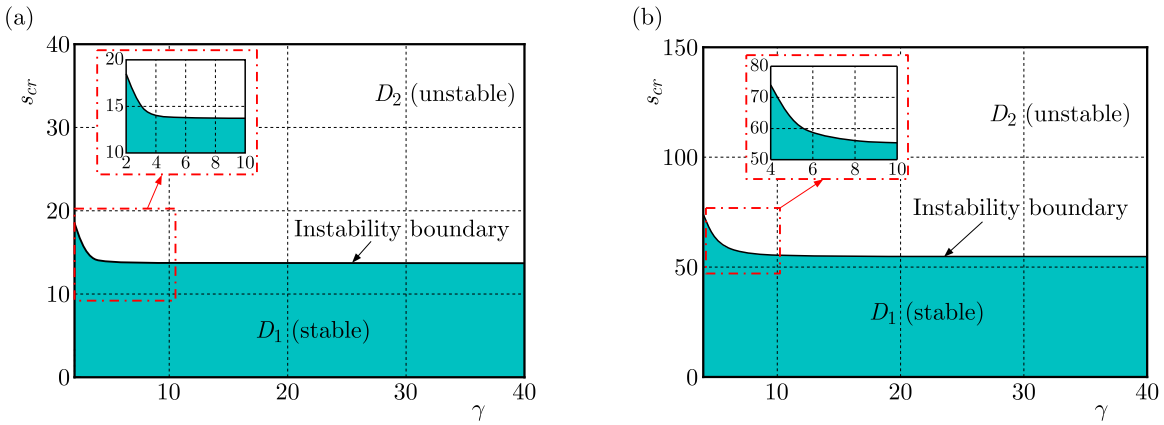

Fig. 9. Effects of the slenderness ratio γ on the instability of the spinning shaft system for different mode numbers: (a) $n = 1$, (b) $n = 2$

critical spinning speed experiences a smooth decrease and then converges to a constant value with an increase of the slenderness ratio. Also, the instability boundary is formed, and the whole speed domain is divided into two parts, D_1 and D_2, where D_1 is the stable region and D_2 is

the unstable region. As shown in the subfigure of Fig. 9, the instability boundary only changes when the slenderness ratio is small enough for both the first and second modes. Therefore, it can be concluded that at higher slenderness ratios, say $\gamma > 10$, the effect of rotary inertia on the system stability can be negligible.

The dimensionless natural frequency and damping of the considered spinning shaft system versus the dimensionless spinning frequency for a variety of density ratios at $n = 1$ and $\gamma = 10$ are plotted in Fig. 10. Figure 10a demonstrates that a higher value of density ratio leads to a lower value of natural frequency. Also, it can be observed in Fig. 10b that as the density ratio increases, the instability critical spinning speeds are reduced. This means that for larger density ratios, the system is more prone to lose its stability. Figure 11 shows the effect of density ratio on the instability of the system. As can be seen, the instability boundary decreases with respect to the density ratio. The instability critical spinning speed gradually moves towards the low-speed region. The results indicate that the density of the external fluid plays a dominant role in the stability of the shaft system.

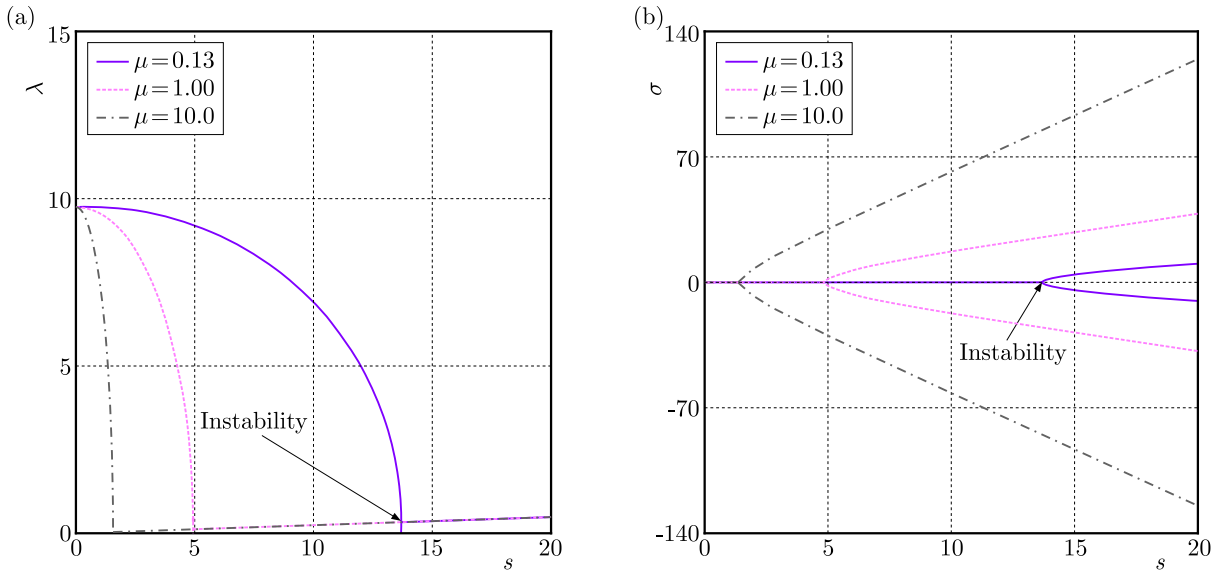

Fig. 10. Dimensionless natural frequency and damping of the spinning shaft versus the dimensionless spinning frequency with $n = 1$ and $\gamma = 10$ for various values of the density ratio: (a) dimensionless natural frequency, (b) dimensionless damping

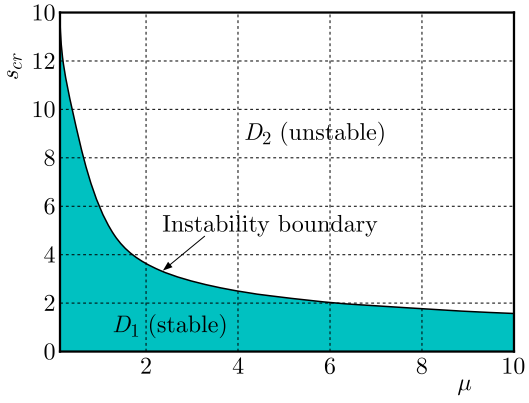

Fig. 11. Effects of the density ratio μ on the instability of the spinning shaft system

Moreover, the variations of critical spinning speeds for the considered spinning shaft versus the density ratio and slenderness ratio are presented in Fig. 12. In this figure, by increasing the

density ratio, the critical spinning speeds of the shaft decrease in each order. Also, by increasing the slenderness ratio, the critical spinning speeds change smoothly. In particular, the critical spinning speed approaches almost a constant value when the aspect ratio is sufficiently large.

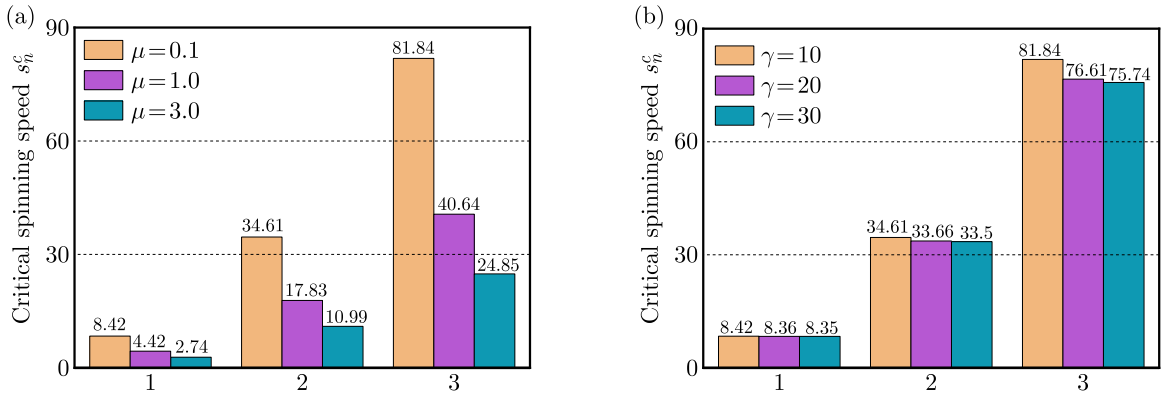

Fig. 12. Effects of main parameters on the critical spinning speed S_n^c: (a) density ratio μ, (b) slenderness ratio γ

5. Conclusions

In this study, stability of a spinning shaft in a concentric cylinder filled with an incompressible fluid has been theoretically addressed. The two-dimensional Navier-Stokes equations and continuity equation for the external fluid in the steady state were established, and the external fluid forces exerted on the shaft were calculated by using Taylor expansion. The governing equation of motion of the spinning shaft was formulated on the basis of Rayleigh beam theory. For pinned--pinned end supports, the explicit characteristic frequency equation has been derived analytically. The effects of slenderness ratio and density ratio on the natural frequencies and instability of the spinning shaft were investigated. The results showed that the critical spinning speed of each order for the system becomes smaller and the shape of the whirl speed map changed significantly due to the influence of the external fluid. Also, it was found that the shaft became unstable at a certain speed. This result indicated that the external fluid was the main source of the rotational shaft instability. Based on the present work, it could be concluded that the instability of the system is not very sensitive for a large slenderness ratio. However, the density ratio plays a determinant role in the natural frequency and stability of the system. It was shown that by increasing the density ratio, the natural frequency of the system was reduced and the stability became weaker. In addition, the results revealed that the external fluid had a significant effect on the critical spinning speed of the shaft. It was seen that as the density ratio increased, the critical speed value of the system decreased gradually.

Acknowledgments

The authors would like to acknowledge the financial support of the National Natural Science Foundation of China (No. 51775093), Natural Science Foundation of Anhui Province (2208085QE150), and University Natural Science Research Project of Anhui Province (No. KJ2021A0159) to this work.

References

1. Abdollahi R., Firouz-Abadi R.D., Rahmanian M., 2021, On the stability of rotating pipes conveying fluid in annular liquid medium, *Journal of Sound and Vibration*, **494**, 115891
2. Aouadi M.A., Lakrad F., 2018, On mathematical modelling of linear flexural vibrations of spinning Rayleigh beams, *Journal of Sound and Vibration*, **430**, 17-35

3. Arvin H., 2019, On parametrically excited vibration and stability of beams with varying rotating speed, *Iranian Journal of Science and Technology-Transactions of Mechanical Engineering*, **43**, 2,177-185

4. Bahaadini R., Dashtbayazi M.R., Hosseini M., Khalili-Parizi Z., 2018, Stability analysis of composite thin-walled pipes conveying fluid, *Ocean Engineering*, **160**, 311-323

5. Bahaadini R., Saidi A.R., 2018, Stability analysis of thin-walled spinning reinforced pipes conveying fluid in thermal environment, *European Journal of Mechanics; A/Solids*, **72**, 298-309

6. Chen L.W., Ku D.M., 1990, Dynamic stability analysis of a rotating shaft by the finite element method, *Journal of Sound and Vibration*, **143**, 1, 143-151

7. Dwivedi A.R., Dhiman A., Sanyal A., 2022, Stratified shear-thinning fluid flow past tandem cylinders in the presence of mixed convection heat transfer with a channel-confined configuration, *Journal of Fluids Engineering*, **144**, 5, 051301

8. Ebrahimi-Mamaghani A., Forooghi A., Sarparast H., Alibeigloo A., Friswell M.I., 2021, Vibration of viscoelastic axially graded beams with simultaneous axial and spinning motions under an axial load, *Applied Mathematical Modelling*, **90**, 131-150

9. ElNajjar J., Daneshmand F., 2020, Stability of horizontal and vertical pipes conveying fluid under the effects of additional point masses and springs, *Ocean Engineering*, **206**, 106943

10. Firouz-Abadi R.D., Haddadpour H., 2010, The flexural instability of spinning flexible cylinder partially filled with viscous liquid, *Journal of Applied Mechanics*, **77**, 1, 1001

11. Gross P., Gürgöze M., Kliem W., 1993, Bifurcation and stability analysis of a rotating beam, *Quarterly of Applied Mathematics*, **51**, 4, 701-711

12. Katz R., 2001, The dynamic response of a rotating shaft subject to an axially moving and rotating load, *Journal of Sound and Vibration*, **246**, 5, 757-775

13. Kern D., Jehle G., 2016, Dynamics of a rotor partially filled with a viscous incompressible fluid, *PAMM*, **16**, 1, 279-280

14. Kheiri M., Païdoussis M.P., Del Pozo G.C., Amabili M., 2014, Dynamics of a pipe conveying fluid flexibly restrained at the ends, *Journal of Fluids and Structures*, **49**, 360-385

15. Li C., Miao X., Qiao R., Tang Q., 2021, Modeling method of bolted joints with micro--slip features and its application in flanged cylindrical shell, *Thin-Walled Structures*, **164**, 107854

16. Li Q., 2022, New approach for bearing fault diagnosis based on fractional spatio-temporal sparse low rank matrix under multichannel time-varying speed condition, *IEEE Transactions on Instrumentation and Measurement*, **71**, 1-12

17. Li S.J., Liu G.M., Kong W.T., 2014, Vibration analysis of pipes conveying fluid by transfer matrix method, *Nuclear Engineering and Design*, **266**, 78-88

18. Li X., Qin Y., Li Y. H., Zhao X., 2018, The coupled vibration characteristics of a spinning and axially moving composite thin-walled beam, *Mechanics of Advanced Materials and Structures*, **25**, 9, 722-731

19. Liang F., Gao A., Yang X.D., 2020, Dynamical analysis of spinning functionally graded pipes conveying fluid with multiple spans, *Applied Mathematical Modelling*, **83**, 454-469

20. Liang F., Yang X.D., Qian Y.J., Zhang W., 2018, Transverse free vibration and stability analysis of spinning pipes conveying fluid, *International Journal of Mechanical Sciences*, **137**, 195-204

21. Manchi V., Sujatha C., 2021, Torsional vibration reduction of rotating shafts for multiple orders using centrifugal double pendulum vibration absorber, *Applied Acoustics*, **174**, 107768

22. Michaelides E.E., Feng Z.G., 2023, Drag coefficients of non-spherical and irregularly-shaped particles, *Journal of Fluids Engineering*, **145**, 6, 1-74

23. Oyelade A.O., Oyediran A.A., 2020, Imperfect bifurcation and chaos of slightly curved carbon nanotube conveying hot pressurized fluid resting on foundations, *Journal of Fluids Engineering*, **142**, 11

24. Païdoussis M.P., Issid N.T., 1974, Dynamic stability of pipes conveying fluid, *Journal of Sound and Vibration*, **33**, 3, 267-294

25. Qian Q., Wang L., Ni Q., 2009, Instability of simply supported pipes conveying fluid under thermal loads, *Mechanics Research Communications*, **36**, 3, 413-417

26. Saeed N.A., 2019, On vibration behavior and motion bifurcation of a nonlinear asymmetric rotating shaft, *Archive of Applied Mechanics*, **89**, 9, 1899-1921

27. Sahebnasagh M., Nikkhah-Bahrami M., Firouz-Abadi R.D., 2018, Effect of multiphase fluid and functionally graded density fluid on the stability of spinning partially-filled shells, *International Journal of Mechanical Sciences*, **140**, 109-118

28. Shahgholi M., Khadem S.E., Bab S., 2014, Free vibration analysis of a nonlinear slender rotating shaft with simply support conditions, *Mechanism and Machine Theory*, **82**, 128-140

29. Sheu G.J., Yang S.M., 2005, Dynamic analysis of a spinning Rayleigh beam, *International Journal of Mechanical Sciences*, **47**, 157-169

30. Tao M.D., Zhang W., 2002, Dynamic stability of a flexible spinning cylinder partially filled with liquid, *Journal of Applied Mechanics*, **69**, 5, 708-710

31. Wang G.D., Yuan H.Q., 2018, An analysis of dynamic stability for a flexible rotor filled with liquid, *Physics of Fluids*, **30**, 3, 037101

32. Wang G., Yuan H., 2019a, Dynamic stability analysis of a flexible rotor filled with liquid based on three-dimensional flow, *Journal of Fluids Engineering*, **141**, 5

33. Wang G.D., Yuan H.Q., 2019b, Stability analysis of a flexible rotor partially filled with two liquid phases, *Physics of Fluids*, **31**, 017103

34. Wang G.D., Yuan H.Q., 2021, Dynamics and stability analysis of an axially functionally graded hollow rotor partially filled with liquid, *Composite Structures*, **266**, 113821

35. Wang H.F., Chen C., 2020, Stability analysis of a rotor system with fluid applying wave resonance theory, *Physics of Fluids*, **32**, 5, 054106

36. Wang H.F., Chen G., Jiang G.Y., 2021, Stability analysis of an anisotropic rotor partially filled with viscous incompressible fluid based on Andronov-Hopf bifurcation, *Physics of Fluids*, **33**, 6, 064111

37. Yang S., Hu H., Mo G., Zhang X., Qin J., Yin S., Zhang J., 2021, Dynamic modeling and analysis of an axially moving and spinning Rayleigh beam based on a time-varying element, *Applied Mathematical Modelling*, **95**, 409-434

38. Zhang Y., Yang X., Zhang W., 2020a, Modeling and stability analysis of a flexible rotor based on the Timoshenko beam theory, *Acta Mechanica Solida Sinica*, **33**, 3, 281-293

39. Zhang J.W., Zhu L., Chen P., Wu Q.M., Wei M., Yin C.L., Li G.L., 2020b, Flowing interaction between cutting edge of ploughbreast with soil in shifting tillage operations, *Engineering Applications of Computational Fluid Mechanics*, **14**, 1, 1404-1415

40. Zhou X.W., Dai H.L., Wang L., 2018, Dynamics of axially functionally graded cantilevered pipes conveying fluid, *Composite Structures*, **190**, 112-118

41. Zhu K., Chung J., 2019, Vibration and stability analysis of a simply-supported Rayleigh beam with spinning and axial motions, *Applied Mathematical Modelling*, **66**, 362-382

42. Zhu L., Luo F., Qi Y.Y., Wei M., Ge J.R., Liu W.L., Li G.L., Jen T.C., 2018, Effects of spray angle variation on mixing in a cold supersonic combustor with kerosene fuel, *Acta Astronautica*, **144**, 1-11

Manuscript received March 7, 2023; accepted for print June 12, 2023

JOURNAL OF THEORETICAL AND APPLIED MECHANICS
61, 4, pp. 673-685, Warsaw 2023
https://doi.org/10.15632/jtam-pl/170730

STUDY ON SEISMIC GROUND MOTION OF *P*-WAVE INCIDENT ELASTIC FOUNDATION FREE FIELD UNDER THERMAL EFFECT

Yiqi Yang
School of Civil Engineering, Qinghai University, Xining, China
Qiang Ma
School of Civil Engineering, Qinghai University, Xining, China; and
Qinghai Provincial Key Laboratory of Energy-saving Building Materials and Engineering Safety, Xining, China
corresponding author Qiang Ma, e-mail: maqiang0104@163.com

This study extends the traditional problem of a seismic response of elastic foundations under isothermal conditions when considering thermal effects. Firstly, a free-field model of the elastic foundation is established under the incidence of plane *P*-waves. Then, utilizing the principles of wave propagation in a homogeneous and isotropic thermoelastic medium and the principle of Helmholtz vector decomposition, the influence of thermal physical parameters such as thermal conductivity, medium temperature on seismic ground motion of the free--field on elastic foundation is investigated, which provides a reasonable explanation for the ground motion of a site under thermal effects.

Keywords: single-phase thermoelastic medium, free field, seismic ground motion, plane *P*-wave

1. Introduction

The problem of a site seismic respons, or the influence of site conditions on seismic wave propagation, has attracted much attention as one of the two major fluctuation problems in seismic engineering. The initial research on the seismic response problem of elastic foundations has been considering isothermal conditions. However, with the accelerated industrialization and modernization in various countries, the fields of petroleum engineering, pavement engineering, thermal engineering and chemical engineering are thriving. The impact of thermal effects, such as temperature fluctuations, on wave propagation characteristics in elastic media has garnered an increased attention of numerous scholars. Due to the mutual coupling between heat and force, the propagation of waves in elastic media is more complicated. Therefore, it is crucial to establish a free-field model that can reflect the actual site soil properties under non-isothermal conditions by considering thermal effects and studying seismic ground motion of the free field with elastic foundations.

The theory of uncoupled thermoelasticity was introduced by Duhamel (1837) and Neuman (1885), but it has two main limitations. The first limitation is that the theory assumes that the temperature does not affect the mechanical state of an elastomer, which does not follow the actual physical experiments. Secondly, the theory assumes that the propagation velocity of thermal waves is infinite, which is also physically unreasonable. Then Biot (1956) proposed the thermoelastic coupling theory, which resolves the first issue with the uncoupled theory, but unfortunately, the coupled theory still has the second limitation. To overcome this drawback, scholars proposed two generalized thermoelastic theories that allow thermal waves to propagate at finite velocities. Lord and Shulman (1967) introduced a new thermoelastic coupling theory to modify

Fourier's heat conduction theorem based on considering the effect of a flux-rate term, which allows prediction of finite velocities when thermal waves propagate. Green and Lindsay (1972) presented a generalized theory of thermoelasticity that modifies the Duhamel-Neumann relation and the energy balance equation. Based on previous studies, Green and Naghdi (1991) developed a novel thermodynamic model of deformed media, which explained the phenomenon of the thermal wave propagating at a finite speed in detail under the heat flow environment in rigid solids. Green and Naghdi (1993) then gave a detailed explanation and constructed a new thermoelasticity theory based on the thermodynamic model, which defined the heat flow as a heat wave propagating at a finite velocity. Tzou (1995a,b) introduced the heat flux phase delay time and temperature gradient phase delay time based on the previous studies to make corrections to Fourier's heat conduction theorem with a modification and proposed a two-phase lag model for single-phase thermoelastic media. Hetnarski and Ignaczak (1999) published a review paper on the representation within the scope of generalized thermoelasticity theory. Abouelregal (2011) presented basic control equations for generalized isotropic thermal elastomers without body forces and heat sources.

Scholars have extensively researched the propagation of thermoelastic waves in elastic media using the aforementioned generalized thermoelasticity theory. Sinha and Sinha (1974) as well as Sinha and Elsibai (1996, 1997) studied the reflection of thermoelastic waves at the interface of two semi-infinite media and from the free surface of a solid half-space, respectively. Abd--Alla and Al-Dawy (2000) explored the reflection phenomenon of SV waves in a thermoelastic medium. Sharma *et al.* (2003) investigated the problem of thermoelastic wave reflection from various boundaries of a solid half-space under different theories of generalized thermoelasticity. Furthermore, Singh (2005b) focused on the reflection of SV waves from the free surface of an elastic medium. Then Singh (2005a) went on to study the phenomenon of reflection of P and SV waves from the free surface of an elastic medium with thermal diffusion properties. Kumar and Sharma (2005) examined the reflection of a plane wave on a thermoelastic half-space boundary.

Although scholars at home and abroad have executed some studies on the propagation of thermoelastic waves in single-phase media and the reflection trouble on the interface of such media, there are few studies on seismic ground motion of a free field on a elastic foundation. Wang and Zhao (2022) studied the seismic response of subsurface structures in single--phase soils. Zhao *et al.* (2022) studied the seismic response of elastic foundations under the action of Rayleigh waves. However, previous studies have been on the seismic ground motion of the free field of elastic foundations under isothermal conditions. No papers have investigated the effect of the incident plane waves on the free field of elastic foundations on the seismic ground motion under thermal effects. However, the thermal effect significantly affects the wave propagation characteristics. The impact of heat on elastic wave propagation is related to numerous seismological and astrophysical issues, thereby holding far-reaching significance for researching seismic motion analysis of free sites considering the effect of heat. Moreover, this study offers a plausible explanation for the seismic ground motion of a site under the impact of heat and provides technical support for the seismic design of large structures in the area.

In this paper, based on the fluctuation equation of a single-phase thermoelastic medium established by Liu *et al.* (2021), the corresponding fluctuation equation of a thermoelastic medium is solved in the right-angle coordinate system. The free-field model of the elastic foundation is established, the wave field of the site is analyzed, and the analytical solution of each amplitude coefficient is obtained by combining the wave field function and the corresponding boundary conditions. Finally, the impact of thermal physical parameter such as medium temperature on the ground motion of the earthquake site is analyzed.

2. Field fluctuation equation for elastic media

Bedrock layers I and II are simulated with the use of a single-phase thermoelastic medium. According to the generalized thermoelasticity theory, the fluctuation equation for a single-phase thermoelastic medium was proposed (Liu *et al.*, 2021) as follows

$$\begin{aligned}&\mu_e\nabla^2\mathbf{u}^s+(\lambda_e+\mu_e)\nabla(\nabla\cdot\mathbf{u}^s)-3K_b\beta_s\nabla T=\rho^e\ddot{\mathbf{u}}^s\\&3K_b\beta_sT_0\nabla\cdot(\dot{\mathbf{u}}^s+\tau_{qe}\ddot{\mathbf{u}}^st)+\rho^ec_{se}(\dot{T}+\tau_{qe}\ddot{T})=K_e\nabla^2(T+\tau_{\theta e}\dot{T})\end{aligned}\tag{2.1}$$

where $K_b=(\lambda_e+2\mu_e)/3$ – bulk modulus, λ_e and μ_e – Lame's constant of the single-phase medium, β_s – thermal expansion coefficient, ρ_e – density, c_{se} – specific heat capacity of the solid phase, τ_{qe} – phase-lag of the heat flux, $\tau_{\theta e}$ – phase-lag of the gradient of temperature, T – Kelvin medium temperature, T_0 – initial temperature, K_e – thermal conductivity, $\mathbf{u}^s$ – solid phase displacement.

According to the decomposition principle of the Helmholtz vector, the solid phase displacement vector can be decomposed as follows

$$\mathbf{u}^s=\nabla\psi_s+\nabla\times\mathbf{H}^s\tag{2.2}$$

where ψ_s denotes the scalar potential function of the solid skeleton and $\mathbf{H}^s$ denotes the vector potential function of the solid skeleton.

The potential function in a solid-phase medium can be assumed as

$$\begin{aligned}&\psi^s=A^s\exp[\mathrm{i}(k_px-\omega t)]\qquad\mathbf{H}^s=\mathbf{B}^s\exp[\mathrm{i}(k_sx-\omega t)]\\&T=A^T\exp[\mathrm{i}(k_px-\omega t)]\end{aligned}\tag{2.3}$$

where A^s and $\mathbf{B}^s$ represent amplitudes of the corresponding potential functions, k_p denotes the complex wave number of P-wave (including T-wave), k_s denotes the complex wave number of S-wave, i denotes the imaginary number which satisfies $\mathrm{i}=\sqrt{-1}$, ω is the angular frequency.

Substiting Eq. (2.2) into Equations (2.1) and then combining the resulting equations with Eqs. (2.3), the theoretical derivation leads to the characteristic equation for the bulk wave in a thermoelastic single-phase solid medium as follows

$$\begin{vmatrix}k_{11}&k_{12}\\k_{21}&k_{22}\end{vmatrix}=0\qquad|\rho^e\omega^2-\mu_ek_s^2|=0\tag{2.4}$$

By solving characteristic equations (2.4), it is known that there are two compressional waves (containing thermal waves) and one shear wave in a single-phase thermoelastic medium.

3. Wavefield analysis

Consider a plane P-wave with a frequency of ω that is incident upon the interface between single-phase thermoelastic media I and II at an arbitrary angle φ, originating from the bedrock layer. The resulting wave propagates and generates three types of reflected waves (reflected P-, S- and T-wave) as well as three types of transmitted waves (transmitted P-, T- and S-wave) within both media. The entire process is depicted in Fig. 1. As the seismic wave continues to propagate in the elastic medium, the reflected P-, T- and S-wave are generated at the interface between the single-phase thermoelastic medium II and the free surface.

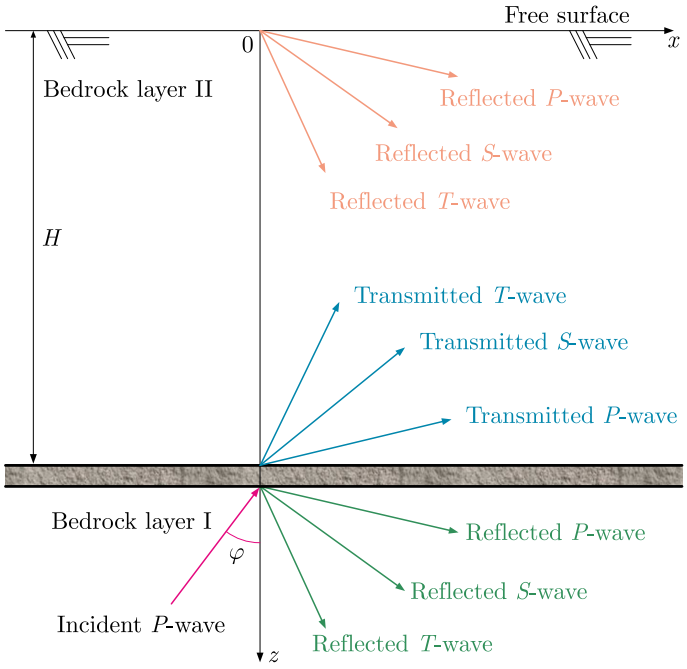

Fig. 1. Simplified model of the elastic foundation free field

3.1. Wave field functions and their solutions

The paper expresses the functional form of the wave field in both single-phase media I and II as follows:

(1) In bedrock layer I ($z > H$)

— P-wave

$$\begin{aligned}\psi^e = {} & A^s_{ip1}\exp[\mathrm{i}k_{ip1}(l_{ip1}x - n_{ip1}z - c_{ip1}t)] \\ & + \sum_{n=1}^{2} A^s_{1rpn}\exp[\mathrm{i}k_{1rpn}(l_{1rpn}x + n_{1rpn}z - c_{1rpn}t)]\end{aligned} \tag{3.1}$$

— T-wave

$$\begin{aligned}T^e = {} & A^s_{ip1}\delta^e_{Tp1}\exp[\mathrm{i}k_{ip1}(l_{ip1}x - n_{ip1}z - c_{ip1}t)] \\ & + \sum_{n=1}^{2} A^s_{1rpn}\delta^e_{Tpn}\exp[\mathrm{i}k_{1rpn}(l_{1rpn}x + n_{1rpn}z - c_{1rpn}t)]\end{aligned} \tag{3.2}$$

— S-wave

$$\mathbf{H}^e = \mathbf{B}_{1rs}\exp[\mathrm{i}k_{1rs}(l_{1rs}x + n_{1rs}z - c_{1rs}t)] \tag{3.3}$$

(2) In bedrock layer II ($0 < z < H$)

— P-wave

$$\begin{aligned}\psi^u = {} & \sum_{n=1}^{2} A_{tpn}\exp[\mathrm{i}k_{tpn}(l_{tpn}x - n_{tpn}z - c_{tpn}t)] \\ & + \sum_{n=1}^{2} A_{2rpn}\exp[\mathrm{i}k_{2rpn}(l_{2rpn}x + n_{2rpn}z - c_{2rpn}t)]\end{aligned} \tag{3.4}$$

— T-wave

$$T^u = \sum_{n=1}^{2} A^s_{tpn}\delta^u_{Tpn}\exp[\mathrm{i}k_{tpn}(l_{tpn}x - n_{tpn}z - c_{tpn}t)] + \sum_{n=1}^{2} A^s_{2rpn}\delta^u_{Tpn}\exp[\mathrm{i}k_{2rpn}(l_{2rpn}x + n_{2rpn}z - c_{2rpn}t)] \tag{3.5}$$

— S-wave

$$\mathbf{H}^u = \mathbf{B}_{2ts}\exp[\mathrm{i}k_{2ts}(l_{2ts}x - n_{2ts}z - c_{2ts}t)] + \mathbf{B}_{2rs}\exp[\mathrm{i}k_{2rs}(l_{2rs}x + n_{2rs}z - c_{2rs}t)] \tag{3.6}$$

where the subscripts i, r and t correspond to the incident, reflected and transmitted waves, respectively. β denotes different reflected P-wave (including T-wave) in single-phase medium I ($\beta = 1, 2$), and n denotes different reflected and transmitted P-wave (including T-wave) in single-phase medium II ($n = 1, 2$). k_{ip1} and c_{ip1} represent the wave number and velocity of the incident P-wave, respectively. $k_{1rp\beta}$ and k_{1rs} denote complex wave numbers of two reflected compressional waves (P-wave and T-wave) and one reflected shear wave (S-wave) in single-phase thermoelastic medium I, respectively. $c_{1rp\beta}$ and c_{1rs} denote wave velocities of the two reflected compressional waves (P-wave, T-wave) and one reflected shear wave (S-wave) in single-phase thermoelastic medium I, respectively. k_{tpn} and k_{2ts} represent wave numbers of the transmitted P-wave (including T-wave) and transmitted S-wave in single-phase thermoelastic medium II, respectively. c_{tpn} and c_{2ts} represent velocities of the transmitted P-wave (including T-wave) and transmitted S-wave in single-phase medium II. k_{2rpn} and k_{2rs} represent wave numbers of the reflected P-wave (including T-wave) and reflected S-wave in single-phase medium II, respectively. c_{2rpn} and c_{2rs} denote velocities of the reflected P-wave (including T-wave) and reflected S-wave in single-phase medium II, respectively. l, n denotes the direction vector of the corresponding wave.

According to Snell's theorem, in single-phase medium I and adjacent single-phase medium II, the number of waves in the horizontal direction of each bulk wave must be equal, as follows

$$l_{ip}k_{ip} = l_{1rp1}k_{1rp1} = l_{1rp2}k_{1rp2} = l_{1rs}k_{1rs} = l_{tp1}k_{tp1} = l_{tp2}k_{tp2} = l_{2ts}k_{2ts} \tag{3.7}$$

Upon taking the derivative of Eqs. (2.4), one arrives at the amplitude ratio of the potential function between the P-wave and T-wave in the single-phase thermoelastic medium:

$$\delta_{Tpn} = \frac{A_T}{A_S} = -\frac{k_{11}}{k_{12}} \qquad n = 1, 2 \tag{3.8}$$

3.2. Boundary conditions

(1) The boundary conditions at the interface between single-phase thermoelastic media I and II ($z = H$) are as follows:

— stress continuity at the cross-interface

$$\sigma_{zz} = \sigma^e_{zz} \qquad \sigma_{xz} = \sigma^e_{xz} \tag{3.9}$$

— the solid phase displacement at the interface is continuous

$$u^s_z = u^e_z \qquad u^s_x = u^e_x \tag{3.10}$$

— temperature and its change rate at the interface are continuous

$$T = T^e \qquad K\frac{\partial T}{\partial z} = K^e\frac{\partial T^e}{\partial z} \tag{3.11}$$

(2) At the interface between single-phase thermoelastic medium II and the free surface ($z = 0$), the following hold

$$\sigma_{zz} = 0 \qquad \sigma_{xz} = 0 \qquad \frac{\partial T}{\partial z} = 0 \tag{3.12}$$

The expression for the stress displacement in a single-phase medium is as follows

$$\begin{aligned} u_x &= \frac{\partial \psi^s}{\partial x} - \frac{\partial \mathbf{H}^s}{\partial z} \qquad u_z = \frac{\partial \psi^s}{\partial z} + \frac{\partial \mathbf{H}^s}{\partial x} \\ \sigma_{xz} &= \mu\Big(2\frac{\partial^2 \psi_s}{\partial x \partial z} + \frac{\partial^2 \mathbf{H}_s}{\partial x^2} - \frac{\partial^2 \mathbf{H}_s}{\partial z^2}\Big) \\ \sigma_{zz} &= \lambda\Big(\frac{\partial^2 \psi^s}{\partial x^2} + \frac{\partial^2 \psi^s}{\partial z^2}\Big) + 2\mu^e\Big(\frac{\partial^2 \psi^s}{\partial z^2} + \frac{\partial^2 \mathbf{H}^s}{\partial x \partial z}\Big) - 3K_b\beta_T T \end{aligned} \tag{3.13}$$

The wave field functions Eqs. (3.1) to (3.3) and Eqs. (3.4) to (3.6) are substituted into the boundary conditions Eqs. (3.9) to (3.11) and (3.12) to obtain each amplitude coefficient, which may be represented as a system of linear equations

$$\mathbf{FN} = A_{ip}\mathbf{G} \tag{3.14}$$

where $\mathbf{N} = [A^s_{1rp1}, A^s_{1rp2}, B^s_{1rs}, A^s_{tp1}, A^s_{tp2}, B^s_{2ts}, A^s_{2rp1}, A^s_{2rp2}, B^s_{2rs}]^{\mathrm{T}}$, the elements f_{11}-f_{99} and g_1-g_9 in the matrix are given in Appendix A.

4. Free surface displacement

Upon determining the wave field, it is possible to calculate the displacement and stress on the site. By substituting Eqs. (3.4)-(3.6) into the relevant expression, the expressions for surface displacement U_x and U_z can be obtained

$$\begin{aligned} U_x &= A^s_{tp1}\mathrm{i}k_{tp1}l_{tp1} + A^s_{tp2}\mathrm{i}k_{tp2}l_{tp2} + A^s_{2rp1}\mathrm{i}k_{2rp1}l_{2rp1} + A^s_{2rp2}\mathrm{i}k_{2rp2}l_{2rp2} \\ &\quad + B^s_{2ts}\mathrm{i}k_{2ts}n_{2ts} - B^s_{2rs}\mathrm{i}k_{2rs}n_{2rs} \\ U_z &= -A^s_{tp1}\mathrm{i}k_{tp1}n_{tp1} - A^s_{tp2}\mathrm{i}k_{tp2}n_{tp2} + A^s_{2rp1}\mathrm{i}k_{2rp1}n_{2rp1} + A^s_{2rp2}\mathrm{i}k_{2rp2}n_{2rp2} \\ &\quad + B^s_{2ts}\mathrm{i}k_{2ts}l_{2ts} + B^s_{2rs}\mathrm{i}k_{2rs}l_{2rs} \end{aligned} \tag{4.1}$$

In this paper, the displacement amplification coefficients u_x/u_0 and u_z/u_0 of the free-field surface are used to characterize the surface displacement of the elastic foundation free-field, where the displacement amplification coefficient is expressed as the ratio of the displacement amplitude in the corresponding direction to the displacement amplitude of the incident wave u_0.

5. Numerical analysis

Through numerical calculations, the P-wave incident elastic foundation free site seismic ground motion under the thermal effects is studied, and the impact of parameters such as medium temperature, on seismic ground motion produced by the site are specifically analyzed. Among them, the material parameters of the single-phase thermoelastic medium are chosen according to Liu *et al.* (2021). Table 1 illustrates the necessary parameters for numerical simulations.

Table 1. Physical parameters of single-phase thermoelastic media

Material parameters						
Thermal conductivity K_e [J/s/m/K]	Density of soil particle ρ^e [Kg/m^3]	Solid phase heat c_{se} [J/kg/K]	Phase lag of the heat flux τ_{qe} [s]	Phase lag of gradient of temperature $\tau_{\theta e}$ [s]	Medium temperature T [K]	Thermal expansion coefficient β_{Te} [1/K]
3	2700	1046	$2.0 \cdot 10^{-7}$	$1.5 \cdot 10^{-7}$	293.2	$4.0 \cdot 10^{-4}$

Lamé constant λ_e [kPa]	Lamé constant μ^e [kPa]	Thermal conductivity K^u [[J/s/m/K]	The density of soil particle ρ^u [Kg/m^3]	Solid phase heat c_{ue} [J/kg/K]	Phase lag of heat flux τ_{qu} [s]	Phase lag of gradient of temperature $\tau_{\theta u}$ [s]
$12 \cdot 10^6$	$8 \cdot 10^6$	3	2700	1046	$2.0 \cdot 10^{-7}$	$1.5 \cdot 10^{-7}$

Medium temperature T [K]	Thermal expansion coefficient β_{Tu} [1/K]	Lamé constant λ^u [kPa]	Lamé constant μ^u [kPa]
293.2	$4.0 \cdot 10^{-4}$	$9 \cdot 10^6$	$4 \cdot 10^6$

5.1. Effect of thermal conductivity at different incident angles

As is commonly understood, the magnitude of thermal conductivity is indicative of the soil capacity for heat transmission. A higher thermal conductivity results in more intense atomic thermal motion and faster propagation of heat. Conversely, a lower thermal conductivity leads to slower atomic thermal motion and slower propagation of heat. To investigate the regularity of how changes in thermal conductivity affect the amplification coefficient of surface displacement, one must keep other parameters constant. Figure 2 illustrates the curves depicting the surface displacement amplification coefficient as a function of the angle of incidence for varying levels of thermal conductivity. Firstly, observing Fig. 2, it is apparent that the horizontal and vertical

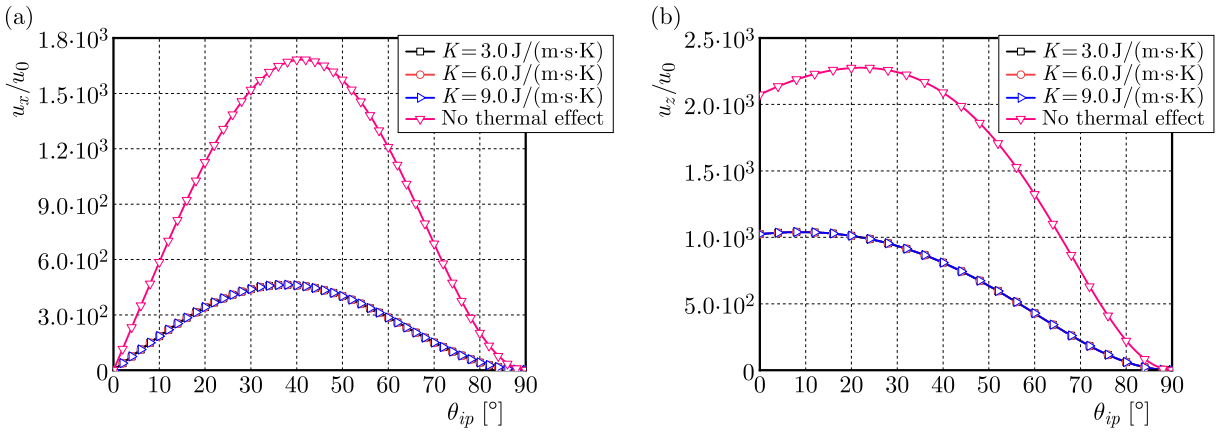

Fig. 2. Variation curve of the surface displacement amplification coefficient with the incident angle under different thermal conductivity

displacement amplification coefficients obtained for the two theoretical models considering the thermal effect and the other neglecting it have significant differences. When considering the thermal effect, the horizontal displacement amplification coefficient is similar to that without the thermal effect. However, the horizontal displacement amplification coefficient is smaller with the thermal effect. In the case of the vertical displacement amplification coefficient, both the

peak angle and the magnitude of the amplification coefficient are lower when thermal effects are considered. Furthermore, as depicted in Fig. 2, when taking thermal effects into account, both surface displacement amplification coefficients increase first and then decrease with a rise in the incidence angle. The horizontal and vertical displacement amplification coefficients reach the peak at the incidence angle $\varphi = 40°$ and $\varphi = 15°$, respectively. As the thermal conductivity increases, the surface displacement amplification coefficients undergo tiny changes. Thus, it is clear that the influence of considering thermal effects on the surface displacement amplification coefficient should not be disregarded.

5.2. Effect of thermal expansion coefficient at different incidence angles

To examine the influence of variations in thermal expansion coefficients on amplification coefficients of surface displacement, the other parameters are kept constant. Figure 3 displays the curves of the latter as a function of the incidence angle for varying levels of thermal expansion coefficients. Firstly, observing Fig. 3 that regardless of the value of the thermal expansion coefficient, when the P-wave is incident horizontally from the bedrock layer, the surface horizontal and vertical displacement amplification coefficients will be 0. The reason is that since the incident P-wave propagates in the horizontal direction, the transmission and reflection in single-phase medium II will disappear. That is, the free surface will not produce displacement. In addition, as the incident angle increases, the surface displacement amplification coefficients increase and then decrease, reaching the peak at the incident $\varphi = 40°$ and $\varphi = 15°$, respectively. Secondly, it can be found from Fig. 3 that with an increase in the thermal expansion coefficient, both the surface horizontal and vertical displacement amplification coefficient gradually decrease. As the incidence angle shifts, the impact of thermal expansion coefficients on the amplification coefficient of surface displacement becomes notably significant and thus cannot be dismissed.

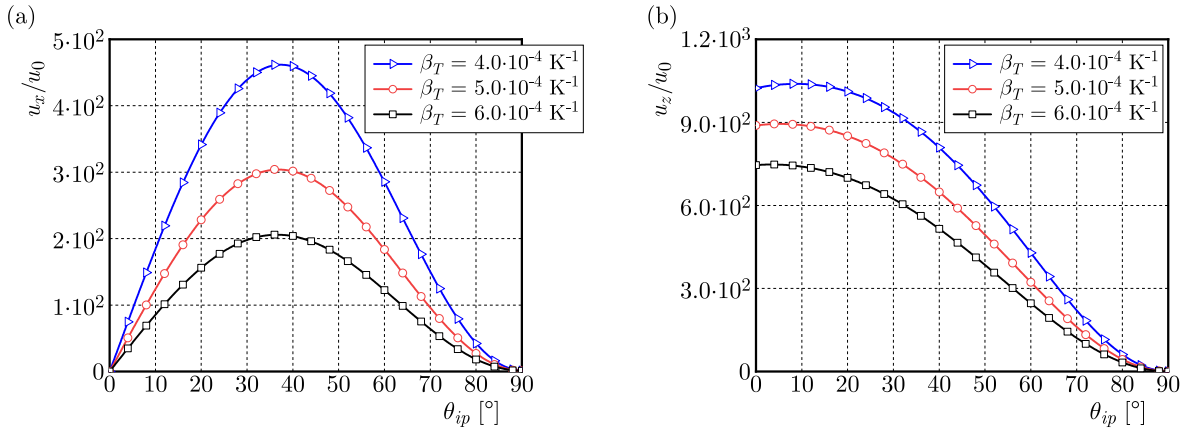

Fig. 3. Variation curve of the surface displacement amplification coefficient with the incident angle under different thermal expansion coefficient

5.3. Effect of medium temperature at different incidence angles

To investigate the impact of changing medium temperature on the displacement amplification coefficient of the ground surface, the other parameters are kept constant. Figure 4 illustrates how the amplification coefficient of ground surface displacement varies with the incidence angle for varying medium temperature levels. Firstly, observing Fig. 4, no matter what value the medium temperature takes with a change of the incident angle, the trend of the horizontal and vertical displacement amplification coefficient is the same. That is to say, with an increase in the incident angle, the displacement amplification of both factors increase first and then decrease, reaching the peak at the incident angle $\varphi = 40°$ and $\varphi = 15°$,respectively. Furthermore, it

is evident from Fig. 4 that the horizontal and vertical displacement amplification coefficient gradually decrease with a rise in medium temperature. It is apparent that changes in medium temperature significantly affect the ground displacement amplification coefficient as the incidence angle varies, and thus cannot be disregarded.

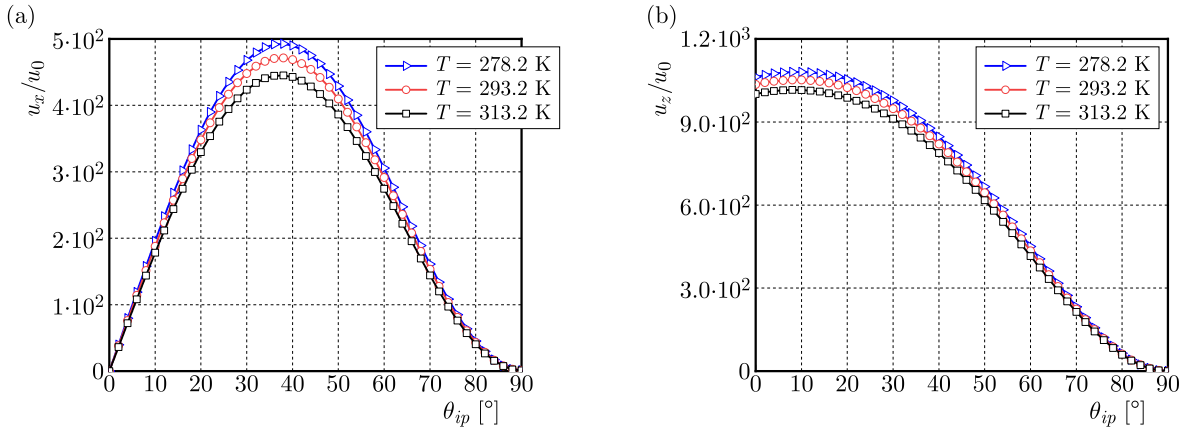

Fig. 4. Curves of the surface displacement amplification coefficient with the incident angle at different medium temperatures

5.4. Effect of the phase lag of the heat flux at different incidence angles

Compared the porous medium theory under isothermal conditions with thermoelastic theory, the T-wave will be generated. The phase lag of the heat flux plays a vital role in determining the fluctuation Eq. $(2.1)_2$ of the T-wave, and subsequently, affects its velocity. To investigate the influence of changes in the phase lag of the heat flux on the surface displacement amplification coefficient, the other parameters remain constant. Figure 5 displays the curves of the latter as a function of the incident angle for varying levels of the phase lag of the heat flux. Firstly, observing

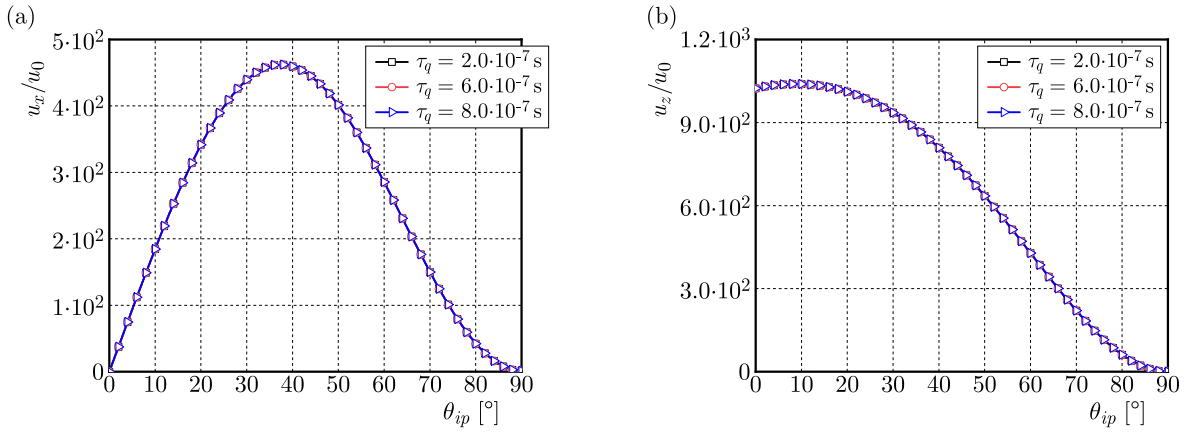

Fig. 5. The variation curve of the surface displacement amplification coefficient with the incidence angle under different phase lag of the heat flux

Fig. 5, both surface displacement amplification coefficients increase first and then decrease with a rise in the incidence angle and reach the peak at $\varphi = 40°$ and $\varphi = 15°$, respectively. Furthermore, it is evident from Fig. 5 that the horizontal and vertical displacement amplification coefficients just change slightly with an increase in the phase lag of the heat flux. According to the literature (Liu *et al.*, 2021), the change of the phase lag of the heat flux only affects the wave velocity of the T-wave but has little effect on the P-, S-wave. The velocity of the T-wave are several orders of magnitude lower than that of the P-, S-wave, so the horizontal and vertical displacement

amplification coefficients only change slightly with a rise in the phase lag of the heat flux, which also proves the correctness of the results in this paper. Observing Fig. 5, it becomes apparent that changes in the phase lag of the heat flux have a negligible impact on the surface displacement amplification factors as the incident angle is varied.

5.5. Effect of incident frequency at different incidence angles

To analyze the impact of altering the incident frequency on the amplification coefficient of surface displacement, the other parameters are constant. Figure 6 displays the relationship curves between the surface displacement amplification coefficient and incident angle as the frequency ω increases from 5 Hz to 15 Hz, 30 Hz, and finally 50 Hz. Upon initial observation of Fig. 6, it is apparent that both surface displacement amplification coefficients increase first and then decrease with a rise in the incidence angle. The horizontal and vertical displacement amplification coefficients reach the peak at the incidence angle $\varphi = 40°$ and $\varphi = 15°$, respectively. Furthermore, it can be observed from Fig. 6 that both the horizontal and vertical displacement amplification coefficients increase with a rise in the incident frequency, and the magnitude of the increase in displacement amplitude increases continuously. It can be seen that the effect of considering the change of incident frequency on the surface displacement amplification coefficient is not negligible.

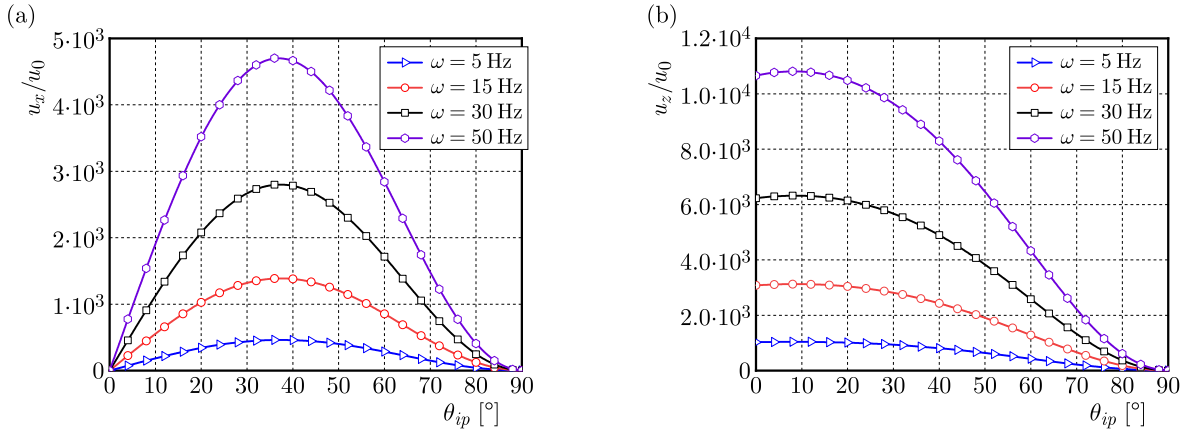

Fig. 6. The variation curve of the surface displacement amplification coefficient with the incidence angle under different incident frequencies

6. Conclusion

Based on the wave propagation theory in single-phase thermoelastic media, this paper studies seismic ground motion of the free field on an elastic foundation under a plane P-wave incidence. The influence of thermal physical parameters such as medium temperature on the seismic ground motion of the site is analyzed. The results indicate that:

- Significant differences are evident between the surface displacement amplification coefficients obtained under two theoretical models – one considering thermal effects and the other neglecting them.
- The surface displacement amplification coefficients decrease as the thermal expansion coefficient and medium temperature increase when the plane P-wave is incident upon the elastic foundation free-field under the thermal effects. The phase lag of the heat flux has a negligible impact on the surface displacement amplification coefficient.
- With a rise in the incident frequency, the surface displacement amplification coefficients gradually increase, and the amplitude of the increase becomes larger and larger.

Appendix A

$$f_{11}=[-(\lambda^e+2\mu^e n_{1rp1}^2)k_{1rp1}^2-3K_b^e\beta_T^e\delta_{TP1}^e]\exp(\mathrm{i}k_{1rp1}n_{1rp1}H)$$
$$f_{12}=[-(\lambda^e+2\mu^e n_{1rp2}^2)k_{1rp2}^2-3K_b^e\beta_T^e\delta_{TP2}^e]\exp(\mathrm{i}k_{1rp2}n_{1rp2}H)$$
$$f_{13}=-2\mu^e l_{1rs}n_{1rs}k_{1rs}^2\exp(\mathrm{i}k_{1rs}n_{1rs}H)$$
$$f_{14}=[(\lambda^u+2\mu^u n_{tp1}^2)k_{tp1}^2+3K_b^u\beta_T^u\delta_{TP1}^u]\exp(-\mathrm{i}k_{tp1}n_{tp1}H)$$
$$f_{15}=[(\lambda^u+2\mu^u n_{tp2}^2)k_{tp2}^2+3K_b^u\beta_T^u\delta_{TP2}^u]\exp(-\mathrm{i}k_{tp2}n_{tp2}H)$$
$$f_{16}=-2\mu^u l_{2ts}n_{2ts}k_{2ts}^2\exp(-\mathrm{i}k_{2ts}n_{2ts}H)$$
$$f_{17}=[(\lambda^u+2\mu^u n_{2rp1}^2)k_{2rp1}^2+3K_b^u\beta_T^u\delta_{TP1}^u]\exp(\mathrm{i}k_{2rp1}n_{2rp1}H)$$
$$f_{18}=[(\lambda^u+2\mu^u n_{2rp2}^2)k_{2rp2}^2+3K_b^u\beta_T^u\delta_{TP2}^u]\exp(\mathrm{i}k_{2rp2}n_{2rp2}H)$$
$$f_{19}=2\mu^u l_{2rs}n_{2rs}k_{2rs}^2\exp(\mathrm{i}k_{2rs}n_{2rs}H)$$
$$f_{21}=2\mu^e l_{1rp1}n_{1rp1}k_{1rp1}^2\exp(\mathrm{i}k_{1rp1}n_{1rp1}H)\qquad f_{22}=2\mu^e l_{1rp2}n_{1rp2}k_{1rp2}^2\exp(\mathrm{i}k_{1rp2}n_{1rp2}H)$$
$$f_{23}=\mu^e(l_{1rs}^2-n_{1rs}^2)k_{1rs}^2\exp(\mathrm{i}k_{1rs}n_{1rs}H)\qquad f_{24}=2\mu^u l_{tp1}n_{tp1}k_{tp1}^2\exp(-\mathrm{i}k_{tp1}n_{tp1}H)$$
$$f_{25}=2\mu^u l_{tp2}n_{tp2}k_{tp2}^2\exp(-\mathrm{i}k_{tp2}n_{tp2}H)\qquad f_{26}=\mu(n_{2ts}^2-l_{2ts}^2)k_{2ts}^2\exp(-\mathrm{i}k_{2ts}n_{2ts}H)$$
$$f_{27}=-2\mu^u l_{2rp1}n_{2rp1}k_{2rp1}^2\exp(\mathrm{i}k_{2rp1}n_{2rp1}H)$$
$$f_{28}=-2\mu^u l_{2rp2}n_{2rp2}k_{2rp2}^2\exp(\mathrm{i}k_{2rp2}n_{2rp2}H)$$
$$f_{29}=\mu^u(n_{2rs}^2-l_{2rs}^2)k_{2rs}^2\exp(\mathrm{i}k_{2rs}n_{2rs}H)\qquad f_{31}=n_{1rp1}k_{1rp1}\exp(\mathrm{i}k_{1rp1}n_{1rp1}H)$$
$$f_{32}=n_{1rp2}k_{1rp2}\exp(\mathrm{i}k_{1rp2}n_{1rp2}H)\qquad f_{33}=l_{1rs}k_{1rs}\exp(\mathrm{i}k_{1rs}n_{1rs}H)$$
$$f_{34}=n_{tp1}k_{tp1}\exp(-\mathrm{i}k_{tp1}n_{tp1}H)\qquad f_{35}=n_{tp2}k_{tp2}\exp(-\mathrm{i}k_{tp2}n_{tp2}H)$$
$$f_{36}=-l_{2ts}k_{2ts}\exp(-\mathrm{i}k_{2ts}n_{2ts}H)\qquad f_{37}=-n_{2rp1}k_{2rp1}\exp(\mathrm{i}k_{2rp1}n_{2rp1}H)$$
$$f_{38}=-n_{2rp2}k_{2rp2}\exp(\mathrm{i}k_{2rp2}n_{2rp2}H)\qquad f_{39}=-l_{2rs}k_{2rs}\exp(\mathrm{i}k_{2rs}n_{2rs}H)$$
$$f_{41}=-l_{1rp1}k_{1rp1}\exp(\mathrm{i}k_{1rp1}n_{1rp1}H)\qquad f_{42}=-l_{1rp2}k_{1rp2}\exp(\mathrm{i}k_{1rp2}n_{1rp2}H)$$
$$f_{43}=n_{1rs}k_{1rs}\exp(\mathrm{i}k_{1rs}n_{1rs}H)\qquad f_{44}=l_{tp1}k_{tp1}\exp(-\mathrm{i}k_{tp1}n_{tp1}H)$$
$$f_{45}=l_{tp2}k_{tp2}\exp(-\mathrm{i}k_{tp2}n_{tp2}H)$$
$$f_{46}=n_{2ts}k_{2ts}\exp(-\mathrm{i}k_{2ts}n_{2ts}H)\qquad f_{47}=l_{2rp1}k_{2rp1}\exp(\mathrm{i}k_{2rp1}n_{2rp1}H)$$
$$f_{48}=l_{2rp2}k_{2rp2}\exp(\mathrm{i}k_{2rp2}n_{2rp2}H)\qquad f_{49}=-n_{2rs}k_{2rs}\exp(\mathrm{i}k_{2rs}n_{2rs}H)$$
$$f_{51}=-\delta_{Tp1}^e\exp(\mathrm{i}k_{1rp1}n_{1rp1}H)\qquad f_{52}=-\delta_{Tp2}^e\exp(\mathrm{i}k_{1rp2}n_{1rp2}H)\qquad f_{53}=0$$
$$f_{54}=\delta_{Tp1}^u\exp(-\mathrm{i}k_{tp1}n_{tp1}H)\qquad f_{55}=\delta_{Tp2}^u\exp(-\mathrm{i}k_{tp2}n_{tp2}H)\qquad f_{56}=0$$
$$f_{57}=\delta_{Tp1}^u\exp(\mathrm{i}k_{2rp1}n_{2rp1}H)\qquad f_{58}=\delta_{Tp2}^u\exp(\mathrm{i}k_{2rp2}n_{2rp2}H)\qquad f_{59}=0$$
$$f_{61}=K^e n_{1rp1}k_{1rp1}\delta_{Tp1}^e\exp(\mathrm{i}k_{1rp1}n_{1rp1}H)\qquad f_{62}=K^e n_{1rp2}k_{1rp2}\delta_{Tp2}^e\exp(\mathrm{i}k_{1rp2}n_{1rp2}H)$$
$$f_{63}=0\qquad f_{64}=K^u n_{tp1}k_{tp1}\delta_{Tp1}^u\exp(-\mathrm{i}k_{tp1}n_{tp1}H)$$
$$f_{65}=K^u n_{tp2}k_{tp2}\delta_{Tp2}^u\exp(-\mathrm{i}k_{tp2}n_{tp2}H)\qquad f_{66}=0$$
$$f_{67}=-K^u n_{2rp1}k_{2rp1}\delta_{Tp1}^u\exp(\mathrm{i}k_{2rp1}n_{2rp1}H)$$
$$f_{68}=-K^u n_{2rp2}k_{2rp2}\delta_{Tp2}^u\exp(\mathrm{i}k_{2rp2}n_{2rp2}H)\qquad f_{69}=0\qquad f_{71}=f_{72}=f_{73}=0$$
$$f_{74}=(\lambda^u+2\mu^u n_{tp1}^2)k_{tp1}^2+3K_b^u\beta_T^u\delta_{TP1}^u\qquad f_{75}=(\lambda^u+2\mu^u n_{tp2}^2)k_{tp2}^2+3K_b^u\beta_T^u\delta_{TP2}^u$$
$$f_{76}=-2\mu^u l_{2ts}n_{2ts}k_{2ts}^2\qquad f_{77}=(\lambda^u+2\mu^u n_{2rp1}^2)k_{2rp1}^2+3K_b^u\beta_T^u\delta_{TP1}^u$$
$$f_{78}=(\lambda^u+2\mu^u n_{2rp2}^2)k_{2rp2}^2+3K_b^u\beta_T^u\delta_{TP2}^u\qquad f_{79}=2\mu^u l_{2rs}n_{2rs}k_{2rs}^2$$
$$f_{81}=f_{82}=f_{83}=0\qquad f_{84}=2\mu^u l_{tp1}n_{tp1}k_{tp1}^2\qquad f_{85}=2\mu^u l_{tp2}n_{tp2}k_{tp2}^2$$
$$f_{86}=\mu^u(n_{2ts}^2-l_{2ts}^2)k_{2ts}^2\qquad f_{87}=-2\mu^u l_{2rp1}n_{2rp1}k_{2rp1}^2$$
$$f_{88}=-2\mu^u l_{2rp2}n_{2rp2}k_{2rp2}^2\qquad f_{89}=\mu^u(n_{2rs}^2-l_{2rs}^2)k_{2rs}^2\qquad f_{91}=f_{92}=f_{93}=0$$

$$f_{94} = n_{tp1}^2 k_{tp1}^2 \delta_{Tp1}^u \qquad f_{95} = n_{tp2}^2 k_{tp2}^2 \delta_{Tp2}^u \qquad f_{96} = 0$$
$$f_{97} = n_{2rp1}^2 k_{2rp1}^2 \delta_{Tp1}^u \qquad f_{98} = n_{2rp2}^2 k_{2rp2}^2 \delta_{Tp2}^u \qquad f_{99} = 0$$
$$g_1 = (\lambda^e + 2\mu^e n_{ip1}^2) k_{ip1}^2 \exp(-\mathrm{i} k_{ip1} n_{ip1} H) + 3K_b^e \beta_T^e \delta_{Tp1}^e \exp(-\mathrm{i} k_{ip1} n_{ip1} H)$$
$$g_2 = 2\mu^e l_{ip1} n_{ip1} k_{ip1}^2 \exp(-\mathrm{i} k_{ip1} n_{ip1} H) \qquad g_3 = k_{ip1} n_{ip1} \exp(-\mathrm{i} k_{ip1} n_{ip1} H)$$
$$g_4 = l_{ip1} k_{ip1} \exp(-\mathrm{i} k_{ip1} n_{ip1} H) \qquad g_5 = \delta_{Tp1}^e \exp(-\mathrm{i} k_{ip1} n_{ip1} H)$$
$$g_6 = K^e n_{ip1} k_{ip1} \delta_{Tp1}^e \exp(-\mathrm{i} k_{ip1} n_{ip1} H) \qquad g_{7(1)} = g_{8(1)} = g_{9(1)} = 0$$

Acknowledgments

The authors gratefully acknowledge the financial support of the Qinghai Province Science and Technology Department Project (No. 2021-ZJ-943Q) and the Chinese Natural Science Foundation (Grant No. 52168053).

References

1. Abd-Alla A.N., Al-Dawy A.A.S., 2000, The reflection phenomena of SV-waves in a generalized thermoelastic medium, *International Journal of Mathematics and Mathematical Sciences*, **23**, 529-546
2. Abouelregal A.E., 2011, Rayleigh waves in a thermoelastic solid half space using dual-phase-lag model, *International Journal of Engineering Science*, **49**, 781-791
3. Biot M.A., 1956, Thermoelasticity and irreversible thermodynamics, *Journal of Applied Physics*, **27**, 240-253
4. Duhamel J., 1837, Some memoire sur les phenomenes phenomenon thermo-mechanique, *Journal de l'Ecole Polytechnique*, **15**
5. Green A.E., Lindsay K.A., 1972, Thermoelasticity, *Journal of Elasticity*, **2**, 1-7
6. Green A.E., Naghdi P.M., 1991, A re-examination of the basic postulates of thermomechanics, *Proceedings: Mathematical and Physical Sciences*, **432**, 1885
7. Green A.E., Naghdi P.M., 1993, Thermoelasticity without energy dissipation, *Journal of Elasticity*, **31**, 189-208
8. Hetnarski R.B., Ignaczak J., 1999, Generalized thermoelasticity, *Journal of Thermal Stresses*, **22**, 451-476
9. Kumar R., Sharma J.N., 2005, Reflection of plane waves from the boundaries of a micropolar thermoelastic half-space without energy dissipation, *International Journal of Applied Mechanics and Engineering*, **10**, 4
10. Liu H.B, Dai G.L, Zhou F.X., Mu Z.L., 2021, Propagation behavior of homogeneous plane-P1--wave at the interface between a thermoelastic solid medium and an unsaturated porothermoelastic medium, *The European Physical Journal Plus*, **136**, 1163
11. Lord H.W., Shulman Y., 1967, A generalized dynamical theory of thermoelasticity, *Journal of the Mechanics and Physics of Solids*, **15**, 299-309
12. Neumann F., 1885, *Vorlesungen Uber die Theorie der Elasticitat*, Meyer: Brestau
13. Sharma J.N., Kumar V., Chand D., 2003, Reflection of generalized thermoelastic waves from the boundary of a half-space, *Journal of Thermal Stresses*, **26**, 925-942
14. Singh B., 2005a, Reflection of P and SV waves from free surface of an elastic solid with generalized thermodiffusion, *Journal of Earth System Science*, **114**, 2
15. Singh B., 2005b, Reflection of SV waves from the free surface of an elastic solid in generalized thermoelastic diffusion, *Journal of Sound and Vibration*, **291**, 3-5, 764-778

16. Sinha A.N., Sinha S.B., 1974, Reflection of thermoelastic waves at a solid half-space with thermal relaxation, *Journal of Physics of the Earth*, **22**, 237-244

17. Sinha S.B., Elsibai K.A., 1996, Reflection of thermoelastic waves at a solid half-space with two relaxation times, *Journal of Thermal Stresses*, **19**, 749-762

18. Sinha S.B., Elsibai K.A., 1997. Reflection and refraction of thermoelastic waves at an interface of two semi-infinite media with two relaxation times, *Journal of Thermal Stresses*, **20**, 129-146

19. Tzou D.Y., 1995a, A unified field approach for heat conduction from macro- to micro-scales, *Journal of Heat Transfer*, **117**, 1, 8-16

20. Tzou D.Y., 1995b, Experimental support for the lagging behavior in heat propagation, *Journal of Thermophysics and Heat Transfer*, **9**, 4, 686-693

21. Wang X.B., Zhao F., 2022, Comparative study of seismic response of subsurface structures in single-phase soils and saturated soil, *Sichuan Cement*, **3**, 22-23+26

22. Zhao W.S., Chen W.Z., Yang D.S., Gao H., Xie P.Y., 2022, Analytical solution for seismic response of tunnels with composite linings in elastic ground subjected to Rayleigh waves, *Soil Dynamics and Earthquake Engineering*, **153**, 107113

Manuscript received May 16, 2023; accepted for print June 26, 2023

JOURNAL OF THEORETICAL AND APPLIED MECHANICS
61, 4, pp. 687-700, Warsaw 2023
https://doi.org/10.15632/jtam-pl/170243

NUMERICAL STUDY OF THE EFFECTS OF PROSTHESIS FOOT ASYMMETRY ON ENERGY CHARACTERS AND ROLL-OVER CHARACTERISTICS

Meijiao Jiang, Junxia Zhang

College of Mechanical Engineering, Tianjin University of Science and Technology, Tianjin, China

correspondence author Junxia Zhang, e-mail: zjx@tust.edu.cn

There is limited research available on the effect of asymmetric structure on the performance of the prosthesis. In this paper, 12 sets of prosthetic feet with asymmetric structures were developed using a planar polar coordinate system. The effect of asymmetry on the prosthesis performance was investigated. The prosthetic feet with asymmetric structures were modeled in a gradient manner within a polar coordinate system. A finite element (FE) model of the prosthetic walking process was formulated, and dynamic simulations were conducted to simulate the loading of the prosthesis during the support phase. Evaluation indices such as energy characteristics, contact pressure and roll-over shape were selected to investigate the effects of the asymmetric structure. The results indicate that θ_1 and θ_3 asymmetry significantly affects strain energy density. Moreover, incorporating heel asymmetry proves to be more advantageous in reducing contact pressure of the prosthesis during the middle stance moment. The optimal parameters for asymmetric prostheses are determined based on these findings.

Keywords: biometric prosthetic foot, carbon fiber epoxy composites, roll-over shape, energy store and return character

1. Introduction

Proper amputee prosthetic component selection is critical in the improvement of the amputee care (Fridman *et al.*, 2003). Asymmetrically shaped prostheses were designed to improve patients' rehabilitation and quality of life. Preliminary studies were conducted on an asymmetrically shaped keel (Allard *et al.*, 1995) in the prosthetic foot design, and the results indicated that the asymmetrically shaped keel was more active in storing energy and improving amputee gait (Handzic, 2014) compared with a completely symmetrical one. However, the effect of asymmetric design of the prosthetic foot on user gait performance is unclear. There are three main types of methods for studying prostheses: theoretical calculations, testing of mechanical properties of prostheses and amputation gait analysis. The theoretical analysis method is primarily employed to calculate the angular stiffness of the forefoot and hindfoot (Adamczyk and Kuo, 2013). Calculated was mechanical efficiency during gait in adults with transtibial amputation (Prince *et al.*, 1998), and determined energy stored, dissipated and recovered in different ankle-foot prostheses (Prince *et al.*, 1994). Additionally, models of rigid segments of the prosthetic foot were developed (Fey *et al.*, 2013), and FE models provided to anticipate mechanical reactions to forces, moments and displacements (Tryggvason *et al.*, 2020). Furthermore, the finite element approach was used for dynamic simulation of prosthetic walking (Jang *et al.*, 2001).

Mechanical tests provide a valuable means to examine prosthetics, including forefoot and hindfoot stiffness, prosthetic energy storage characteristics and dynamic walking characteristics. For instance, Adamczyk *et al.*, (2013) used the linear compression method to measure angular

stiffness, whereas Adamczyk *et al.* (2017) adjusted stiffness of the forefoot and hindfoot components. They subsequently computed energy return of the prosthesis and assessed sensitivity of these variables to changes in component stiffness. Fey *et al.* (2011) conducted a comprehensive biomechanical investigation to evaluate the influence of foot stiffness on the prosthetic energy storage, energy return and mechanical efficiency during amputee walking. They incorporated forward dynamics models of amputee walking to further explore the impact of altered prosthetic foot stiffness on muscle and foot functions.

Gait analysis is used to study various parameters of amputee walking such as energy expenditure, gait asymmetry and prosthetic deformation. Gait characteristics under various types of walking conditions such as horizontal ground, ramps, self-selected and varying travel speeds are studied for their effects on gait, and dynamic joint stiffness is analyzed (Ármannsdóttir *et al.*, 2021). Among them, several specific gait moments such as heel strike, middle stand and toe-off are focused in (Adamczyk *et al.*, 2017). In previous studies, stiffness, energy, gait parameters and roll-over shape were the most commonly used prosthetic performance indicators (De Asha *et al.*, 2013; Adamczyk *et al.*, 2013; Hansen *et al.*, 2004a,n; Hansen and Childress, 2005).

The primary objective of this study is to examine the effect of asymmetric structure on the performance of prostheses. Addressing the limitations of prior research, this paper adopts a polar coordinate system to describe the location and degree of asymmetry of prostheses, thus filling the gap in quantitative investigations of structural asymmetry. The asymmetric foot model was established based on a commercially available carbon fiber ESAR foot (Össur Vari--flex®). Gait characteristics during the support phase of transtibial amputees were explored using a dynamic walking model. The asymmetric design of the prosthetic foot was investigated. Notably, this research presents an innovative application of contact pressure as an index for studying the effects of prosthetic asymmetry. The prosthetic model was derived from the Flex--Foot® Variflex® architecture and was studied both analytically and quantitatively using curved elements analysis as well as the Castigliano theorem (Hansen *et al.*, 2000).

2. Materials and methods

2.1. FE model

The transtibial prosthesis design model is based on the Össur Vari-flex® architecture (long $l = 241.523\,\text{mm}$, category 5). The prosthesis is made up of two carbon fiber (CF) composite leaf springs: one for the keel and one for the heel (see Fig. 1a). Both the keel and heel were made of laminates with the stack sequence $[\pm 45/0_n]_s$ as shown in Fig. 1b, with 45° cross-ply layers on top and bottom, n is the 0° fiber layer number which is determined according to the prostheses thickness H, s indicates symmetrical plied layers. The value of n can be obtained from the following equation

$$H = h(2+n)2 \tag{2.1}$$

where h is the thickness of the fiber layer.

The carbon blades are represented as flexible surface bodies. Each layer of the blades has its layer thickness, material characteristics, and fiber angle in the FE model. The model is created using ABAQUS.

In this work, a high strength carbon/epoxy prepreg (T300) was used. Its material properties are $E_{11} = 132\,\text{GPa}$, $E_{22} = E_{33} = 10.3\,\text{GPa}$, $G_{12} = 6.5\,\text{GPa}$, $G_{13} = 6.5\,\text{GPa}$, $G_{23} = 3.91\,\text{GPa}$, $\nu_{12} = 0.25$, $\nu_{13} = 0.25$, $\nu_{23} = 0.38$ and $\rho = 1570\,\text{kg/m}^3$.

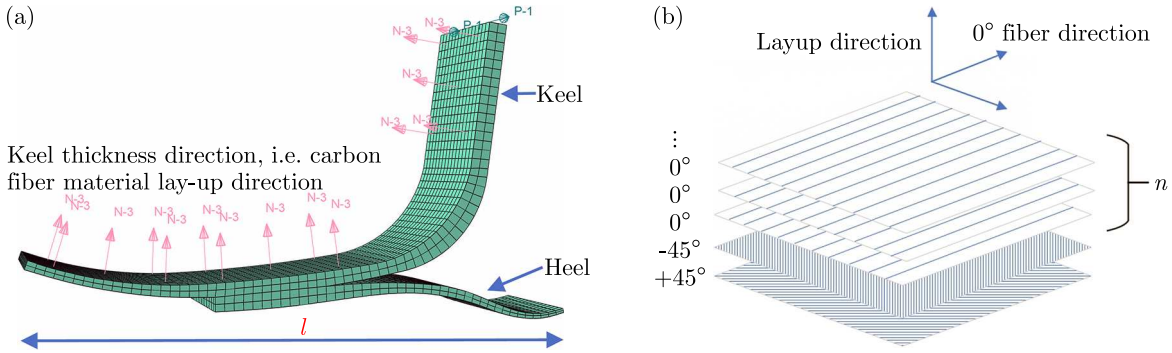

Fig. 1. (a) FE model of the prosthetic foot and (b) CF composite layer

2.2. Asymmetric prosthetic foot model

A planar polar coordinate system was established by taking the horizontal top view section of the prosthetic foot device. As shown in Fig. 2, l is length and w is width of the prosthesis. 'Toe' shows the toe direction, and 'Heel' is the position of the heel. Taking the geometric center of the insole as the origin of the polar coordinate system, denoted by O, ρ and θ are used to describe any point within the polar coordinates. Creating an asymmetric fillet at the left front position shown in Fig. 2, the radius of the fillet is denoted by r. The polar coordinates of this position are: $\rho = \sqrt{l^2 + w^2}/2 = \tan^{-1} w/l$, see Fig. 2.

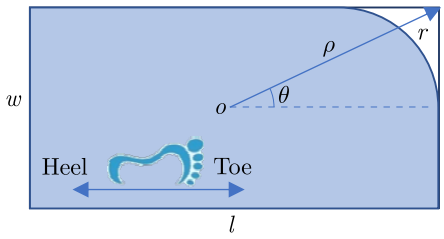

Fig. 2. Coordinate system of the asymmetric model

Fillets of different radii were created at each of the four corners of the prosthesis to create asymmetric models. The variables ρ, θ and r were used to describe the location and size of the asymmetric fillet (see Table 1). A total of twelve asymmetric prosthesis models were created.

Table 1. Asymmetric model fillet locations

ρ [mm]	θ [rad]	R_1 [mm]	R_2 [mm]	R_3 [mm]
$\rho = \sqrt{l^2 + w^2}/2$	$\theta_1 = \tan^{-1} w/l$	0	30	50
$\rho = \sqrt{l^2 + w^2}/2$	$\theta_2 = (\pi/2) + \tan^{-1} w/l$	0	20	30
$\rho = \sqrt{l^2 + w^2}/2$	$\theta_3 = \pi + \tan^{-1} w/l$	0	20	30
$\rho = \sqrt{l^2 + w^2}/2$	$\theta_4 = (3\pi/2) + \tan^{-1} w/l$	0	30	50

θ_1 and θ_4 are located at the front end of the keel placed on the inner and outer sides of the prosthetic foot, respectively. θ_2 and θ_3 are located at the back end of the keel, inside and outside.

2.3. Roll-over simulation

The prosthetic foot, loading frame and rotating platform are created for dynamic walking simulation according to ISO/TS 16955 (2016). The simulation shows results for a full roll-over

task of the prosthetic foot. One simulation cycle consists of the dynamic walking stance phase of a single gait step. The loading frame and the rotating platform were constructed as rigid bodies. A rigid beam is used to connect the fixed ankle of the foot to the loading frame, and rough contact without sliding is defined between the prosthetic foot and the surface of the rotating platform. The assembly model is shown in Fig. 3c. Transient structural analysis is carried out for the FE model of the foot. Figure 3a shows the simulation load-time curve according to ISO/TS 16955 (2016). The total time is a stance phase (0.6 s) of a standard gait cycle (1 s), and this load represents the ground reaction force of the stance phase of the amputation gait. Figure 3b shows the angle-time curve according to ISO/TS 16955 (2016). The loading frame is applied to simulate the amputee walking with a prosthesis in the right-side limb. The movement freedom of the top point A of the loading frame is equal to zero in the transverse plane, and the load Fig. 3a is applied to the top point of the loading frame, as shown in Fig. 3c. The rotating platform is assembled at a distance of 700 mm from the top point of the loading frame. The rotating platform is used to simulate the ground, where the platform rotates around point B. In the ISO standard, the ankle joint angle during walking is converted into ground rotation. During the support phase, the foot moves downward while the platform rotates, and it is pushed by point A. The ankle joint angle of the support phase is achieved by rotating the platform around point B. This can be seen in Fig. 3c, where the ankle angle is translated into rotation of the rotating platform around point B, and the load (Fig. 3b) is applied to the outside point B of the rotating platform to drive the rotation of the rotating platform to simulate the support phase in the amputation gait.

Taking three typical moments at $t_1 = 10$ ms $t_2 = 300$ ms and $t_3 = 600$ ms as 'heel-strike', 'middle-stance' and 'toe-off' positions of the prosthesis, the loading frame and the tilted rotating platform as well as the corresponding stress and deformations of the prosthesis are shown in Figs. 3d, 3e, 3f.

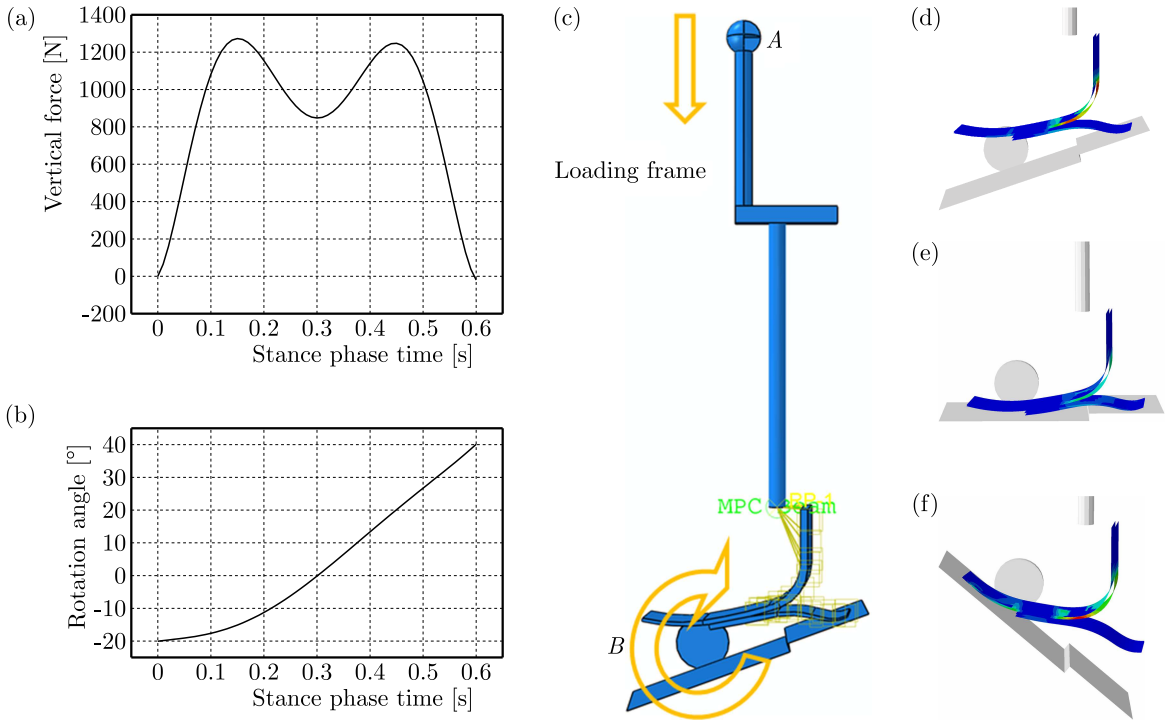

Fig. 3. Simulation process and the boundary condition diagram: (a) vertical force on the ball joint according to ISO/TS 16955, (b) rotation of tilt-table, as functions of the stance phase time, (c) boundary condition of full model transient simulation of ISO 16955 test procedure for a 600 ms loop, (d) showing stress at early heel-strike, at 10 ms, (e) mid-stance, at 300 ms, (f) toe-off at 600 ms

Twelve asymmetric prosthetic foot models were established according to the parameters ρ, θ and r in Table 1. The stance phase dynamic walking simulation was carried out for all the prosthetic foot models.

The strain energy, strain energy density, contact pressure and roll-over shape were extracted from the roll-over simulation, and used to discuss the gait characteristics of the asymmetric prosthetic foot structure.

2.4. Validation of simulation models

The simulation model was validated using the roll-over shape test data of the same series of different types of the prosthetic foot. The roll-over shape is expressed by the simulated CoP, the CoP is extracted from the foot and rotating contact points during the support phase roll--over simulation. No coordinate transformation is required because the simulation is set up with ground platform rotation and the relative position of the simulated leg is fixed. The comparison between the test data and the simulation data is shown in Fig. 4. The x-direction is the length direction of the prosthesis, and Y indicates the compression displacement of the foot-ground contact point on the lower surface of the prosthesis at each instant of the support phase.

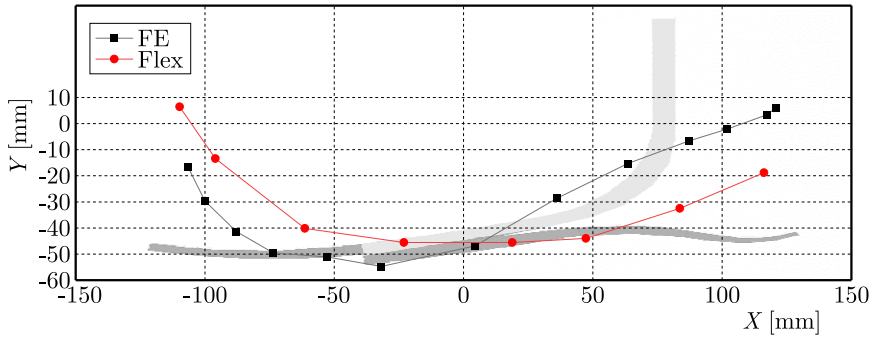

Fig. 4. Comparison of FE roll-over shape of the symmetrical-keel prosthetic foot and the test roll-over shape of the Össur Flexwalk prosthetic foot

As shown in the figure, the roll-over shape of the Flexwalk foot (Hansen *et al.*, 2000) is similar to the roll-over shape of the symmetric prosthetic foot simulation model, which proves that the simulation results are reliable.

3. Results and discussion

3.1. Strain energy density

The strain energy in the model is mainly stored in the heel part from the heel-strike to mid-stance period, and the keel part plays the main role in energy storage from the mid-stance to toe-off period. The following figure shows the heel strain energy density distribution at the heel-strike moment and the keel strain energy density cloud map at the toe-off moment. The strain energy density distribution for each asymmetric shape of the prosthesis are shown in Fig. 5, with the radius of the fillet in the first column, the polar angle in the first and fifth row to classify the asymmetric prosthesis model.

At the heel-strike moment, the strain energy is distributed in the middle and rear of the heel. The larger the asymmetric fillet, the larger the strain energy density distribution area is.

The keel component of the prosthetic foot is the main deformation component at the toe--off moment, and the strain energy is mainly distributed in the forefoot and midfoot. Forefoot

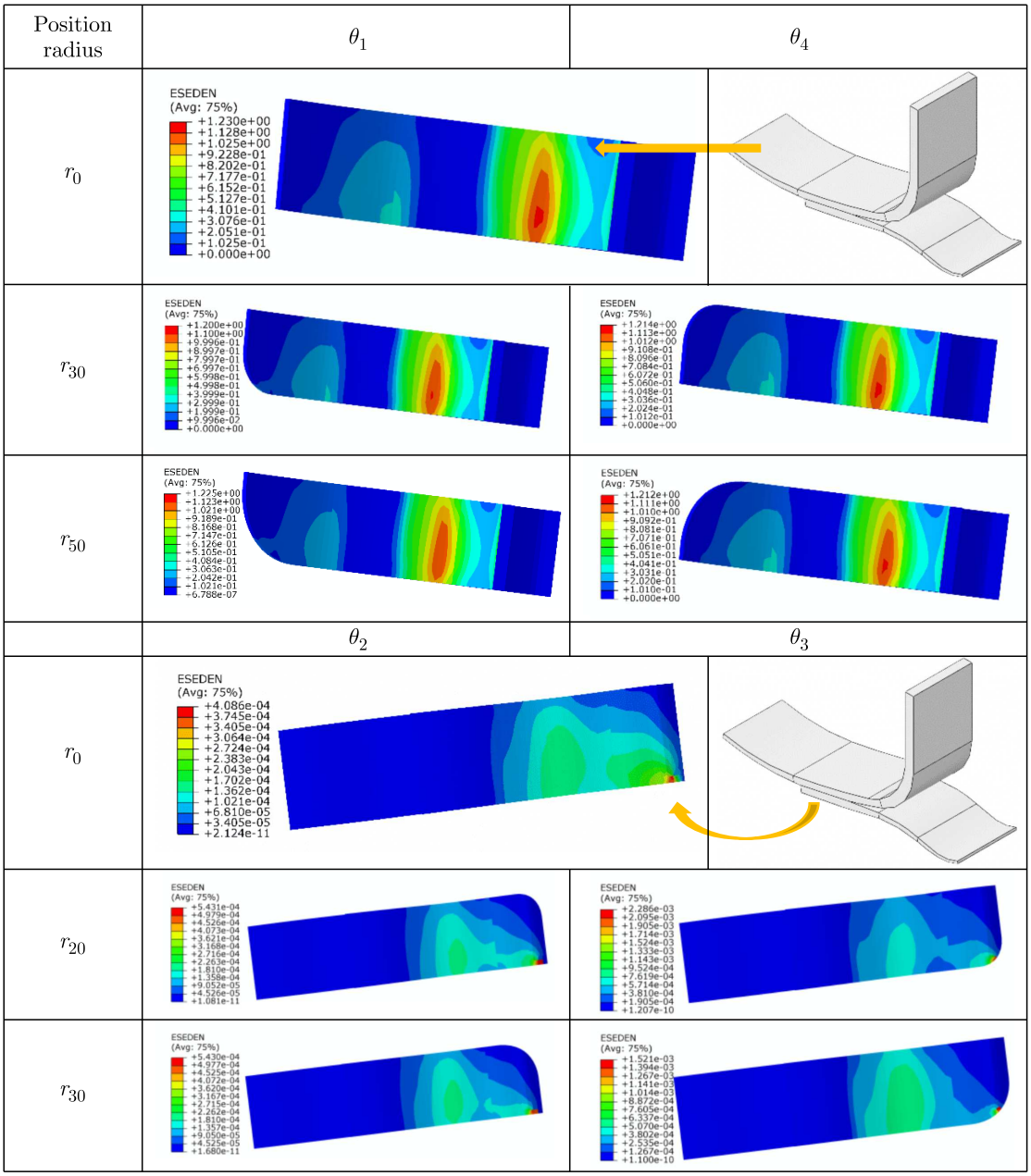

Fig. 5. Strain energy density distribution in the prosthetic foot model

asymmetry decreases the peak strain energy density, and forefoot asymmetry almost does not change the midfoot strain energy density distribution.

Figure 6 shows a comparison of the peak strain energy density for each prosthetic foot model. As shown in the figure, compared with the shape-symmetric prosthesis model, the peak strain energy density of the shape-asymmetric prosthesis model shows that the forefoot asymmetry slightly reduces the peak strain energy density. Compared with the heel symmetric prosthesis model, the heel asymmetry show an increase in the peak strain energy density, increase of θ_3 is significant, and the strain energy density of the r_{20} fillet shape asymmetric prosthetic model increases even more significantly.

As shown in Fig. 6, the strain energy density fluctuates considerably in magnitude due to the change of the asymmetry fillet radius. The θ_1 and θ_3 of the asymmetry shape prosthetic foot

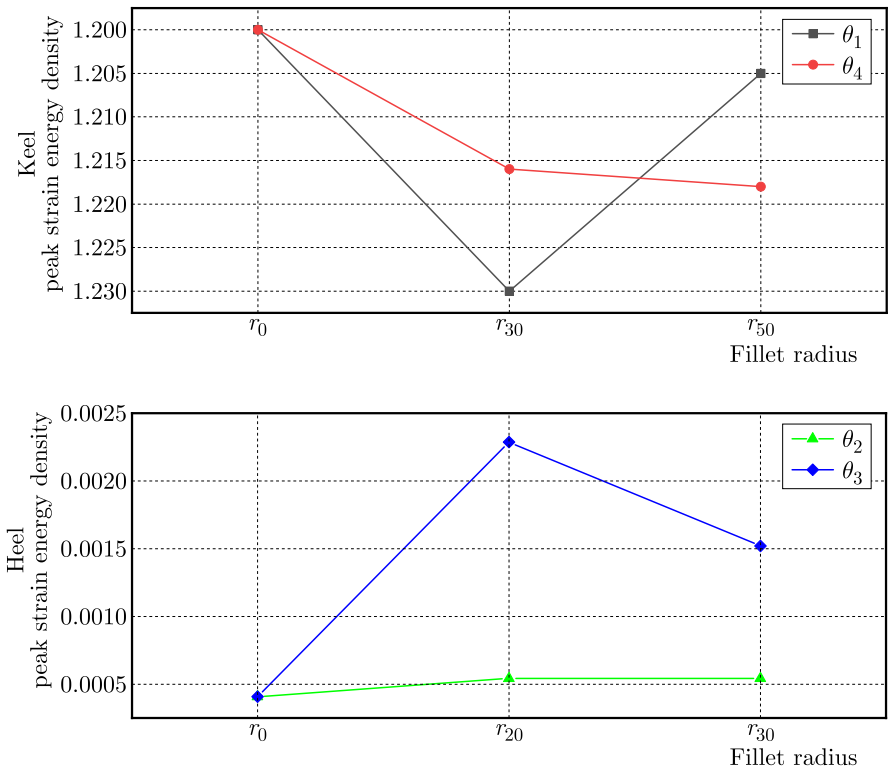

Fig. 6. Peak strain energy density of prosthetic foot models

have a relatively large effect on the strain energy density. The θ_2 and θ_4 of the asymmetry shape prosthetic foot have the least effect on the strain energy density.

3.2. Contact pressure

A comparison of the contact pressure between the symmetric and asymmetric shape prosthetic foot at the three characteristic moments of the support phase is shown in Fig. 7.

Comparing the contact pressure of the four groups of prosthetic foots, one can observe that the contact pressure of the θ_3 asymmetric prosthesis at the heel-strike is significantly higher than that of the symmetric prosthesis (Fig. 7 θ_3), and the contact pressure of the θ_1 and θ_4 asymmetric prosthesis at the toe-off is higher than that of the symmetric prosthesis (Fig. 7 θ_1, Fig. 7 θ_4). The θ_1 and θ_4 group of the prosthetic foot have an asymmetric shape in the keel front, i.e. toe shape asymmetric model, and the contact pressure of the asymmetric prosthetic at the toe-off for both θ_1 and θ_4 groups is higher than that of the symmetric model at the toe-off moment. At the two aforementioned contact transients, the contact area is inversely proportional to the material elastic modulus, inversely proportional to the prosthesis thickness, and proportionate to the prosthesis horizontal projected area (Fig. 2). Due to the fact that we used the same elastic materials and the thickness in the simulation and that only the horizontal projection area of the prosthesis differed between the symmetric and asymmetric models, the horizontal projection area (asymmetric parameters) of the prosthesis is regarded as the primary factor influencing the contact area. According to the correspondence between the pressure and contact area, the magnitude of pressure p is inversely proportional to the contact area s for the same load f

$$p = \frac{f}{s} \tag{3.1}$$

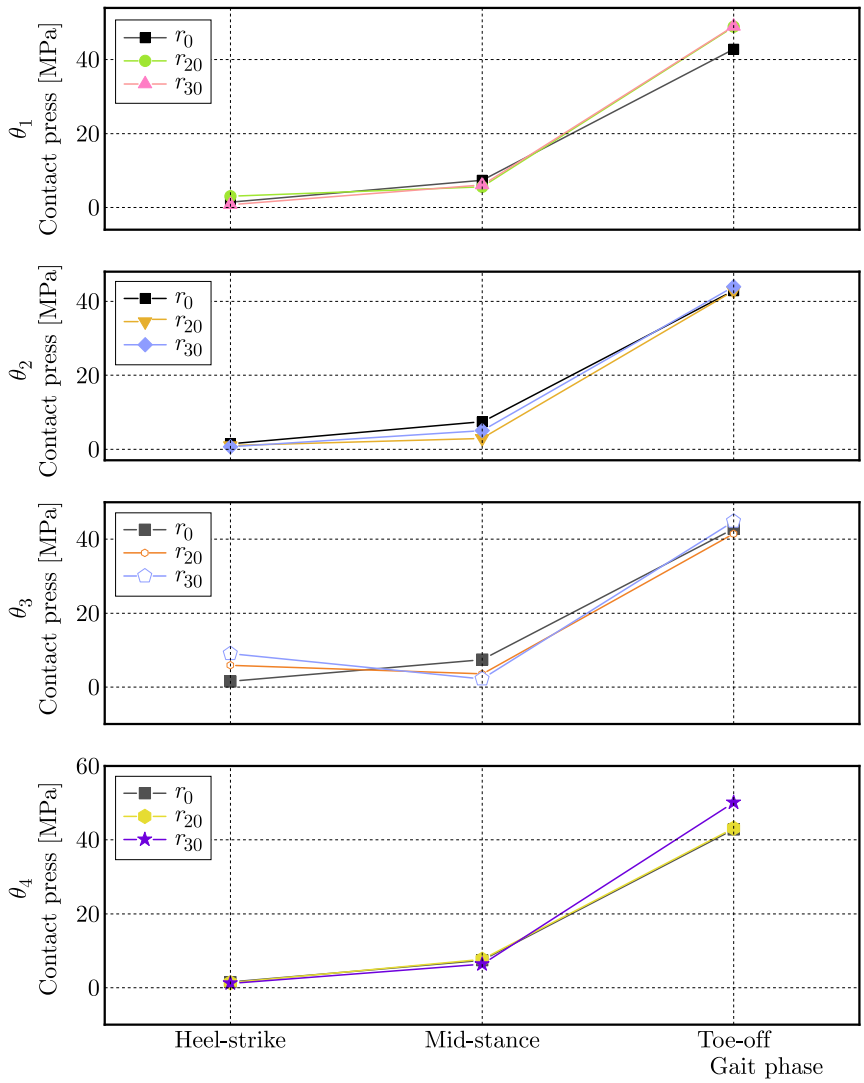

Fig. 7. Contact press at the heel-strike, mid-stance and toe-off moments

This phenomenon is because the force area of the asymmetric model is smaller than that of the symmetric model, which again proves the reliability of the analytical results.

Specifically analyzing the contact pressure at each moment, an interesting phenomenon is worth noting. At the moment of heel-strike, with the same heel asymmetry, the contact pressures of the θ_2 asymmetric model are lower than those of the 0-fillet symmetric model, in contrast to the phenomenon that the contact pressure of the asymmetric model of the θ_3 group is significantly higher than that of the 0-fillet symmetric model. The reason for this phenomenon may be that the inner asymmetric shape prosthetic model has a smaller contact area and lower model stiffness, but the impact reaction force is applied for a longer term than that of the symmetric model. The results indicate that the θ_2 asymmetry is beneficial to reduction of the heel-strike contact pressure. The asymmetry increases, and the contact pressure decreases subsequently. The θ_3 asymmetry has a negative effect on the contact pressure, the larger the asymmetry, the greater the contact pressure.

The contact pressure of θ_1, θ_2, θ_3 and θ_4 groups of asymmetric prosthesis models at the middle stance moment is smaller than that of the symmetric prosthesis models at that moment, which may be related to the decreased mass of the asymmetric prosthesis models compared with the symmetric prosthetic foot models. It indicates that the shape asymmetry can reduce the

contact pressure at the middle stance moment of the prosthesis; however, the contact pressure of the θ_2 and θ_3 asymmetric models is smaller than that of θ_1 and θ_4 asymmetric models, which indicates that the contact pressure at the middle stance moment is more influenced by the heel leaf, and this phenomenon is related to the location characteristics of the heel component of the prosthesis. The above results indicate that heel asymmetry is more beneficial to reduction of the contact pressure of the prosthesis at the middle stance moment compared to keel asymmetry.

3.3. Strain energy

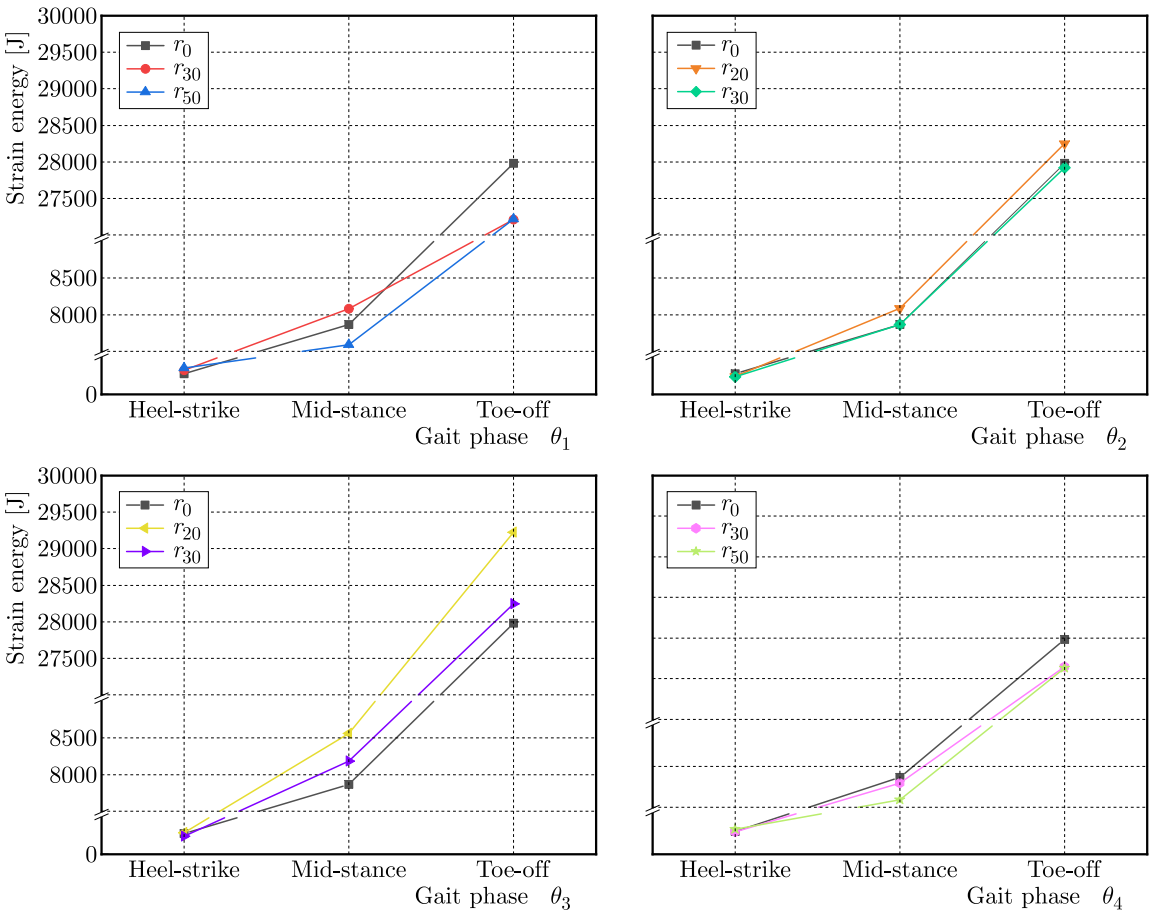

Fig. 8. The strain energy of each prosthetic foot

The strain energy of each prosthesis model at the three typical moments is shown in Fig. 8. The models are divided into θ_1, θ_2, θ_3 and θ_4 four categories according to the location of the shape asymmetry, and each of the three lines in each subgraph represents the size of an asymmetric fillet. The typical moments are heel-strike, middle stance and toe-off gait events.

The strain energy of the asymmetric prosthesis model at position θ_1 and θ_4 is smaller than that of the symmetric prosthesis model at the moment of toe-off. θ_1 is smaller, which indicates that the shape asymmetry at position θ_1 has the greatest negative impact on the strain energy, and the shape asymmetry at position θ_4 has a relatively small negative impact it. The strain energy of the prosthesis decreases as the asymmetry increases, but the correlation is not sensitive. The θ_2 and θ_3 asymmetries at positions θ_2 and θ_3 increase the strain energy, asymmetry at position θ_2 is more favorable to the strain energy, and the most favorable results are obtained when the radius of the fillet of the shape asymmetry at position θ_2 is 20 mm. The strain energy of the asymmetric fillet at 30 mm is similar to that of the symmetric prosthesis model. Asymmetry

at position θ_3 is partially favorable, but the results are uncertain and further studies should be conducted.

3.4. Strain energy calculations

It is necessary to analyze the energy generated in the foot module in order to determine the energy to be taken into the articulated area. This is achieved through the analysis of strain energy from the Castigliano theorem and the free body diagram of the foot module.

By employing the homogenization procedure, the keel structure is simplified into a cantilever model and a straightforward curved beam model (Fig. 9). The letters c and s stand for curved and straight (cantilever) beams. Axial, shear forces and bending moments combine to produce vertical deflection at the foot point of contact with the ground. When the radius-to-thickness ratio ($r = h$) is more than 10, the effects of the axial stress and shear are minimal (Boresi *et al.*, 1993).

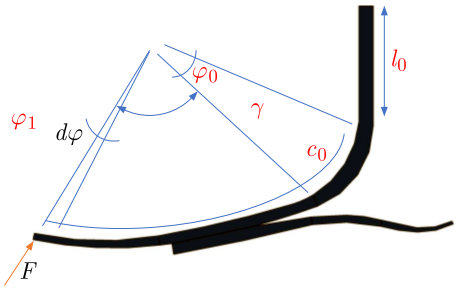

Fig. 9. Diagram of the toe-off working condition force

To determine beam deflection in this investigation, the strain energy that is exclusively attributable to bending is employed

$$\Delta = \frac{\partial U}{\partial F} \tag{3.2}$$

where F is the ground reaction force of the composite foot. The total strain energy U of the bionic prosthetic foot is expressed as follows

$$U = U_S + U_C \tag{3.3}$$

where the strain energy of the straight part U_S is expressed as follows

$$U_S = \int \frac{F_N^2}{2EA}\, dl + \int \frac{M_s^2}{2EI}\, dl \tag{3.4}$$

and the strain energy of the curved beam part is

$$U_C = \int \frac{F_S^2 \gamma}{2AG}\, d\varphi + \int \frac{F_N^2 \gamma}{2EA}\, d\varphi + \int \frac{A_m M_c^2}{2EA(\gamma A_m - A)}\, d\varphi \tag{3.5}$$

where E is longitudinal Young's modulus of the composite foot, A is the cross-sectional area, I is the moment of inertia, and dl is differential of the straight part length l_0, γ is the curvature radius of curved parts c_0, A_m is the distance from the center of the circumference of the curved beams, F_N is the axial stress, F_S is the shear stress, M_S and M_C represent the bending moments, and G is the shear modulus.

3.5. Roll-over shape

The roll-over shape of all prosthetic models is extracted as shown in Fig. 10, where the curve from the toe endpoint to $X = -75$ is defined as the toe region. $X = -75$ to $X = 0$ is defined as the forefoot region, and $X > 0$ is defined as the heel region according to the bionic structure. The X-axis direction is the length direction of the prosthesis, the heel is in the positive direction

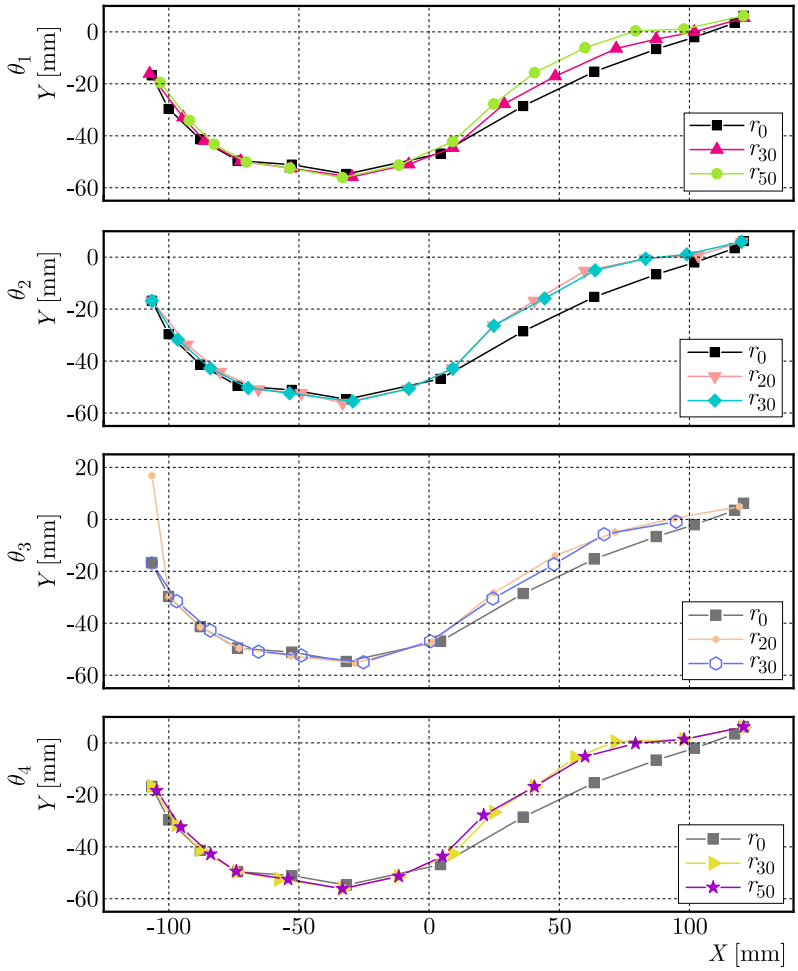

Fig. 10. The roll-over shape of the asymmetric prosthetic foot model compared with the roll-over shape of the symmetric prosthetic foot model. The upper subfigure shows the roll-over shape of the forefoot asymmetric prosthetic foot model compared with the symmetric model; the lower subfigure shows the roll-over shape of the heel asymmetric prosthetic foot model compared with the symmetric model

of the X-axis, the heel-strike corresponds to the right endpoint and is the starting point of the roll-over shape, the toe-off corresponds to the negative direction of the X-axis. The toe-off corresponds to the left endpoint of the curve and is defined as the endpoint of the roll-over shape.

The roll-over shape radius at the toe of the forefoot of the asymmetric prosthesis is reduced compared to that of the symmetric prosthesis, with the smallest roll-over shape radius at the toe of the 50 mm fillet prosthesis on the left side of the forefoot.

The radius of the roll-over shape at the toe of the forefoot of the asymmetric prosthesis is the smallest, and the radius of the roll-over shape is similar and slightly larger than that of the symmetric prosthesis.

The toe-off points of the four θ_1 , θ_2 , θ_3 and θ_4 asymmetric prosthetic feet models are compared with the toe-off points of the symmetric model prosthetic feet. Only the toe-off point

of the right heel 20 mm fillet asymmetric model is much higher than the toe-off point of the symmetric model of the prosthetic foot, and the toe-off points of the rest of the heel of the asymmetric model almost overlapped with those of the symmetric model.

The asymmetry of the heel results in a reduced roll-over shape radius of the toe compared to the symmetric prosthetic foot. Specifically, the roll-over shape radius of the toe exhibits a 20 mm fillet on the left side of the heel and a 30 mm fillet on the right side of the heel, overlapping with the roll-over shape of the symmetric model.

Furthermore, the roll-over shape radius at the forefoot of the heel of the asymmetric prosthetic foot is similar to, and slightly larger than, the roll-over shape radius at the forefoot of the symmetric prosthetic foot. The shape asymmetry reduces the stiffness of the prosthesis relative to that of the fully symmetric model, making the roll-over deformation of the asymmetric prosthetic foot model larger than that of the symmetric prosthetic foot model. Among them, the roll-over shapes of the asymmetric fillets at positions θ_1 and θ_3 are of interest. The results in Fig. 10 show that the asymmetry at positions θ_1 and θ_3 has a greater effect on the roll-over shape of the prosthesis, and the asymmetry at positions θ_2 and θ_4 has a less effect on the roll-over shape of the prosthesis.

4. Conclusions

The effect of asymmetric shape on prosthetic performance has been innovatively studied, and the polar coordinate method has been innovatively used to describe the asymmetric position and degree of asymmetry. The amputee gait process of the support phase of the prosthetic foot was studied using the Össur prosthetic foot as the base model, and the gait behavior of the prosthetic foot in the support phase was investigated using dynamic walking numerical analysis. The design parameters of the asymmetric prosthetic foot were investigated using energy characteristics, contact pressure and roll-over shape of the support phase as performance indexes.

The θ_1 and θ_3 asymmetry shape prosthetic foot has a relatively large effect on the strain energy density. The θ_2 and θ_4 asymmetry shape prosthetic foot has the least effect on the strain energy density.

The heel asymmetry is more beneficial to reduction of the contact pressure of the prosthesis at the middle stance moment compared to the keel asymmetry.

The shape asymmetry at position θ_1 has a negative impact on the strain energy of the prosthesis, and the shape asymmetry at position θ_4 has a relatively small negative impact on the strain energy of the prosthesis. The most favorable results were obtained for the radius of the fillet of the shape asymmetry at position θ_2 was 20 mm. Asymmetry at position θ_3 was partially favorable.

The asymmetry at position θ_1 and θ_3 has a greater effect on the roll-over shape of the prosthesis, and the asymmetry at position θ_2 and θ_4 has a less effect on the roll-over shape of the prosthesis.

In summary, the optimal asymmetric prosthesis parameters are derived in this paper as shown in Table 2.

Table 2. Asymmetric prosthetic model

ρ [mm]	θ [rad]	R_1 [mm]
$\rho = \sqrt{l^2 + w^2}/2$	$\theta_1 = \tan^{-1} w/l$	0
$\rho = \sqrt{l^2 + w^2}/2$	$\theta_2 = (\pi/2)/2 + \tan^{-1} w/l$	20
$\rho = \sqrt{l^2 + w^2}/2$	$\theta_3 = \pi + \tan^{-1} w/l$	30
$\rho = \sqrt{l^2 + w^2}/2$	$\theta_4 = (3\pi/2) + \tan^{-1} w/l$	50

Acknowledgment

This work was supported by Tianjin Postgraduate Research Innovation Project (grant No. 2020YJSB065 and 2019YJSB014), Tianjin Science and Technology Plan Project (grant No. 20JCYBJC01430).

References

1. Adamczyk P.G., Kuo A.D., 2013a, Mechanical and energetic consequences of rolling foot shape in human walking, *Journal of Experimental Biology*, **216**, 14, 2722-2731
2. Adamczyk P.G., Roland M., Hahn M.E., 2013b, Novel method to evaluate angular stiffness of prosthetic feet from linear compression tests, *Journal of Biomechanical Engineering*, **135**, 10, 104502-104505
3. Adamczyk P.G., Roland M., Hahn M.E., 2017, Sensitivity of biomechanical outcomes to independent variations of hindfoot and forefoot stiffness in foot prostheses, *Human Movement Science*, **54**, 154-171
4. Allard P., Trudeau F., Prince F., Dansereau J., Labelle H., Duhaime M., 1995, Modelling and gait evaluation of asymmetrical-keel foot prosthesis, *Medical and Biological Engineering and Computing*, **33**, 1, 2-7
5. Ármannsdóttir A.L., Lecomte C., Brynjólfsson S., Briem K., 2021, Task dependent changes in mechanical and biomechanical measures result from manipulating stiffness settings in a prosthetic foot, *Clinical Biomechanics*, **89**, 105476
6. Boresi A.P., Schmidt R.J., Sidebottom O.M., 1993, *Advanced Mechanics of Materials*, New York: Wiley
7. De Asha A.R., Johnson L., Munjal R., Kulkarni J., Buckley J.G., 2013, Attenuation of centre-of-pressure trajectory fluctuations under the prosthetic foot when using an articulating hydraulic ankle attachment compared to fixed attachment, *Clinical Biomechanics*, **28**, 2, 218-224
8. Fey N.P., Klute G.K., Neptune R.R., 2011, The influence of energy storage and return foot stiffness on walking mechanics and muscle activity in below-knee amputees, *Clinical Biomechanics*, **26**, 10, 1025-1032
9. Fey N.P., Klute G.K., Neptune R.R., 2013, Altering prosthetic foot stiffness influences foot and muscle function during below-knee amputee walking: a modeling and simulation analysis, *Journal of Biomechanics*, **46**, 4, 637-644
10. Fridman A., Ona I., Isakov E., 2003, The influence of prosthetic foot alignment on trans-tibial amputee gait, *Prosthetics and Orthotics International*, **27**, 1, 17-22
11. Handzic I., 2014, *Analysis and Application of Passive Gait Rehabilitation Methods*, University of South Florida
12. Hansen A.H., Childress D.S., 2005, Effects of adding weight to the torso on roll-over characteristics of walking, *Journal of Rehabilitation Research and Development*, **42**, 3
13. Hansen A.H., Childress D.S., Knox E.H., 2000, Prosthetic foot rollover shapes with implications for alignment of transtibial prostheses, *Prosthetics and Orthotics International*, **24**, 3, 205-215
14. Hansen A.H., Childress D.S., Knox E.H., 2004a, Roll-over shapes of human locomotor systems: effects of walking speed, *Clinical Biomechanics*, **19**, 4, 407-414
15. Hansen A.H., Childress D.S., Miff S.C., 2004b, Roll-over characteristics of human walking on inclined surfaces, *Human Movement Science*, **23**, 6, 807-821
16. ISO/TS 16955: 2016, Prosthetics – quantification of physical parameters of ankle foot devices and foot units

17. Jang T.S., Lee J.J., Lee D.H., Yoon Y.S., 2001, Systematic methodology for the design of a flexible keel for energy-storing prosthetic feet, *Medical and Biological Engineering and Computing*, **39**, 1, 56-64

18. Prince F., Winter D.A., Sjonnensen G., Powell C., Wheeldon R.K., 1998, Mechanical efficiency during gait of adults with transtibial amputation: a pilot study comparing the SACH, Seattle, and Golden-Ankle prosthetic feet, *Journal of Rehabilitation Research and Development*, **35**, 2, 177-185

19. Prince F., Winter D.A., Sjonnesen G., Wheeldon R.K., 1994, A new technique for the calculation of the energy stored, dissipated, and recovered in different ankle-foot prostheses, *IEEE Transactions on Rehabilitation Engineering*, **2**, 4, 247-255

20. Tryggvason H., Starker F., Lecomte C., Jonsdottir F., 2020, Use of dynamic FEA for design modification and energy analysis of a variable stiffness prosthetic foot, *Applied Sciences*, **10**, 2, 650

Manuscript received February 16, 2023; accepted for print June 6, 2023

JOURNAL OF THEORETICAL AND APPLIED MECHANICS
61, 4, pp. 701-714, Warsaw 2023
https://doi.org/10.15632/jtam-pl/170712

INVESTIGATION ON THE ANTI-PENETRATION PERFORMANCE OF UD – A THREE-DIMENSIONAL ORTHOGONAL WOVEN FABRIC COMPOSITE REINFORCED STRUCTURE

Chaoming Shen, Yang Chen
School of Naval Architecture and Ocean Engineering, Jiangsu University of Science and Technology, Zhenjiang, China
Lei Liu
School of Naval Architecture and Ocean Engineering, Jiangsu University of Science and Technology, Zhenjiang, China; and China Merchants Jinling Shipyard (Yangzhou) Dingheng Co., Ltd., Yangzhou, China
Zexin Zhang
School of Naval Architecture and Ocean Engineering, Jiangsu University of Science and Technology, Zhenjiang, China
Baijian Tang
School of Naval Architecture and Ocean Engineering, Jiangsu University of Science and Technology, Zhenjiang, China; and School of Civil Engineering, Suzhou University of Science and Technology, Suzhou, China
Fushan Li
China Special Equipment Inspection and Research Institute, Jiaxing, China
Denghui Qian
School of Naval Architecture and Ocean Engineering, Jiangsu University of Science and Technology, Zhenjiang, China
e-mail: dhqian@just.edu.cn

A uni-direction (UD) laminate and three-dimensional (3D) orthogonal woven fabric made of ultra high molecular weight polyethylene (UHMWPE) are used as main reinforced units combined with aluminum alloy plates to form a reinforced sandwich structure. Penetration tests are carried out on four composite reinforced structures with different structure forms by a 7.62 mm steel core projectile. The target plate size is 150 mm×150 mm. Besides, Ansys/LS-Dyna software is applied to simulate the penetration process, and the simulation results are in good agreement with the test results. All the results demonstrate that with the same total thickness of UD laminates, 20 mm UD laminates have better penetration resistance than four 5 mm UD laminates. The less the number of UD laminates, the better anti-penetration performance of the overall structure. The 3D orthogonal woven fabric has the advantage of spatial integrity, which can effectively restrain deformation of laminates and absorb energy behind UD laminates, so as to obtain better anti-penetration performance. In the core structure with a total thickness of 28 mm, when the thickness ratio of 3D orthogonal woven fabric is between 30% and 35%, the protection ability and lightweight requirements of the sandwich structure can be better considered.

Keywords: three-dimensional orthogonal woven fabric, anti-penetration performance, ultra high molecular weight polyethylene, thickness ratio

1. Introduction

The UD laminate made of UHMWPE fiber, which has characteristics of high specific strength, high specific modulus, excellent impact resistance and so on, is one of the most widely used bulletproof materials in the world. Since the material can transmit stress wave and dissipate impact kinetic energy faster, it has excellent anti-penetration performance. However, the damage

area is large and the interlayer is easily stratified if the UD laminate is impacted, which is not conducive to the resistance of the second impact.

Compared with the fiber laminate used for a spatial integral weaving material, the 3D fabric composite material has greater interlaminar strength and ability to resist lamination damage (Xiong *et al.*, 2018). It is an effective way to improve the anti-penetration performance of the protective structure to compose the 3D fabric composite plate by filling the internal pores with the energy absorbing material. Presently, different 3D fabrics have been researched and applied in aerospace and other protective engineering fields (Liang and Fang, 2014). 3D woven fabric structures are shown in Fig. 1.

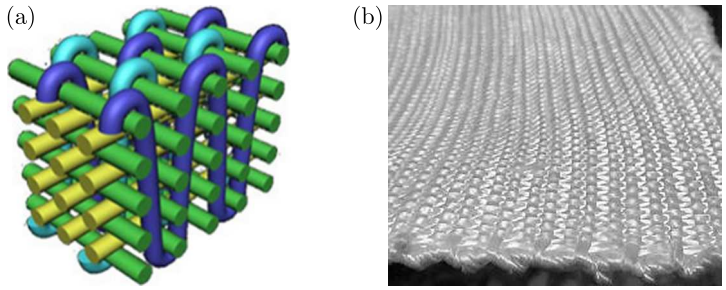

Fig. 1. Structure of the 3D woven fabric: (a) 3D model, (b) physical photo

Penetration tests and numerical simulations are the main methods to study the impact resistance and failure mechanism of 3D fabric composites. Hu *et al.* (2021), Song *et al.* (2020) and Wu *et al.* (2019) analyzed failure modes of several 3D fabrics under the high-speed or low--speed impact, and explored their failure mechanism and energy absorption characteristics. Deng *et al.* (2018) studied penetration resistance characteristics of rigid ogival-nosed projectiles on braided composite laminated plates, and studied the influence law of the impact angle of the projectile body on its ballistic limit. They found that when the impact angle of the projectile body is 45°, the ballistic limit of the target plate was the highest, followed by 0°, and the ballistic limit was the lowest when the impact angle was 30°. Walter *et al.* (2009) explored failure forms of 3D braided fiberglass reinforced composite plates under small caliber projectiles, and found that the main failure mode was laminar failure of the braided surface. By adding yarn in the Z-axis direction of the fiber cloth, laminar failure of fiberglass reinforced composite plates could be limited and the anti-penetration performance could be improved. Tan *et al.* (2018) established a macro-continuum damage finite element model for 3D four-direction braid composites, and found that the calculated residual velocity and experimental error of the model were within 5%, thus verifying the effectiveness of the macro-finite element model. Sun *et al.* (2009) analyzed ballistic impact results of 3D orthogonal woven composites by using a macroscopic finite element model, and found that the results were basically consistent with the experimental results.

In this paper, the UHMWPE 3D orthogonal woven fabric composite plate is added to the aluminum alloy – the UD laminate sandwich structure. Penetration tests and numerical simulations on fabric reinforced composite structures with different structure forms are carried out to explore the anti-penetration performance of the fiber composite structure with the UHMWPE 3D orthogonal woven fabric.

2. Design of penetration test scheme

2.1. Design and preparation of composite reinforced structure target plates

Due to weak anti-ultraviolet aging ability of polymer materials, which is not conducive to connection with existing fabrics, the use of aluminum panels and backplanes can effectively solve

these problems. 7075-T6 aluminum alloy is a cold-treated forged alloy with high strength and provides the highest ballistic resistance, so the front and rear panels of the composite target plates are made of 7075 light and high strength aluminum alloy plates with thickness of 1 mm, 3 mm and 5 mm, respectively. The dimensions are 150 mm×150 mm. The UD laminates are made of the UHMWPE fiber which is tiled and hot-pressed in the manner of 0°-90°. The yarn size is 400D and material density is 0.98 g/cm^3. The thicknesses of UD laminates are 5 mm and 20 mm. The dimensions are 150 mm×150 mm. The 3D fabric composite plate is molded by filling the resin matrix of bisphenol *A* into the 3D orthogonal woven fabric preform. Since the injected bisphenol resin has good fluidity and can freely penetrate into the fiber, all target plates are pressed and solidified by heavy objects to ensure stable solidification of the interface between the materials. After forming, a magnifying glass is used to observe defects at the joint to avoid the influence of quality defects on the experimental results. The areal density of the processed 3D fabric composite plate is 0.94 g/cm^2 and the thickness is 8 mm. The dimensions are 150 mm×150 mm. The plane dimensions of composite target plates are 150 mm×150 mm, and the total areal density is about 44 kg/m^2.

In the case of the same total surface density, using the same basic material, through different arrangements to find the optimal structure, we design four different structural forms as shown in Fig. 2. In the figure, V_0 is the initial impact velocity. The thicknesses of the front and rear panels of structure I and II are 1 mm and 5 mm. The thicknesses of the front and rear panels of structure III and IV are 3 mm. The plates are bonded after mixing with the epoxy *AB* adhesive resin.

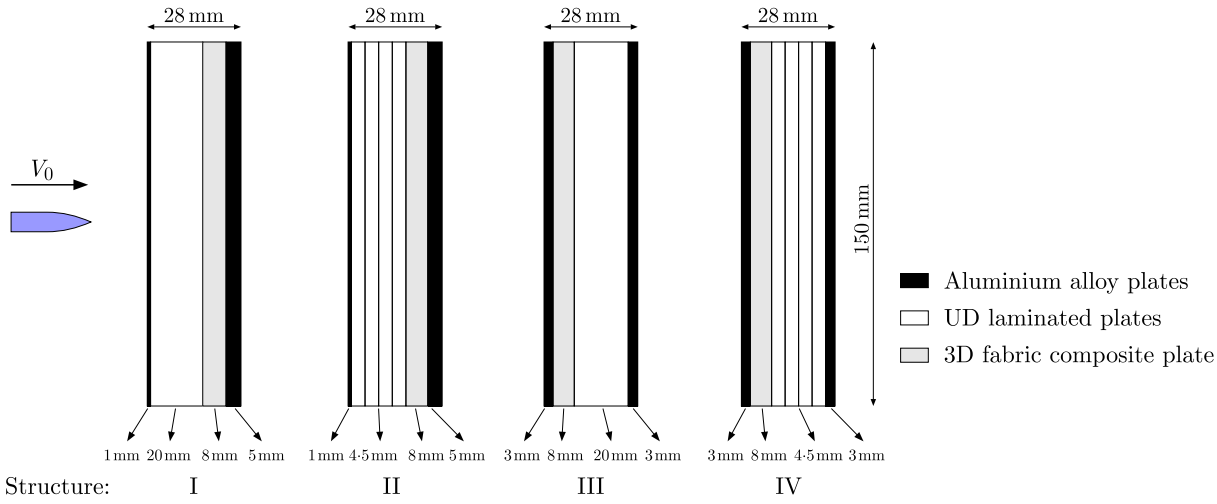

Fig. 2. Schematic of composite target plates

2.2. Test device

The test projectile body is a 7.62 mm steel core projectile. The actual diameter of the warhead is 7.92 mm and the mass is about 8.4 g. The size and shape of the projectile body are shown in Fig. 3.

The main equipment of the penetration test includes a ballistic gun, gun holding device, high-speed image recording system, calibrated plate, target plate clamping device and projectile recovery device. The high-speed camera is placed on the side of the clamping device of the target plate and facing the calibrated plate. The velocity of the projectile is calculated mainly by processing the image of the high-speed camera. The layout of the penetration device and the test site are shown in Fig. 4.

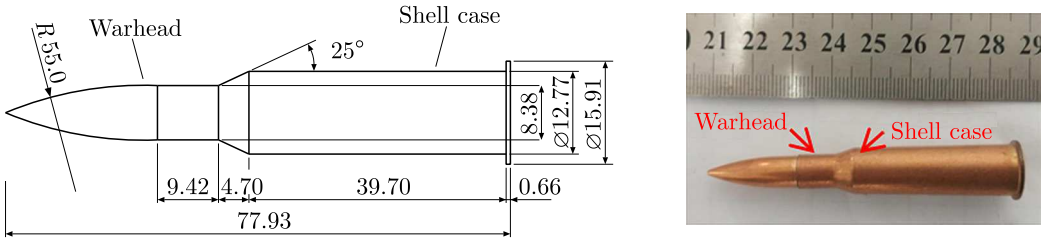

Fig. 3. Size and shape of the projectile (unit: mm)

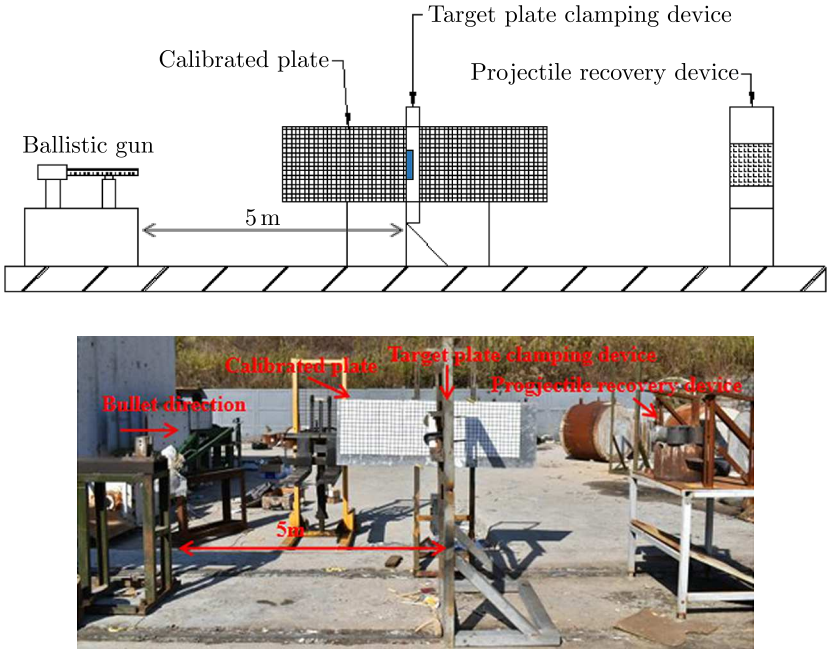

Fig. 4. Layout of the penetration device and test site

3. Test results

The ballistic test results are listed in Table 1, and the valid data are obtained from each of the four tests. The range of projectile incident velocity is 855.48 m/s to 861.71 m/s, STDEV is 2.79, so it can be considered that the incidence velocity is basically the same, where the residual velocity is 0, indicating that the projectile does not penetrate the composite target plate.

Table 1. Ballistic test results

Structure of target plates	Incident velocity [m/s]	Residual velocity [m/s]	Degree of breakage of backplane
I	861.71	0	not penetrated, cracked, slightly uplifted
II	859.63	286.14	penetrated, large area of cataclastic damage
III	855.48	0	not penetrated, cracked, uplift about 32 mm
IV	856.81	412.91	penetrated, cataclastic damage, uplift about 25 mm

3.1. Failure patterns of the panel

The failure patterns of the front panel after being penetrated by the projectile are shown in Fig. 5. The front panel can be observed with obvious shear and chisel marks, which makes

two failure patterns generate: I and II are circular holes which are directly penetrated and accompanied by cracks; III and IV are outward curled petal-like holes of aluminum alloy at the edge of bullet holes. The reason for this phenomenon is that the 3 mm aluminum alloy plate is thick, so it has the ability to produce enough plastic deformation under the condition of the impact of the projectile body. The diameters of all bullet holes did not differ much, being about 9 mm.

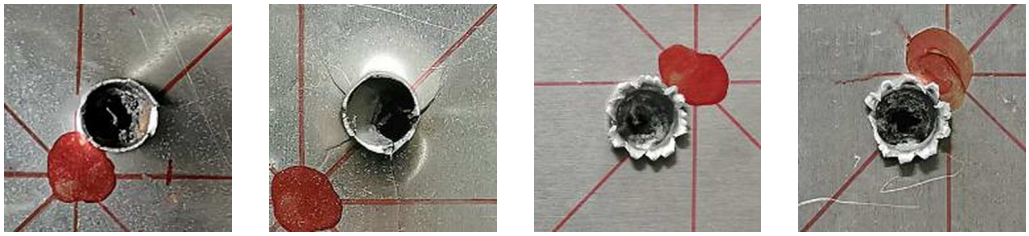

Fig. 5. Failure patterns of the front panel of composite target plates

The failure patterns of the rear panel of the composite target plates are shown in Fig. 6. It can be seen from the figure that the failure patterns of the rear panel are completely different. From the perspective of penetrating and non-penetrating, the failure patterns can be roughly divided into uplift and radial crack (I, III) and cataclastic failure (II, IV). Further speaking, although structure III is not penetrated, the maximum amplitude of uplift is 32 mm and accompanied by multiple cracks; structure II is penetrated and the maximum breakage range is 45 mm×53 mm; The breakage condition of structure IV is between the former two, the height of uplift is 25 mm and the diameter of the hole is about 11 mm. Not only structure I is not penetrated, but also the uplift amplitude is the lowest, and there is only one crack. Therefore, it can be considered that the anti-penetration performance of structure I is better than in the other three structures.

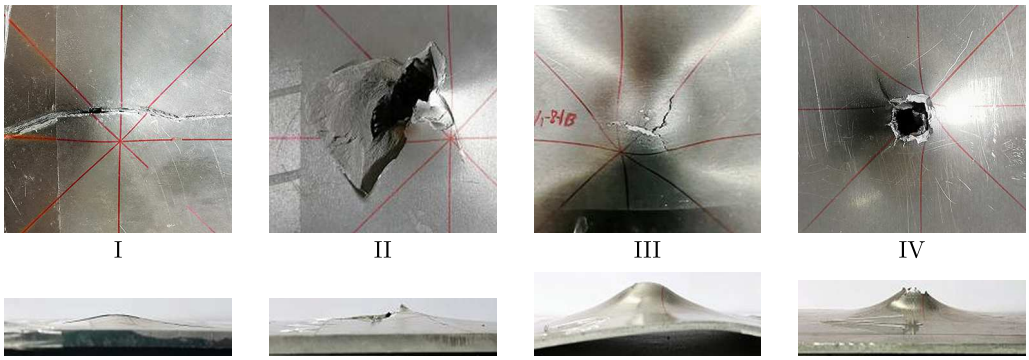

Fig. 6. Failure patterns of the rear panel of composite target plates

3.2. Failure patterns of the core layer

In order to observe deformation and breakage of the 3D fabric composite plate and its effect on the composite target plates, the cemented aluminum alloy plates are disassembled from the core layer after the test. Figure 7 shows the failure morphology of the core layer facing the surface, internal surface and back surface of each structure. Figure 8 shows the failure side view of the core layer of each structure.

In Figs. 7a and 7b, when the projectile body impacts the polyethylene plate at high speed, the target plate exhibits adiabatic shear failure. Local high temperature is generated in the shear band, which leads to fiber fusing in the penetration zone, and the outer matrix is scorched and

some black substances are produced. Structure I projectile body does not penetrate even the laminated plates, and a small amount of deformation occurs in the 3D fabric plate. Structure II is penetrated and a small number of fiber bundles are observed to be damaged and surround the bullet holes in the 3D fabric plate. According to Figs. 7c and 7d, the high temperature generated by the projectile body after penetrating the 3D fabric plate and impacting the laminates will make the internal holes gradually become bigger, but the shape of the breach does not change greatly.

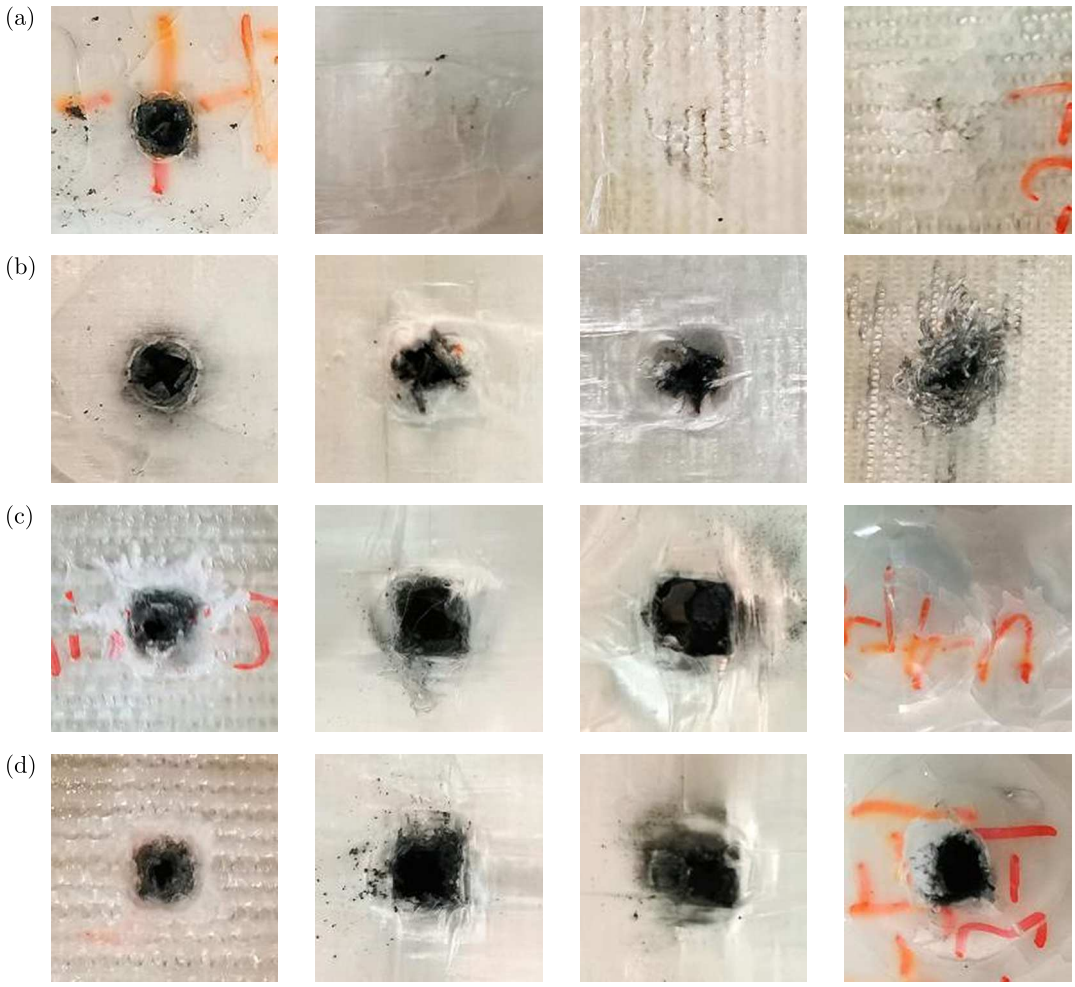

Fig. 7. Failure morphology of the core layer of each structure: (a) structure I, (b) structure II, (c) structure III, (d) structure IV

In Fig. 8, different degrees of delamination occur in each laminated plate, and the structure with four laminated plates is more serious. The factor of whether structure I and II, III and IV are penetrated is the number of laminated plates. Therefore, it can be considered that the less the number of laminated plates with the same total thickness, the better anti-penetration performance of the composite reinforced structure.

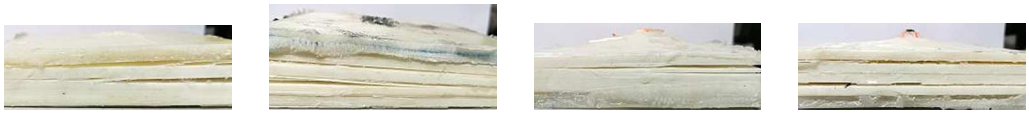

Fig. 8. Failure side view of each structure core layer

Based on Figs. 6, 7 and 8, it is found that when the 3D fabric plate is placed in front of the laminated plate, the projectile body quickly penetrates the 3D fabric plate and impacts the rear laminated plates, resulting in a large deflection deformation of the laminated plates and driving the back plate to the arch back. When the 3D fabric is placed behind the laminate and the projectile body impacts the front laminate, the 3D fabric plate can resist the deformation of the laminates to a large extent and absorb a large amount of energy due to the integrity of the space. Therefore, it can be considered that the anti-penetration performance of the composite reinforced structure is better when the 3D fabric plate is placed behind the laminated plates.

4. Numerical simulation of the penetration response of the target plate

4.1. Numerical simulation model

Since the UHMWPE fiberboard is made of hot pressing in the way of 0°-90°, and the thickness of each layer is about 0.168 mm, the modeling in accordance with this thickness will require very high hardware conditions and cause unacceptable time cost. In order to give consideration to calculation accuracy and efficiency, a macro equivalent modeling is adopted. The idea of the macro equivalent modeling is to model the fiber and matrix as a whole. This paper uses ANSYS/LS-DYNA software to carry out the macro modeling of composite target plates in the test. In order to simulate the layered effect of laminates, it is assumed that 2 mm in the thickness direction is a more appropriate layer. Considering the symmetry between the projectile and the target plate as well as reducing the amount of calculation, this paper establishes a 1/4 model and sets symmetry constraints on the symmetry plane and fixed constraints around the target plate.

The projectile model and the center area impacted of the target plate model are mesh-refined, and the size length is 0.5 mm. Face erosion contact is arranged between the projectile body and the target plate, and face automatic contact with fixed connection is arranged between layers. Taking structure I as an example, the projectile body and target plate after grid division are shown in Fig. 9.

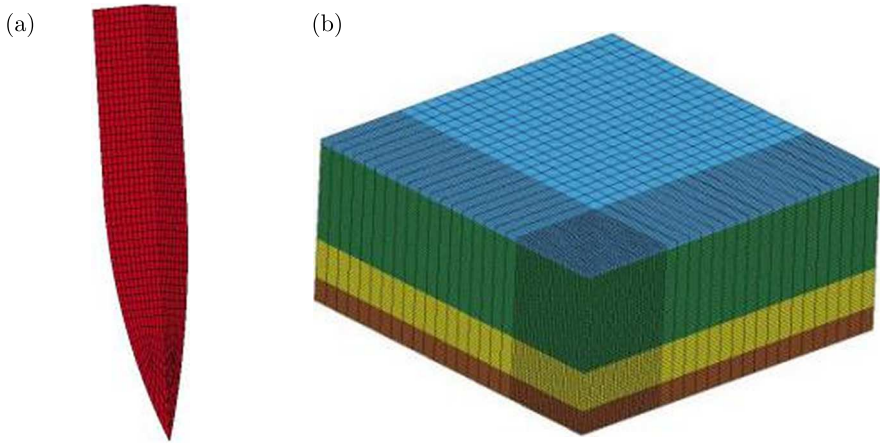

Fig. 9. Numerical simulation model of structure I: (a) projectile body, (b) target plate of structure I

4.2. Material model

4.2.1. Constitutive model of the projectile body and aluminum alloy

The model of the projectile body does not consider the copper coating on the actual projectile surface, and its interior is high strength tool steel. The composite target panel is made of 7075

aluminum alloy as described above. Johnson and Cook's (1983) model is used for both metal material models, and the equation is shown in Eq. (4.1). The corresponding Johnson-Cook damage (You-Zhi *et al.*, 2008) model is shown in Eq. (4.2). The material parameters of the projectile body and aluminum alloy (Liu, 2020; Chen *et al.*, 2019) are shown in Table 2

$$\sigma_y = (A + B\overline{\varepsilon}^{n''})(1 + C\ln\dot{\varepsilon}^*)\left[1 - \left(\frac{T - T_r}{T_m - T_r}\right)^m\right] \tag{4.1}$$

where σ_y is the equivalent stress, A, B, C, n and m are material constants, $\overline{\varepsilon}^p$ is effective plastic strain, $\dot{\varepsilon}^* = \dot{\varepsilon}^P/\dot{\varepsilon}_0$ is dimensionless plastic strain rate, T is temperature, T_r is indoor temperature, and T_m is the melting point of the material

$$\varepsilon^f = (D_1 + D_2 \exp D_3\sigma^*)(1 + D_4 \ln\varepsilon^*)(1 + D_5 T^*) \tag{4.2}$$

where D_1-D_5 are fracture parameters of materials.

Table 2. Constitutive and damage parameters of the projectile and aluminum alloy

Material parameters	Projectile	Aluminum alloy	Material parameters	Projectile	Aluminum alloy
ρ [kg/m^3]	7830	2700	m	1.61	1.015
G [GPa]	0.77	0.27	$\dot{\varepsilon}_0$	$0.1 \cdot 10^{-5}$	$2.1 \cdot 10^{-3}$
T_r [K]	293	293	D_1	5.00	0.209
T_m [K]	1795	910	D_2	0.00	2.426
A [MPa]	792	547	D_3	0.00	−7.989
B [MPa]	510	687	D_4	0.00	0.036
n	0.26	0.740	D_5	0.00	0.697
C	0.014	0.017			

4.2.2. UHMWPE laminates and the 3D fabric constitutive model

This paper adopted MAT_COMPOSITE_DAMAGE (MAT_22) statement in LS-DAYNA for UHMWPE fiberboard. Mat_022 model characterizes orthotropic composite materials with optional brittle failure criteria following the failure model proposed by Qu *et al.* (2020), see Table 3 for related material parameters.

Table 3. Material parameters of UD laminates

ρ [g/cm^3]	E_1 [GPa]	E_2 [GPa]	E_3 [GPa]	ν_{12} [–]	ν_{13} [–]	ν_{23} [–]	G_{12} [GPa]	G_{13} [GPa]
0.98	30.7	30.7	1.97	0.008	0.044	0.044	0.73	0.67

G_{23} [GPa]	H_{fail} [GPa]	S_c [GPa]	X_t [GPa]	Y_t [GPa]	Y_c [GPa]	S_n [GPa]	S_{yz} [GPa]	S_{xz} [GPa]
0.67	2.2	0.36	3.0	3.0	2.5	0.95	0.95	0.95

Note: E_1 and E_2 are in-plane moduli, E_3 is normal modulus, G_{12} is normal shear modulus, G_{23} and G_{13} are in-plane shear moduli, ν_{12} is in-plane Poisson's ratio, and ν_{23} and ν_{13} are normal Poisson's ratios. S_c is shear strength, X_t is in-plane tensile strength, Y_t is normal tensile strength, Y_c is normal compressive strength, S_n is general tensile strength, S_{yz} and S_{xz} are normal shear strengths.

The elastic-plastic material model suitable for the strain rate is selected for the 3D fabric composite plate. Its equation is shown in Eq. (4.3), and the relevant material parameters (Chen *et al.*, 2019) are shown in Table 4

$$\sigma = k\varepsilon^m \dot{\varepsilon}^n \tag{4.3}$$

where σ is the yield stress, ε is the effective plastic strain, and $\dot{\varepsilon}$ is the effective total strain rate. k, m and n are constants relative to the plastic strain.

Table 4. Material parameters of the UHMWPE 3D fabric plate

ρ [g/cm^3]	E [GPa]	ν	k	m	n
0.94	12.5	0.14	350	1.5	2

4.3. Verification of numerical simulation method

In order to verify the correctness of the numerical method, four kinds of composite target plates are simulated. Figure 10 takes structure I and IV as examples to compare the test mode and numerical mode of different failure modes. Table 5 shows the experimental and numerical results of the four structures.

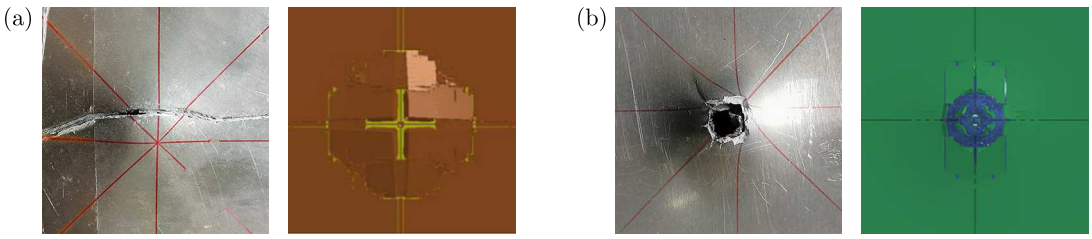

Fig. 10. Failure modes of the penetration test and numerical simulation: (a) structure I back plate, (b) structure IV back plate

Table 5. Comparison of numerical simulation and test results

Structure of target plates	Initial velocity [m/s]	Test residual velocity [m/s]	Simulated residual velocity [m/s]	Error [%]
I	861.71	0	0	–
II	859.63	286.14	259.27	−9.39
III	855.48	0	0	–
IV	856.81	412.91	376.43	−8.83

From the numerical simulation, it can be seen that the simulated failure mode of the projectile penetrating the composite target plate is basically consistent with the test. Comparing the residual velocity of the test and simulation, the absolute error is within 10%. This is due to the error caused by the macro modeling used in UHMWPE fiberboard, which makes the simulation residual velocity decrease, but it can still be explained by the numerical simulation, which has a good accuracy, indicating that the numerical calculation method is validated effectively.

5. Failure mechanism and performance analysis

5.1. Analysis of the anti-penetration failure mechanism

Since structure I has the best anti-penetration performance in the test, only structure I is further analyzed. In the simulation, the projectile velocity is increased so that it is able to

penetrate the target plate, which facilitates the analysis of the whole process. Figure 11 shows the destruction process of the projectile body penetrating structure I at a velocity of 1100 m/s.

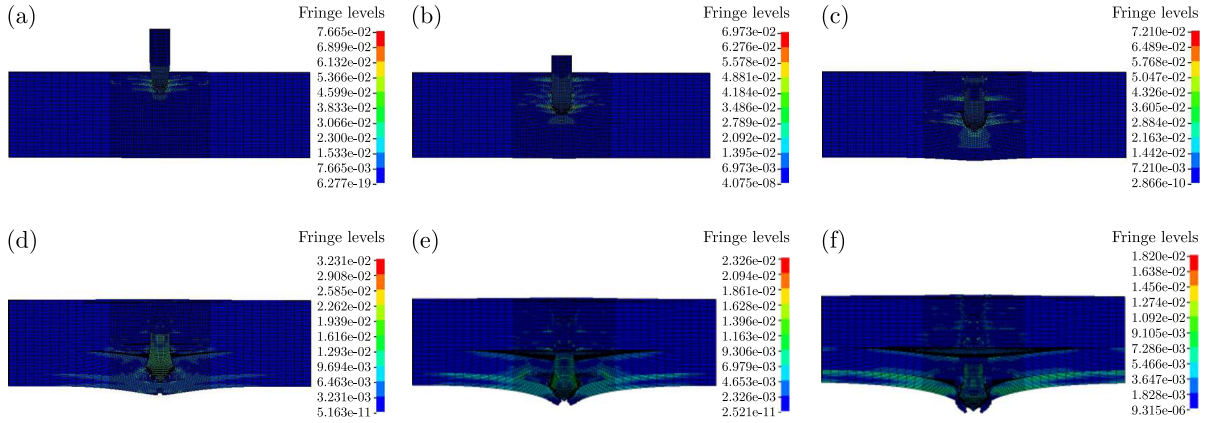

Fig. 11. Damage process of projectile penetration structure I: (a) $t = 12\,\mu$s, (b) $t = 20\,\mu$s, (c) $t = 30\,\mu$s, (d) $t = 45\,\mu$s, (e) $t = 60\,\mu$s, (f) $t = 70\,\mu$s

When the time t is shorter than 20 μs and the high-speed projectile penetrates through the front panel and part of the fiber laminar plates, the failure mode of the target plate is mainly shear failure, which generates a compression wave propagating along the thickness direction and the shear wave propagating along the in-plane direction with the impact point as the center. The compression wave causes local compression deformation in the contact area of the projectile and target. The in-plane shear wave causes a large velocity difference between the contact and non-contact regions of the projectile and target, and the fiber layer begins to undergo a shear failure. At this time, the pressure on the fiber layer along the thickness gradually increases from 418 MPa near the panel to 557 MPa and reaches the maximum pressure of 627 MPa near the core. The unidirectional arrangement of the fibers of UD laminates is conducive to the rapid expansion of the shockwave generated instantly by the projectile, and there is no doubt that the fibers are broken due to superposition of the shockwave and reflected wave at the interleaving point, so as to preliminarily consume the kinetic energy of the projectile and erode the projectile. At this point, the UD cloth fiber is subjected to 209 MPa of pressure near the core. When the time t is 20-30 μs, the projectile penetrates into the remaining fiber laminates. At this time, due to the upsetting deformation of the projectile, the fiber laminates are not only sheared, but also subjected to a certain tensile force in the transverse direction. At this time, the pressure on the remaining fiber laminates gradually drops to 360 MPa. However, the 3D fabric and aluminum alloy plate placed on the back provide strong support, and no large deflection occurs on the back of the fiber laminates. Most of the generated energy is absorbed by the interlocking 3D fabric and the energy-absorbing matrix filled in the pores, so that the kinetic energy of the projectile body is rapidly consumed, the pressure on the core is reduced to 216 MPa. When $t = 45\,\mu$s, the projectile body penetrates the fiber laminates and begins to penetrate the 3D fabric plates. At this time, a part of the core is basically abrasive. The fibers of the 3D orthogonal structure pull with each other, which brings great resistance to the advance of the projectile body, and the fracture of the fiber bundles causes kinetic energy of the projectile to be consumed further. At this time, the pressure on the three-dimensional orthogonal fabric and core comes to the minimum value of 161 MPa and 193 MPa. When time $t = 70\,\mu$s, the projectile body impinges the rear aluminum alloy plate and penetrates out, and the residual velocity of the projectile body is 452 m/s.

5.2. Influence of the thickness ratio of 3D fabric on anti-penetration performance

In order to study the influence of different thickness ratios of the 3D fabric on the anti-penetration performance of structure I and obtain the optimal structure proportion, in this Section, the total thickness of the core layer and the thickness of the front and rear panels are kept unchanged. The 3D fabric thickness ratio is shown as

$$\eta = \frac{t_s}{t_c} \cdot 100\% \tag{5.1}$$

where η represents the 3D fabric thickness ratio, t_s represents the thickness of the 3D fabric plate, t_c represents the overall thickness of the core layer.

According to the failure mechanism of the upper segment, the UD laminates should still occupy a large proportion in the core structure, otherwise it is not conducive to the initial resistance to projectile intrusion. Nine kinds of composite structures with different proportions of 3D fabrics are selected for simulation and multiple structures are selected within 50%. Among them, two categories of structures with a single core material are selected for comparison, as shown in Table 6. In order to fully reflect the protective performance of different structures, the projectile velocity should not be set too high or too low. It is suitable to set the initial velocity of the projectile at 1100 m/s by calculation.

Table 6. Composite target plate with different 3D fabric thickness ratios

Structure number	Thickness of front panel [mm]	Thickness of laminates [mm]	3D fabric plate thickness [mm]	Thickness of rear panel [mm]	Total thickness [mm]	Thickness ratio η [%]
1	1	28	0	5	34	0
2		24.5	3.5			12.5
3		21	7			25
4		19	9			32.14
5		17.5	10.5			37.5
6		16	12			42.86
7		14	14			50
8		7	21			75
9		0	28			100

Figure 12 shows the numerical calculation results. According to Fig. 12a, it can be found that the velocity of the projectile body changes with time in the same trend, which gradually decreases without great fluctuation. It can be seen from Fig. 12b that with an increase of the 3D fabric thickness ratio, the residual velocity of the projectile body increases first, then decreases, then increases and decreases again. The minimum residual velocity of the projectile penetrating No. 4 structure is 410.7 m/s.

Because of the density difference between UD laminates and 3D fabrics, the structure quality of different numbers is not exactly the same. Therefore, the energy absorption characteristics of different structures are characterized by the energy absorption coefficient (EAC), which is the ratio of energy absorbed to the mass of the target plate when the projectile penetrates the target plate (Tang *et al.*, 2002), defined as follows

$$EAC = \Big(\frac{1}{2}m_p v_i^2 - \frac{1}{2}m_q v_r^2\Big)\frac{1}{M} \tag{5.2}$$

where m_p and m_q are the original mass and residual mass of the projectile body respectively, v_i and v_r are the initial velocity and residual velocity of the projectile body respectively, and M is mass of the target plate.

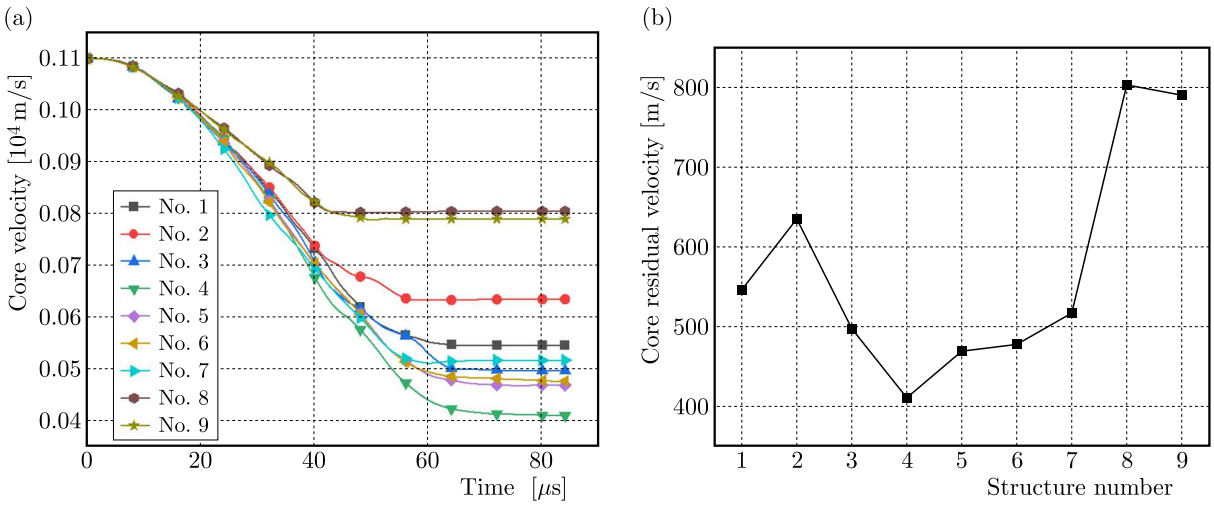

Fig. 12. Numerical simulation results: (a) time history curve of projectile velocity, (b) relation curve between the structure form and residual velocity

The EAC of the structure and its related parameters are shown in Table 7, where m_p is 8.4 g and not listed in the table. The relationship between the 3D fabric thickness ratio and EAC of different numbered structures is shown in Fig. 13.

Table 7. Structural EAC and its related parameters

Structure number	Thickness ratio η [%]	Initial velocity [m/s]	Residual velocity [m/s]	Residual mass of projectile m_q [g]	The mass of target plates M [g]	EAC [J/kg]
1	0		546.2	7.72	998.19	3937.56
2	12.5		634.8	7.60	993.63	3573.47
3	25		497.3	7.56	989.06	4193.05
4	32.14		410.7	7.60	987.04	4499.35
5	37.5	1100	469.1	7.36	985.84	4333.56
6	42.86		477.3	7.52	983.95	4294.34
7	50		517.4	7.60	982.05	4139.03
8	75		803.1	8.04	975.94	2550.59
9	100		790.3	8.20	969.70	2600.03

According to Fig. 13a, No. 4 structure has the highest EAC, which is 14.27% higher than that of No. 1 only using UD laminates as the core material, and is 73.05% higher than that of No. 9 only using 3D fabric as the core material. The EAC of No. 8 and 9 structures is much less than that of other structures. The reason is that the proportion of the 3D fabric is too high, which leads to the existence of a large number of nodes between 3D orthogonal structures. The fibers at these nodes are prone to fracture under superposition of the shock and reflected waves, which reduces the local impact resistance. According to Fig. 13b, as the 3D fabric thickness ratio increases, the EAC decreases first, then increases, then decreases and increases again. Equation (5.3) can be obtained by fitting data points

$$EAC = 3931.9 - 11709\eta + 101174\eta^2 - 260207.3\eta^3 + 253721.2\eta^4 - 84312.2\eta^5 \tag{5.3}$$

where EAC represents the energy absorption coefficient and represents the 3D fabric thickness ratio.

In the figure, the 3D fabric thickness ratio corresponding to the maximum point of EAC is 32.14%. Therefore, for the composite structure designed in this paper, the optimal proportion of

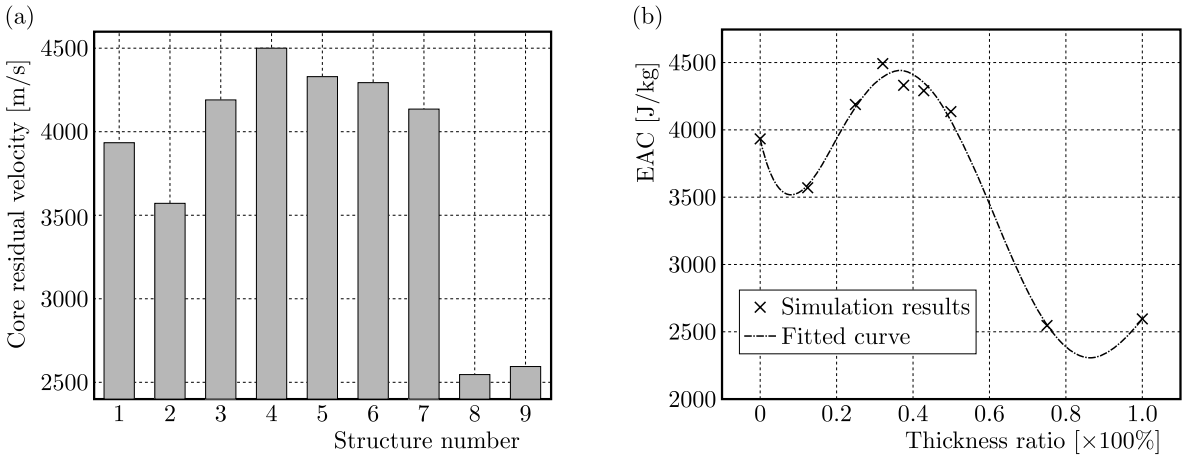

Fig. 13. (a) The relationship between EAC of different structures, (b) relationship between 3D fabric thickness ratio and EAC

the 3D fabric is 25%-37.5%. If considering the requirements of practical engineering lightweight, the 3D fabric thickness ratio is 30%-35% for a better choice.

6. Conclusions

In this paper, a UD/3D orthogonal woven fabric composite reinforced structure is designed based on the UHMWPE fiber material, and penetration tests are carried out on target plates with various reinforced structure forms by using a 7.62 mm steel core projectile. Combined with numerical simulations, the main conclusions are as follows:

- If the total thickness of UD laminates is the same, the 20 mm UD laminates have better penetration resistance than the four 5 mm UD laminates. The less number of UD laminates, the better anti-penetration performance of the composite reinforced structure.
- From analysis of the failure mechanism if occurs that the 3D orthogonal woven fabric has the advantage of spatial integrity, and can effectively resist deformation of UD laminates when placed behind the UD laminates together with an aluminum alloy plate. The fibers pull with each other, which can hinder the advance of the projectile. The fracture of a fiber bundle can enhance consumption of kinetic energy of the projectile.
- In order to ensure the protection capability and take the requirements of lightweight into account, in the structure with a core thickness of 28 mm, the 3D fabric thickness ratio can be controlled between 30% and 35%.

Acknowledgments

This research was supported by the National Natural Science Foundation of China (No. 52301373), the Young Elite Scientists Sponsorship Program by CAST (2022QNRC001), the Natural Science Foundation of Jiangsu Higher Education Institutions of China (No. 22KJB580005).

References

1. Chen L., Du T., Xiao X., et al., 2019, Experimental and numerical simulation of 7075 aluminum target impacted with ogival-nosed projectiles, *Ordnance Materials Science and Engineering*, **42**, 5, 27-32
2. Deng Y., Yuan J., Xu J., 2018, Effect of impact angle of rigid oval projectile on penetration characteristics of braided composite laminates, *Journal of Composite Materials*, **35**, 8

3. Hu M., Sun B., Gu B., 2021, Microstructure modeling multiple transverse impact damages of 3D braided composite based on thermo-mechanical coupling approach, *Composites: Part B: Engineering*, **214**
4. Johnson G.R., Cook W.H., 1983, A constitutive model and data for metals subjected to large strains, high strain rates and high temperature, *Proceeding of the 7th International Symposium on Ballistics*, Hague, Netherlands: International Ballistics Committee, 541-547
5. Liang J., Fang G., 2014, *Mechanical Properties Analysis Method of Three-Dimensional Braided Composites*, Harbin: Harbin University of Technology Press
6. Liu L., 2020, *Research on Anti-Penetration Performance of Ship Protection Module Based on Fiber Reinforcement*, Jiangsu University of Science and Technology
7. Qu K.F., Wu C.Q., Liu J., Yao Y., Deng Y., Yi C., 2020, Ballistic performance of multi--layered aluminium and UHMWPE fibre laminate targets subjected to hypervelocity impact by tungsten alloy ball, *Composite Structures*, **253**
8. Song M., Xuan H, He Z., et al., 2020, A review of research on 3D braided – woven composite casing containment, *Journal of Mechanical Engineering*, **8**, 31-35+40
9. Sun B., Liu Y., Gu B., 2009, A unit cell approach of finite element calculation of ballistic impact damage of 3D orthogonal woven composite, *Composites: Part B: Engineering*, **40**, 6, 552-560
10. Tan H., Xu S., Huang X., et al. 2018, Impact damage simulation and experimental verification of 3D four-way braided composite macro-finite element model, *Journal of Composites*, **35**, 5, 1139-1148
11. Tang D., Zhou B., Zhou Z., 2002, Experimental study on energy absorption characteristics of steel tube under lateral explosion shock wave loading, *Explosion and Impact*, **22**, 2, 41-46
12. Walter T.R., Subhash G., Sankar B.V., Yen C.F., 2009, Damage modes in 3D glass fiber epoxy woven composites under high rate of impact loading, *Composites: Part B*, **40**, 584-589
13. Wu L., Wang W., Jiang Q., Xiang C., Lou C.-W., 2019, Mechanical characterization and impact damage assessment of hybrid three-dimensional five-directional composites, *Journal of Polymers*, **11**, 9
14. Xiong Z., Liu X., Zhang Z., et al., 2016, Preliminary study on three-dimensional knitted fabric and its engineering protection application, *Journal of Natural Science of Xiangtan University*, **40**, 5, 65-70
15. You-Zhi L., Guo-Xin Z., Yue-Ming Z., 2008, Study on concrete moisture and drying shrinkage based on mesoscopical damage model, *Engineering Mechanics*, **25**, 7, 196-201

Manuscript received March 7, 2023; accepted for print June 14, 2023

JOURNAL OF THEORETICAL AND APPLIED MECHANICS
61, 4, pp. 715-728, Warsaw 2023
https://doi.org/10.15632/jtam-pl/170854

MECHANICAL PERFORMANCE OF ASPHALT PAVEMENT WITH ORTHOTROPIC UNBOUND GRANULAR SUB-BASE UNDER VEHICLE LOAD

Yuanyuan Gao
School of Civil Engineering and Mechanics, Yanshan University, Qinhuangdao, China
e-mail: gaoyuanyuan2286@ysu.edu.cn
Key Laboratory of Green Construction and Intelligent Maintenance for Civil Engineering of Hebei Province, Yanshan University, Qinhuangdao, China
Hebei High Performance Building Material Technology Innovation Center, Qinhuangdao Municipal Building Materials Group Co. Ltd., Qinhuangdao, China

Nkosilathi Lovewell Hlupo
School of Civil Engineering and Mechanics, Yanshan University, Qinhuangdao, China
e-mail: lovewell1996@gmail.com

Quan Qian
Hebei High Performance Building Material Technology Innovation Center, Qinhuangdao Municipal Building Materials Group Co. Ltd., Qinhuangdao, China; e-mail: qhdjcjc@126.com

Hongtao Jiang
School of Civil Engineering and Mechanics, Yanshan University, Qinhuangdao, China
e-mail: jht0122@stumail.ysu.edu.cn

The nonlinear mechanical response and orthotropy are the main properties of an unbound granular material as a sub-base in an asphalt pavement. To investigate the impact of stress and orthotropy characteristics simultaneously in an unbound granular sub-base, a constitutive relation and a finite model were proposed. The distribution of the sub-base resilience modulus and dynamic response of the pavement under vehicle loads were calculated. The results show an increase in the resilience modulus with a decrease in the orthotropic coefficient. Stress and orthotropy affect the stress distribution near the pavement layer, and vehicle velocity significantly impacts the vertical displacement.

Keywords: asphalt pavement, unbound granular sub-base, stress dependency, orthotropy, mechanical response

1. Introduction

The exponential growth of use of asphalt in the construction worldwide shows its importance to modern transport infrastructure. Understanding the mechanical performance of pavements has become essential for ensuring durability and stability. An unbound granular material is typically used as a base or sub-base of asphalt pavements in China because of its excellent water permeability, diffusion stress and bearing transition performance. Unbound granular materials consist of gravel, crushed stone and fine aggregate (sand) forming a crucial layer that supports and stabilizes the pavement system. The properties of unbound granular materials play a vital role in the overall performance of the asphalt pavement by distributing vehicle loads on the underlying soil. Therefore, the arrangement of particles of different sizes and loading conditions applied to the structures substantially impact the mechanical performance of the unbound granular material. Many researchers have confirmed that the resilience modulus of the unbound granular

material as a pavement layer increases with growth of the stress of the pavement, and the vertical resilience modulus is always larger than the horizontal one (Al-Qadi *et al.*, 2015). In particular, due to the layer-by-layer paving and rolling technology for constructing the road, the unbound granular base in an asphalt pavement exhibits more obvious nonlinear elastic and orthotropic properties. Therefore, the unbound granular properties must be considered when analyzing the mechanical response of the asphalt pavement. Researchers have been exploring the relationship between microstructural properties of the asphalt pavement and its macroscopic behavior by using upscaling techniques to improve the reliability and realism of pavement design, maintenance and performance evaluation (Lackner *et al.*, 2006). Hence the findings of this study will provide valuable insights into the existing knowledge on asphalt pavements ad will contribute to improving pavement designs and maintenance strategies.

In the pavement, the asphalt layer contains a viscoelastic material that exhibits viscous and elastic behavior when subjected to vehicle loads. This behavior provides more accurate calculation results on temperature sensitivity and time-dependent behavior. Additionally, viscoelastic models offer a better and more realistic representation of the mechanical response of the asphalt layer. In particular, Specht *et al.* (2017) used theory of viscoelasticity to investigate the resilient modulus of asphalt mixtures. The results show the difference in stiffness, and the differences substantially affect the resilient modulus response. Many other studies have also demonstrated that considering such viscoelastic behavior during analysis provides greater accuracy when calculating the mechanical response of the asphalt pavement under vehicle loads (Wu *et al.*, 2020). Therefore, the viscoelastic property of the asphalt layer in the pavement is considered in the model proposed in this paper.

The commonly used model for calculating the unbound granular resilience modulus includes the k-θ model, the Uzan model and the NCHRP 1-28A model *et al.* (González *et al.*, 2007). Because of the complexity of determining the unbound granular resilience modulus, researchers have experimented with several models to obtain a more accurate results. The chord formulation has been adopted to describe the resilience modulus of unbound granular materials. It has demonstrated its ability to characterize the mechanical behavior of these materials through calibration using laboratory test results (Aswegen *et al.*, 2015). Bilodeau *et al.* (2016) analyzed factors affecting the unbounded granular base modulus variation. They proposed a new model to calculate the resilient modulus of this base considering the effect of grading, fraction between crushed stones and moisture. Furthermore, Ullah *et al.* (2022) modified the Uzan model by considering the influence of grading, stress level and moisture content. That modification was based on the linear relationship between the resilience modulus and moisture observed in laboratory triaxial test results. Based on the shakedown theory, an elastoplastic constitutive model for unbound granular materials used in pavement applications was established. This model captures the deformation behavior of the material at different stages through the application of repeated loads. The proposed model was validated through a precision unbound material analyzer measuring mixed-size aggregate deformation (Li and Hao, 2020). In calculating the resilience modulus for unbound granular materials, the NCHRP 1-28A model is an effective and widely utilized approach (Sandjak *et al.*, 2020). Its application in assessing the resilience modulus of unbound granular materials has gained prominence due to its reliability and practicality.

To obtain the mechanical performance of an asphalt pavement containing an orthotropic unbound granular base, building a finite element model is one of the most effective methods according to the constitutive relation of the base. During the process of building a finite element model, one of the vital parts is using the finite element method to characterize the constitutive relation of pavement materials. In particular, the resilient modulus of an unbound granular material is a key input parameter in the model. The k-θ model, Uzan model and NCHRP 1-28A model of the resilience modulus are also commonly implemented as crucial information for building the asphalt pavement model containing an unbound granular layer (González *et al.*, 2007).

Cortes *et al.* (2012) adopted a nonlinear elastoplastic material model to capture the unbound granular base performance in a finite-element model. This model satisfies the Hertzian-type stress-dependent stiffness of the unbound granular base and the skeletal softening caused by deviatoric loads that approach failure. The Drucker-Prager model is used to consider the stress dependency of the unbound granular material for building flexible pavement models (Gupta *et al.*, 2015). However, convergence is a challenging issue for the nonlinear model. To deal with this problem, limiting the tensile stress of the unbound granular base to be non-negative and minimum, the value of the unbounded granular resilience modulus is usually adopted (Sahoo and Reddy, 2010). In the asphalt pavement model containing an unbound granular base, changing the stress-dependent constitutive model into a strain-dependent one effectively tackles the convergence difficulties. Then, a new strain tensor updating algorithm can be derived (Li and Guo, 2016). Tension stress can exist in unbound granular materials to a certain degree. Li and Hao (2020) modified the original asphalt pavement model by limiting the maximum tensile stress in the integral point. The calculation results received using this method are closer to the actual working state. According to the literature, most models of the asphalt pavements with an unbound granular base only take into account stress-dependent materials. However, orthotropy is another essential characteristic of the unbound granular layer in simulating the behavior of the asphalt pavement. Therefore, further research is required to provide more precise conclusions regarding the mechanical response of pavements containing the unbound granular layer.

Pavement structures face a multitude of loads during their lifetime, including both static and impact loads. Although a considerable amount of investigation has been conducted on how a static load impacts pavement durability, there is a growing recognition of the importance of considering the effects of impact loads. Vehicle speed significantly affects pavement deformations. For asphalt pavements in China, Assogba *et al.* (2021) reported that the current design code and mechanical analysis procedures are based on laminar elastic theory under static vehicle loads. In this approach, a low traffic volume was primarily analyzes, without considering the actual overload phenomena, vehicle running speed, viscoelastic behavior of the asphalt concrete layer and dynamic characteristics of the load induced by vehicle tires. Therefore, a considerable gap emerges between the proposed design theory and the actual loads on the pavement from moving vehicles. Karamanli *et al.* (2023) found that under moving loads, the structure may exhibit greater stress and displacement compared to static loads. Numerous studies have been conducted considering moving loads to evaluate performance of the structures under various conditions, assessed their structural capacity, and developed more accurate design methodologies for durability and resilience of the structure (Abdelrahman *et al.*, 2021; Esen *et al.*, 2021; Attia *et al.*. 2022; Karamanli *et al.*, 2023). Hence the moving load is a vital factor in the mechanical performance in the pavement analysis.

In this paper, based on the NCHRP 1-28A model, considering both stress dependency and orthotropic properties of an unbound granular material simultaneously, the constitutive relation of the unbound granular sub-base is established. By performing complex derivation, we obtain the consistent tangent modulus of the material. And then, based on the formulation of this consistent tangent modulus, the UMAT material program is compiled to describe properties of the unbound granular sub-base. Furthermore, an asphalt pavement model containing an unbound granular sub-base is constructed. By this model, the resilience modulus distributions in the subbase and the mechanical response of the pavement are received. The influence of stress dependency and orthotropic properties on the mechanical response of the asphalt pavement is analyzed. The proposed method and the results obtained from this paper could provide some suggestions on the design stage of a flexible pavement and asphalt pavement containing an unbound granular layer.

2. Constitutive relation

Based on the elastic theory and the generalized Hooke's law, the stress-strain relationship at any point can be expressed as (Rao, 2018)

$$\boldsymbol{\sigma} = \mathbf{D}\boldsymbol{\varepsilon} \tag{2.1}$$

where $\boldsymbol{\sigma} = [\sigma_{xx}, \sigma_{yy}, \sigma_{zz}, \sigma_{xy}, \sigma_{yz}, \sigma_{zx}]^{\mathrm{T}}$, $\boldsymbol{\varepsilon} = [\varepsilon_{xx}, \varepsilon_{yy}, \varepsilon_{zz}, \varepsilon_{xy}, \varepsilon_{yz}, \varepsilon_{zx}]^{\mathrm{T}}$, σ_{xx}, σ_{yy},σ_{zz}, σ_{xy}, σ_{yz} and σ_{zx} are 6 stress components under 3 stress states, respectively. ε_{xx}, ε_{yy}, ε_{zz}, ε_{xy}, ε_{yz} and ε_{zx} are 6 strain components, respectively. Each element in the stiffness matrix $\mathbf{D}$ represents the elastic properties of the material.

In engineering, the elastic modulus E and Poisson's ratio ν are often used to express the stress-strain relationship. Then, the matrix $\mathbf{D}$ can be expressed as (Rao, 2018)

$$\mathbf{D} = \begin{bmatrix} d_{11} & d_{12} & d_{13} & 0 & 0 & 0 \\ d_{21} & d_{22} & d_{23} & 0 & 0 & 0 \\ d_{31} & d_{32} & d_{33} & 0 & 0 & 0 \\ 0 & 0 & 0 & d_{44} & 0 & 0 \\ 0 & 0 & 0 & 0 & d_{55} & 0 \\ 0 & 0 & 0 & 0 & 0 & d_{66} \end{bmatrix} \tag{2.2}$$

In Eq. (2.2)

$$d_{11} = \frac{1-\nu_{yz}\nu_{yz}}{E_{yy}E_{zz}\Delta} \qquad d_{22} = \frac{1-\nu_{xz}\nu_{zx}}{E_{xx}E_{zz}\Delta} \qquad d_{33} = \frac{1-\nu_{xy}\nu_{yx}}{E_{xx}E_{yy}\Delta}$$

$$d_{12} = \frac{\nu_{yx}+\nu_{zx}\nu_{yz}}{E_{yy}E_{zz}\Delta} \qquad d_{21} = \frac{\nu_{xy}+\nu_{xz}\nu_{zy}}{E_{xx}E_{zz}\Delta} \qquad d_{23} = \frac{\nu_{zy}+\nu_{xy}\nu_{zx}}{E_{xx}E_{zz}\Delta}$$

$$d_{32} = \frac{\nu_{yz}+\nu_{yx}\nu_{xz}}{E_{xx}E_{yy}\Delta} \qquad d_{31} = \frac{\nu_{xz}+\nu_{xy}\nu_{yz}}{E_{xx}E_{yy}\Delta} \qquad d_{13} = \frac{\nu_{zx}+\nu_{yx}\nu_{zy}}{E_{yy}E_{zz}\Delta}$$

$$d_{44} = \frac{E_{xx}}{2(1+\nu_{xy})} \qquad d_{55} = \frac{E_{yy}}{2(1+\nu_{yz})} \qquad d_{66} = \frac{E_{zz}}{2(1+\nu_{zx})}$$

$$\Delta = \frac{1-\nu_{xy}\nu_{yx}-\nu_{yz}\nu_{zy}-\nu_{zx}\nu_{xz}-2\nu_{xy}\nu_{yz}\nu_{zx}}{E_{xx}E_{yy}E_{zz}}$$

where E_{xx}, E_{yy}, E_{zz} are the elastic modulus in the x, y, z directions, respectively, and G_{yz}, G_{zx}, G_{xy} are the shear moduli in the yz, zx, xy planes, respectively. ν_{yz}, ν_{zx} and ν_{xy} are Poisson's ratios in the x, y and z directions, respectively.

Because Poisson's ratio ν in the x, y and z direction has a little difference, Poisson's ratio is regarded as isotropic, and only an orthotropic elastic modulus E is considered in this paper. In the unbound granular layer of an asphalt pavement, the elastic modulus in the vertical direction is usually larger than that in the horizontal direction. If it is assumed that $E_{xx} = n_1 E_{zz}$, $E_{yy} = n_2 E_{zz}$, the values of n_1 and n_2 are greater than 0 and less than 1. Then Eq. (2.2) can be modified as (Rao, 2018)

$$\mathbf{D} = \begin{bmatrix} \frac{1-\nu}{(1-2\nu)(1+\nu)}\frac{1}{n_1}E_{zz} & \frac{1-\nu}{(1-2\nu)(1+\nu)}\frac{1}{n_1}E_{zz} & \frac{1-\nu}{(1-2\nu)(1+\nu)}\frac{1}{n_1}E_{zz} & 0 & 0 & 0 \\ \frac{1-\nu}{(1-2\nu)(1+\nu)}\frac{1}{n_2}E_{zz} & \frac{1-\nu}{(1-2\nu)(1+\nu)}\frac{1}{n_2}E_{zz} & \frac{1-\nu}{(1-2\nu)(1+\nu)}\frac{1}{n_2}E_{zz} & 0 & 0 & 0 \\ \frac{1-\nu}{(1-2\nu)(1+\nu)}E_{zz} & \frac{1-\nu}{(1-2\nu)(1+\nu)}E_{zz} & \frac{1-\nu}{(1-2\nu)(1+\nu)}E_{zz} & 0 & 0 & 0 \\ 0 & 0 & 0 & \frac{1}{n_1}\frac{E_{zz}}{2(1+\nu)} & 0 & 0 \\ 0 & 0 & 0 & 0 & \frac{1}{n_2}\frac{E_{zz}}{2(1+\nu)} & 0 \\ 0 & 0 & 0 & 0 & 0 & \frac{E_{zz}}{2(1+\nu)} \end{bmatrix} \tag{2.3}$$

Since the stiffness matrix of isotropic elastic materials can be expressed as

$$\mathbf{K}=\begin{bmatrix} \frac{1-\nu}{(1-2\nu)(1+\nu)}E_{zz} & \frac{1-\nu}{(1-2\nu)(1+\nu)}E_{zz} & \frac{1-\nu}{(1-2\nu)(1+\nu)}E_{zz} & 0 & 0 & 0 \\ \frac{1-\nu}{(1-2\nu)(1+\nu)}E_{zz} & \frac{1-\nu}{(1-2\nu)(1+\nu)}E_{zz} & \frac{1-\nu}{(1-2\nu)(1+\nu)}E_{zz} & 0 & 0 & 0 \\ \frac{1-\nu}{(1-2\nu)(1+\nu)}E_{zz} & \frac{1-\nu}{(1-2\nu)(1+\nu)}E_{zz} & \frac{1-\nu}{(1-2\nu)(1+\nu)}E_{zz} & 0 & 0 & 0 \\ 0 & 0 & 0 & \frac{E_{zz}}{2(1+\nu)} & 0 & 0 \\ 0 & 0 & 0 & 0 & \frac{E_{zz}}{2(1+\nu)} & 0 \\ 0 & 0 & 0 & 0 & 0 & \frac{E_{zz}}{2(1+\nu)} \end{bmatrix} \tag{2.4}$$

therefore, the stiffness matrix can be expressed as

$$\mathbf{D}=\mathbf{HK} \tag{2.5}$$

where $\mathbf{H}$ is a diagonal matrix presented as

$$\mathbf{H}=\begin{bmatrix} \frac{1}{n_1} & 0 & 0 & 0 & 0 & 0 \\ 0 & \frac{1}{n_2} & 0 & 0 & 0 & 0 \\ 0 & 0 & 1 & 0 & 0 & 0 \\ 0 & 0 & 0 & \frac{1}{n_1} & 0 & 0 \\ 0 & 0 & 0 & 0 & \frac{1}{n_2} & 0 \\ 0 & 0 & 0 & 0 & 0 & 1 \end{bmatrix} \tag{2.6}$$

Seed *et al.* (1967) introduced the concept of resilience modulus while investigating the relationship between the resilience characteristic of a subgrade soil and fatigue damage of an asphalt pavement. The resilience modulus is the ratio of the maximal deviator stress to the maximal resilience strain after deformation is stabilized under a repeated load. It can be expressed as

$$M_r=\frac{\sigma_d}{\varepsilon_r} \tag{2.7}$$

where M_r is the resilience modulus. $\sigma_d=\sigma_1-\sigma_3$ is the resilience stress (deviator stress). σ_1 and σ_3 are the maximun and minimun stress, respectively, and ε_r is the maximum resilience strain.

The NCHRP 1-28A model provides a calculation formula for the dynamic resilience modulus, and it can be expressed as (Sandjak *et al.*, 2020)

$$M_r(\theta,\tau_{oct})=k_1P_a\Big(\frac{\theta}{P_a}\Big)^{k_2}\Big(\frac{\tau_{oct}}{P_a}+1\Big)^{k_3} \tag{2.8}$$

where M_r is the resilience modulus, θ is the volume stress and τ_{oct} is the shear stress $\tau_{oct}=\sqrt{(\sigma_1-\sigma_2)^2+(\sigma_2-\sigma_3)^2+(\sigma_3-\sigma_1)^2}/3$. P_a is atmospheric pressure, and it is generally 100 kPa. k_1, k_2 and k_3 are material constants coming from the test data.

Considering the nonlinear stress dependency of the unbound granular sub-base, the modulus E_{zz} in Eq. (2.3) can be replaced by the dynamic resilience modulus calculated by the NCHRP 1-28A model.

3. Numerical model

3.1. Model of the asphalt pavement containing an unbound granular layer

An asphalt model is established using the finite element software ABAQUS to analyze the effect of stress dependency and orthotropic properties of the unbound granular layer on the dynamic response of the asphalt pavement. To balance the accuracy and time consumption, the

model size is 6 m×6 m×3.76 m. The pavement structure and boundary of the model are adopted the same as in the literature (Yan and Wang, 2016), and the same material parameters of the asphalt layer given in the literature (Yan and Wang, 2016) are also used in this paper. The contact area between the vehicle and the pavement surface is simplified as a rectangle, and the size is 0.184 m×0.192 m×2. It assumes that the vehicle load is located in this area. The distance between the two wheels is 0.225 m, and the contact pressure is $P = 700$ kPa. Figure 1 is a sketch map of the vehicle load. Because of symmetry, a half model is selected to analyze. To capture the

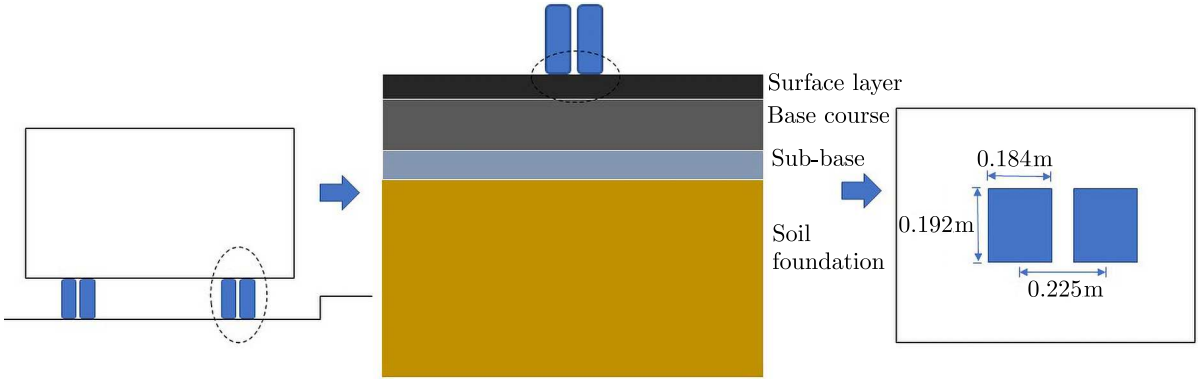

Fig. 1. Vehicle load sketch map

pavement behavior caused by a vehicle driving on the road, the loaded track starts at 1.464 m from one end of the model, the track length is 3.072 m, and the vehicle speed is 90 km/h. Figure 2 presents the asphalt model containing an unbound granular sub-base and the vehicle track. The details of geometry and material parameters are shown in Table 1. In this model shown in Fig. 2,

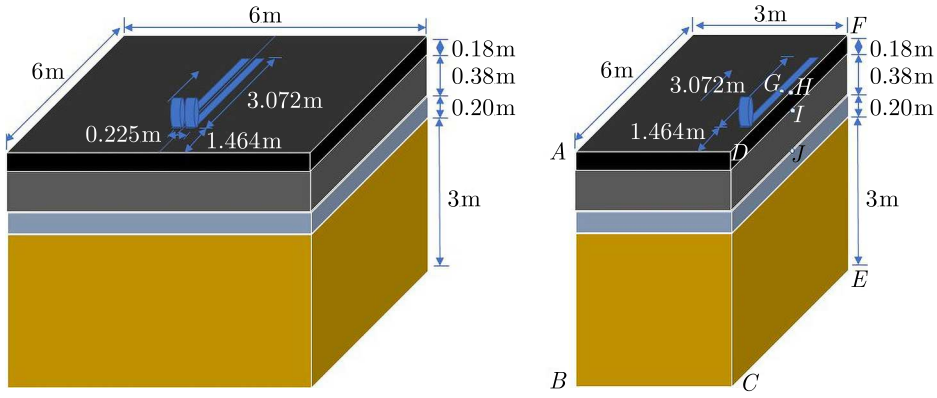

Fig. 2. Asphalt pavement containing an unbound granular sub-base

the boundary at the bottom is fixed, the displacement in the normal direction and rotation in the two tangential directions in the symmetry plane are constrained, and the normal displacement in the plane along the long edge and the two planes along the short edge of the model is 0. The asphalt pavement model is meshed by C3D8R element, which is an 8-node linear brick, reduced integration and hourglass control element. Adopting this element reduces the calculation time and avoids the shear-locking phenomenon to obtain relatively accurate results. The geometry, boundary conditions and mesh of the pavement model are shown in Figs. 3a-3c.

ABAQUS is an effective tool for solving dynamic problems. Because the growth of strain is a function of strain and the strain rates are lower than 10 units per second in this model, the Dynamic Implicit solver is adopted to calculate the dynamic response of this model. This solver uses the Newton-Raphson numerical algorithm and Newmark-β method to solve dynamic equilibrium equations, and the stiffness matrix is updated in each increment. This method is

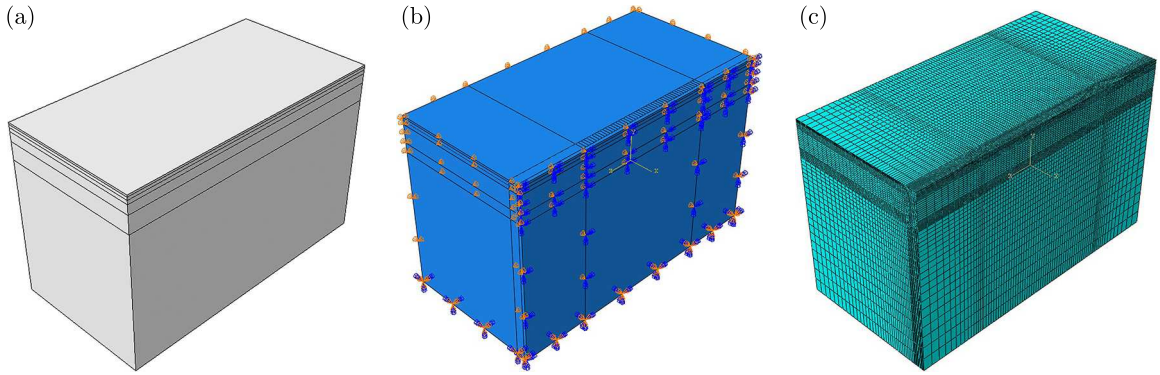

Fig. 3. Finite element model of the asphalt pavement: (a) geometry, (b) boundary conditions, (c) meshing

Table 1. Pavement geometry and material parameters

Pavement structure		Material name	Thickness [m]	Modulus [MPa]	Poisson's ratio	Density [kg/m^3]
Asphalt layer	Upper layer	AC-13C	0.040	Same with literature (Yan and Wang, 2016)	0.3	2300
	Middle layer	Sup-20	0.060	Same with literature (Yan and Wang, 2016)	0.3	2300
	Lower layer	Sup-25	0.080	Same with literature (Yan and Wang, 2016)	0.3	2300
Base course		Cement stabilized macadam	0.380	15000	0.2	2300
Sub-base		Unbound granular	0.200	$k_1 = 3170$, $k_2 = 0.06$, $k_3 = 0.43$ (Wang *et al.*, 2022)	0.3	2100
Soil foundation		Compacted soil	3.000	45	0.4	1850

unconditionally stable, for any initial assumption of Δt, the solution converges, and there is no mathematical time limit for the solution. In this model, the vehicle travelling time is 0.11776 s, and the increment size is 0.00256 s.

3.2. Tangent stiffness matrix

Newton's iterative method is an effective tool for solving nonlinear finite element models, and obtaining the tangent stiffness matrix is necessary for this method. The tangent stiffness modulus is a matrix that describes the relationship between stress differential and strain differential according to the current state of variables (stress, strain, etc.). Finding the tangent stiffness modulus generally starts from the constitutive relation of this material. Due to the resilience modulus being a function of stress and the orthotropic constitutive equations, it enhances difficulties of the formula derivation. This paper presents a new feature for obtaining the tangent stiffness matrix considering the stress dependency and orthotropy of the constitutive relationship.

The linear elastic constitutive equation in a tensor form can be expressed as

$$\boldsymbol{\sigma} = \frac{E}{1+\nu}\boldsymbol{\varepsilon} + \lambda \operatorname{tr}(\boldsymbol{\varepsilon})\mathbf{1} \tag{3.1}$$

where $\boldsymbol{\sigma} = [\sigma_{xx}, \sigma_{yy}, \sigma_{zz}, \sigma_{xy}, \sigma_{yz}, \sigma_{zx}]^{\mathrm{T}}$, $\boldsymbol{\varepsilon} = [\varepsilon_{xx}, \varepsilon_{yy}, \varepsilon_{zz}, \varepsilon_{xy}, \varepsilon_{yz}, \varepsilon_{zx}]^{\mathrm{T}}$, $\mathbf{1} = [1, 1, 1, 0, 0, 0]^{\mathrm{T}}$, $\operatorname{tr}(\boldsymbol{\varepsilon})$ is the volume strain.

Similar to the linear elastic constitutive relation, based on Eq. (3.1), the nonlinear elastic constitutive equation of the unbound granular sub-base can be rewritten as

$$\boldsymbol{\sigma} = \frac{M_r}{1+\nu}\boldsymbol{\varepsilon} + \lambda \operatorname{tr}(\boldsymbol{\varepsilon})\mathbf{1} \tag{3.2}$$

As known in Eq. (2.8), M_r is a function of the volume stress θ and shear stress τ_{oct}.

If orthotropy of the unbound granular sub-base is considered, based on constitutive relation Eq. (2.5), equation (3.2) can be modified as

$$\widetilde{\boldsymbol{\sigma}} = \frac{M_r}{1+\nu}\overline{\mathbf{H}}\boldsymbol{\varepsilon} + \lambda \operatorname{tr}(\boldsymbol{\varepsilon})\overline{\mathbf{H}}\mathbf{1} \tag{3.3}$$

According to the relationship between Eqs. (3.2) and (3.3), one can obtain

$$\widetilde{\boldsymbol{\sigma}} = \overline{\mathbf{H}}\boldsymbol{\sigma} \tag{3.4}$$

where $\overline{\mathbf{H}}$ is a tensor form of the matrix $\mathbf{H}$.

According to equation (3.3), the consistent tangent modulus can be expressed as

$$\frac{\partial \widetilde{\boldsymbol{\sigma}}}{\partial \boldsymbol{\varepsilon}} = \frac{\partial \widetilde{\boldsymbol{\sigma}}}{\partial \boldsymbol{\sigma}}\frac{\partial \boldsymbol{\sigma}}{\partial \boldsymbol{\varepsilon}} \tag{3.5}$$

where

$$\frac{\partial \widetilde{\boldsymbol{\sigma}}}{\partial \boldsymbol{\sigma}} = \overline{\mathbf{H}} \tag{3.6}$$

Therefore, if $\partial\boldsymbol{\sigma}/\partial\boldsymbol{\varepsilon}$ is obtained, the consistent tangent modulus $\partial\widetilde{\boldsymbol{\sigma}}/\partial\boldsymbol{\varepsilon}$ will also be received.

To simplify the process of formula derivation, let

$$B(\theta, \tau_{oct}) = \frac{M_r(\theta, \tau_{oct})}{1+\nu} = kP_a\Big(\frac{\theta}{P_a}\Big)^{k_2}\Big(\frac{\tau_{oct}}{P_a} + 1\Big)^{k_3} \tag{3.7}$$

where $k = k_1/(1+\nu)$.

And then, Eq. (3.2) can be rewritten as

$$\boldsymbol{\sigma} = B(\theta, \tau_{oct})[\boldsymbol{\varepsilon} + \alpha \operatorname{tr}(\boldsymbol{\varepsilon})\mathbf{1}] \tag{3.8}$$

where $\alpha = \nu/(1-2\nu)$, and the incremental relationship of Eq. (3.8) can be expressed as follows

$$\begin{aligned} &\Delta\boldsymbol{\sigma}_{n+1} = B(\theta, \tau_{oct})_{n+1}[\Delta\boldsymbol{\varepsilon}_{n+1} + \alpha \operatorname{tr}(\Delta\boldsymbol{\varepsilon}_{n+1})\mathbf{1}] \\ &B(\theta, \tau_{oct})_{n+1} = kP_a\Big(\frac{\theta_n}{P_a}\Big)^{k_2}\Big[\frac{(\tau_{oct})_n}{P_a} + 1\Big]^{k_3} \end{aligned} \tag{3.9}$$

where the subscript $n+1$ represents the calculation result under the current incremental step and n represents the calculation result of the previous step.

Based on Eq. (3.8), the volume stress and deviatoric stress are expressed as

$$\operatorname{tr}(\boldsymbol{\sigma}) = \overline{\alpha}B(\theta, \tau_{oct}) \operatorname{tr}(\boldsymbol{\varepsilon}) \qquad \overline{\boldsymbol{\sigma}} = B(\theta, \tau_{oct})\overline{\boldsymbol{\varepsilon}} \tag{3.10}$$

where $\overline{\alpha} = 3\alpha + 1 = (1+\nu)/(1-2\nu)$ and $\overline{\boldsymbol{\varepsilon}}$ is the deviatoric stress tensor, $\overline{\boldsymbol{\varepsilon}} = \boldsymbol{\varepsilon} - \operatorname{tr}(\boldsymbol{\varepsilon})\mathbf{1}/3$.

After a series of formula deductions and simplifications, $\partial\boldsymbol{\sigma}/\partial\boldsymbol{\varepsilon}$ can be gained as

$$\frac{\partial\boldsymbol{\sigma}}{\partial\boldsymbol{\varepsilon}} = B(\mathbf{I} + \alpha\mathbf{1}\otimes\mathbf{1}) + \Big(\frac{1}{3}\overline{\alpha}\boldsymbol{\varepsilon}\mathbf{1} + \overline{\boldsymbol{\varepsilon}}\Big)\otimes\nabla_{\varepsilon}B = B(\mathbf{I} + \alpha\mathbf{1}\otimes\mathbf{1} + m\mathbf{L}) \tag{3.11}$$

where

$$\mathbf{L} = \frac{\overline{\alpha}k_2(\tau_{oct}+P_a)}{3}\mathbf{1}\otimes\mathbf{1} + \frac{\overline{\alpha}k_2(\tau_{oct}+P_a)}{\operatorname{tr}(\boldsymbol{\sigma})}\overline{\boldsymbol{\sigma}}\otimes\mathbf{1} + \frac{\operatorname{tr}(\boldsymbol{\sigma})k_3}{9\tau_{oct}}\mathbf{1}\otimes\overline{\boldsymbol{\sigma}} + \frac{k_3}{3\tau_{oct}}\overline{\boldsymbol{\sigma}}\otimes\overline{\boldsymbol{\sigma}}$$

Therefore, the consistent tangent modulus $\partial\widetilde{\boldsymbol{\sigma}}/\partial\boldsymbol{\varepsilon}$ can be expressed as

$$\frac{\partial\widetilde{\boldsymbol{\sigma}}}{\partial\boldsymbol{\varepsilon}} = \frac{\partial\widetilde{\boldsymbol{\sigma}}}{\partial\boldsymbol{\sigma}}\frac{\partial\boldsymbol{\sigma}}{\partial\boldsymbol{\varepsilon}} = B\overline{\mathbf{H}}(\boldsymbol{I} + f_1\mathbf{1}\otimes\mathbf{1} + f_2\overline{\boldsymbol{\sigma}}\otimes\mathbf{1} + f_3\mathbf{1}\otimes\overline{\boldsymbol{\sigma}} + f_4\overline{\boldsymbol{\sigma}}\otimes\overline{\boldsymbol{\sigma}}) \tag{3.12}$$

where

$$f_1 = \alpha + m\frac{\overline{\alpha}k_2(\tau_{oct}+P_a)}{3} \qquad f_2 = m\frac{\overline{\alpha}k_2(\tau_{oct}+P_a)}{\operatorname{tr}(\boldsymbol{\sigma})}$$

$$f_3 = m\frac{\operatorname{tr}(\boldsymbol{\sigma})k_3}{9\tau_{oct}} \qquad f_4 = m\frac{k_3}{3\tau_{oct}}$$

Based on the formulation of the consistent tangent modulus $\partial\widetilde{\boldsymbol{\sigma}}/\partial\boldsymbol{\varepsilon}$, the UMAT program of the orthotropic nonlinearly elastic material is compiled. And then, by limiting the allowable maximum tensile stress, the mechanical response of the asphalt pavement model can be obtained.

4. Results and discussion

To analyze the influence of the orthotropic degree of the unbound granular sub-base on the mechanical response of the asphalt pavement based on the proposed procedure, the resilience modulus distribution in the unbound granular sub-base and the stress and displacement of the asphalt pavement are calculated. The results are shown in Figs, 4-8.

Because the resilient modulus distribution in the unbound granular sub-base is almost symmetrical on both sides of the wheel, so Figs. 4a-4d present the contour maps of the resilient modulus distribution in the unbound granular sub-base in the symmetry plane (plane CDFE) of the model with different orthotropic coefficients after the vehicle running at 0.00512 s. Compared with Figs. 4a-4d, the resilience modulus in each figure almost decreases from the top to the bottom of this layer. However, the gradients of the resilience modulus are different with different orthotropic coefficients. In Fig. 4a, the orthotropic coefficient $n_1 = n_2 = 1$, which means the material is isotropic in the unbound granular sub-base, and the maximum and minimum values of the resilience modulus are 301.37 MPa and 275.652 Mpa, respectively. The maximum values of the resilience modulus in Figs. 4b and 4c all emerge directly below the wheel center and the top of the sub-base layer. The minimum values of the resilience modulus in Figs. 4b and 4c all emerge directly below the wheel center and the bottom of this layer. The maximum and minimum values are approximately 326 MPa and 250 MPa, respectively, larger than the gradients shown in Fig. 4a. It means that the orthotropic coefficients in the transverse and longitudinal directions have almost the same effect on the distribution of the resilience modulus. Furthermore, when the unbound granular sub-base is transversaly isotropic $n_1 = n_2 = 0.2$, the difference in the resilience modulus value between the top and bottom of the layer is larger than those shown in Figs. 4a-4c. The maximum and minimum values are 350 MPa and 250 MPA. Therefore, the resilience modulus gradient increases as the orthotropic coefficients decrease in the unbound granular sub-base layer.

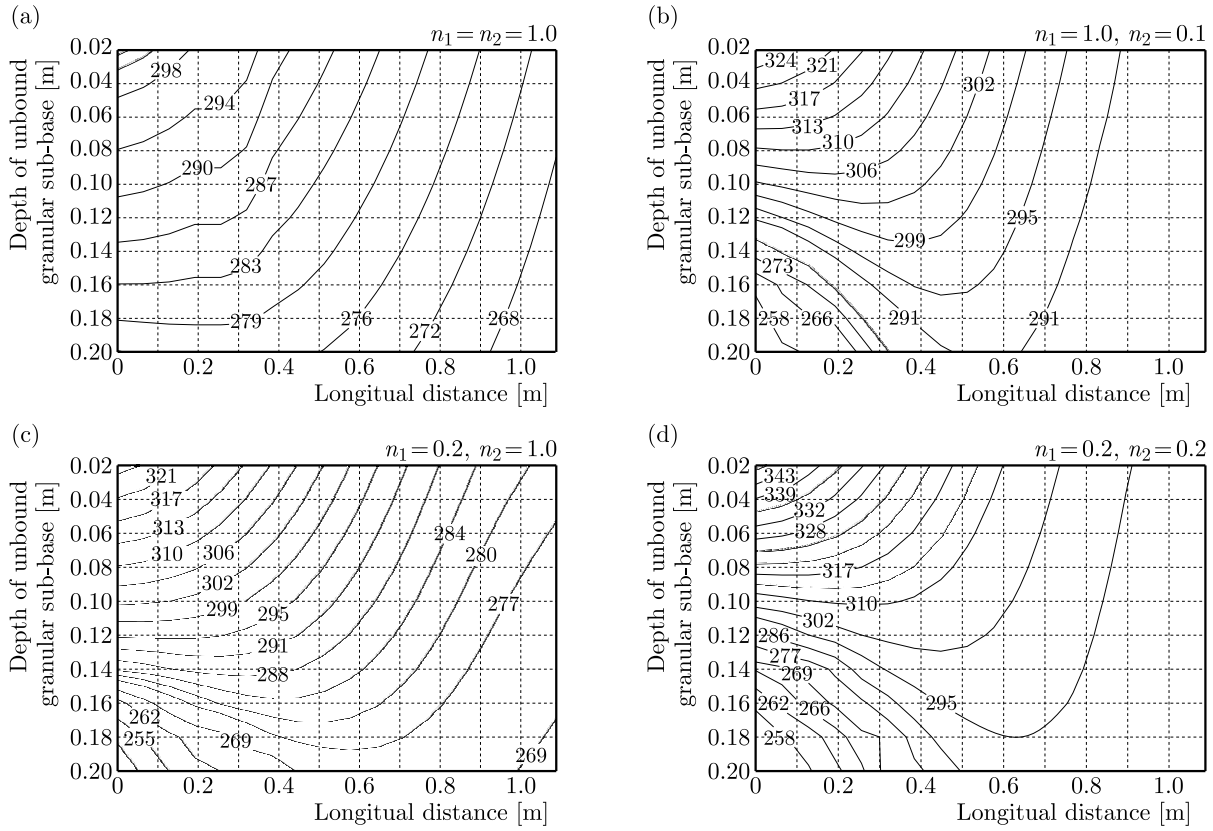

Fig. 4. Distribution of the resilience modulus of the unbound granular material with different orthotropic coefficients

The resilience modulus distribution changing in the unbound granular sub-base causes variation of the stress distribution in this layer. Even this affects the displacement and stress in other layers of this asphalt pavement model. Therefore, in this paper, the influence of the orthotropic coefficient in the sub-base on the mechanical response of the pavement is analyzed by comparing the tensile stress at the bottom of the asphalt layer and base and the displacement on the pavement surface. At the middle of the asphalt layer bottom (point I in the model), the transverse and longitudinal stresses generated by the vehicle driving load are calculated, and the results are shown in Figs. 5a and 5b.

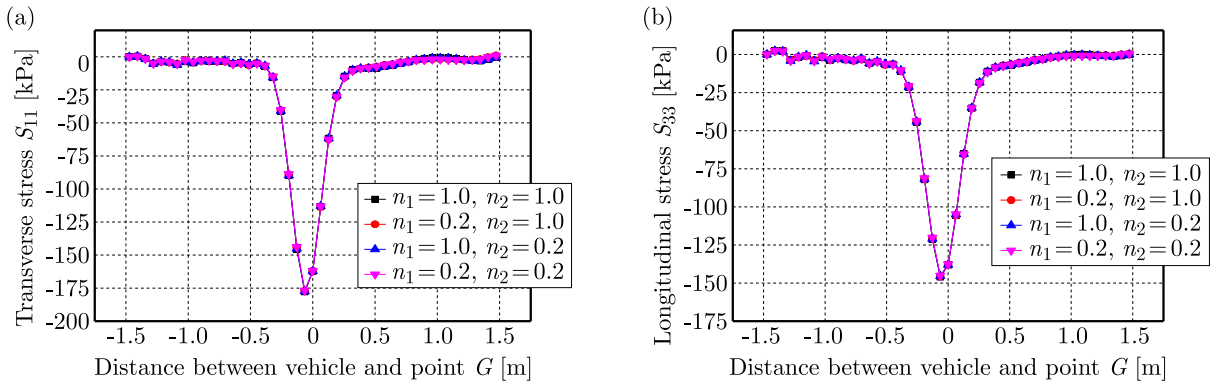

Fig. 5. Calculation results of transverse and longitudinal stresses (at point I) at the bottom of the asphalt pavement

Figures 6a and 6b present the variation of the transverse and longitudinal stress at the top center of the base (point J in the model) under a vehicle load. The pavement surface displacement variation (point G and point H in this model) is shown in Figs. 7a and 7b.

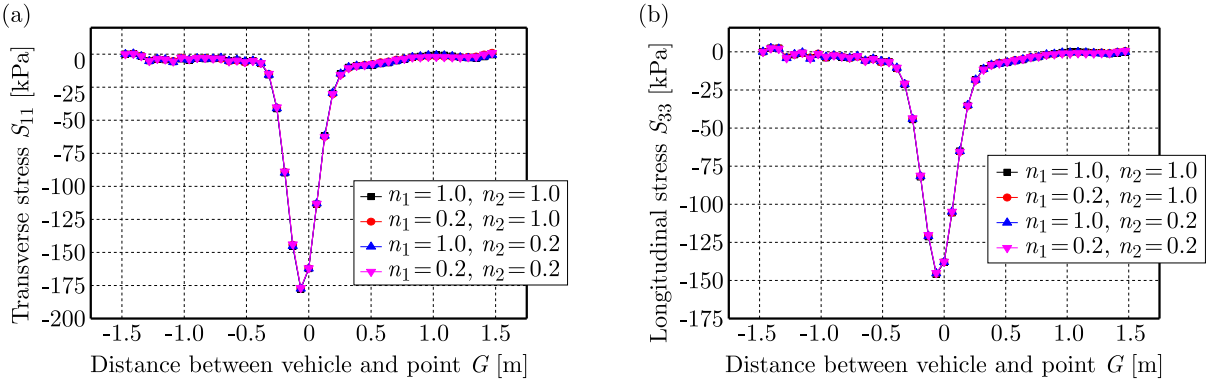

Fig. 6. Calculation results of transverse and longitudinal stresses (at point J) at the bottom of the base layer

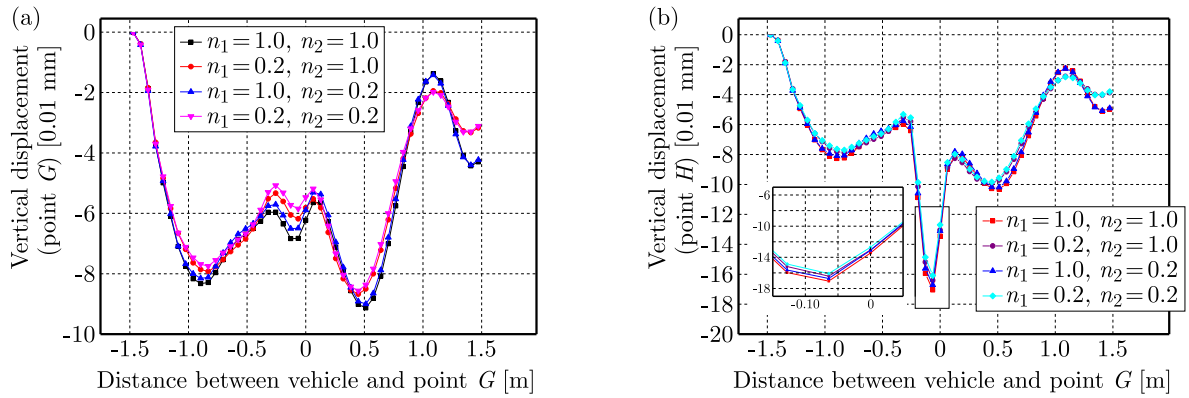

Fig. 7. Calculation results of the vertical displacement at points G and H in the model

The calculation results shown in Figs. 5a and 5b illustrate that the orthotropic coefficient of the sub-base has little effect on the variation of both transverse and longitudinal stresses at the bottom of the asphalt layer. The possible reason is that the unbound granular sub-base is relatively far from the asphalt layer. Therefore, the distribution of the resilience modulus in the sub-base slightly affects the mechanical response in the asphalt layer.

In Fig 6a, the transverse stress in the base sharply decreases with the longitudinal resilience modulus decreasing. In contrast, in Fig. 6b, the longitudinal resilience modulus reduction in the unbounded granular sub-base enlarges the longitudinal stress in the base. On one hand, compared with the asphalt layer, the base is closer to the sub-base, which causes the resilience modulus distribution in the unbounded granular sub-base to considerably affect the stress distribution in the base. On the other hand, the distribution of stress and resilience modulus always has the same variation tendency, which is consistent with our basic understanding. Therefore, to reduce the early damage and extend the pavement service life, the modulus of any layer or one direction of the modulus in the pavement can be manually adjusted through the pavement materials selection to make the stress distribution in the pavement more reasonable.

Figure 7 indicates that the vertical displacement at points G and H of the model decreases as the orthotropic coefficient decreases in the unbound granular sub-base. Compared with the longitudinal orthotropic coefficient, the transverse orthotropic coefficient contributes more to the displacement of the pavement. The vertical displacement of the asphalt pavement is one

of the essential indexes used in evaluating quality of the pavement. In the case of ignoring the orthotropic property, the displacement calculation results are always larger than the real values because the vertical resilience modulus of the unbounded granular base is always larger than its horizontal resilience modulus. Therefore, the results will affect the prediction and assessment of service conditions of the asphalt pavement to a certain extent.

Considering the velocity of a moving vehicle, vertical displacements at point H in this model are calculated with orthotropic coefficients $n_1 = n_2 = 1$ and $n_1 = n_2 = 0.5$. The results are presented in Figs. 8a and 8b, respectively. The velocity of the moving vehicle significantly affects the magnitude and variation of the vertical displacement of the asphalt pavement. It means that the velocity of a moving vehicle is one of the considerable factors for pavement design and assessment. Because of the paper length limitation, the stress distribution in this model with different velocities of a moving vehicle will be presented in the future work.

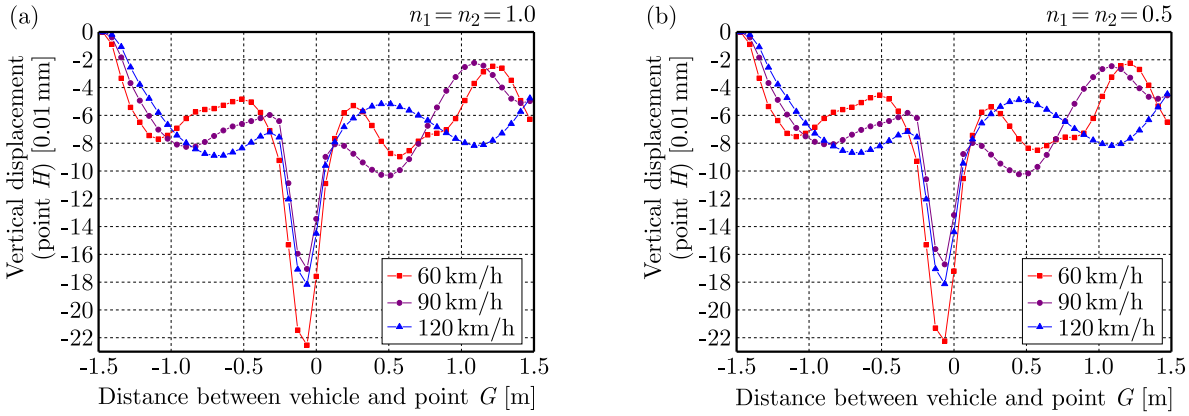

Fig. 8. Calculation results of vertical displacement at points G in the model considering different vehicle speeds

5. Conclusion

Considering the orthotropic and stress dependencies of the unbounded granular base, the NCHRP 1-28A model is adopted to calculate the resilience modulus in this paper. Based on the constitutive relation of an unbound granular sub-base, the consistent tangent modulus is derived for establishing the finite element model of the asphalt pavement containing an unbound granular sub-base. In this pavement model, the asphalt layer is assumed to be a viscoelastic material, and the base is considered elastic. The distribution of the resilience modulus in the sub-base and the mechanical response of the pavement are calculated. Some conclusions can be drawn from the results.

- The stress dependency and orthotropy are fundamental properties of the unbound granular sub-base. As the orthotropic coefficient decreases, the gradient of the resilience modulus increases.
- Orthotropy of the unbound granular sub-base affects the mechanical response of pavement, especially the mechanical response of the layers closer to the sub-base.
- Vertical displacement is an essential index for evaluating the overall stiffness of the pavement during the procedure of pavement performance evaluation and pavement design. The vertical displacement of the pavement is affected to some extent by considering the orthotropy of the unbound granular sub-base. Therefore, it again illustrates the necessity of treating the unbound granular layer as an orthotropic material in the calculation model.

- The velocity of a moving vehicle on the asphalt pavement is also a considerable factor influencing vertical displacement of the pavement. It is necessary to consider it in the pavement design and evaluation.

Acknowledgments

The authors would like to acknowledge the financial support by Heibei Natural Science Foundation (E2019203559).

References

1. Abdelrahman A.A., Esen I., Özarpa C., Eltaher M.A., 2021, Dynamics of perforated nanobeams subject to moving mass using the nonlocal strain gradient theory, *Applied Mathematical Modelling*, **96**, 215-235
2. Al-Qadi I., Wang H., Tutumluer E., 2015, Dynamic analysis of thin asphalt pavements by using cross-anisotropic stress-dependent properties for granular layer, *Transportation Research Record: Journal of the Transportation Research Board*, **2154**, 156-163
3. Assogba O.C., Tan Y., Sun Z., Lushinga N., Bin Z., 2021, Effect of vehicle speed and overload on dynamic response of semi-rigid base asphalt pavement, *Road Materials and Pavement Design*, **22**, 3, 572-602
4. Aswegen E., Steyn W., Theyse H., 2015, Development of a saturation and stress-dependent chord modulus model for unbound granular material, *Journal of the South African Institution of Civil Engineering*, **57**, 2, 8-21
5. Attia M.A., Melaibari A., Shanab R.A., Eltaher M.A., 2022, Dynamic analysis of sigmoid bidirectional FG microbeams under moving load and thermal load: Analytical Laplace solution, *Mathematics*, **10**, 24, 4797
6. Bilodeau J.P., Plamondon C.O., Doré G., 2016, Estimation of resilient modulus of unbound granular materials used as pavement base: combined effect of grain-size distribution and aggregate source frictional properties, *Materials and Structures*, **49**, 4363–4373
7. Cortes D.D., Shin H., Santamarina J.C., 2012, Numerical simulation of inverted pavement systems, *Journal of Transportation Engineering*, **138**, 12, 1507-1519
8. Esen I., Eltaher M.A., Abdelrahman A.A., 2023, Vibration response of symmetric and sigmoid functionally graded beam rested on elastic foundation under moving point mass, *Mechanics Based Design of Structures and Machines*, **51**, 5, 2607-2631
9. González A., Saleh M., Ali A., 2007, Evaluating nonlinear elastic models for unbound granular materials in accelerated testing facility, *Transportation Research Record: Journal of the Transportation Research Board*, **1990**, 1, 141-149
10. Gupta A., Kumar P., Rastogi R., 2015, Critical pavement response analysis of low-volume pavements considering nonlinear behavior of materials, *Transportation Research Record: Journal of the Transportation Research Board*, **2474**, 1, 3-11
11. Karamanli A., Eltaher M.A., Thai S., Vo T.P., 2023. Transient dynamics of 2D-FG porous microplates under moving loads using higher order finite element model, *Engineering Structures*, **278**, 115566
12. Lackner R., Blab R., Eberhardsteiner J., Mang H.A., 2006, Characterization and multiscale modeling of asphalt-recent developments in upscaling of viscous and strength properties, *III European Conference on Computational Mechanics: Solids, Structures and Coupled Problems in Engineering*, Springer, Netherlands
13. Li N., Ma B., Wang H., Sun W., 2020, Development of elasto-plastic constitutive model for unbound granular materials under repeated loads, *Transportation Geotechnics*, **23**, 100347

14. Li S., Guo Z., 2016, Applicability and verification of unbound granular material elastic deformation constitutive model, *Journal of Tongji University: Natural Science*, **44**, 8, 1227-1233

15. Li S., Hao P., 2020, Stress dependent and redistribution behaviour of unbound granular material, *International Journal of Pavement Engineering*, **21**, 3, 347-356

16. Rao S.S., 2018, *The Finite Element Method in Engineering*, 6th Ed., Elsevier

17. Sahoo U.C., Reddy K.S., 2010, Effect of nonlinearity in granular layer on critical pavement responses of low volume roads, *International Journal of Pavement Research and Technology*, **3**, 6, 320-325

18. Sandjak K., Ouanani M., Tiliouine B., 2020, Experimental characterisation and numerical modelling of the resilient behaviour of unbound granular materials for roads, *Journal of Building Materials and Structures*, **7**, 2, 159-177

19. Seed H.B., Mitry F.G., Monismith C.L., Chan C.K., 1967, Prediction of flexible pavement deflections from laboratory repeated-load tests, NCHRP report

20. Specht L.P., Babadopulos L.F.D.A.L., Di Benedetto H., Sauzat C., Soares J.B., 2017, Application of the theory of viscoelasticity to evaluate the resilient modulus test in asphalt mixes, *Construction and Building Materials*, **149**, 15, 648-658

21. Ullah S., Jamal A., Almoshaogeh M., Alharbi F., Hussain J., 2022, Investigation of resilience characteristics of unbound granular materials for sustainable pavements, *Sustainability*, **14**, 6874

22. Wang M., Yu Q., Xiao Y., Li W., 2022, Resilient modulus behavior and prediction models of unbound permeable aggregate base materials derived from tunneling rock wastes, *Materials*, **15**, 6005

23. Wu C., Wang H., Zhao J., Jiang X., Yanjun Q., Yusupov B., 2020, Prediction of viscoelastic pavement responses under moving load and nonuniform tire contact stresses using 2.5-D finite element method, *Mathematical Problems in Engineering*, 1029089

24. Yan M., Wang J., 2016, *Application of ABAQUS Finite Element Software in Pavement Structure Analysis*, Zhejiang University Press

Manuscript received March 24, 2023; accepted for print July 20, 2023

JOURNAL OF THEORETICAL AND APPLIED MECHANICS
61, 4, pp. 729-739, Warsaw 2023
https://doi.org/10.15632/jtam-pl/170840

SELF-SYNCHRONIZATION OF DRIVE VIBRATORS OF AN ANTIRESONANCE VIBRATORY CONVEYOR

Grzegorz Cieplok

AGH University of Science and Technology, Department of Mechanical Engineering and Robotics, Cracow, Poland
e-mail: cieplok@agh.edu.pl

A theoretical analysis of synchronization of inertial vibrators of a vibratory conveyor with a dynamic damper is presented in this paper. It is shown that for the over-resonance regime and counter-running drive vibrators, there is only one stable state of the system warranting formation of necessary sectional vibrations of the trough. The analytical form of the moment--synchronizing vibrators is also determined, and on the basis of this, the influence of angular vibrations of the body on the synchronizing process of the drive vibrators is determined. Due to the differences in the participation of angular vibrations in the self-synchronizing process in relation to classical solutions, the presented results fundamentally influence the design of long antiresonance conveyors.

Keywords: stability, vibratory conveyor, antiresonance, self-synchronizstion

1. Introduction

Among vibratory conveyors, antiresonance conveyors have become increasingly popular in recent years (Surówka and Czubak, 2021; Czubak and Gajowy, 2022; Gajowy, 2019). Such conveyors use dynamic dampers (Asami, 2019; Ascari, 1980; Fasana and Giorcelli, 2010) based on Frahm's patent from 1911 (Frahm, 1911) to decrease vibrations of drive frames as well as related harmful effects on the surrounding environment. The solution shown in Fig. 1, which is presently under prototype investigation, is one of the newest solutions of this type.

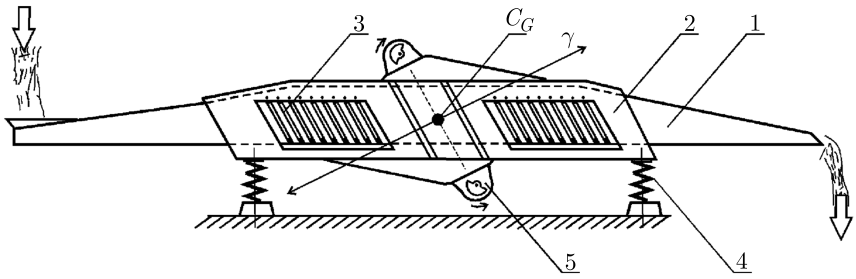

Fig. 1. Patent application No P.434041. Antiresonance vibratory conveyor (application drawing Fig. 2 in P. 434041 document). KMC Global Europe (2020), Opole, PL. Author: Jerzy Michalczyk, Cracow

It is written in the patent description that "This antiresonance vibratory conveyor is characterized by the fact that its body (2) is of a stiff structure, while trough (1) (functioning as a mass of the dynamic eliminator) is of a self-supporting structure and in its central segment is suspended inside body (2) with a clearance allowing for its effect on vibratory motion. The mass centres of trough (1) and of body (2) with vibrators (5) and leaf springs (3) overlap each other and – in addition – trough (1) is suspended inside body (2) on leaf springs (3), which are mounted in pairs symmetrically relative to the conveyor axial plane of symmetry, near the nodal points of the first form of the natural trough vibrations (1)".

The author of this solution aimed to build a long conveyor (several metres), which due to construction difficulties (mainly related to maintaining sufficient stiffness of the frame and trough) is not an easy task.

In addition to structural problems, issues arise related to the vibrator drive and self--synchronization processes of vibrators. When length of the conveyor is increased, its mass moment of inertia is also increased, which in turn leads to decreasing angular vibrations of the body and decreasing the synchronizing moment of the vibrators.

Knowledge concerning self-synchronization of unbalanced masses is very wide and includes problems of deterministic (Paz and Cole, 1992) and chaos theory (Chedjou *et al.*, 2008). Fundamental works in this area were published by Blekhman (1971, 2000). He formulated, among other concepts, the stability criterion for synchronized motion of unbalanced masses and, on its basis, developed detailed rules for constructing drive structures of inertial vibrators, which were cited later in papers by several authors (Michalczyk and Cieplok, 2014; Hou *et al.*, 2017; Li *et al.*, 2020).

Analyses concerning nonlinear systems are especially interesting. The conditions of synchronizing systems of two vibrators installed on a common platform and the criterion of global stability of the solutions obtained on the basis of analysing nonlinear equations were presented in (Smirnova and Proskurnikov, 2021). The synchronization of two exciters under the nonlinear influence of elastic elements of sectional-linear characteristics was investigated in (Zhang *et al.*, 2016). A system with a tri-motor was analysed in (Zou *et al.*, 2020), where the conditions of achieving the synchronous state were determined by means of the small-parameters method, while the stability criterion of synchronous motion was determined by means of the Poincaré--Lyapunov method. In (Zhao *et al.*, 2011), the problem of synchronizing two pairs of vibrators elastically placed on a common frame was reduced to the stability problem of two generalized systems. One of them was the generalized system of angular velocity disturbance parameters for four unbalanced rotors, and the other was the generalized system of three-phase disturbance parameters. Researchers have also obtained satisfactory results regarding the synchronization of unbalanced masses in spatial motion (Zhao, 2010; Cieplok and Wójcik, 2020; Fang *et al.*, 2019). Because of strong nonlinear connections between unbalanced masses and the body of the device (Dimentberg *et al.*, 1997), some analyses concerning transient processes are still based on numerical investigation (Zhang *et al.*, 2019; Shokhin *et al.*, 2021).

2. Theoretical analysis

The conveyor of a structure corresponding to the one presented in Fig. 1 was analyzed in this study. The analyses dealt with three problems: dynamic equations of motion of the system, analysis of motion stability of drive vibrators, and determination of an analytical formula for the synchronizing moment of vibrators. Realization of the last two problems required knowing the analytical solutions of equations of motion of the system. They were determined for the steady state, for which it was possible to assume a constant rotational speed of vibrators. This assumption allowed one to obtain linear equations and to lower the number of degrees of freedom by two. The dynamic equations of motion became also the basis for verifying analytical results.

2.1. Dynamic equations of the conveyor

Let us discuss the system presented in Fig. 2. It consists of four solid bodies representing: drive frame of a conveyor m_k with mass inertia J_{Ck}, transporting trough m_r with mass inertia J_{Cr} and two inertial vibrators each of them having mass m_w and radius of unbalance e_w. The conveyor is placed on a viscoelastic suspension described by parameters k_x, k_y, b_x, b_y; while the trough is connected with the body by means of a leaf springs system described by parameters k_{si}, b_{si}.

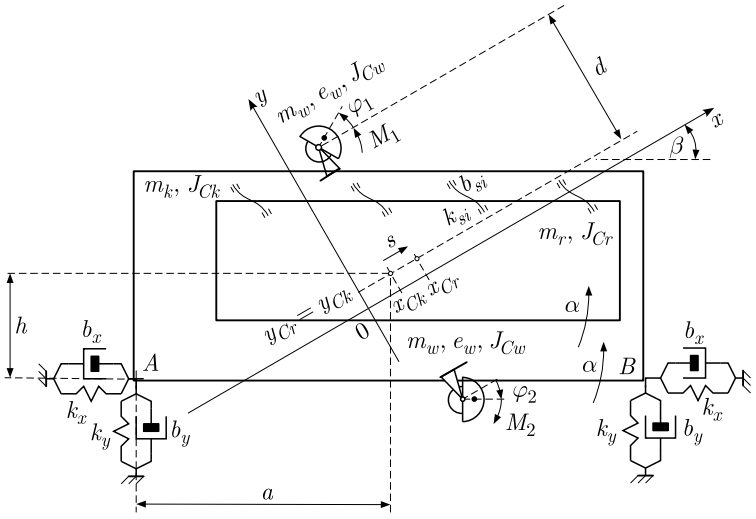

Fig. 2. Schematic presentation of the system.

Inertial vibrators are driven counter running by means of two asynchronous motors of identical drive characteristics M_1 and M_2. The total value of the axial moment of inertia of the motor and the central moment of inertia of the vibrator mass is marked as J_w. Vibrators are placed in the line perpendicular to the direction of motion of the transporting trough. They are placed symmetrically at a distance d, in relation to the mass centre of the drive frame. 6 generalized coordinates were used to describe the system location. Coordinates x_{Ck}, y_{Ck} represent the mass centre of the drive frame, α – angle of rotation of the drive frame and transporting trough, s – displacement of the trough in relation to the frame, and angles φ_1, φ_2 describe angular positions of the vibrators. On the basis of Fig. 2 the kinematic dependencies imposed on the positions of mass centres of the trough and drive vibrators were determined

$$\begin{aligned} &x_{Cr} = x_{Ck} + s \qquad y_{Cr} = y_{Ck} \\ &x_{C1} = x_{Ck} + e_w \cos\varphi_1 + d\alpha \qquad y_{C1} = y_{Ck} + e_w \sin\varphi_1 \\ &x_{C2} = x_{Ck} + e_w \cos\varphi_2 - d\alpha \qquad y_{C2} = y_{Ck} - e_w \sin\varphi_2 \end{aligned} \tag{2.1}$$

Geometrical dependencies imposed on shifting of springs of the suspension system were also determined

$$\begin{aligned} &\Delta x_A = h\alpha + x_{Ck}\cos\beta - y_{Ck}\sin\beta \qquad \Delta y_A = -a\alpha + y_{Ck}\cos\beta + x_{Ck}\sin\beta \\ &\Delta x_B = h\alpha + x_{Ck}\cos\beta - y_{Ck}\sin\beta \qquad \Delta y_B = a\alpha + y_{Ck}\cos\beta + x_{Ck}\sin\beta \end{aligned} \tag{2.2}$$

These dependencies allowed one to formulate the Lagrange kinetic potential of the system in the form

$$\begin{aligned} L = {} & \frac{1}{2}m_k\Big(\frac{d}{dt}x_{Ck}\Big)^2 + \frac{1}{2}(m_k + m_r)\Big(\frac{d}{dt}y_{Ck}\Big)^2 + \frac{1}{2}(J_{Ck} + J_{Cw})\Big(\frac{d}{dt}\alpha\Big)^2 + \frac{1}{2}m_r\Big(\frac{d}{dt}x_{Cr}\Big)^2 \\ & + \frac{1}{2}m_w\Big(\frac{d}{dt}x_{C1}\Big)^2 + \frac{1}{2}m_w\Big(\frac{d}{dt}y_{C1}\Big)^2 + \frac{1}{2}J_{Cw}\Big(\frac{d}{dt}\varphi_1\Big)^2 + \frac{1}{2}m_w\Big(\frac{d}{dt}x_{C2}\Big)^2 + \frac{1}{2}m_w\Big(\frac{d}{dt}y_{C2}\Big)^2 \\ & + \frac{1}{2}J_{Cw}\Big(\frac{d}{dt}\varphi_2\Big)^2 - \Big(\frac{1}{2}k_x\Delta x_A^2 + \frac{1}{2}k_y\Delta y_A^2 + \frac{1}{2}k_x\Delta x_B^2 + \frac{1}{2}k_y\Delta x_B^2 + \frac{1}{2}k_s s^2\Big) \end{aligned} \tag{2.3}$$

and on its basis and by making use of the Lagrange formula

$$\frac{d}{dt}\frac{\partial L}{\partial \dot{q}_i} - \frac{\partial L}{\partial q_i} + \frac{1}{2}\frac{\partial N}{\partial \dot{q}_i} = Q_i \tag{2.4}$$

to determine the dynamic equation of motion. In Eq. (2.4) marked are: by q_i the i-th generalized coordinate, by Q_i – i-th generalized force and by N – value of linear loses. The last quantity (2.5) was determined on account of a damping present in elements of the system suspension and in leaf springs of the trough

$$N = b_x\Big(\frac{d\Delta x_A}{dt}\Big)^2 + b_y\Big(\frac{d\Delta y_A}{dt}\Big)^2 + b_x\Big(\frac{d\Delta x_B}{dt}\Big)^2 + b_y\Big(\frac{d\Delta y_B}{dt}\Big)^2 + b_s\Big(\frac{ds}{dt}\Big)^2 \tag{2.5}$$

Dependencies from (2.6) to (2.11) present dynamic equations of motion determined one after another in the coordinates: x_{Ck}, y_{Ck}, s, α, φ_1 and φ_2

$$\begin{aligned}
&[\sin(2\beta)b_y - \sin(2\beta)b_x]\Big(\frac{d}{dt}y_{Ck}\Big) + [\sin(2\beta)k_y - \sin(2\beta)k_x]y_{Ck}\\
&\quad + (2m_w + m_r + m_k)\Big(\frac{d^2}{dt^2}x_{Ck}\Big) + [(1-\cos(2\beta))b_y + (\cos(2\beta)+1)b_x]\Big(\frac{d}{dt}x_{Ck}\Big)\\
&\quad + [(1-\cos(2\beta))k_y + (\cos(2\beta)+1)k_x]x_{Ck} + m_r\Big(\frac{d^2}{dt^2}s\Big)\\
&\quad - e_w m_w \sin(\varphi_2)\Big(\frac{d^2}{dt^2}\varphi_2\Big) - e_w m_w \cos(\varphi_2)\Big(\frac{d}{dt}\varphi_2\Big)^2 - e_w m_w \sin(\varphi_1)\Big(\frac{d^2}{dt^2}\varphi_1\Big)\\
&\quad - e_w m_w \cos(\varphi_1)\Big(\frac{d}{dt}\varphi_1\Big)^2 + 2\alpha\cos(\beta)hk_x + 2\Big(\frac{d}{dt}\alpha\Big)\cos(\beta)b_x h = 0
\end{aligned} \tag{2.6}$$

$$\begin{aligned}
&(2m_w + m_r + m_k)\Big(\frac{d^2}{dt^2}y_{Ck}\Big) + [(\cos(2\beta)+1)b_y + (1-\cos(2\beta))b_x]\Big(\frac{d}{dt}y_{Ck}\Big)\\
&\quad + [(\cos(2\beta)+1)k_y + (1-\cos(2\beta))k_x]y_{Ck} + [\sin(2\beta)b_y - \sin(2\beta)b_x]\Big(\frac{d}{dt}x_{Ck}\Big)\\
&\quad + [\sin(2\beta)k_y - \sin(2\beta)k_x]x_{Ck} - e_w m_w \cos(\varphi_2)\Big(\frac{d^2}{dt^2}\varphi_2\Big) + e_w m_w \sin(\varphi_2)\Big(\frac{d}{dt}\varphi_2\Big)^2\\
&\quad + e_w m_w \cos(\varphi_1)\Big(\frac{d^2}{dt^2}\varphi_1\Big) - e_w m_w \sin(\varphi_1)\Big(\frac{d}{dt}\varphi_1\Big)^2 - 2\alpha\sin(\beta)hk_x\\
&\quad - 2\Big(\frac{d}{dt}\alpha\Big)\sin(\beta)b_x h = 0
\end{aligned} \tag{2.7}$$

$$m_r\Big(\frac{d^2}{dt^2}x_{Ck}\Big) + m_r\Big(\frac{d^2}{dt^2}s\Big) + b_s\Big(\frac{d}{dt}s\Big) + k_s s = 0 \tag{2.8}$$

$$\begin{aligned}
&-2\sin(\beta)b_x h\Big(\frac{d}{dt}y_{Ck}\Big) - 2\sin(\beta)hk_x y_{Ck} + 2\cos(\beta)b_x h\Big(\frac{d}{dt}x_{Ck}\Big) + 2\cos(\beta)hk_x x_{Ck}\\
&\quad + de_w m_w \sin(\varphi_2)\Big(\frac{d^2}{dt^2}\varphi_2\Big) + de_w m_w \cos(\varphi_2)\Big(\frac{d}{dt}\varphi_2\Big)^2 - de_w m_w \sin(\varphi_1)\Big(\frac{d^2}{dt^2}\varphi_1\Big)\\
&\quad - de_w m_w \cos(\varphi_1)\Big(\frac{d}{dt}\varphi_1\Big)^2 + 2\Big(\frac{d^2}{dt^2}\alpha\Big)d^2 m_w + 2a^2\alpha k_y + 2\alpha h^2 k_x\\
&\quad + 2\Big(\frac{d}{dt}\alpha\Big)b_x h^2 + 2a^2\Big(\frac{d}{dt}\alpha\Big)b_y + (J_{Cr} + J_{Ck})\Big(\frac{d^2}{dt^2}\alpha\Big) = -M_1 + M_2
\end{aligned} \tag{2.9}$$

$$\begin{aligned}
&e_w m_w \cos(\varphi_1)\Big(\frac{d^2}{dt^2}y_{Ck}\Big) - e_w m_w \sin(\varphi_1)\Big(\frac{d^2}{dt^2}x_{Ck}\Big) + (e_w^2 m_w + J_{Cw})\Big(\frac{d^2}{dt^2}\varphi_1\Big)\\
&\quad - \Big(\frac{d^2}{dt^2}\alpha\Big)de_w m_w \sin(\varphi_1) = M_1 - \frac{1}{2}M_{desync}
\end{aligned} \tag{2.10}$$

$$\begin{aligned}
&-e_w m_w \cos(\varphi_2)\Big(\frac{d^2}{dt^2}y_{Ck}\Big) - e_w m_w \sin(\varphi_2)\Big(\frac{d^2}{dt^2}x_{Ck}\Big) + (e_w^2 m_w + J_{Cw})\Big(\frac{d^2}{dt^2}\varphi_2\Big)\\
&\quad + \Big(\frac{d^2}{dt^2}\alpha\Big)de_w m_w \sin(\varphi_2) = M_2 + \frac{1}{2}M_{desync}
\end{aligned} \tag{2.11}$$

where M_{desync} is the moment desynchronizing the vibrators.

2.2. Equations of the steady state above resonances of the suspension system

The analyzed machine is of the over-resonance type, for which the effect of the suspension system elements on the drive frame can be omitted in relation to influences of inertial vibrators. In turn, on account of the application – in the further part of this study – the self-synchronization criterion of vibrators, which is based only on the Lagrange kinematic potential, a component of damping forces between the drive frame and trough was also omitted in the equations.

Steady state equations were obtained assuming the constant value of angular velocities of vibrators $d\varphi_1/dt = d\varphi_2/dt = \omega$. Angular positions of the vibrators are then

$$\varphi_1 = \omega t + \varphi_{10} \qquad \varphi_2 = \omega t + \varphi_{20} \tag{2.12}$$

where φ_{10} and φ_{20} denote constants during the pathway phases.

In the equations of steady state, an expression for the adjusting frequency of the dynamic damper (in the analyzed case, the transporting trough) to the excitation frequency originating from forces of the drive vibrators, was also taken into account

$$k_s = m_r\omega^2 \tag{2.13}$$

In such a way, equations (2.14) were determined

$$\begin{aligned}
&(2m_w + m_r + m_k)\Big(\frac{d^2}{dt^2}x_{Ck}\Big) + m_r\Big(\frac{d^2}{dt^2}s\Big) \\
&\quad = e_w m_w \omega^2 \cos(\omega t + \varphi_{10}) + e_w m_w \omega^2 \cos(\omega t + \varphi_{20}) \\
&(2m_w + m_r + m_k)\Big(\frac{d^2}{dt^2}y_{Ck}\Big) \\
&\quad = e_w m_w \omega^2 \sin(\omega t + \varphi_{10}) - e_w m_w \omega^2 \sin(\omega t + \varphi_{20}) \\
&m_r\Big(\frac{d^2}{dt^2}x_{Ck}\Big) + m_r\Big(\frac{d^2}{dt^2}s\Big) + m_r\omega^2 s = 0 \\
&(J_{Cr} + J_{Ck})\Big(\frac{d^2}{dt^2}\alpha\Big) + 2\Big(\frac{d^2}{dt^2}\alpha\Big)d^2 m_w \\
&\quad = d e_w m_w \omega^2 \cos(\omega t + \varphi_{10}) - d e_w m_w \omega^2 \cos(\omega t + \varphi_{20})
\end{aligned} \tag{2.14}$$

It can be noticed that equations are of a linear form, heterogeneous, in which forcing elements are composed of harmonic expressions. Equations of this type can be solved by symbolic calculation, transforming the time depending differential equations into algebraic equations, also linear and depending on $\mathrm{i}\omega$, where i is the imaginary unit.

Defining representations of coordinates

$$x_{Ck}(t) \rightleftharpoons \underline{X}(\mathrm{i}\omega) \qquad y_{Ck}(t) \rightleftharpoons \underline{Y}(\mathrm{i}\omega) \qquad s(t) \rightleftharpoons \underline{S}(\mathrm{i}\omega) \qquad \alpha(t) \rightleftharpoons \underline{\alpha}(\mathrm{i}\omega) \tag{2.15}$$

excitations

$$\sin(\omega t + \varphi_{10}) \rightleftharpoons \mathrm{e}^{\mathrm{i}\varphi_{10}} \qquad \cos(\omega t + \varphi_{20}) \rightleftharpoons \mathrm{i}\mathrm{e}^{\mathrm{i}\varphi_{20}} \tag{2.16}$$

operators

$$\frac{d}{dt} \rightleftharpoons \mathrm{i}\omega \qquad \frac{d^2}{dt^2} \rightleftharpoons -\omega^2 \tag{2.17}$$

solutions of the system motion can be obtained in a complex form

$$\begin{aligned}
&\underline{X} = 0 \qquad \underline{Y} = \frac{e_w m_w}{2m_w + m_r + m_k}\Big(\mathrm{e}^{\mathrm{i}\varphi_{20}} - \mathrm{e}^{\mathrm{i}\varphi_{10}}\Big) \\
&\underline{S} = -\frac{\mathrm{i}e_w m_w}{m_r}\Big(\mathrm{e}^{\mathrm{i}\varphi_{20}} + \mathrm{e}^{\mathrm{i}\varphi_{10}}\Big) \qquad \underline{\alpha} = \frac{\mathrm{i}d e_w m_w}{2d^2 m_w + J_{Cr} + J_{Ck}}\Big(\mathrm{e}^{\mathrm{i}\varphi_{20}} - \mathrm{e}^{\mathrm{i}\varphi_{10}}\Big)
\end{aligned} \tag{2.18}$$

Time waveforms corresponding the above numbers are obtained on the basis of the formula

$$\begin{aligned} &y_{Ck}(t) = \Re(\underline{Y})\sin(\omega t) + \Im(\underline{Y})\cos(\omega t) \\ &s(t) = \Re(\underline{S})\sin(\omega t) + \Im(\underline{S})\cos(\omega t) \qquad \alpha(t) = \Re(\underline{\alpha})\sin(\omega t) + \Im(\underline{\alpha})\cos(\omega t) \end{aligned} \tag{2.19}$$

where $\Re$ and $\Im$ denote the real and imaginary parts of complex numbers.

Coordinates determined in such a way were used in the analysis of the kinematic potential and in calculating the moment synchronizing the drive vibrators in the steady state operations of the machine.

2.3. Problem of the stability of the system motion

The position of the stable equilibrium of vibrators was determined on the basis of the criterion

$$D(\varphi_{10}, \varphi_{20}) = \frac{1}{T}\int_0^T L\,dt \to \min \tag{2.20}$$

formulated in the studies by Blekhman (2000). According to these findings, vibrators obtain stable positions when the average value of the Lagrange function L, determined for the vibration period T of the system, obtains its minimal value. On the basis of (2.3) and solutions (2.19), the function D in the explicit analytical form was derived

$$\begin{aligned} D(\varphi_{10}, \varphi_{20}) &= m_w^2 e_w^2 \omega^2 [\cos(\varphi_{20} - \varphi_{10}) - 1](4d^4 m_k m_w^2 + 8J_{Ck}d^2 m_w^2 + 8J_{Ck}d^2 m_r m_w \\ &+ 4J_{Cr}d^2 m_k m_w + 12J_{Ck}d^2 m_k m_w + 2J_{Ck}d^2 m_r^2 + 4J_{Ck}d^2 m_k m_r + 2J_{Ck}d^2 m_k^2 \\ &+ J_{Cr}^2 m_k + 2J_{Ck}J_{Cr}m_k + J_{Ck}^2 m_k)/[2(2m_w + m_r + m_k)^2(2d^2 m_w + J_{Cr} + J_{Ck})^2] \end{aligned} \tag{2.21}$$

Its cosinusoidal dependence on the difference of angles φ_{20} and φ_{10} means, that there is only one minimum of the function and it occurs for the angle

$$\gamma = \varphi_{20} - \varphi_{10} = \pi \tag{2.22}$$

The obtained result allows one to state that in the case of the counter running drive the system has only one state of stable work, in which vibrators generate a sinusoidally variable force of a rectilinear direction, perpendicular to the segment connecting the points of its fastening to the machine body, Fig. 3.

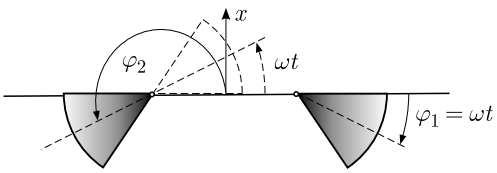

Fig. 3. System of phase angles of vibrators in the synchronous running state

2.4. Moment synchronizing the drive vibrators

Left sides of equations (2.10) and (2.11), apart from the components $(J_{Cr} + m_r \mathrm{e}^2)(d^2/dt^2)$, present the effect of the drive frame on drive vibrators. When transferred them into the right hand side of equations, they represent vibration moments as (Dimentberg *et al.*, 1997)

$$\begin{aligned} M_{vibr1}(t) &= \Big(\frac{d^2}{dt^2}\alpha\Big)de_w m_w \sin\varphi_1 - e_w m_w \cos\varphi_1 \Big(\frac{d^2}{dt^2}y_{Ck}\Big) + e_w m_w \sin\varphi_1 \Big(\frac{d^2}{dt^2}x_{Ck}\Big) \\ M_{vibr2}(t) &= -\Big(\frac{d^2}{dt^2}\alpha\Big)de_w m_w \sin\varphi_2 + e_w m_w \cos\varphi_2 \Big(\frac{d^2}{dt^2}y_{Ck}\Big) + e_w m_w \sin\varphi_2 \Big(\frac{d^2}{dt^2}x_{Ck}\Big) \end{aligned} \tag{2.23}$$

Depending on the mutual positions of the vibrators these moments may obtain different values. However, from the practical point of view, the most essential value is the average difference of moments (2.24). This value decides on the size of disphasing of the vibrators and on the reserve of stability related to the stable equilibrium of vibrators

$$M_{sync} = \frac{1}{T}\int_0^T [M_{vibr2}(t) - M_{vibr1}(t)]\,dt \tag{2.24}$$

After calculating two times the derivative of (2.19) versus time and inserting it into equation (2.24), the synchronizing moment was determined in the form

$$M_{sync} = m_w^2 e^2 \omega^2 \frac{(4m_w + m_r + m_k)d^2 + J_{Cr} + J_{Ck}}{(2m_w + m_r + m_k)(2m_w d^2 + J_{Cr} + J_{Ck})} \sin\gamma \tag{2.25}$$

Transferring to the boundary $(J_{Ck} + J_{Cr}) \to \infty$ or inserting into equation $d = 0$, provides an interesting result. In such a situation, we obtain the formula

$$M_{sync}^0 = \frac{m_w^2 e^2 \omega^2}{2m_w + m_r + m_k} \sin \tag{2.26}$$

which allows one to state that when there is a lack of angular vibrations, the synchronizing moment will still exist and will have a high enough value to maintain synchronous motion of the drive vibrators. This property is quite different than that of the conveyors without dynamic damper systems, for which the coaxial fastening of vibrators does not generate any synchronizing moments.

3. Numerical analysis

The verification of analytical formulas derived in Section 2 is based on dynamic equations (2.6)-(2.11) and on parameters of the exemplary conveyor. Parameters presented in Table 1 are related to the long conveyor, approximately 5 m, for which – due to a high value of $J_{Ck} + J_{Cr}$ – there is a danger of a low level of body angular vibration and difficulties with self-synchronizing of vibrators.

Table 1. Physical parameters of the system

Parameter	Value	Unit	Parameter	Value	Unit
m_k	500.0	kg	k_x	65023.3	N/m
m_r	350.0	kg	k_y	1.30E+05	N/m
$m_w e_w$	0.9625	kg m	b_x	114.0	Ns/m
a	1.5	m	b_y	161.3	Ns/m
h	0.5	m	β	$\pi/6$	rad
d	0.5	m	k_s	3.84E+06	N/m
J_{Cw}	0.001	kg m^2	b_s	733.04	Ns/m
J_{Ck}	416.67	kg m^2	ω	$100\pi/3$	rad/s
J_{Cr}	729.17	kg m^2			

However, the main investigations should be veryfied because of errors resulting from simplifications made while formulating equations of steady state (2.14).

On the basis of analytical formulas (2.18), the following results were obtained

$$\begin{aligned}
&\underline{Y} = -0.0011073 + 0.0011073\mathrm{i} = 0.0015659\mathrm{e}^{+\mathrm{i}135^0}\ \mathrm{m}\\
&\underline{S} = -0.0011073 + 0.0011073\mathrm{i} = 0.0038891\mathrm{e}^{-\mathrm{i}45^0}\ \mathrm{m}\\
&\underline{\alpha} = -0.0011073 + 0.0011073\mathrm{i} = 0.00059149\mathrm{e}^{-\mathrm{i}135^0}\ \mathrm{rad}
\end{aligned} \tag{3.1}$$

and on the basis of equation (2.25) it was found

$$M_{sync} = 13.89\ \mathrm{Nm} \tag{3.2}$$

Analogous procedure was applied in the case of $d = 0$. Then, it was obtained

$$\begin{aligned}
&\underline{Y} = -0.0011073 + 0.0011073\mathrm{i} = 0.0015659\mathrm{e}^{+\mathrm{i}135^0}\ \mathrm{m}\\
&\underline{S} = +0.0027500 - 0.0027500\mathrm{i} = 0.0038891\mathrm{e}^{-\mathrm{i}45^0}\ \mathrm{m}\\
&\underline{\alpha} = 0\ \mathrm{rad}
\end{aligned} \tag{3.3}$$

and

$$M_{sync} = 11.68\ \mathrm{Nm} \tag{3.4}$$

The dynamic equations of motion enabled obtaining the pathways as presented in Figs. 4-6.

Figure 4 presents the pathways of coordinates of conveyor motion in the steady work state at the maximal desynchronizing moment. On the basis of the data read from the figure, it is possible to determine error values for individual pathways

$$\begin{aligned}
&\delta y_{Ck} = \frac{0.00155 - 0.0015659}{0.0015659}100\% = 1\% \qquad \delta s = \frac{0.00397 - 0.0038891}{0.00397}100\% = 2\%\\
&\delta\alpha = \frac{0.00397 - 0.0038891}{0.00397}100\% = 2\%
\end{aligned} \tag{3.5}$$

The simulation results for the vibrators loaded by external desynchronizing moments are presented in Fig. 5 for three values: 3 Nm, 14.2 Nm and 14.3 Nm. The load was applied at 10 s, 20 s and 35 s of the simulation time. It can be noticed that breaking of the synchronizing bond occurred above 14.2 Nm. Thus, it is possible to determine the error of synchronizing moment to be

$$\delta M_{sync} = \frac{14.2 - 13.89}{14.2}100\% = 2.1\% \tag{3.6}$$

The pathways of coordinates of the mass centre of the drive frame, corresponding with loads from Fig. 5, are presented in Fig. 6. From Figs. 4-6 a change in the direction and amplitude of vibrations of the conveyor trough can be pointed out. When the desynchronizing moment is increasing then vibrations of the trough are smaller and more bent in the direction of transport.

4. Summary

The self-synchronization process of drive vibrators (of the inertial type) in a vibratory conveyor with a dynamic damper was analyzed in this study. This type of solution allows us to use the antiresonance effect to achieve a significant decrease in the drive frame vibration amplitude and, consequently, a significant decrease in forces transmitted to the foundation. It was revealed that in this type of solution, the nonzero average value of the synchronizing moment allowed for mutual synchronization of the vibrators and that these vibrators could assume only one

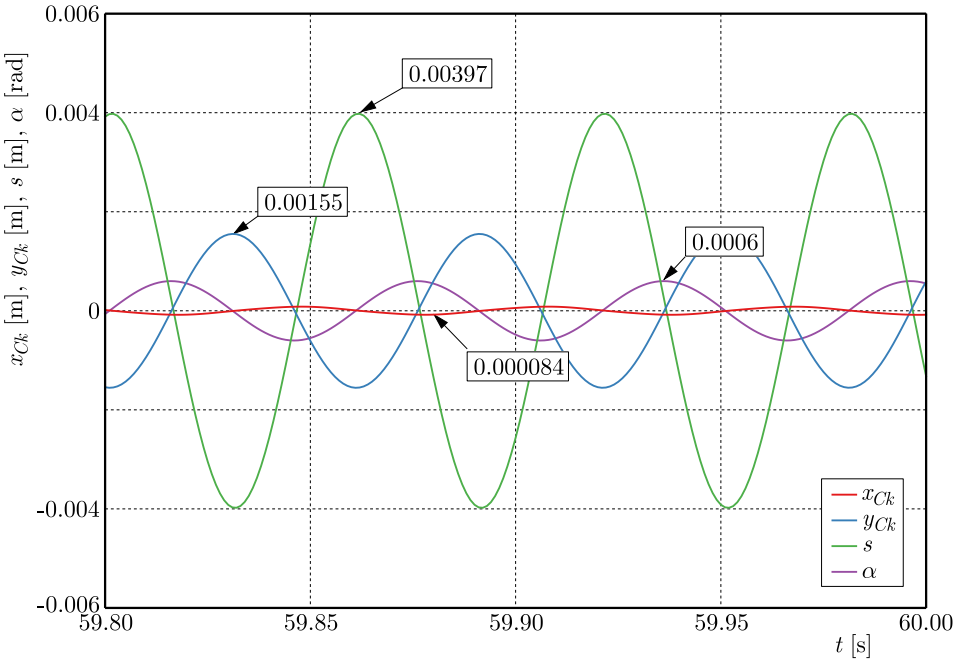

Fig. 4. Pathways of generalized coordinates in the steady state obtained on the basis of dynamic equations (2.6)-(2.11)

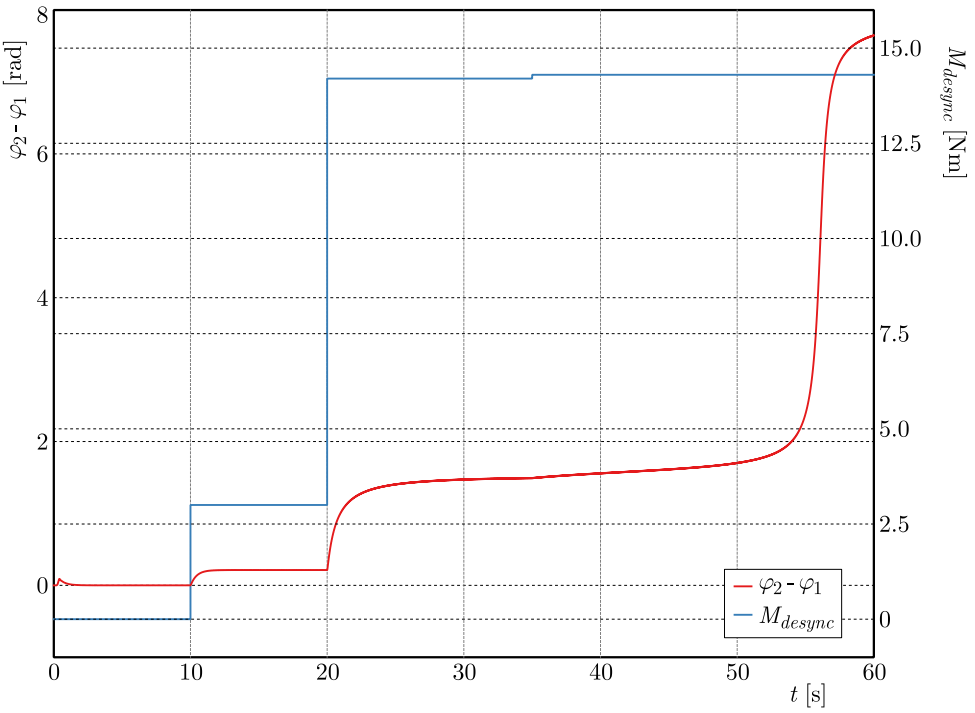

Fig. 5. Pathways of the disphasing angle of drive vibrators and desynchronizing moment

stable position with respect to each other. It was shown that in the case of counter running, the drive vibrators generated a force that was sinusoidally variable in the rectilinear direction and perpendicular to the segment connecting the mounting points to the machine body. The analytical formula for the average value of the synchronizing moment was determined, and on the basis of it, the meaning of the component originating from angular vibrations of the conveyor was determined. It was shown that in a system containing a dynamic damper, the synchronization of

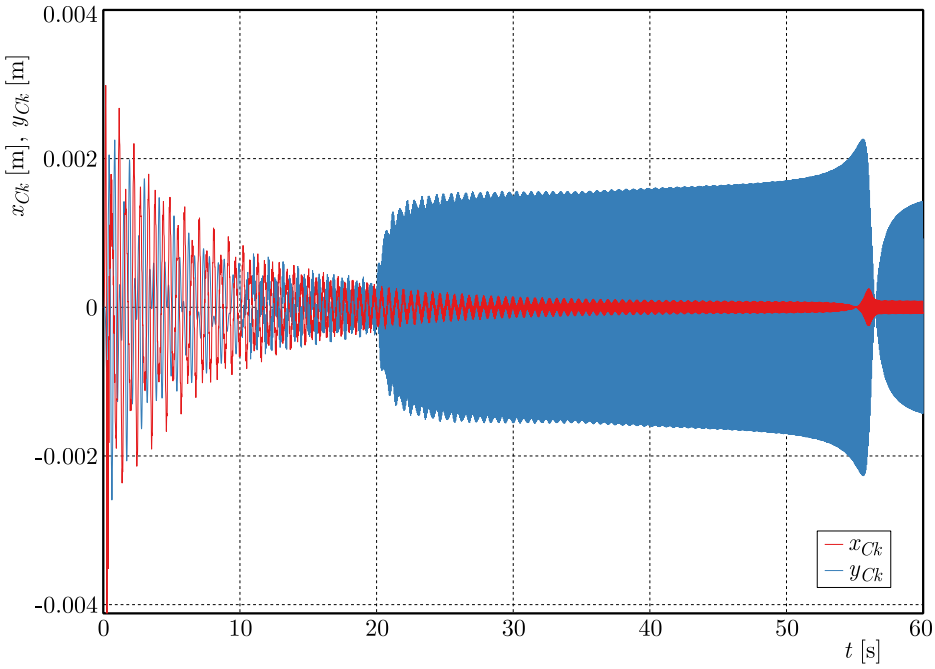

Fig. 6. Pathways of coordinates of the mass centre of the drive frame

vibrators was possible without angular vibrations of the machine, which provided the possibility of installing drive vibrators on the same axis. This is completely different than the situation for conveyors without a dynamic damper system, in which the coaxial mounting of vibrators does not generate a synchronizing moment.

The last conclusions have fundamental importance for building long conveyors, in which mass moments of inertia of the drive frame and trough take high values, which leads to low values of angular vibrations.

References

1. Asami T., 2019, Exact algebraic solution of an optimal double-mass dynamic vibration absorber attached to a damped primary system, *Journal of Vibration and Acoustics*, **141**, 5, 051013
2. Ascari A., 1980, The transient behaviour of the dynamic vibration absorber for linear frequency rise, *Meccanica*, **15**, 2, 107-111
3. Blekhman I.I., 1971, *Synchronisation of Dynamic Systems* (in Russian), Nauka, Moscow
4. Blekhman I.I., 2000, *Vibrational Mechanics*, World Scientific
5. Chedjou J.C., Kyamakya K., Mathis W., Moussa I., Fomethe A., Fono V.A., 2008, Chaotic synchronization in ultra-wide-band communication and positioning systems, *Journal of Vibration and Acoustics*, **130**, 1, 011012
6. Cieplok G., Wójcik K., 2020, Conditions for self-synchronization of inertial vibrators of vibratory conveyors in general motion, *Journal of Theoretical and Applied Mechanics*, **58**, 2, 513-524
7. Czubak P., Gajowy M., 2022, Influence of selected physical parameters on vibroinsulation of base-exited vibratory conveyors, *Open Engineering*, **12**, 1, 382-393
8. Dimentberg M.F., McGovern L., Norton R.L., Chapdelaine J., Harrison R., 1997, Dynamics of an unbalanced shaft interacting with a limited power supply, *Nonlinear Dynamics*, **13**, 2, 171-187

9. Fang P., Zou M., Peng H., Du M., Hu G., Hou Y., 2019, Spatial synchronization of unbalanced rotors excited with paralleled and counterrotating motors in a far resonance system, *Journal of Theoretical and Applied Mechanics*, **57**, 3, 723-738
10. Fasana A., Giorcelli E., 2010, A vibration absorber for motorcycle handles, *Meccanica*, **45**, 1, 79-88
11. Frahm H., 1911, *Device for Damping Vibrations of Bodies*, U.S. Patent 989958
12. Gajowy M., 2019, Operational properties of vibratory conveyors of the anti-resonance type, *2019 20th International Carpathian Control Conference (ICCC)*, 1-7
13. Hou Y., Du M., Fang P., Zhang L., 2017, Synchronization and stability of an elastically coupled tri-rotor vibration system, *Journal of Theoretical and Applied Mechanic*, **55**, 1, 227-240
14. KMCGlobalEurope, 2020, *Antyrezonansowy przenośnik wibracyjny*, PL Patent P.434041
15. Li Y., Ren T., Meng X., Zhang M., Zhao P., 2020, Experimental and theoretical investigation on synchronization of a vibration system flexibly driven by two motors, *Proceedings of the Institution of Mechanical Engineers, Part C: Journal of Mechanical Engineering Science*, **234**, 13, 2550-2562
16. Michalczyk J., Cieplok G., 2014, Disturbances in self-synchronisation of vibrators in vibratory machines, *Archives of Mining Sciences*, **59**, 1, 225-237
17. Paz M., Cole J.D., 1992, Self-synchronization of two unbalanced rotors, *Journal of Vibration and Acoustics*, **114**, 1, 37-41
18. Shokhin A.E., Krestnikovskii K.V., Nikiforov A.N., 2021, On self-synchronization of inertial vibration exciters in a vibroimpact three-mass system, *IOP Conference Series: Materials Science and Engineering*, **1129**, 1, 012041.
19. Smirnova V.B., Proskurnikov A.V., 2021, Self-synchronization of unbalanced rotors and the swing equation, *IFAC-PapersOnLine*, **54**, 17, 71-76, *6th IFAC Conference on Analysis and Control of Chaotic Systems, Chaos*
20. Surówka W., Czubak P., 2021, Transport properties of the new vibratory conveyor at operations in the resonance zone, *Open Engineering*, **11**, 1, 1214-1222
21. Zhang N., Wu S., Li Y., 2019, Synchronous behavior analysis of two rotors in self-synchronization system, *IOP Conference Series: Materials Science and Engineering*, **631**, 3, 032013
22. Zhang X., Wen B., Zhao C., 2016, Theoretical study on synchronization of two exciters in a nonlinear vibrating system with multiple resonant types, *Nonlinear Dynamics*, **85**, 1, 141-154
23. Zhao C., Zhao Q., Gong Z., Wen B., 2011, Synchronization of two self-synchronous vibrating machines on an isolation frame, *Shock and Vibration*, **55**, 1-2, 73-90
24. Zhao C., Zhu H., Zhang Y., Wen B., 2010, Synchronization of two coupled exciters in a vibrating system of spatial motion, *Acta Mechanica Sinica*, **26**, 477-493
25. Zou M., Fang P., Hou Y., Chai G., Chen J., 2020, Self-synchronization theory of tri-motor excitation with double-frequency in far resonance system, *Proceedings of the Institution of Mechanical Engineers, Part C: Journal of Mechanical Engineering Science*, **234**, 16, 3166-3184

Manuscript received February 3, 2023; accepted for print June 29, 2023

JOURNAL OF THEORETICAL AND APPLIED MECHANICS
61, 4, pp. 741-754, Warsaw 2023
https://doi.org/10.15632/jtam-pl/171470

NUMERICAL STUDY ON THE INFLUENCE OF TOP AND VALLEY SHAPE OF THE TRANSVERSE GROOVE ON THE DRAG REDUCTION RATE

Zhiping Li, Yueren Zuo
Research Institute of Aero-Engine, Beihang University, Beijing, China
Hanan Lu
School of Energy and Power Engineering, Beihang University, Beijing, China
corresponding author Hanan Lu, e-mail: luhanan2013@163.com
Long He
Research Institute of Aero-Engine, Beihang University, Beijing, China
Bo Meng
AECC Hunan Aviation Powerplant Research Institute, Zhuzhou, China

This study investigates the drag reduction effect and mechanism of modified transverse grooves by employing "Constant Width" and "Constant Height" filleting methods on the top and valley of two-dimensional transverse V-shaped grooves. Results revealed a significant increase in the total drag reduction rate, from 13.29% to 23.24%, when a constant width fillet was applied to the grooves top at $r_3 = 0.3/\sqrt{2}\,\mathrm{mm}$. However, minimal or negative effects were observed in other cases. These findings establish a preliminary theoretical basis for future transverse groove design and processing.

Keywords: grooves, drag reduction rate, flow control, optimized structure

1. Introduction

Amidst the exacerbation of energy scarcity, there is a growing emphasis on drag reduction strategies. Remarkably, a research conducted by NASA Langley Research Center highlighted that a mere 1% decrease in drag translates to a significant 5% to 10% augmentation in subsonic aircraft payload capacity (Bushnell, 1990). Delving into drag reduction performance, scholars have explored bio-inspired microstructures since the last century (Walsh and Lindemann, 1984). These microstructures are categorized into riblets and transverse grooves oriented parallel and perpendicular to the flow direction, respectively. Notably, current drag reduction investigations have predominantly focused on transverse grooves due to their impressive drag reduction attributes and versatile applicability (Sareen *et al.*, 2014; Ghazali *et al.*, 2016).

The drag reduction mechanism of transverse grooves has garnered scholarly attention. The MABS (Micro-Air Bearings) theory, initially developed by NASA (Bushnell, 1983) in the 1980s, posits that stable boundary vortices formed by a fluid within grooves act as bearings, akin to converting sliding friction into rolling friction, thereby reducing drag. Pan (1996) experimentally validated this theory and observed that these "bearings" attenuated vertical momentum exchange in the boundary layer without affecting the mainstream flow. Choi (1989) employed hotwire/film anemometry, flow visualization techniques and laser light sheets to investigate structural changes in the turbulent boundary layer near riblet surfaces. They noted a turbulence intensity reduction of up to 10%, which was further confirmed by DNS (direct numerical simulations) conducted by Choi *et al.* (1993). Subsequent research by other scholars (García-Mayoral and Jiménez, 2011a,b) entailed experimental and simulation studies to analyze flow

characteristics within the grooves and corroborated the vortex-related nature of drag reduction properties, aligning with the qualitative description of the MABS theory. These findings offer valuable insights into the drag reduction mechanisms associated with transverse grooves.

Other scholars focused on parametric studies of transverse grooves. Bai *et al.* (2016) conducted numerical simulations to investigate the drag reduction efficiency of four different geometries: V-shaped, zigzag, rectangular and semi-circular. They discovered that a V-shaped groove textured surface achieved the highest friction coefficient. Oak Ridge National Laboratory (Barbier *et al.*, 2012) conducted experimental tests on grooves of various sizes at low speeds and observed a drag reduction rate of 13% for a 1 mm deep groove. However, as the flow velocity increased, the secondary flow developed, leading to a lower drag reduction rate. Nevertheless, even for larger grooves, the drag reduction rate remained above 15%. To provide a quantitative theoretical foundation for groove parameter design, Li *et al.* (2022a) proposed a physical model that established the relationship between dimensionless depth of a transverse groove, dimensionless inflow velocity and drag reduction rate. They quasi-analytically solved for the optimal and maximum transverse groove depths based on Reynolds numbers. Moreover, the grooves exhibitted favorable applications in heat transfer compared to flat plates (Belhocine and Wan Omar, 2015; Bilen *et al.*, 2009).

Parametric studies have promoted the engineering application of the grooves. However, little research has focused on the local structural optimization of such grooves. Recent experiments by Leitl *et al.* (2022) revealed that defects occurring in the microstructure, either due to processing or prolonged usage, could significantly affect drag reduction. We contend that the top and valley, also as the most subtle components within the grooves, possess the highest potential for machining errors and are susceptible to wear and contamination during usage. Hence, we aimed to investigate the influence of geometric modifications to the top and valley on the flow characteristics in the vicinity of the grooves. This study modified the shape of commonly used two-dimensional transverse V-grooves top and valley and analyzed the corresponding drag reduction effects through numerical simulations. The results shed light on the significance of these shape alterations in influencing the drag reduction rate. This research provides a theoretical basis for the future groove design and processing, enabling an improved performance in various applications.

2. Models and methods

2.1. Geometric modification of the transverse groove

From the study of Cui and Fu (2012), a symmetric V-shape is the simplest structure of transverse grooves and has certain improvement potential in the drag reduction effect. Consequently, a geometric prototype groove (V-shape) was selected, as shown in Fig. 1a, where the dimensions w and h denote width and height of the transverse groove. The flow state near the groove is visually represented by red lines.

The drag reduction model proposed by Li *et al.* (2022a) has high accuracy for Reynolds numbers below 2.18E5. Consequently, a Reynolds number of Re = 1.5E5 is selected near the groove (incompressible). So, the dimensionless incoming flow velocity ($U_\infty^+ = U_\infty/u_\tau$) is 19.34, while the dimensionless height of the groove ($H^+ = Hu_\tau/\nu$) reaches approximately 10.26, resulting in the maximum drag reduction. Here, U_∞ denotes the actual incoming flow velocity, H represents the groove depth, and u_τ is the friction velocity that characterizes turbulent shear stress and related parameters. In this case, the prototype groove depth is 0.5 mm. To maintain vortex stability within the groove, the prototype groove width W is set to 1 mm, ensuring an aspect ratio $AR = W/H$ of approximately 2 (Li *et al.*, 2022b).

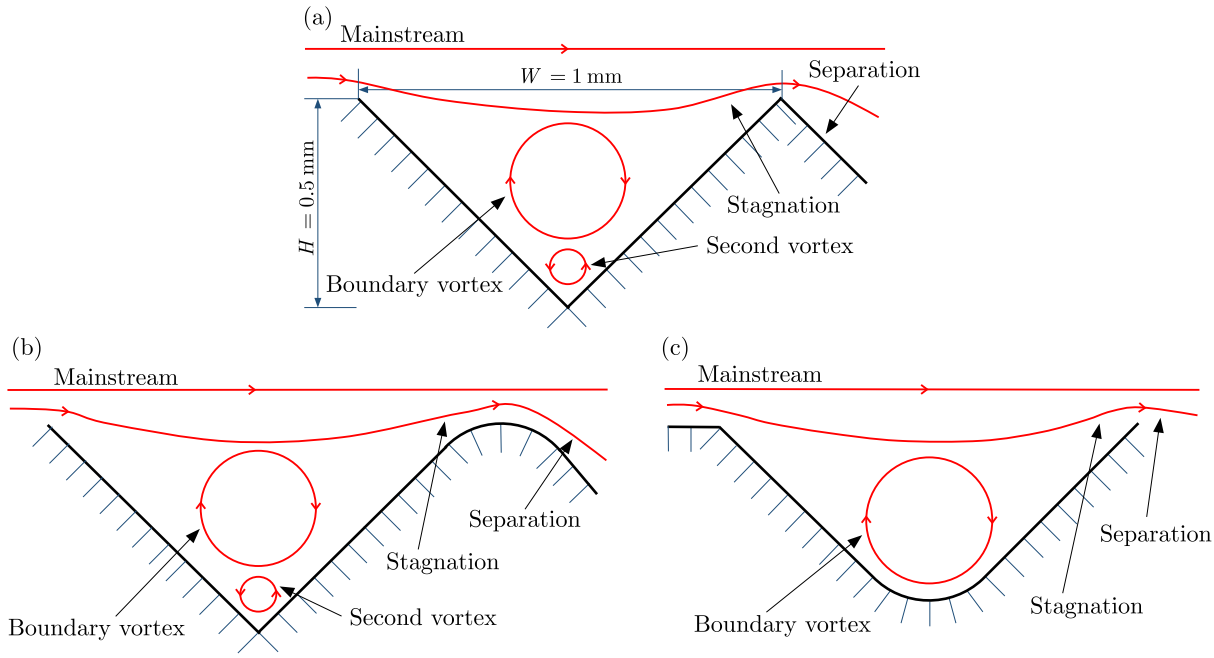

Fig. 1. Flow field with different geometry: (a) prototype groove, (b) fillet top, (c) fillet valley

In Fig. 1a, two vortices are exhibited in a single groove, differing in scale, position and direction. The small secondary vortex located at the groove valley experiences intense shearing against the wall, which is usually detrimental to the overall drag reduction effect. Meanwhile, a larger scale boundary vortex makes the boundary layer of the mainstream slip, acting akin to the "rolling bearing" (Bushnell, 1983). While, the mainstream stagnates at the windward side of the grooves and produces local separation at the leeward side, resulting in an extra pressure drag at the top.

From the above analysis, it can be concluded that the flow inside the grooves is influenced by geometry of the valley and top. Speculatively, modifying the fillet on the top and valley (Figs. 1b and 1c) could eliminate shear from the secondary vortex and weaken the high-pressure area caused by the boundary vortex. This modification has potential to significantly enhance the overall drag reduction rate of the grooves.

Considering the actual processing and other aspects, two kinds of fillet methods are finally adopted to optimize the top and valley geometry of the grooves:

- Constant Width (CW): Reduce the height of the individual groove and remain the width of geometry unchanged, as shown in Figs. 2a and 2c;
- Constant Height (CH): Expand the width of the individual groove and remain the height unchanged, as shown in Figs. 2b and 2d.

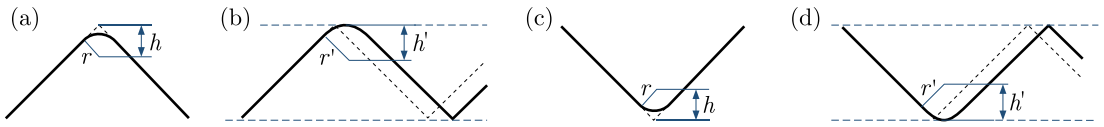

Fig. 2. Different fillet: (a) constant width top, (b) constant height top, (c) constant width valley, (d) constant height valley

In practical machining, these two geometric modification methods are easily attainable. For instance, in the case of metal groove machining, the desired modified geometry can be obtained by simply altering the shape of the cutting tool based on the prototype. This facilitates subsequent experimental validation and facilitates widespread application of the modified grooves on

a larger scale. Defects exceeding 60%h (0.3 mm) in geometric changes are rare, thus not requiring further investigation.

The two methods involve maintaining the wall inclination constant, and h is the distance from the prototype groove vertex to the fillet center, whose relationship with the fillet radius as

$$h = \sqrt{2}r \qquad h' = r' \tag{2.1}$$

The specific geometric modification scheme is outlined in Table 1, detailing the fillet location (FL), fillet radius (FR) and fillet method (FM).

Table 1. Geometric modification scheme

FL	FR [mm]	FM
Top	$r_1 = 0.05/\sqrt{2}$	CW
	$r_2 = 0.1/\sqrt{2}$	CW
	$r_3 = 0.3/\sqrt{2}$	CW
	$r'_1 = 0.05$	CH
	$r'_2 = 0.1$	CH
	$r'_3 = 0.3$	CH
Valley	$r_1 = 0.05/\sqrt{2}$	CW
	$r_2 = 0.1/\sqrt{2}$	CW
	$r_3 = 0.3/\sqrt{2}$	CW
	$r'_1 = 0.05$	CH
	$r'_2 = 0.1$	CH
	$r'_3 = 0.3$	CH

2.2. Computational domain and boundary conditions

A schematic representation of the computational domain and boundary conditions is presented in Fig. 3. The computational domain possesses a height and length of 500 mm, significantly larger than the boundary layer thickness. The freestream allows for the transition from a laminar to turbulent flow over the upstream smooth wall, which extends over a length of 365 mm. The downstream smooth wall with a length of 300 mm ensures minimal pressure perturbations at the outlet. Situated between the two smooth walls is a grooved wall, approximately 12 mm in length, comprising symmetric V-groove profiles. The grooves have an aspect ratio of 2 ($AR = W/H$) and a depth of 0.5 mm.

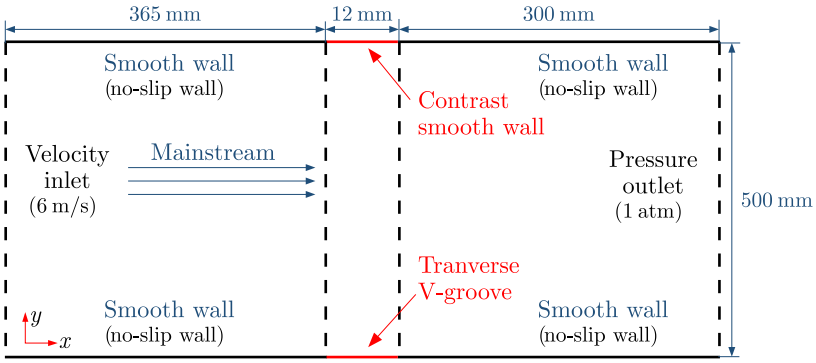

Fig. 3. Computational domain and boundary conditions

The computational fluid dynamics analysis (CFD) of the groove surface is performed using the Fluent 18.2 commercial software. The inlet boundary condition is defined as a constant

velocity of 6 m/s. And the upstream smooth wall extends for a length of 365 mm, resulting in minimal impact of pressure disturbances on the velocity inlet. The pressure outlet condition is set with a constant gauge pressure of 0 (Operating Pressure = 101325 Pa). Additionally, all smooth walls are assigned the no-slip wall condition. In simulation, the key lies in solving the Navier-Stokes equations as (Belhocine and Abdullah, 2019)

$$\frac{\partial}{prtt}(\rho u_i) + \frac{\partial}{\partial x_j}(\rho u_i u_j) = -\frac{\partial p}{\partial x_i} + \frac{\partial \tau_{ij}}{\partial x_j} + \rho g_i + F_i \tag{2.2}$$

where p is the static pressure, τ_{ij} is the surface stress tensor, g_i and F_i are gravity and external volume force. To solve the system of partial differential equations composed of the Navier-Stokes equation, continuity equation and energy equation, numerical methods are required.

DeGroot *et al.* (2016) conducted an extensive investigation on a turbulent flow in grooved channels and their potential for reducing friction factors. They validated the RANS (Reynolds--Averaged Navier-Stokes) modeling approach by comparing it with DNS (direct numerical simulations), confirming its accuracy and computational efficiency for studying the turbulent flow in grooved channels. In this study, the steady Reynolds-Averaged Navier-Stokes approach is employed for CFD (computational fluid dynamics) simulations. The Reynolds-Averaged Navier--Stokes (RANS) method is extensively employed for tackling turbulent flow phenomena. It involves the temporal averaging of the governing Navier-Stokes equations to obtain a set of time-averaged equations. Subsequently, additional turbulence models are employed to account for the influence of turbulence on the flow. Considering that the Transition SST four-equation turbulence model is more sensitive to flow separation, pressure gradient, and can capture flow characteristics in the near-wall region well (Menter *et al.*, 2006; Aftab *et al.*, 2016), it is used to determine the flow field.

2.3. Grid delineation and independence study

The structured mesh shown in Fig. 4 is generated using the Ansys ICEM meshing tool. To ensure accurate boundary layer flow simulation, the Transition SST turbulence model requires the Y plus value below 1. In order to capture the flow details near the grooves $h = 0.5$ mm with enhanced precision, considering the Reynolds number and the physical parameters of the medium, the normal distance from the nodes of the first grid layer to the wall surface is set to 0.003 mm. Consequently, the actual Y plus range near the grooved wall falls within the range of 0.0599-0.06.

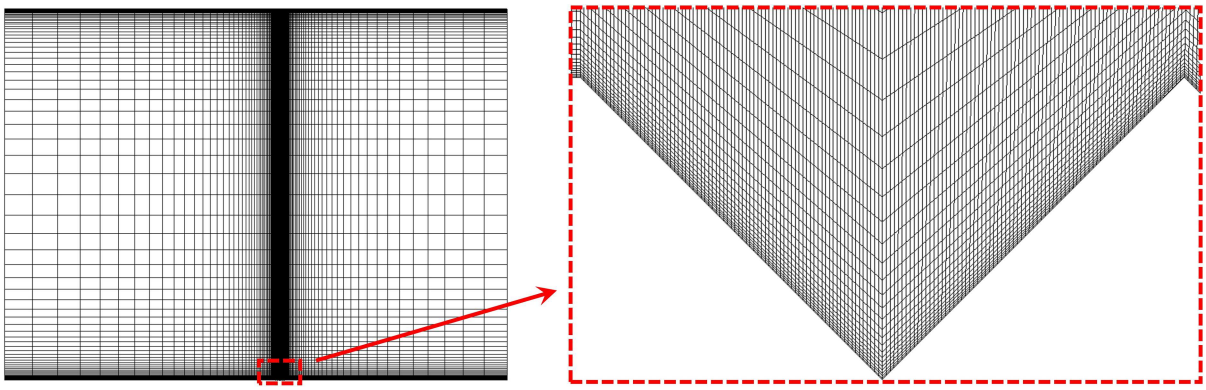

Fig. 4. Mesh distribution around the transverse V-groove

Figure 5 shows the relative error of the total drag of the grooved plate compared with that of the smooth plate at different grid-refinement levels. It can be observed that when the number of grid cells exceeds 297 463, the relative error for both drags remains below 0.05%.

Consequently, to strike a balance between the computational accuracy and resource efficiency, the subsequent calculations utilize approximately 297 463 grid cells to ensure accurate results while saving computational resources.

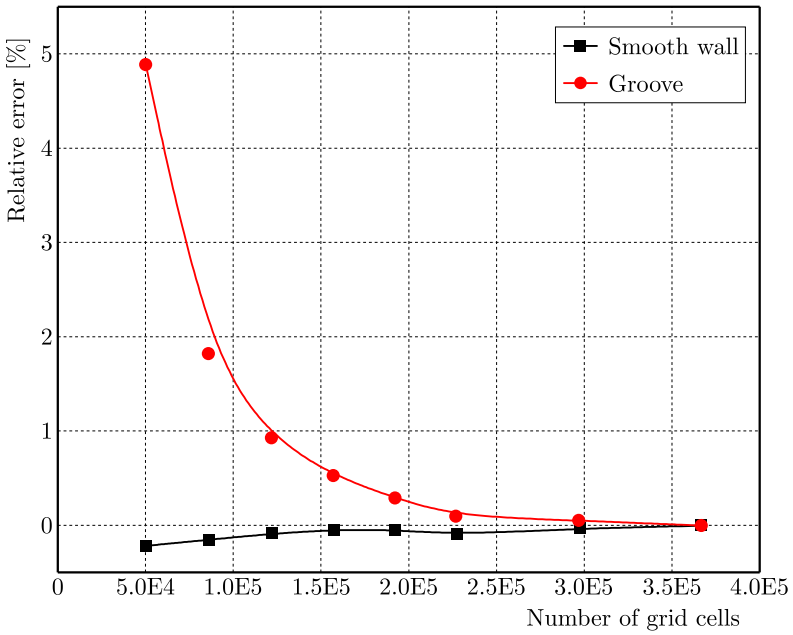

Fig. 5. Verification of grid independence

2.4. Numerical method validation

To assess the accuracy of the numerical method, a numerical simulation of a grooved plate with depth of 1.62 mm and width of 3.57 mm was conducted in a wind tunnel. The simulation results were then compared to relevant experimental data obtained by Ahmadi-Baloutaki *et al.* (2013), Fig. 6. When considering a turbulence intensity of 0.5% and a Reynolds number of 1.85E5, the relative errors between the numerical calculations and the experimental results were all below 5%. These findings, coupled with the conclusions drawn by DeGroot *et al.* (2016), validate the accuracy of the numerical method employed in this study for accurately predicting the drag reduction effect of transverse grooves.

3. Law of the drag reduction rate

The drag of a grooved plate is formed by viscous drag F_{CV} and pressure drag F_{CP}, defined as (Li *et al.*, 2022a)

$$F_{GV} = \int_0^{l_s})\boldsymbol{\tau} \cdot \mathbf{e}_x \, dl \qquad F_{CP} = \int_0^{l_s} (p - p_\infty)\mathbf{n} \cdot \mathbf{e}_x \, dl \tag{3.1}$$

Here, $\boldsymbol{\tau}$ is the shear stress on the wall surface, $\mathbf{e}_x$ is the unit vector along the x direction (flow direction), l_s is length of the wetted wall of grooves, p_∞ is the ambient pressure, l is the unit area along the groove wall, and $\mathbf{n}$ represents the normal vector to the wall. Further, the drag reduction rate can be denoted by Eq. (3.2) (Li *et al.*, 2022a), where F_G and F_R represent the drag of the grooved and smooth plate, respectively

$$\eta = \frac{F_G - F_R}{F_R} = \frac{F_G V - F_R}{F_R} + \frac{F_{GP}}{F_R} = \eta_v + \eta_p \tag{3.2}$$

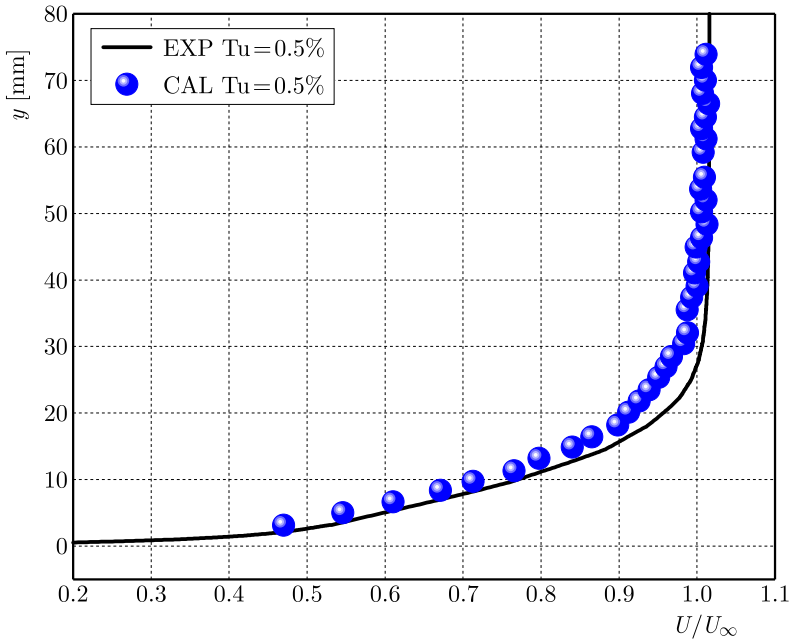

Fig. 6. The comparison of numerical and experimental results (Ahmadi-Baloutaki *et al.*, 2013)

Here, η_v denotes the reduction rate of viscous drag which is negative. η_p denotes the increased rate of pressure drag which is positive. A negative value of η indicates a reduction in the total drag with a higher absolute value indicating a higher drag reduction rate. The drag reduction characteristics of the grooves with different fillet radii (FR) after using two fillet methods (FM), constant height (CH) and constant width (CW), at two fillet positions (FP), top and valley, are presented in Table 2.

Table 2. Calculation results of drag reduction characteristics

FP	FR	FM	η_p	η_v	η
Prototype	$r_0 = 0$	-	78.24%	−91.53%	−13.29%
Top	r_1	CW	65.38%	−80.62%	−15.24%
	r_2	CW	59.22%	−76.16%	−16.94%
	r_3	CW	44.45%	−67.69%	−23.24%
	r_1'	CH	64.95%	−77.26%	−12.31%
	r_2	CH	59.38%	−70.90%	−11.52%
	r_3'	CH	46.28%	−56.03%	−9.77%
Valley	r_1	CW	78.14%	−91.49%	−13.35%
	r_2	CW	78.23%	−91.55%	−13.32%
	r_3	CW	81.60%	−93.21%	−11.62%
	r_1'	CH	78.80%	−92.06%	−13.26%
	r_2'	CH	79.32%	−92.71%	−13.39%
	r_3'	CH	82.14%	−95.74%	−13.60%

3.1. Fillet top

The calculation results shown in Table 2 indicate that the geometric modifications at the top of the groove significantly impact the drag reduction rate, consistent with findings reported for riblets in the previous studies (Leitl *et al.*, 2022). Comparing the cases with a constant height, the grooves exhibit improved drag reduction effects when filleted using a constant width.

Among the existent constant width cases, the drag reduction rate increases with the increasing fillet radius, with a substantial increase from 13.29% to 23.24% observed when the fillet radius reaches r_3. Conversely, when filleted using a constant height, the grooves display a lower drag reduction rate compared to the prototype grooves, primarily due to the greater decline in the absolute value of η_v.

In terms of specific changes in the drag reduction rate, the fillet top results in a decrease of η_p (cost) and the absolute value of η_v (benefit). Ultimately, the actual variation in the drag reduction rate is determined by the delicate balance between the benefits and costs associated with these changes.

3.2. Fillet valley

The influence of filleting the valley on the drag reduction rate of the groove is relatively minimal compared to the filleting of the top. From the perspective of η_v, η_p and η, when the fillet radius is small, the variation of these values with the two fillet methods are almost the same compared with the prototype groove. While the fillet radius reaches r_3, the η_p of the groove in the constant width cases suddenly significantly increases and the absolute value of η_v increases less, leading to a reduction in the drag reduction rate from 13.29% to 11.62%.

While this Section presents the observed patterns of the drag reduction ratio in fillet transverse grooves based on the changes in η_v and η_p, it does not provide an explanation for these variations. In the upcoming Section, we delve into the flow details to uncover the underlying mechanisms that drive these changes.

4. Mechanism analysis

4.1. Characteristics of drag reduction induced by the fillet top

4.1.1. Fillet top and pressure drag

Figure 7 describes the pressure distribution in a unit groove on the wall with different fillet radii at the top. In the vicinity of the prototype groove (Fig. 7a), a region of high pressure is observed on the windward side of the top, while a localized low-pressure region is present on the leeward side. In Figs. 7h and 7i, these regions manifest as sharp positive and negative pressure peaks, respectively, at the top of the prototype groove r_0. Filleting the top with a constant width leads to a more uniform pressure distribution on both sides of the transverse groove, as depicted in Figs. 7b, 7d, 7f, and 7h. The drag reduction effect improves with the increasing fillet radius. For instance, in Fig. 7h, with a fillet radius of r_3, the difference between the positive and negative peaks of gauge pressure is approximately 0.05 Pa, whereas on the prototype groove, this difference reaches 0.45 Pa. The closer pressure on either side near the top of the groove signifies a lower pressure drag in that region.

Filleting the top of the groove with a constant height also leads to a reduction in pressure peaks, as shown in Fig. 7i, although not as much as in the constant width method. In the constant height cases, the minimum value of differences between the positive and negative peaks is 0.12 (at r_3'), which is nearly twice the corresponding value achieved by the constant width filleting. However, the constant height method widens the individual grooves, resulting in wider regions of the local low and high pressure. This leads to a decrease in pressure gradient. Consequently, the actual reduction in pressure drag achieved by this fillet method is comparable to that of the constant width method.

The streamline patterns depicted in Fig. 8 provide further insights into the underlying mechanism behind the changes in the drag reduction rate after filleting. It is evident that the streamlines exhibit periodic variations in the response to the groove structure. In Fig. 8a, as the fluid

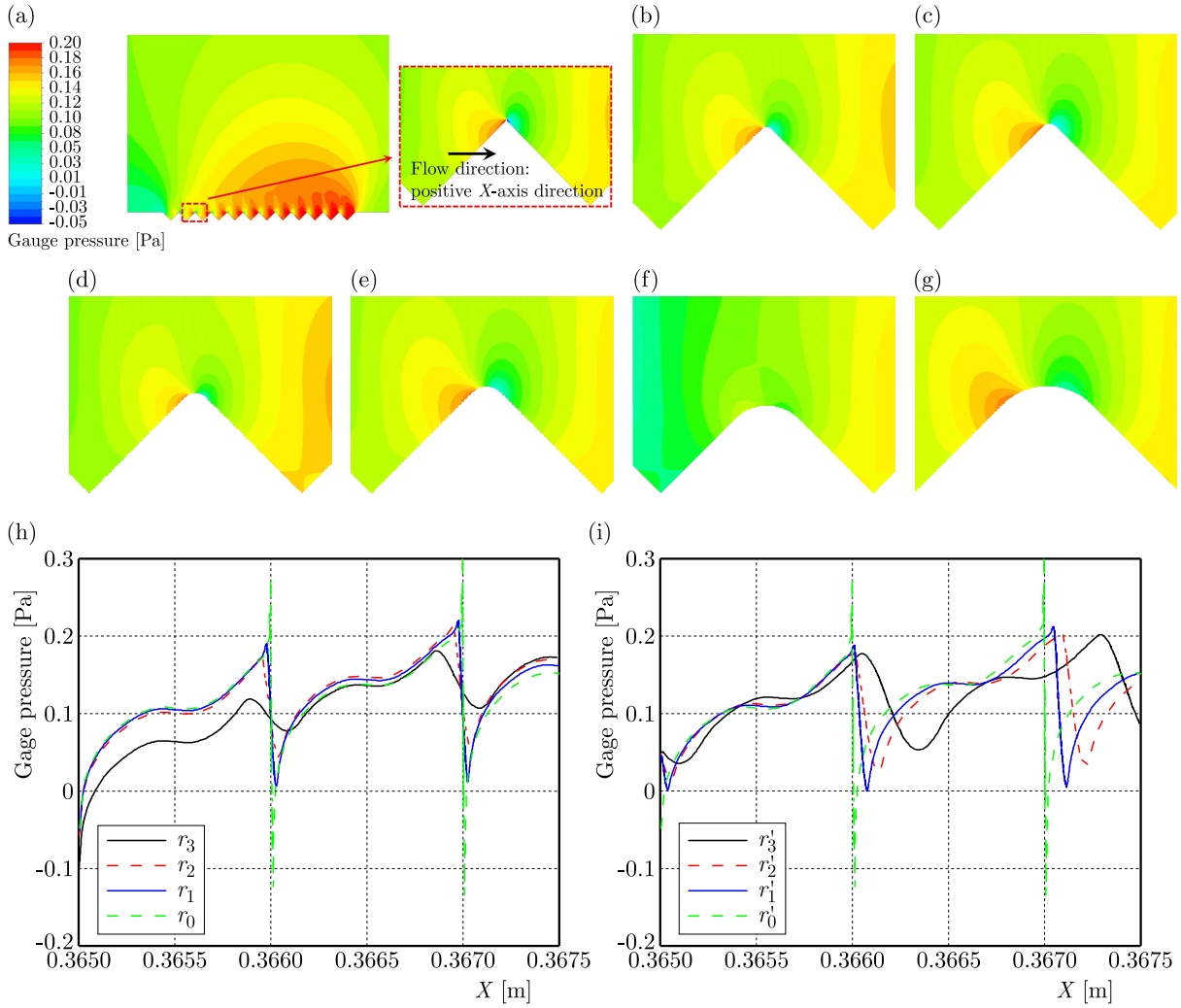

Fig. 7. Pressure distribution with the fillet top: (a) prototype groove r_0, (b) CW r_1, (c) CH r_1', (d) CW r_2, (e) CH r_2', (f) CW r_3, (g) CH r_3', (h) CW, (i) CH

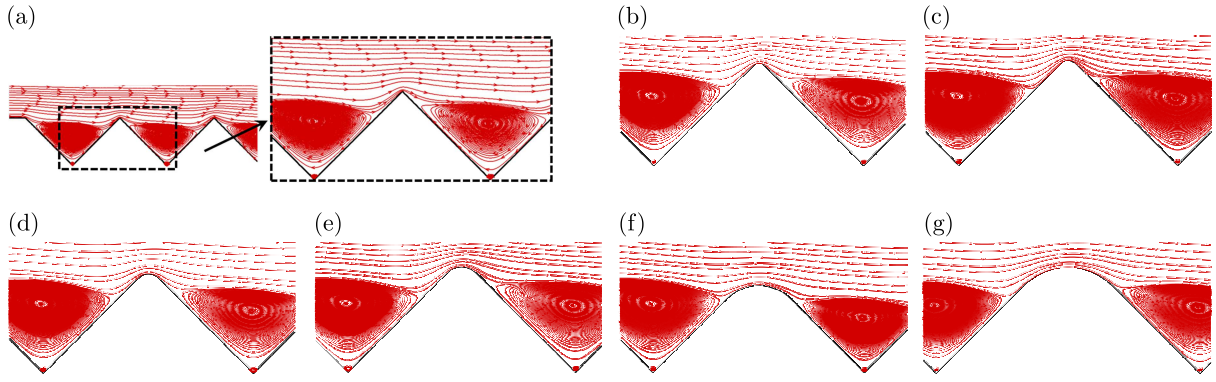

Fig. 8. Streamlines with the fillet top: (a) prototype groove r_0, (b) CW r_1, (c) CH r_1', (d) CW r_2, (e) CH r_2', (f) CW r_3, (g) CH r_3'

enters the V-shaped groove and forms a vortex, it experiences stagnation on the windward side of the groove top, leading to generation of a high-pressure region. As the fluid crosses the top, a sharp turning angle induces separation, resulting in a local low-pressure region. However, when the groove is filleted either by a constant height or constant width, the turning structure becomes

smoother, mitigating the stagnation and separation effects. Therefore, the pressure distribution on both sides of the groove top becomes more uniform, and the streamlines are closer to the geometric structure, resulting in a reduced pressure drag at the top of the groove.

4.1.2. Fillet top and viscous drag

Based on the above analysis, it is evident that the pressure drag of the V-groove decreases with both the constant height and constant width filleting methods. However, the drag reduction rate of the top filleted by the constant height is inferior to that of the prototype groove, as shown in Table 2. Hence, further investigation is required to understand the correlation between the reduction in the drag reduction rate and wall shear stress.

Figure 9 presents the wall shear stress distribution on the filleted top of the groove. It is evident that the wall shear stress follows a periodic pattern corresponding to the groove structure. The shear stress near the valley exhibits M shaped peaks, which are higher than the corresponding smooth wall shear stress. The fillet top has a little impact on the positive shear stress region near the M peaks, particularly in the constant width cases. The shear stress at the top is represented by a sharp negative peak. With an increase in the fillet radius, the peak shear stress near the groove top significantly decreases, resulting in a reduction in the extent of negative shear stress and an increase in the total viscous drag. In the constant height cases, the range of wall shear stress exceeding that of the smooth wall also increases, leading to a sharp rise in the total drag. This observation indicates that while filleting by the constant height reduces the pressure drag of the groove, it substantially increases the viscous drag, resulting in an inferior drag reduction rate compared to the prototype groove.

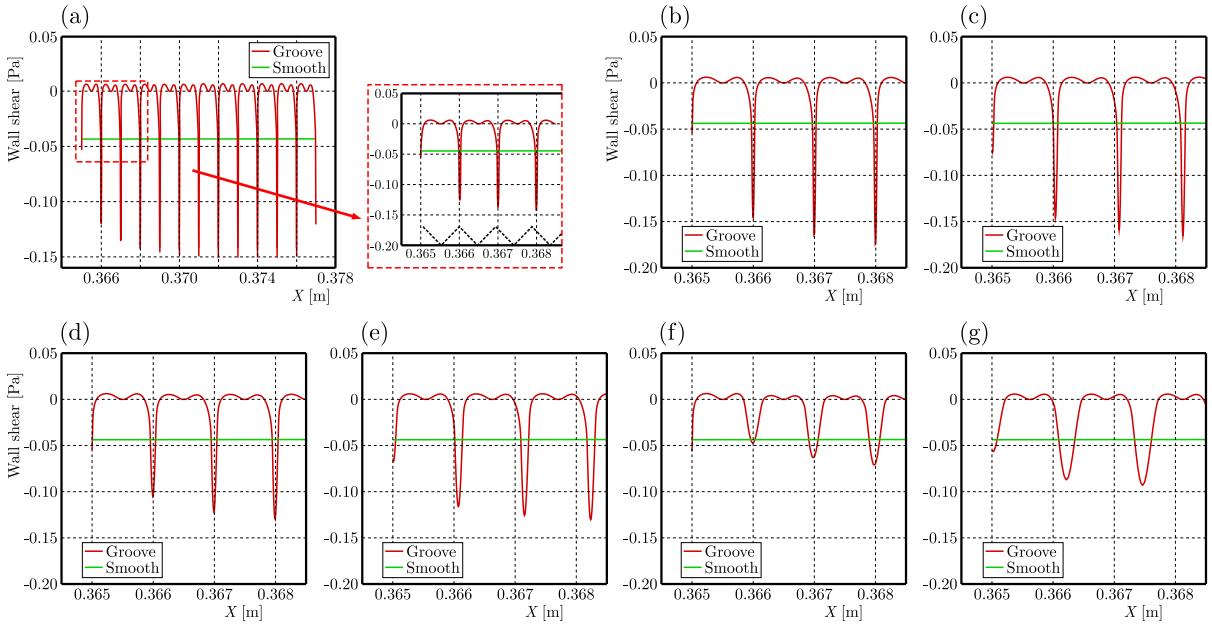

Fig. 9. Wall shear distribution with the fillet top: (a) prototype groove r_0, (b) CW r_1, (c) CH r_1', (d) CW r_2, (e) CH r_2', (f) CW r_3, (g) CH r_3'

4.2. Characteristics of drag reduction induced by the fillet valley

4.2.1. Fillet valley and pressure drag

The pressure distribution in Fig. 10 reveals that the fillet valley has almost no major effect on the pressure distribution near the V-groove when the fillet radius is small, resulting in slight changes to the local pressure. In the constant width cases, the pressure distribution curves of

the fillet groove almost coincide with that of prototype groove (Fig. 10h). For instance, when the fillet radius reaches r_2, the overall pressure variation compared to the prototype groove is within 0.02 Pa. Similarly, in the constant height cases, the pressure peaks hardly change after filleting at r_1' and r_2'. However, as the fillet radius increases, the effect of local pressure becomes more pronounced. For example, in the constant width cases, when the fillet radius reaches r_3, and in the constant height cases, when it reaches r_3', the positive and negative pressure peaks in Figs. 10h and 10i, respectively, are significantly larger than those in the prototype grooves. In these cases, the pressure drag is higher.

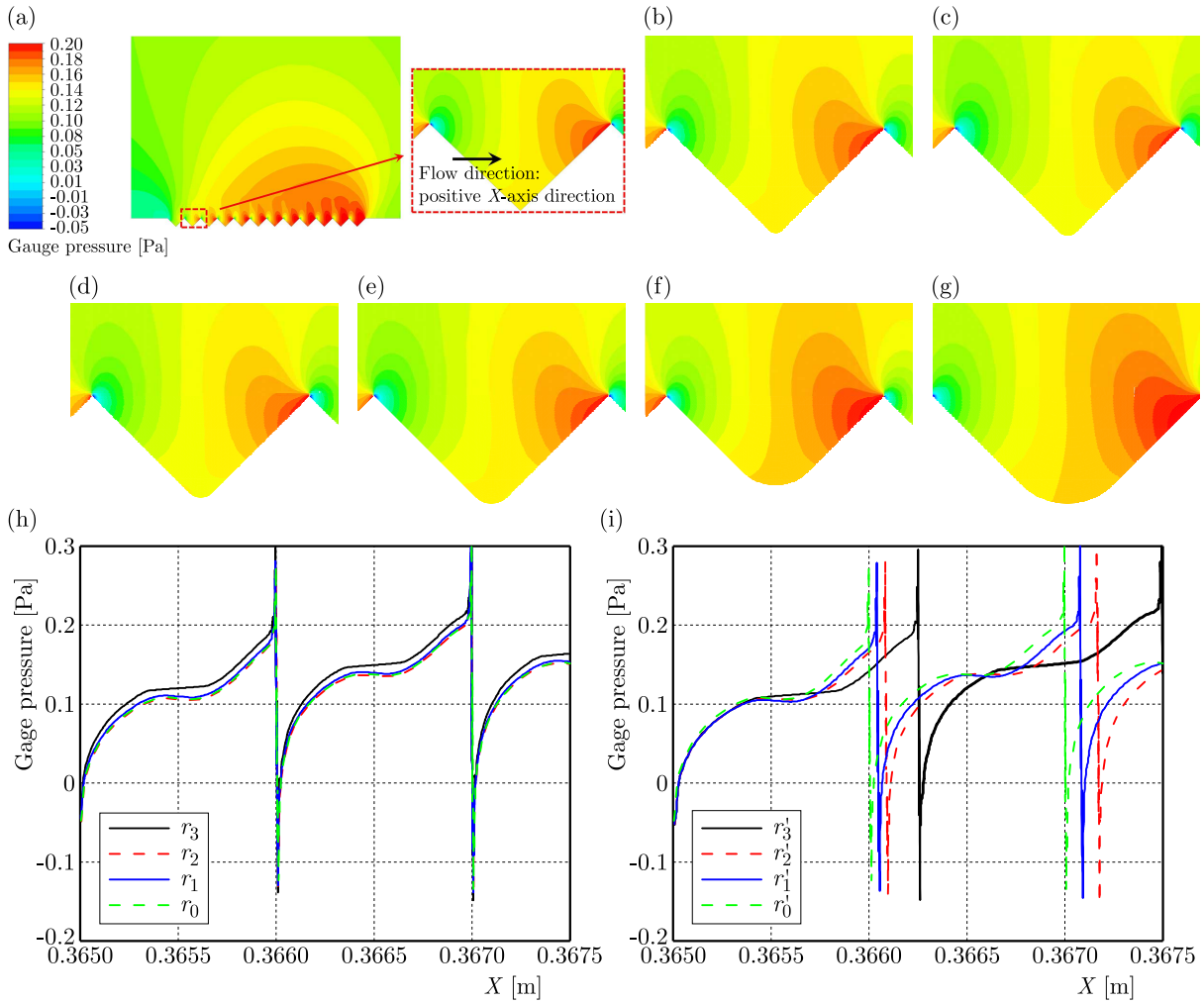

Fig. 10. Pressure distribution with the fillet valley: (a) prototype groove r_0, (b) CW r_1, (c) CH r_1', (d) CW r_2, (e) CH r_2', (f) CW r_3, (g) CH r_3', (h) CW, (i) CH

The streamline diagram in Fig. 11 illustrates that filleting the groove leads to a closer fit of the streamline with the corner of the turn, resulting in the elimination of secondary vortex structures and a moderation of velocity as well as pressure gradient at the groove valley. The fluid near the valley is influenced by the central vortex and moves in the clockwise direction. While the reduction in pressure gradient suggests a potential decrease in the pressure drag, it is important to note, as stated in the earlier findings in Section 4.2, that this advantage is very small and may even have a negative impact when the fillet radius is large. Moreover, the reduction in the velocity gradient may affect the viscous drag, which will be further discussed in the subsequent Section.

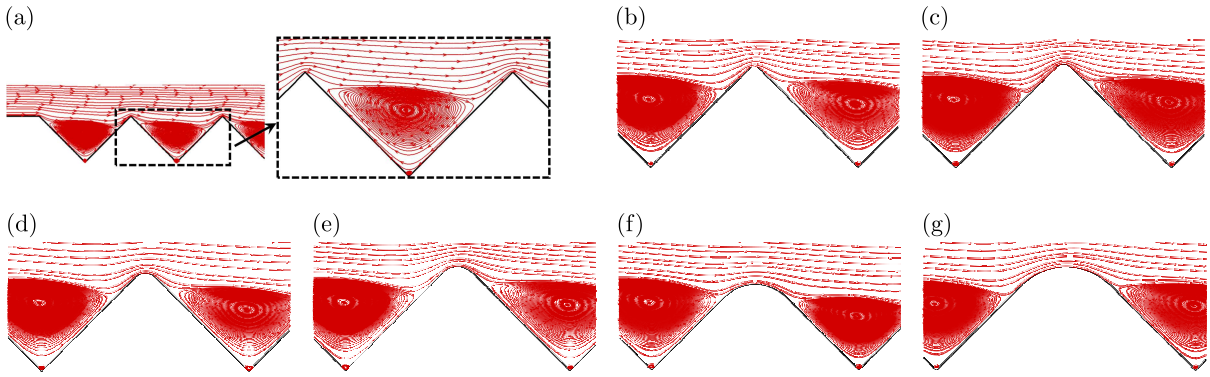

Fig. 11. Streamline distribution with the fillet valley (a) prototype groove r_0, (b) CW r_1, (c) CH r_1', (d) CW r_2, (e) CH r_2', (f) CW r_3, (g) CH r_3'

4.2.2. Fillet valley and viscous drag

Figures 12a-12e demonstrate that the wall shear stress in cases with small fillet radius remains largely unchanged compared to the prototype groove, corroborating the findings in Table 2. Combined with the streamline diagram shown in Fig. 11, the absence of secondary vortex structures leads to an increase of the valley range of the M peak, indicating a reduction in the viscous drag. This reduction becomes particularly prominent with a larger fillet radius, as depicted in Figs. 12f and 12g. Consequently, in the cases with a large fillet radius, while the elimination of secondary vortex structures may contribute to an increase in the pressure drag at the groove valley, the decrease in the viscous drag can offset this effect, ultimately resulting in a higher drag reduction rate.

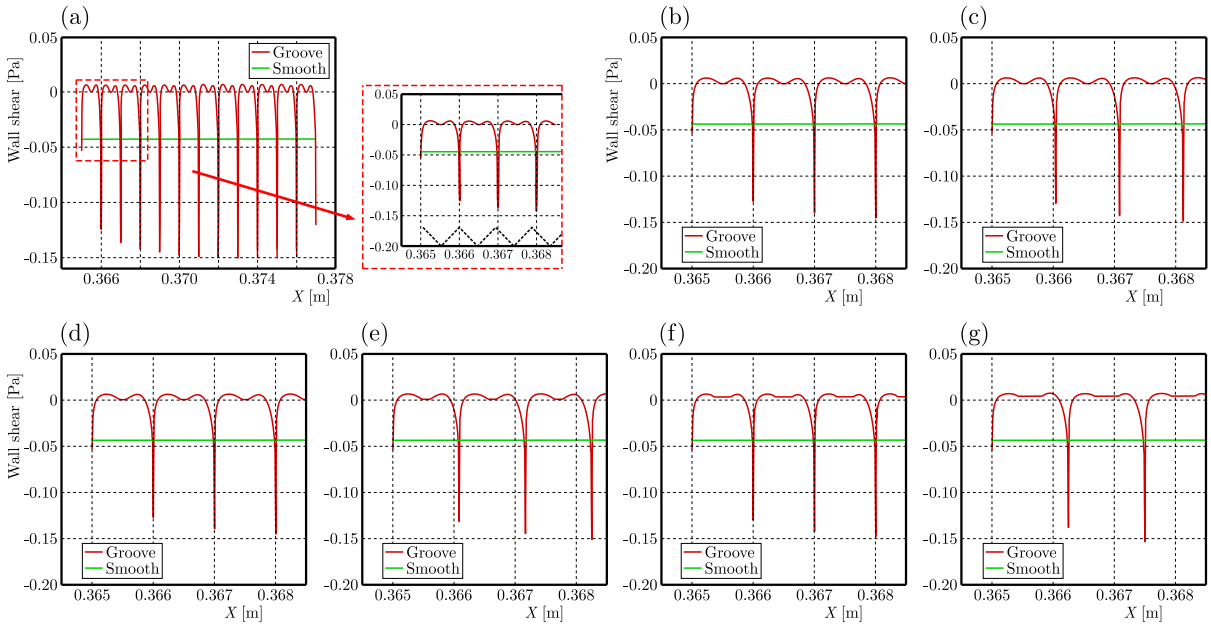

Fig. 12. Wall shear distribution with the fillet valley: (a) prototype groove r_0, (b) CW r_1, (c) CH r_1', (d) CW r_2, (e) CH r_2', (f) CW r_3, (g) CH r_3'

5. Conclusion

In this study, numerical simulations were performed to investigate flow characteristics of a flat plate with two-dimensional V-shaped transverse grooves. The effects of two filleting methods, namely "Constant Width" (CW) and "Constant Height" (CH), at the top and valley of the

grooves were examined to understand the changes in the flow mechanism. The key findings are summarized as follows:

- The filleting of the top of transverse grooves has an obvious impact on the drag reduction characteristics compared to the prototype grooves plate. Filleting the top leads to a decrease in the rate of increase in the pressure drag η_p, but it also reduces the absolute value of the viscous drag reduction rate η_v. When applying a constant width filleting, the total drag reduction rate significantly increases with a larger fillet radius, reaching a maximum of 23.24% at $r_3 = 0.3/\sqrt{2}$ mm from 13.29% due to a faster decrease in the cost (pressure drag). Conversely, filleting the top using a constant height results in a larger rise in the viscous drag, leading to a decrease in the total drag reduction rate with the increasing fillet radius.
- Both constant width and constant height filleting methods eliminate the secondary steady vortex at the valley of the groove, thereby reducing the viscous drag. However, at a larger fillet radius, these methods also increase the rate of increase in the pressure drag, leading to a reduction in the overall drag reduction rate. In the case of the constant height filleting, the drag reduction rate remains relatively unchanged compared to the prototype grooved plate, as the benefits and costs are balanced. On the other hand, the constant width filleting results in a lower total drag reduction rate of 11.62% at $r_3 = 0.3/\sqrt{2}$ mm due to the higher η_p.

In summary, our study analyzed the impact of modifying the top and groove of transverse grooves on drag reduction performance. We found that geometric changes of the top, resembling the "constant width" approach discussed earlier, are effective in improving the actual drag reduction performance of the grooves. So, engineers can intentionally design grooves with similar geometries to enhance the drag reduction performance even further. In the future, we will focus on investigating the impact of other forms of geometric variations on the drag reduction performance after a long-term use of the grooves.

Acknowledgements

This work was supported by the National Natural Science Foundation of China (No. 52176032), National Science and Technology Major Project (2017-k-0005-0016).

References

1. Aftab S.M.A., Mohd Rafie A.S., Razak N.A., Ahmad K.A., 2016, Turbulence model selection for low Reynolds number flows, *PLOS One*, **11**, 4, e0153755
2. Ahmadi-Baloutaki M., Carriveau R., Ting D.K., 2013, Effect of free-stream turbulence on flow characteristics over a transversely-grooved surface, *Experimental Thermal and Fluid Science*, **51**, 56-70
3. Bai Q., Bai J., Meng X., Ji C., Liang Y., 2016, Drag reduction characteristics and flow field analysis of textured surface, *Friction*, **4**, 165-175
4. Barbier C., Jenner E., D'Urso B., 2012, Drag reduction with superhydrophobic riblets, *ASME International Mechanical Engineering Congress and Exposition*, **45240**, 199-205
5. Belhocine A., Abdullah O.I., 2019, Numerical simulation of thermally developing turbulent flow through a cylindrical tube, *The International Journal of Advanced Manufacturing Technology*, **102**, 2001-2012
6. Belhocine A., Wan Omar W., 2015, Numerical study of heat convective mass transfer in a fully developed laminar flow with constant wall temperature, *Case Studies in Thermal Engineering*, **6**, 116-127

7. Bilen K., Cetin M., Gul H., Balta T., 2009, The investigation of groove geometry effect on heat transfer for internally grooved tubes, *Applied Thermal Engineering*, **29**, 4, 753-761
8. Bushnell D., 1983, Turbulent drag reduction for external flows, *21st Aerospace Sciences Meeting*, p. 227
9. Bushnell D., 1990, Supersonic aircraft drag reduction, *21st Fluid Dynamics, Plasma Dynamics and Lasers Conference*, p. 1596
10. Choi H., Moin P., Kim J., 1993, Direct numerical simulation of turbulent flow over riblets, *Journal of Fluid Mechanics*, **255**, 503-539
11. Choi K.S., 1989, Near-wall structure of a turbulent boundary layer with riblets, *Journal of Fluid Mechanics*, **208**, 417-458
12. Cui J., Fu Y., 2012, A numerical study on pressure drop in microchannel flow with different bionic micro-grooved surfaces, *Journal of Bionic Engineering*, **9**, 1, 99-109
13. DeGroot C.T., Wang C., Floryan J.M., 2016, Drag reduction due to streamwise grooves in turbulent channel flow, *Journal of Fluids Engineering*, **138**, 12
14. García-Mayoral R., Jiménez J., 2011a, Drag reduction by riblets, *Philosophical Transactions of the Royal Society A: Mathematical, Physical and Engineering Sciences*, **369**, 1940, 1412-1427
15. García-Mayoral R., Jiménez J., 2011b, Hydrodynamic stability and breakdown of the viscous regime over riblets, *Journal of Fluid Mechanics*, **678**, 317-347
16. Ghazali M.I., Harun Z., Ghopa W.W., Abbas A.A., 2016, Computational fluid dynamic simulation on NACA 0026 airfoil with V-groove riblets, *International Journal on Advanced Science, Engineering and Information Technology*, **6**, 4, 529-533
17. Jiang L., Yang W., Xie L., Liu Y., Wang X., Wu X., Zhou F., Hu H., 2023, Experimental study on mechanism of stable drag reduction with hydrogel interface, *Tribology International*, **178**, 108013
18. Leitl P.A., Shiraishi M., Flanschger A., Tsuchihashi S., Marn A., Schreck S., Ichinose G., Shibazaki Y., Benauer R., Pramstrahler S., 2022, Numerical and experimental investigation of lasered riblets on turbine exit guide vanes and the impact on the performance, *AIAA Scitech 2022 Forum*, p. 917
19. Li Z., He L., Zheng Y., 2022a, Quasi-analytical solution of optimum and maximum depth of transverse V-groove for drag reduction at different Reynolds numbers, *Symmetry*, **14**, 2, 342
20. Li Z., He L., Zuo Y., Meng B., 2022b, Analytic solution of optimal aspect ratio of bionic transverse V-groove for drag reduction based on vorticity kinetics, *Aerospace*, **9**, 12, 749
21. Menter F.R., Langtry R.B., Likki S.R., Suzen Y.B., Huang P.G., Völker S., 2006, A correlation-based transition model using local variables – Part I: model formulation, *Journal of Turbomachinery*, **128**, 3, 413-422
22. Pan J., 1996, An experimental approach to drag reduction of transverse ribbons on turbulent flow, *Acta Aerodynamica Sinica*, **14**, 3, 304-310
23. Pasha A.A., Abdul Raheem M., Islam N., Juhany K.A., Mushtaq A., Halkarni S.S., 2019, CFD study of variable property effects on laminar micro-convective heat transfer, *Arabian Journal for Science and Engineering*, **44**, 5961-5972
24. Sareen A., Deters R.W., Henry S.P., Selig M.S., 2014, Drag reduction using riblet film applied to airfoils for wind turbines, *Journal of Solar Energy Engineering*, **136**, 2
25. Walsh M., Lindemann A., 1984, Optimization and application of riblets for turbulent drag reduction, *22nd Aerospace Sciences Meeting*, p. 347

Manuscript received April 20, 2023; accepted for print July 22, 2023

JOURNAL OF THEORETICAL AND APPLIED MECHANICS
61, 4, pp. 755-768, Warsaw 2023
https://doi.org/10.15632/jtam-pl/170801

AN ENERGY METHOD FOR PREDICTING AND SUPPRESSING THE INSTABILITY OF A THREE-DIMENSIONAL THERMOACOUSTIC COUPLING SYSTEM WITH A MICRO-PERFORATED PLATE

Xue Xing, Bingjie Ma

Shanghai Marine Diesel Engine Research Institute, Shanghai, China, and

National Engineering Research Center of Special Equipment and Power System for Ship and Marine Engineering, Shanghai, China

corresponding author Xue Xing, e-mail: xingxue@hrbeu.edu.cn

Jingtao Du, Yang Liu, Zhigang Liu

College of Power and Energy Engineering, Harbin Engineering University, Harbin, China

Xiao Han

Shanghai Marine Diesel Engine Research Institute, Shanghai, China

The Micro-Perforated Plate (MPP) is widely used in the noise control field with advantages of high temperature resistance and being suitable for high-speed flow fields. In this paper, an analytical model of the three-dimensional thermoacoustic coupling system suppressed by the MPP is established through the energy principle and Rayleigh-Ritz method. A modified Fourier series will be applied to characterize the sound pressure distribution function to meet arbitrary impedance boundary conditions. Based on the sound intensity and divergence, the energy transmission path and distribution law of energy sources and traps are analyzed. The suppression mechanism of a MPP on the thermoacoustic instability is revealed.

Keywords: thermoacoustic coupling system, micro-perforated plate, modified Fourier series

1. Introduction

The thermoacoustic coupling oscillation occuring in combustion systems of gas turbines seriously affects quietness and operation reliability of the equipment (Dowling and Mahmoudi, 2015; Seo, 2003; Lefebvre and Ballal, 2010). The Micro-Perforated Plate (MPP) has the advantage of not being limited by high temperature, high speed and other harsh environments (Zhang, 2020; Schönfeld and Poinsot, 1999; Armitage *et al.*, 2004; Schuller *et al.*, 2003). Therefore, the MPP has attracted attention in the thermoacoustic oscillation control field. However, the effective handling of thermoacoustic coupling system with MPPs in terms of modelling, optimization and mechanism exploration is technically challenging.

At present, scholars have carried out a series of studies on suppression of thermoacoustic coupling oscillation by MPPs. Eldredge and Dowling *et al.* (2003) proposed that the perforated structure on the combustion chamber wall can be simplified as a perforated plate model. Ma (1975) pointed out that the MPP sound absorption structure is a resonant sound absorber which is characterized by a wide frequency band, simple structure and can be used in special environments. Sun (2010) used CFD to simulate the thermoacoustic system and discussed the influence of structural parameters such as perforation rate on the thermoacoustic oscillation characteristics. Chu and Xu (2016) carried out numerical simulation analysis using CAA,

the three-dimensional (3D) acoustic equation was solved to predict the modal information of the thermoacoustic system, and then the inhibition effect of the MPP on unstable modes was simulated. The above investigation proves that, most of the research on suppression of thermoacoustic oscillation by MPPs is still limited to experimental methods and numerical simulation methods. In the experiment, the thermoacoustic coupling oscillation phenomenon is suppressed through empirical debugging. In the numerical simulation, the appropriate MPP parameters and installation positions are determined through a large number of parameter analysis, and there is a lack of understanding of the control mechanism of thermoacoustic coupling oscillation.

Motivated by this, this paper proposes a semi-analytical technique based on the energy principle and Rayleigh Ritz method to reveal the characteristic of thermoacoustic coupling phenomenon and realize effective suppression of thermoacoustic oscillation. The 3D thermoacoustic coupling system is established, taking into account arbitrary impedance boundary conditions and the MPP. The system structure can be decomposed by a substructure method. To ensure smoothness of the field function, a modified Fourier series enriched with auxiliary polynomial terms is constructed for decomposition of the sound pressure. Numerical analyses are performed with a particular focus on the sound field energy transmission path and the control strategy of the MPP on the thermoacoustic coupling instability.

2. Theoretical model

A 3D thermoacoustic coupling system with arbitrary impedance boundary conditions, variable cross-section and MPP is shown in Fig. 1a. According to characteristics of the complex cavity structure, it can be divided into acoustic cavity substructures TAC_1 and TAC_2, which are connected by auxiliary air plates TAA at the interface, as shown in Fig. 1b. The heat source is located in TAC_2, and the MPP can be located at an arbitrary position on the wall. Assuming that the MPP at $y = 0$, the starting coordinate of MPP is expressed as $(x_m, 0, z_m)$.

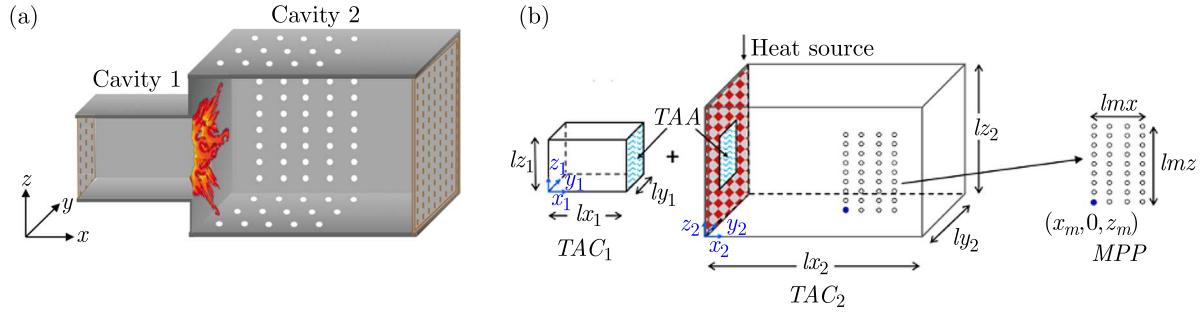

Fig. 1. The 3D thermoacoustic coupling system with the MPP

2.1. Sound pressure distribution function of the acoustic cavity substructure and the displacement function of an auxiliary air plate at the interface

The 3D modified Fourier series expression (Du *et al.*, 2011) is used to describe the sound pressure distribution, expressed as p_{c1} and p_{c2}, respectively

$$
\begin{aligned}
p_{c_i}(x,y,z) = &\sum_{m_x^{c_i}=0}^{\infty}\sum_{m_y^{c_i}=0}^{\infty}\sum_{m_z^{c_i}=0}^{\infty} A_{m_x^{c_i}m_y^{c_i}m_z^{c_i}}\cos\lambda_{m_x^{c_i}}x\cos\lambda_{m_y^{c_i}}y\cos\lambda_{m_z^{c_i}}z\\
&+\sum_{m_y^{c_i}=0}^{\infty}\sum_{m_z^{c_i}=0}^{\infty}\Big[\underbrace{B_{m_y^{c_i}m_z^{c_i}}\xi_{1c_i}(x)}_{x_i=0}+\underbrace{C_{m_y^{c_i}m_z^{c_i}}\xi_{2c_i}(x)}_{x_i=l_{x_i}}\Big]\cos\lambda_{m_y^{c_i}}y\cos\lambda_{m_z^{c_i}}z\\
&+\sum_{m_x^{c_i}=0}^{\infty}\sum_{m_z^{c_i}=0}^{\infty}\Big[\underbrace{D_{m_x^{c_1}m_z^{c_1}}\xi_{1c_i}(y)}_{y_i=0}+\underbrace{E_{m_x^{c_i}m_z^{c_i}}\xi_{2c_i}(y)}_{y_i=l_{y_i}}\Big]\cos\lambda_{m_x^{c_i}}x\cos\lambda_{m_z^{c_i}}z\\
&+\sum_{m_x^{c_i}=0}^{\infty}\sum_{m_y^{c_i}=0}^{\infty}\Big[\underbrace{F_{m_x^{c_i}m_y^{c_i}}\xi_{1c_i}(z)}_{z_i=0}+\underbrace{G_{m_x^{c_i}m_y^{c_i}}\xi_{2c_i}(z)}_{z_i=l_{z_i}}\Big]\cos\lambda_{m_x^{c_i}}x\cos\lambda_{m_y^{c_i}}y
\end{aligned}
\tag{2.1}
$$

where $i=1,2$, $\lambda_{m_x^{c_i}}=m_{x^{c_i}}\pi/(lx_i)$, $\lambda_{m_y^{c_i}}=m_y^{c_i}\pi/(ly_i)$, $\lambda_{m_{z^{c_i}}}=m_z^{c_i}\pi/(lz_i)$. The specific expression of the boundary complementary function shown as the x-axis is

$$
\xi_{1c_i}(x)=x\Big(\frac{x}{lx_i}-1\Big)^2 \qquad \xi_{2c_i}(x)=\frac{x^2}{lx_i}\Big(\frac{x}{lx_i}-1\Big) \tag{2.2}
$$

In the analysis, the TAA can be regarded as a 2D elastic thin plate structure, and the sound field transfer between the adjacent acoustic cavity substructures is transformed into bending vibration. The bending vibration displacement of TAA is expressed by 2D Fourier series, i.e.

$$
w_a(y,z)=\sum_{m_y^a=0}^{\infty}\sum_{m_z^a=0}^{\infty} w_{m_y^a m_z^a}\cos\lambda_{m_y^a}y\cos\lambda_{m_z^a}z \tag{2.3}
$$

where $\lambda_{m_y^a}=m_y^a\pi/(ly_1)$, $\lambda_{m_z^a}=m_z^a\pi/(lz_1)$.

2.2. Lagrange function of the acoustic cavity substructure and the auxiliary air plate at the interface

After obtaining the sound pressure distribution of TAC and the displacement function of TAA, it is necessary to further obtain all the unknown Fourier coefficients. The characteristic equation of the thermoacoustic coupling system with the MPP will be constructed using the energy principle and Rayleigh-Ritz method. Writing Lagrangian for TAC and TAA

$$
\begin{aligned}
L_{c_1} &= V_{c_1}-T_{c_1}-W_{end1}-W_{a\&c_1}-W_S\\
L_{c_2} &= V_{c_2}-T_{c_2}-W_{end2}-W_{MPP}-W_{a\&c_2}-W_{heat}\\
L_a &= V_a-T_a+W_{c_1\&a}+W_{c_2\&a}
\end{aligned}
\tag{2.4}
$$

where V_c, T_c are the potential energy and kinetic energy of TAC, W_{end1} and W_{end2} are the work done by the impedance end of TAC, W_{heat} is the work done by the heat source, $W_{a\&c}$ is the work done by bending vibration of TAA to TAC.

The potential energy and kinetic energy of TAC_1 and TAC_2 are

$$
\begin{aligned}
V_i &= \frac{1}{2\rho_i c_i^2}\int_{V_i} p_i^2(x,y,z)\,dV_i=\frac{1}{2\rho_i c_i^2}\int_0^{lz_i}\int_0^{ly_i}\int_0^{lx_i} p_i^2(x,y,z)\,dx\,dy\,dz \qquad i=1,2\\
T_i &= \frac{1}{2\rho_i\omega^2}\int_{V_i}(\operatorname{grad}p)^2\,dV_i=\frac{1}{2\rho_i\omega^2}\int_0^{lz_i}\int_0^{ly_i}\int_0^{lx_i}\Big[\Big(\frac{\partial p_i}{\partial x}\Big)^2+\Big(\frac{prtp_i}{\partial y}\Big)^2+\Big(\frac{\partial p_i}{\partial z}\Big)^2\Big]\,dx\,dy\,dz
\end{aligned}
\tag{2.5}
$$

The works done by the auxiliary air plate to the acoustic cavity substructure are

$$\begin{aligned} W_{a\&c_1} &= \int\limits_{S_a} p_1(x,y,z)\Big|_{x=lx_1} w_a \, dS_a = \int\limits_0^{lz_1}\int\limits_0^{ly_1} p_1(x,y,z)\Big|_{x=lx_1} w_a \, dy\, dz \\ W_{a\&c_2} &= \int\limits_{S_a} p_2(x,y,z)\Big|_{x=0} w_a \, dS_a = \int\limits_{\frac{lz_2}{2}-\frac{lz_1}{2}}^{\frac{lz_2}{2}+\frac{lz_1}{2}}\int\limits_{\frac{ly_2}{2}-\frac{ly_1}{2}}^{\frac{ly_2}{2}+\frac{ly_1}{2}} p_2(x,y,z)\Big|_{x=0} w_a \, dy\, dz \end{aligned} \tag{2.6}$$

The work done by the inlet impedance of the acoustic cavity substructure TAC_1

$$W_{end1} = -\frac{1}{2}\int\limits_{S_0} \frac{p_1(x,y,z)^2}{j\omega Z_0}\Big|_{x=0} dS_0 = -\frac{1}{2}\int\limits_0^{lz_1}\int\limits_0^{ly_1} \frac{p_1(x,y,z)^2}{j\omega Z_0}\Big|_{x=0} dy\, dz \tag{2.7}$$

The work done by the outlet impedance of the acoustic cavity substructure TAC_2

$$W_{end2} = -\frac{1}{2}\int\limits_{S_L} \frac{p_2(x,y,z)^2}{j\omega Z_L}\Big|_{x=lx_2} dS_L = -\frac{1}{2}\int\limits_0^{lz_2}\int\limits_0^{ly_2} \frac{p_2(x,y,z)^2}{j\omega Z_L}\Big|_{x=lx_2} dy\, dz \tag{2.8}$$

The equivalent impedance of MPP can be expressed as

$$Z_{MPP} = \frac{32\mu t_h}{\delta_h \rho c d_h^2}\left[\left(1+\frac{K^2}{32}\right)^{\frac{1}{2}} + \frac{\sqrt{2}}{32}K\frac{d_h}{t_h}\right] + j\frac{\omega t_h}{\delta_h c}\left[1+\left(9+\frac{K^2}{32}\right)^{-\frac{1}{2}} + 0.85\frac{d_h}{t_h}\right] \tag{2.9}$$

where μ is the aerodynamic viscosity, δ_h is the perforation rate, d_h is the hole diameter, and t_h is the plate thickness.

The acoustic effect of the MPP is characterized by distribution impedance, and the energy dissipation in the sound field can be expressed as

$$W_{MPP} = -\frac{1}{2}\int\limits_{S_{MPP}} \frac{p_2(x,y,z)^2}{j\omega Z_{MPP}} \, dS_{MPP} \tag{2.10}$$

The work done by the heat source can be obtained

$$W_{heat} = \frac{1}{2}\frac{\gamma-1}{\rho_2 c_2^2}\int\limits_0^{lz_2}\int\limits_0^{ly_2} \frac{p_2(x_q)q}{j\omega} \, dy\, dz \qquad q(x,t) = \frac{Q(t)}{S}\delta(x-x_q) \tag{2.11}$$

in which γ is the ratio of specific heats, and q represents the heat release rate per unit area, Q is the heat release rate, x_q is the heating position.

The potential and kinetic energy of the auxiliary air plate at the interface are respectively

$$\begin{aligned} V_a &= \frac{D}{2}\int\limits_0^{lz_1}\int\limits_0^{ly_1}\left[\left(\frac{\partial^2 w_a}{\partial y^2}\right)^2 + \left(\frac{\partial^2 w_a}{\partial z^2}\right)^2 + 2\mu\frac{\partial^2 w_a}{\partial y^2}\frac{\partial^2 w_a}{\partial z^2} + 2(1-\mu)\left(\frac{\partial^2 w_a}{\partial y \partial z}\right)^2\right] dy\, dz \\ T_a &= \frac{1}{2}\omega^2 \rho_a \delta_a \int\limits_0^{lz_1}\int\limits_0^{ly_1} w_a^2 \, dy\, dz \end{aligned} \tag{2.12}$$

where D, μ, ρ_a, δ_a are the bending stiffness, Poisson's ratio, mass density and thickness of the air plate. The temperature of air plate is consistent with the temperature of the acoustic cavity, the particle velocity is determined by the current position, and can be obtained according to the Euler equation of motion.

2.3. Characteristic equation of the thermoacoustic coupling system

In numerical calculation, the Fourier series of the acoustic cavity substructure is truncated at $m_x = M_x$, $m_y = M_y$, $m_z = M_z$, and the Fourier series of the auxiliary air plate is truncated at $m_a = M_a$. Applying the Lagrange equation and Rayleigh-Ritz method with respect to all the unknown coefficients yields the following condensed matrix form

$$\begin{aligned}
&(\mathbf{K}_{c1} - \omega\mathbf{Z}_{c1} - \omega^2\mathbf{M}_{c1})\mathbf{P}_{c_1} + \omega^2\mathbf{C}_{a\&c_1}\mathbf{W}_a = \mathbf{Q}_s \\
&\Big(\mathbf{K}_{c_2} - \frac{1}{2}\frac{b(\gamma-1)}{\rho^2c^2S(1+j\omega t)}\mathbf{R} - \omega\mathbf{Z}_{MPP} - \omega\mathbf{Z}_{c_2} - \omega^2\mathbf{M}_{c_2}\Big)\mathbf{P}_{c_2} + \omega^2\mathbf{C}_{a\&c_2}\mathbf{W}_a = \mathbf{0} \\
&(\mathbf{K}_a - \omega^2\mathbf{M}_a)\mathbf{W}_a + \mathbf{C}_{c_1\&a}\mathbf{P}_{c_1} + \mathbf{C}_{c_2\&a}\mathbf{P}_{c_2} = \mathbf{0}
\end{aligned} \tag{2.13}$$

where $\mathbf{K}_{c1}$, $\mathbf{K}_{c2}$, $\mathbf{K}_a$ are the stiffness matrices of the substructures, $\mathbf{M}_{c1}$, $\mathbf{M}_{c2}$, $\mathbf{M}_a$ are the mass matrices of substructures, $\mathbf{C}_{a\&c}$ and $\mathbf{C}_{c\&a}$ are the auxiliary matrices of the interaction between TAC and TAA, $\mathbf{Z}_{c1}$, $\mathbf{Z}_{c2}$ are the boundary impedance work matrices, $\mathbf{Z}_{MPP}$ is the MPP work matrix, $\mathbf{R}$ is the heat source work matrix, $\mathbf{P}_c$ and $\mathbf{W}_a$ are unknown Fourier coefficient vectors.

Considering that the auxiliary air plate at the interface is a virtual structure, the thickness of the air plate in the numerical calculation is a small value ($\delta_a = 10^{-6}\,\mathrm{m}$), and bending stiffness $D = 0$. Therefore, the potential energy of the air plate is $V_a = 0$, and Eq. $(2.13)_3$ can be simplified to

$$-\omega^2\mathbf{M}_a\mathbf{W}_a + \mathbf{C}_{c_1\&a}\mathbf{P}_{c_1} + \mathbf{C}_{c_2\&a}\mathbf{P}_{c_2} = \mathbf{0} \tag{2.14}$$

Dynamic equations (2.13) and (2.14) are simultaneously established, and the matrix characteristic equation for the thermoacoustic coupling system can be obtained

$$(\mathbf{K} - \omega\mathbf{Z} - \omega^2\mathbf{M} - \omega^2\mathbf{X})\mathbf{P} = \mathbf{Q} \tag{2.15}$$

The coupling characteristics can be obtained by solving the system matrix eigenequation. The most important is that ω is a complex number, whose real part, denoted by $\mathrm{Re}(\omega)$, represents the oscillation frequency, and the minus of the imaginary part of ω, $-\mathrm{Im}(\omega)$ is the growth rate of the oscillation amplitude. The growth rate greater than zero means the unstable mode, less than zero is the stable mode.

3. Numerical simulation and analysis

3.1. Model validation

When the heat source is not considered, the thermoacoustic coupling system degenerates into a pure acoustic system, and the matrix characteristic equation (2.15) of TAC_2 degenerates to

$$(\mathbf{K}_{c2} - \omega\mathbf{Z}_{MPP} - \omega\mathbf{Z}_{c2} - \omega^2\mathbf{M}_{c2})\mathbf{P}_{c_1} + \omega^2\mathbf{C}_{a\&c_2}\mathbf{W}_a = \mathbf{0} \tag{3.1}$$

Dynamic equations $(2.13)_1$, (2.14) and (3.1) are simultaneously established, and the matrix characteristic equation for the pure acoustic system can be obtained.

The geometric parameters of TAC are $l_{x_1} = 0.3\,\mathrm{m}$, $l_{y_1} = 0.5\,\mathrm{m}$, $l_{z_1} = 0.5\,\mathrm{m}$, $l_{x_2} = 0.7\,\mathrm{m}$, $l_{y_2} = 1\,\mathrm{m}$, $l_{z_2} = 1\,\mathrm{m}$. The right end of TAC_2 is the pressure release boundary. Three MPPs are selected, $l_{my} = 0.1\,\mathrm{m}$, $0.3\,\mathrm{m}$ and $0.5\,\mathrm{m}$, respectively, and $l_{mz} = l_{z_2}$. MPP is on $y = 0$, and the starting coordinates are $(0.9\,\mathrm{m}, 0, 0)$, $(0.7\,\mathrm{m}, 0, 0)$ and $(0.5\,\mathrm{m}, 0, 0)$ in turn. The MPP structure parameters are shown in Table 1. COMSOL Multiphysics software has been used for comparative verification of thermoacoustic coupling systems. Firstly, a variable cross-section three-

-dimensional thermoacoustic coupling system is established, and pressure acoustics and frequency domain modules are used to calculate the thermoacoustic coupling characteristics, including the variable cross-section acoustic cavity, heat source domain, wall distributed impedance, and inlet and outlet boundary impedance. The heat source is introduced in the form of local integration, and the coupled iterative calculation between the heat source and the acoustic system is formed by using local ordinary differential and differential algebra equations. The finite element mesh division of its structure, includes 33379 tetrahedral elements, 8232 triangular elements, and 480 edge elements. The average element mass is 0.584, and the mesh volume is 0.85 m^3. The grid at the heat source region is dense, with 9318 tetrahedrons, an average element mass of 0.4047, and a grid volume of 0.01 m^3. The current modal frequencies of the 3D acoustic cavity with MPPs are shown in Table 2. Figure 2 shows a comparison of modal shapes between the results from the current method and FEM.

Table 1. MPP structure parameters

MPP parameters	Value	Unit
Perforation rate	1.2	%
Orifice diameter	0.001	m
Panel thickness	0.003	m
Aerodynamic viscosity	1.789E-5	Pa·s

Table 2. Comparison of modal frequencies of the acoustic system with different MPPs [Hz]

Order	$l_{my} = 0.1$ m		$l_{my} = 0.3$ m		$l_{my} = 0.5$ m	
	Current	FEM	Current	FEM	Current	FEM
1	181.66	182.19	183.70	183.91	187.58	187.29
2	181.96	182.49	187.53	186.74	192.03	191.74
3	202.94	202.48	223.47	222.68	249.22	248.93
4	254.01	253.54	268.04	268.25	284.18	283.89
5	278.23	278.76	278.37	277.58	293.95	293.66
6	307.02	307.55	309.39	309.60	308.88	309.59

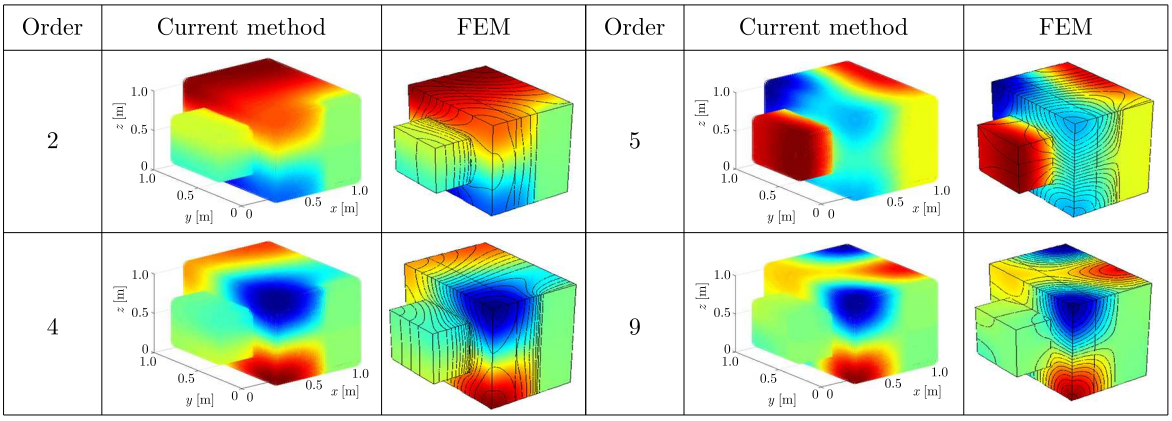

Fig. 2. Comparison of modal shapes of the acoustic system with the 2nd MPP

Through the above comparison, it is found that the results are in good agreement with FEM results, and it is proved that the current method can accurately predict the modal parameters of the acoustic system with the MPP at an arbitrary position. In addition, we also found that the MPP has a significant impact on sound pressure distribution, the sound pressure distribution is

no longer symmetrical, and the sound pressure is almost zero at the MPP position, which proves that the MPP can effectively absorb the sound energy.

Next, the heat release is introduced, with the parameters $b = 200$, $\tau = 0.002\,\mathrm{s}$. Two different acoustic structures are chosen as shown in Table 3. The right end of TAC_2 is the pressure release boundary. Table 3 shows a comparison between the modal frequency and growth rate calculated by the current method and FEM. The comparisons show that the modal frequency and growth rate are in good agreement, which proves the current method can accurately predict stability and corresponding thermoacoustic behavior characteristics of the 3D variable cross-sectional thermoacoustic coupling system.

Table 3. Parameters of cavity

Parameters of cavity 1	Parameters of cavity 2
$l_{x_1} = 0.2\,\mathrm{m}$, $l_{y_1} = 1\,\mathrm{m}$, $l_{z_1} = 1\,\mathrm{m}$	$l_{x_2} = 0.8\,\mathrm{m}$, $l_{y_2} = 1\,\mathrm{m}$, $l_{z_2} = 1\,\mathrm{m}$
$l_{x_1} = 0.2\,\mathrm{m}$, $l_{y_1} = 0.5\,\mathrm{m}$, $l_{z_1} = 0.5\,\mathrm{m}$	$l_{x_2} = 0.8\,\mathrm{m}$, $l_{y_2} = 1\,\mathrm{m}$, $l_{z_2} = 1\,\mathrm{m}$

Table 4. Comparison of frequency and growth rate of the thermoacoustic coupling system

Order	Cavity 1		Cavity 2	
	Frequency [Hz]	Growth rate [rad/s]	Frequency [Hz]	Growth rate [rad/s]
1	$189.31^{[a]}$ $189.33^{[b]}$	$-12.99^{[a]}$ $-12.73^{[b]}$	$98.52^{[a]}$ $97.43^{[b]}$	$-23.40^{[a]}$ $-22.29^{[b]}$
2	$189.31^{[a]}$ $189.39^{[b]}$	$-12.99^{[a]}$ $-12.73^{[b]}$	$205.05^{[a]}$ $205.69^{[b]}$	$5.81^{[a]}$ $5.77^{[b]}$
3	$253.23^{[a]}$ $252.78^{[b]}$	$-34.62^{[a]}$ $-34.61^{[b]}$	$205.05^{[a]}$ $205.69^{[b]}$	$5.80^{[a]}$ $5.77^{[b]}$
4	$254.67^{[a]}$ $254.68^{[b]}$	$-7.56^{[a]}$ $-7.27^{[b]}$	$252.39^{[a]}$ $253.54^{[b]}$	$-59.38^{[a]}$ $-58.79^{[b]}$
5	$305.41^{[a]}$ $304.83^{[b]}$	$-24.48^{[a]}$ $-25.36^{[b]}$	$264.79^{[a]}$ $265.19^{[b]}$	$1.70^{[a]}$ $1.94^{[b]}$
6	$305.41^{[a]}$ $304.85^{[b]}$	$-24.48^{[a]}$ $-25.18^{[b]}$	$333.24^{[a]}$ $334.17^{[b]}$	$-2.18^{[a]}$ $-2.25^{[b]}$

Remarks: $^{[a]}$ – current results, $^{[b]}$ – FEM results

3.2. Analysis of thermoacoustic coupling instability suppressed by the MPP

To explore the mechanism of the thermoacoustic coupling instability suppressed by the MPP separately and avoid energy dissipation of other impedance conditions, the straight and rigid cavity is preferred. The geometric parameters are $l_{x_1} = 0.6\,\mathrm{m}$, $l_{x_2} = 0.4\,\mathrm{m}$, $l_{y_1} = l_{y_2} = 0.3\,\mathrm{m}$, $l_{z_1} = l_{z_2} = 0.3\,\mathrm{m}$. First, it is necessary to master the behavior of the initial system, thus the modal frequency and growth rate of the thermoacoustic coupling system within 1000 Hz are predicted, see Fig. 3. It can be seen that there are 6 unstable modes in the first 1000 Hz of the thermoacoustic coupling system, and the instability of the low-order unstable modes is stronger.

Two unstable modes (176 Hz and 591 Hz) and two stable modes (337 Hz and 850 Hz) marked in Fig. 3 are selected, and the nondimensional sound pressures at $(0.8l_{x_2}, 0.5l_{y_2}, 0.5l_{z_2})$ are shown in Fig. 4. Figure 4a and 4c show the onset of nondimensional sound pressure for unstable modes, and the sound pressure increases exponentially with t. Figure 4b and 4d show the attenuation of nondimensional sound pressure of the stable modes, and the sound pressure gradually tends to zero with t. Since the modal growth rate $-83.13\,\mathrm{rad/s}$ of 337 Hz is far less than the modal growth rate $-5.72\mathrm{E}\text{-}5\,\mathrm{rad/s}$ of 850 Hz, its modal sound pressure attenuation is significantly faster than in the 850 Hz mode.

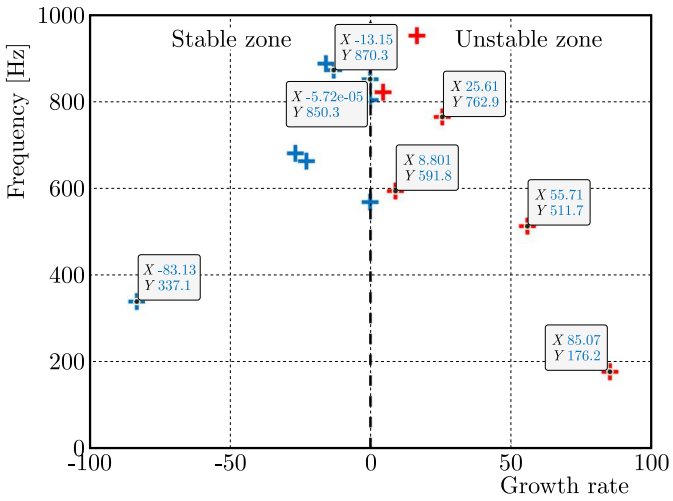

Fig. 3. Distribution of modal stability of the thermoacoustic coupling system without an MPP

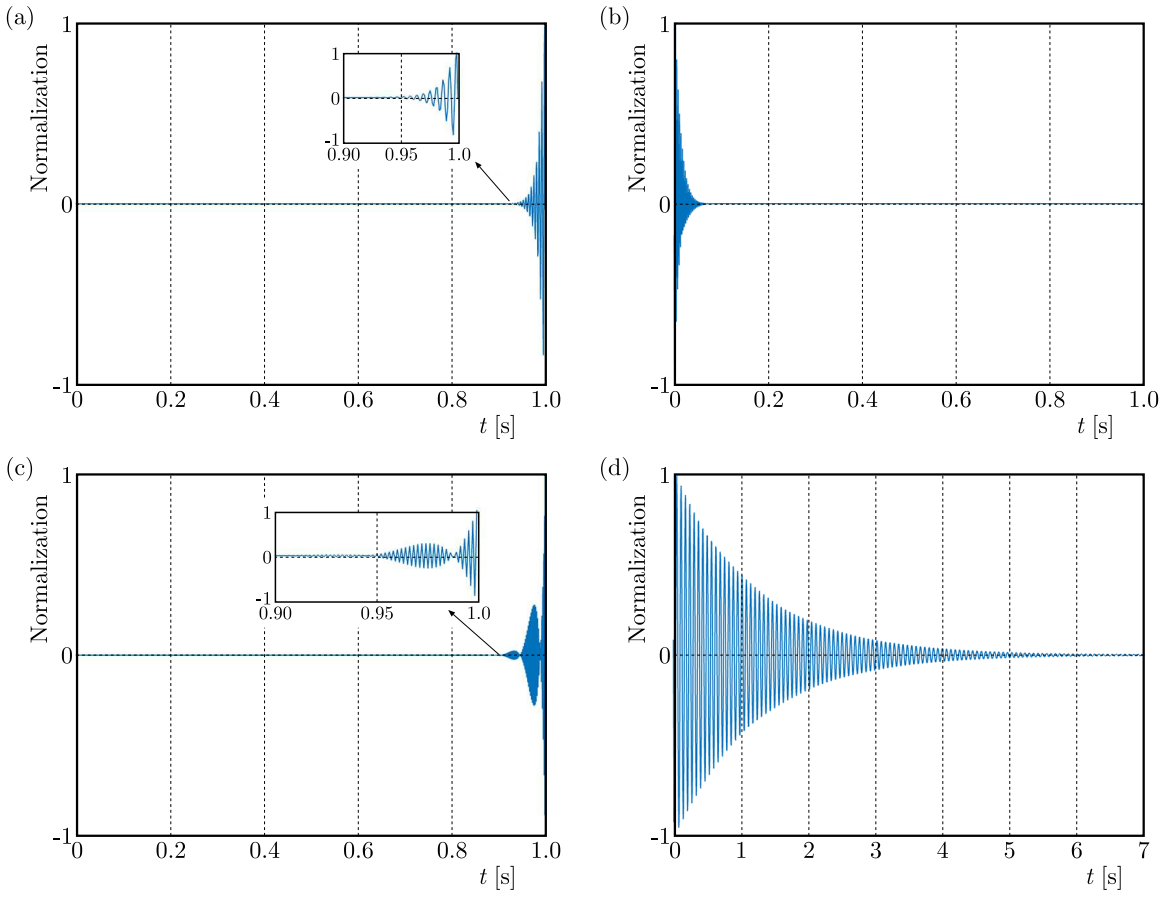

Fig. 4. The variation of nondimensional sound pressure for stable and unstable modes: (a) 175 Hz, (b) 337 Hz, (c) 591 Hz, (d) 850 Hz

Then, the MPP is introduced at $y = 0$ with the initial coordinates of $(0.7\,\mathrm{m}, 0, 0)$, $l_{my} = 0.3\,\mathrm{m}$, $l_{mz} = l_{z_2}$. Figure 5 shows the modal frequency and stability distribution within the first 1000 Hz of the thermoacoustic coupling system with the MPP. Due to the introduction of MPP, the unstable modes are reduced from 6 orders to 4 orders, and the growth rates of still unstable modes are reduced to approaching the critical stable center with the zero growth rate, which

proves that the MPP can control the multi-order modes at the same time and enhance system stability.

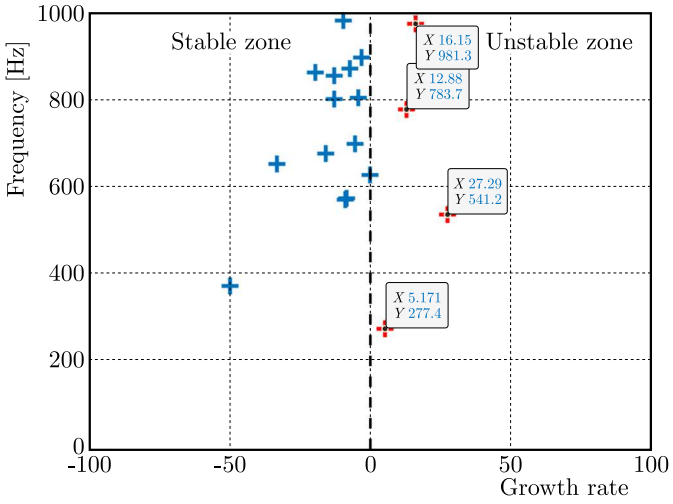

Fig. 5. Distribution of modal stability of the thermoacoustic coupling system with the MPP

Owing to the introduction of the MPP, the instability of the thermoacoustic coupling system is greatly modified, but the system is still not completely stable. This is because the MPP dissipates a part of the energy released by heat but fails to completely dissipate the energy generated by heat release. Therefore, it is necessary to further explore the effective set of the MPP on suppressing thermoacoustic instability.

3.3. Sound intensity distribution and energy transmission in the thermoacoustic coupling system

The thermoacoustic coupling process is essentially mutual conversion between thermal energy and acoustic energy. In order to clearly show the energy exchange characteristics between the heat source and the acoustic system, the sound pressure, sound intensity and its dispersion distribution of the thermoacoustic coupling system will be simulated separately. A combination of the sound intensity and dispersion can evaluate the energy transmission path, source and trap distribution law in the whole system, and provide an effective way to reveal the thermoacoustic characteristics and the instability control mechanism. The sound intensity energy and sound intensity divergence are defined as

$$I = \frac{1}{2} p u^* = S + jG \qquad \operatorname{div}(I) = \nabla(I) = \frac{\partial I_x}{\partial x} + \frac{\partial I_y}{\partial y} + \frac{\partial I_z}{\partial z} \tag{3.2}$$

where S is the active sound intensity, and G is the passive sound intensity.

To study the energy distribution of the thermoacoustic coupling system with/without an MPP, the parameters of acoustic cavity in Section 3.2 are selected. First, the sound pressure, sound intensity and divergence distribution of the thermoacoustic coupling system with/without the MPP are analyzed. The point source is introduced at $(0.3, 0.5l_{y_1}, 0.5l_{z_1})$, and the volume velocity is $2 \cdot 10^{-5}\,\mathrm{m}^3/\mathrm{s}$. $y = 0.5ly$ section is chosen to observe the system characteristics. The excitation frequency is the 6 modal frequencies marked in Fig. 6.

Figure 6 shows a comparison of the passive sound intensity and sound pressure distribution of the acoustic system and the thermoacoustic system. In each figure, the upper subfigure shows characteristics of the acoustic system, and the lower subfigure shows characteristics of the thermoacoustic coupling system. The vector in the figure represents the passive sound intensity, and the color represents the sound pressure distribution. By comparing the passive sound intensity

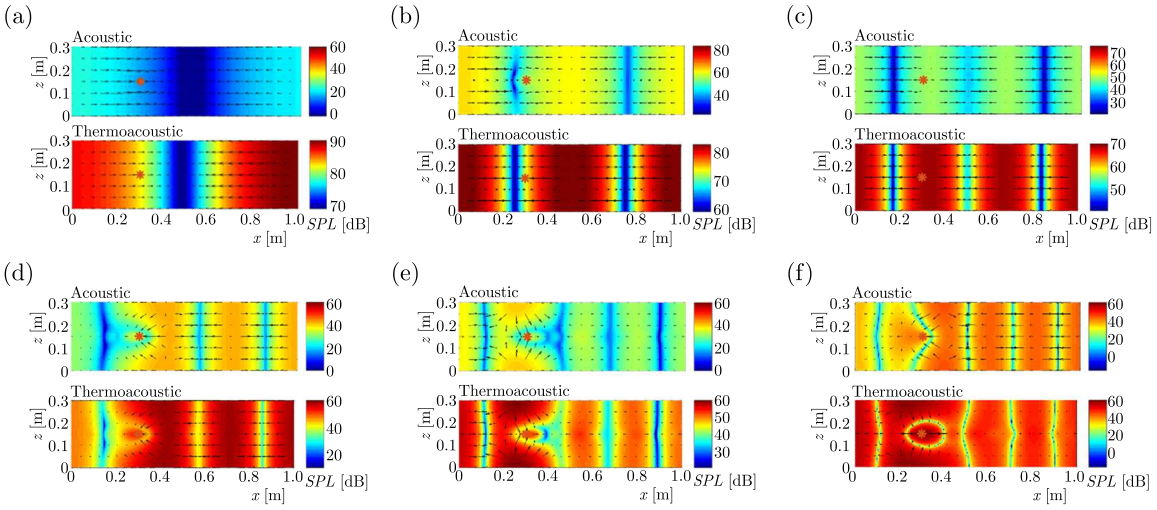

Fig. 6. Distribution of the passive sound intensity and sound pressure response: (a) 176.2 Hz, (b) 337.1 Hz, (c) 511.7 Hz, (d) 591.8 Hz, (e) 762.9 Hz, (f) 850 Hz

vector and sound pressure distribution in Fig. 6, it can be found that the passive sound intensity, as an oscillating energy flow, is always perpendicular to the isobaric surface of the sound field and parallel to the pressure drop direction. From the observation of the sound pressure distribution, it can be seen that the sound pressure response amplitude of the thermoacoustic system increases significantly, especially under a low frequency excitation. It means that the sound pressure of the system will be significantly enhanced after the introduction of the heat source.

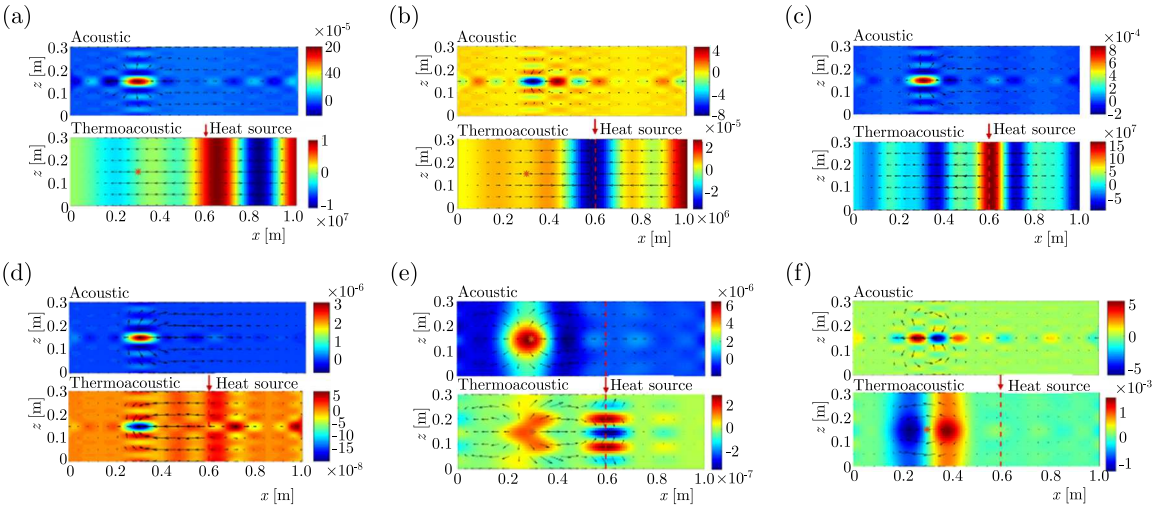

Fig. 7. Distribution of active sound intensity and divergence of the sound field: (a) 176.2 Hz, (b) 337.1 Hz, (c) 511.7 Hz, (d) 591.8 Hz, (e) 762.9 Hz, (f) 850 Hz

Figure 7 shows the active sound intensity and divergence of the system. The vector represents the active sound intensity, the color represents the sound intensity divergence. When the excitation frequency is an unstable mode frequency, as shown in Figs. 7a, 7c, 7d and 7e, there is a region with a divergence value greater than zero, and the energy is significantly increased compared with that in the non-heat source cavity system. By observing the sound intensity vector, we can see that the energy is transferred from the heat source to the whole sound field. It means that the heat source does positive work on the acoustic system, resulting in the system being in an unstable state. When the excitation frequency of the point source is a stable modal

frequency, as shown in Fig. 7b, the divergence near the heat source is negative, and the energy trap is near the heat source. The sound intensity vector shows that energy flows into the heat source position. Due to this phase, the energy generated by the heat source is opposite to the acoustic kinetic energy and potential energy, which reduces the energy of the acoustic system, so the system is in a stable state.

From the above analysis, the stability of the thermoacoustic coupling system depends on whether the heat source transmits energy to the acoustic system in the form of a source. The instability can be modified by adding energy-consuming elements in the thermoacoustic coupling system, blocking the transmission path of the energy source or reducing the energy transmission.

It can be seen from Fig. 7 that for unstable systems, the highest energy point is behind the heat source location rather than the heat source location. Therefore, before introducing the MPP, the energy concentration range of thermoacoustic unstable modes should be determined first. In order to fully cover the energy concentration area in Fig. 7, the MPP position was adjusted from $x_m = 0.7\,\mathrm{m}$ to $x_m = 0.5\,\mathrm{m}$, and the length remained at $l_{my} = 0.3\,\mathrm{m}$. Figure 8 shows the distribution of modal stability within the first 1000 Hz of the thermoacoustic coupling system after only adjusting the MPP position. At this time, the unstable modes are all transformed into stable modes, indicating that the installation of the MPP at this position can effectively control the multimodal instability of the system.

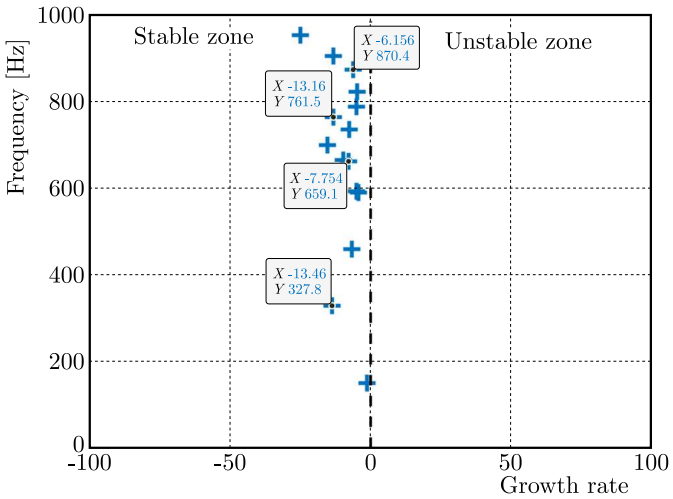

Fig. 8. Distribution of thermoacoustic system modal stability in 1000 Hz with MPP at 0.5 m

Figure 9 shows the passive sound intensity and sound pressure response distribution of the thermoacoustic coupling system under four excitation frequencies marked in Fig. 8. Compared with the amplitude of the sound pressure response at various excitation frequencies in Fig. 4, it can be found that the MPP not only transforms the unstable mode into a stable model, but also reduces the response to the acoustic disturbance. The active sound intensity and dispersion distribution are also shown in Fig. 10. It can be seen that the energy trap appears in the MPP area, the main energy in the system flows locally into the energy trap at the MPP. The MPP impedance blocks the way of the heat source transmitting energy into the system. The above analysis shows that the proper installation position of the MPP can suppress multi-mode instability in the thermoacoustic coupling system.

Finally, the above conclusion is applied to a variable cross-sectional thermoacoustic coupling system to further demonstrate the effectiveness of MPP in suppressing thermoacoustic instability. Cavity 2 in Table 3 is continuously used, where the modal characteristics are shown in Table 4. From Table 4, we can know that three modes are instable in the first six modes. Then active/passive sound intensity, sound pressure and divergence distribution of the thermoacoustic

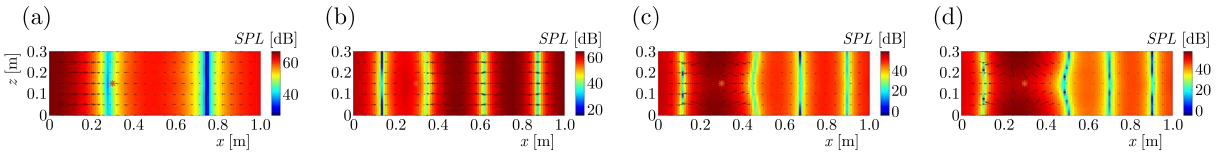

Fig. 9. Distribution of passive sound intensity and sound pressure of the sound field with the MPP at 0.5 m: (a) 327 Hz, (b) 659 Hz, (c) 761 Hz, (d) 870 Hz

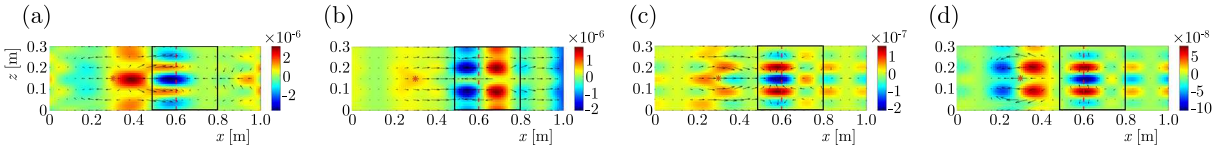

Fig. 10. 10 Active sound intensity and divergence of the sound field with the MPP position at 0.5 m: (a) 327 Hz, (b) 659 Hz, (c) 761 Hz, (d) 870 Hz

system are given in Fig. 11 and 12. From these figures, it can be seen that the distribution of sound intensity, divergence and sound pressure are consistent with the above conclusion, where the passive sound intensity vector is always perpendicular to the isobaric surface of the sound field and parallel to the pressure drop direction, and the heat source does positive work in the unstable thermoacoustic system.

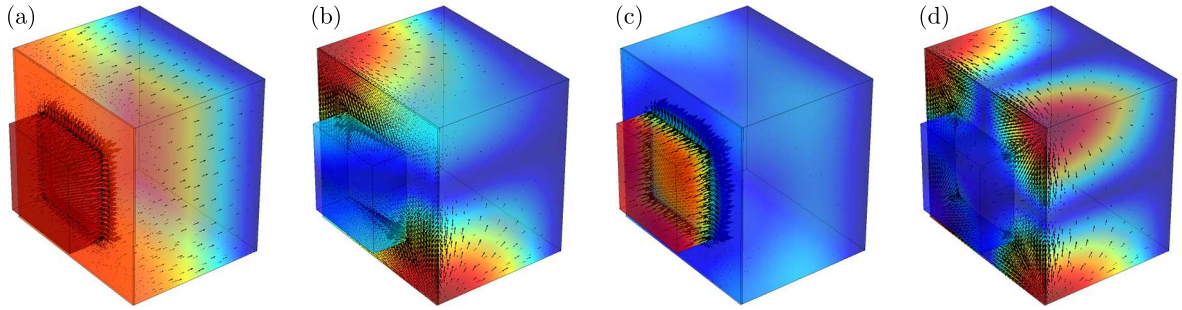

Fig. 11. Passive sound intensity and sound pressure of the variable cross-sectional thermoacoustic system: (a) 98.52 Hz, (b) 205.05 Hz, (d) 252.39 Hz, (e) 264.79 Hz

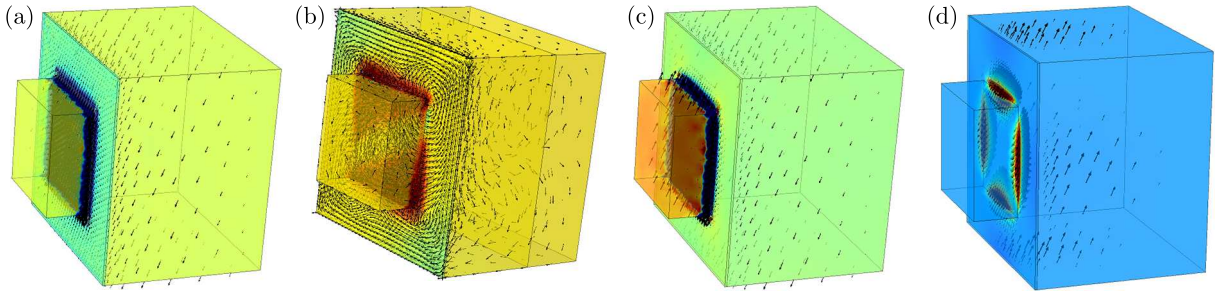

Fig. 12. Active sound intensity and divergence of the variable cross-sectional thermoacoustic system: (a) 98.52 Hz, (b) 205.05 Hz, (d) 252.39 Hz, (e) 264.79 Hz

The MPP is introduced on all six walls at $x_m = 0.2$ m to $x_m = 0.7$ m, which means that the length of the MPP is 0.5 m. Figure 13 shows the distribution of system stability before/after the introduction of MPP. Successfully, the unstable modes are all transformed into stable modes, indicating that the installation of the MPP can effectively control the multimodal instability of the system.

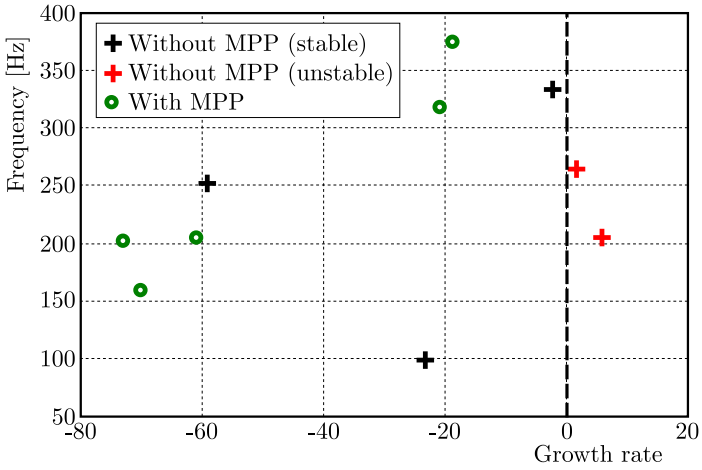

Fig. 13. Modal stability of the variable cross-sectional thermoacoustic system with/without MPP

4. Conclusion

A 3D variable cross-sectional thermoacoustic coupling model with an MPP is established. By a substructure method, the complex cavity is divided into acoustic cavity substructures and auxiliary air plates. The 3D modified Fourier series is used to characterize the sound pressure distribution function in the cavity to meet arbitrary impedance boundary conditions, so that the sound pressure distribution function and its derivatives can be continuously guided in the acoustic field solution domain. The energy formulas of each acoustic cavity substructure and auxiliary air plate are derived, and the modal frequency, growth rate, and corresponding sound pressure, sound intensity and divergence distribution are obtained by using the Lagrange equation and Rayleigh-Ritz method. The main conclusions are as follows:

- The modal characteristics of the thermoacoustic coupling system with the MPP are analyzed. The results show that the MPP can suppress multi-mode instability and improve stability of the thermoacoustic coupling system.
- The dimensionless sound pressure of unstable modes is exponentially amplified with time, and the nondimensional sound pressure of stable modes decay to zero with time. The sound pressure of more stable modes decays faster.
- The distribution of energy transmission path, source and trap is determined based on the sound intensity and divergence. The introduction of a heat source makes the sound pressure response amplitude increase significantly and the variation of divergence distribution more complex. Under the excitation of an unstable mode frequency, the heat source transmits energy to the sound field. Under the excitation of a stable mode frequency, the energy near the heat source is an energy trap, and the energy in the sound field flows into the vicinity of the heat source.
- It is revealed that stability of the thermoacoustic coupling system depends on whether the heat source transmits energy to the acoustic system or not. The instability of the system can be modified by blocking the transmission path or reducing energy transmission. The suppression of multimodal instability of the thermoacoustic coupling system can be achieved and the acoustic disturbance response of the system can be effectively reduced when the MPP is adjusted to the energy concentration area.

Acknowledgments

This work was supported by Marine Power Research and Development (Grant No. DE0305); and the National Natural Science Foundation of China (Grant No. 11972125 and 12102101).

References

1. Armitage C.A., Riley A.J., Cant R.S., *et al.*, 2004, Flame transfer function for swirled LPP combustion from experiments and CFD, *Proceedings of the ASME Turbo Expo 2004: Power for Land, Sea, and Air*, Vol. 1: Turbo Expo, 527-537
2. Chu M., Xu X., 2016, Acoustic numerical simulation of a micro-perforated panel absorber for combustion instability suppression, *Acta Acoustia*, **41**, 2, 236-242
3. Dowling A.P., Mahmoudi Y., 2015, Combustion noise, *Proceedings of the Combustion Institute*, **35**, 1, 65-100
4. Du J.T., Li W.L., Liu Z.G., Xu H.A., Ji Z.L., 2011, Acoustic analysis of a rectangular cavity with general impedance boundary conditions, *Journal of the Acoustical Society of America*, **130**, 2, 807-817
5. Eldredge J.D., Dowling A.P., 2003, The absorption of axial acoustic waves by a perforated liner with bias flow, *Journal of Fluid and Mechanics*, **485**, 307-335
6. Lefebvre A.H., Ballal D.R., 2010, *Gas Turbine Combustion*, CRC Press, 525
7. Leyko M., Nicoud F., Poinsot T., 2012, Comparison of direct and indirect combustion noise mechanisms in a model combustor, *American Institute of Aeronautics and Astronautics Journal*, **47**, 11, 2709-2716
8. Ma D.Y., 1975, Theory and design of micro-perforated panel sound absorption structure, *Scientia Sinica*, **1**, 38-50
9. Schönfeld T., Poinsot T., 1999, Influence of boundary conditions in LES of premixed combustion instabilities, *Center for Turbulence Research Annual Research Briefs*, 73-84
10. Schuller T., Durox D., Candel S., 2003, Self-induced combustion oscillations of laminar premixed flames stabilized on annular burners, *Combustion and Flame*, **135**, 4, 525-537
11. Seo S., 2003, Combustion instability mechanism of a lean premixed gas turbine combustor, *Journal of Mechanical Science and Technology*, **17**, 6, 906-913
12. Sun X.F., 2010, Thermoacoustic oscillating calculation of longitudinal equivalence frequency and stability in aero-engine afterburner, https://api.semanticscholar.org/CorpusID:111882612
13. Zhang X.Q., 2020, *Acoustic Behavior of Micro-Perforated Panels in Grazing Flow*, The Hong Kong Polytechnic University

Manuscript received February 17, 2023; accepted for print June 28, 2023

JOURNAL OF THEORETICAL AND APPLIED MECHANICS
61, 4, pp. 769-781, Warsaw 2023
https://doi.org/10.15632/jtam-pl/171510

DYNAMIC BUCKLING OF THIN-WALLED CYLINDRICAL SHELLS UNDER RADIAL IMPACT PRESSURES RANDOMLY DISTRIBUTED IN THE CIRCUMFERENTIAL DIRECTION

Yanze Li, Jiawei Fu

School of Mechanical Engineering, Nanjing University of Science and Technology, Nanjing, Jiangsu, China
corresponding author J. Fu, e-mail: jwfu@njust.edu.cn

Linfang Qian

School of Mechanical Engineering, Nanjing University of Science and Technology, Nanjing, Jiangsu, China, and Northwest Institute of Mechanical and Electrical Engineering, Xianyang, Shaanxi, China

Shiyu Chen

School of Mechanical Engineering, Nanjing University of Science and Technology, Nanjing, Jiangsu, China

Dynamic buckling of thin-walled cylindrical shells under radial impact pressures randomly distributed in the circumferential direction is investigated by extending widely-used Donnell's shell theory. The buckling model proposed here specifically includes nonlinear terms in the geometrical equation and the curvature change due to significant variation of the shell radius. The finite difference method is adopted to solve the equations, and a parameter is defined to describe the buckling degree of the shell. Numerical results show that nonlinear terms from Green's strain tensors and the change of curvature are important for shell large deformation. Pressure characteristics, materials and thickness of the cylindrical shell affect its buckling behavior remarkably.

Keywords: cylindrical shell, dynamic buckling, randomly radial impact, nonlinear effects

1. Introduction

As a common structure, thin-walled cylindrical shells are extensively used in the field of aerospace, navigation and mining industries (Kumar *et al.*, 2011; Sahu and Datta, 2007; Teng, 1996). In the shell structures, buckling usually becomes a dominated failure pattern rather than damage due to material strength, which is often related to deformation of a structure experiencing a sudden and distinct change when a loading reaches or exceeds a critical value. Buckling analysis of cylindrical shells has been an old but significant topic for a long time and works dealing with this problem are numerous. In static buckling problems, the bearing capacity or critical loading at which the structure buckles is evaluated (Hutchinson, 1965, 2016), however in dynamic buckling problems take the inertia effect as an additive and important factor (Karagiozova and Alves, 2008).

Although dynamic buckling of thin-walled shells under axial loadings has been studied a lot (An *et al.*, 2016; Darabi and Ganesan, 2016; Xu *et al.*, 2006), such a problem of shells under radial pressures received relatively less attention. It should be noted that when thin--walled metallic cylindrical shells are subjected to explosive loadings having significant radial components inward, dynamic buckling becomes an important design consideration. Examples include magnetic confinement devices for producing intense transient magnetic fields (Bykov and Dolotenko, 2015), shape-charge weapons (Saran *et al.*, 2013) or oil well perforators (Farid, 2012) to produce high-velocity metallic jets. Ideally, if the pressure uniformly distributed around the outer surface of a circular cylindrical shell, the shell can move inward without buckling. The

cross section of the shell could remain circular with a decrease of radius over time. However, practically non-axisymmetric motion usually occurs and wrinkles appear on the deformed shells.

The dynamic buckling of thin-walled shells under radial pressures can be caused by defects or disturbances that exist in the manufacturing or application process of the shell (Jones and Okawa, 1976). Geometrically, the initially non-circular shape is frequently regarded as the main factor to make the shell buckle (Ben-Haim, 1993; Elishakoff, 2000; Lindberg, 1992a,b; Wei and Batra, 2006). As to the external loadings, Kumar *et al.* (2015) studied stability of thin-walled cylindrical shells subjected to radial pressures distributed uniformly in the circumferential direction and vibrating over time. In 1987, Lindberg and Florence (1987) systematically studied dynamic pulse buckling behavior of thin-walled cylindrical shells under radial impulses. The impulse effect was equivalently transformed into the initial velocity of the wall with the form of white noise in the circumferential direction. Gu *et al.* (1996) also discussed dynamic plastic buckling of cylindrical shells and rings subjected to initially non-axisymmetric impulsive velocities.

In order to describe deformation behavior of thin-walled cylindrical shells, different models on the premise of various hypotheses have been proposed over the years. Several shell theories, including Donnell's, Novozhilov, Flügge-Luré-Byrne, and Sanders and Koiter have been developed and widely employed (Amabili and Païdoussis, 2003). Amabili (2008) provided a comprehensive overview on these theories. Kumar *et al.* (2015) studied stability of thin-walled cylindrical shells subjected to radial pressures by adopting the Flügge-Luré-Byrne shell theory. But nonlinear terms in the strain-displacement relations were not included in the above works. Xue *et al.* (2013) extended Donnell's shell theory by considering the effect of large deformation on curvature of the shell, and analyzed the large deformation problem of long shells. Lindberg and Florence (1987) developed the equation of motion without any nonlinear terms according to Donnell's theory to study the dynamic pulse buckling of a cylindrical shell under impulsive loadings. Besides, only the raidal displacement was maintained in Lindberg's equations (Lindberg and Florence, 1987). However, linear geometrical equations are limited to infinitesimal deformations, and nonlinear effects due to large derformations are definitely necessary to describe buckling behavior accurately. Another nonlinearity originating from material properties of non-homogeneous materials, such as laminated composite materials and functionally graded materials (Kundalwal and Shingare, 2020; Suresh Kumar *et al.*, 2017), is temporarily out of concern in the current work.

A new buckling model taking nonlinear terms in the geometrical equation and curvature change due to large deformation into account is proposed to investigate the dynamic buckling of a thin-walled cylindrical shell under radial impact pressures randomly distributed in the circumferential direction. The nonlinear partial differential equation (PDE) is solved by the finite difference method (FDM). Subsequently, the effects of pressure characteristics, shell material and thickness on the buckling behavior are discussed.

2. Basic equations

As illustrated in Fig. 1, a thin-walled cylindrical shell with radius R and thickness h is considered. The middle surface where the origin of the coordinate system is located divides the thickness of the shell equally. u_1, u_2 and u_3 are displacements of a generic point of the shell with coordinates (x, θ, z) along the axial, circumferential and radial directions, respectively. The displacements of a point in the middle surface along corresponding directions are denoted by u, v and w. In this paper, the outer surface of the shell is subjected to an impact pressure that is randomly distributed along the circumferential direction. The dynamic buckling is investigated by considering non-linear effects of large deformation within Donnell's theory.

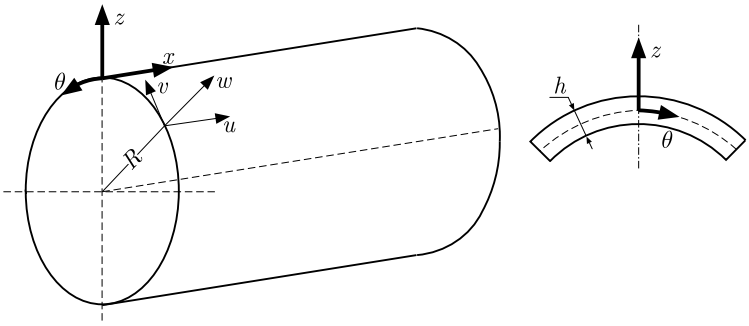

Fig. 1. A thin-walled cylindrical shell

The following assumptions are adopted to study the buckling:

(H1) The shell is thin, namely, $h/R \leqslant 1/10$ (Lindberg and Florence, 1987).

(H2) The Kirchhoff-Love shell assumption holds, that is stresses in the direction normal to the shell middle surface are negligible, and strains vary linearly along the thickness.

(H3) The cylindrical shell is infinitely long. Therefore, all the quantities along the axial direction as well as the axial displacement can be regarded as constant.

Based on assumption (H2), the displacements of a generic point in the shell can be expressed in terms of the displacements of a point in the mid-surface which shares the same radial line with the generic point, as

$$u_1 = u(x,\theta) - z\Theta_1 \qquad u_2 = v(x,\theta) - z\Theta_2 \qquad u_3 = w(x,\theta) \tag{2.1}$$

where the quantities Θ_1 and Θ_2 involve the mid-surface displacements and their derivatives, and different shell theories may propose different expressions for them.

For large deformation problems, the geometrical equations in terms of nonlinear Green's strain tensor should be used instead of Cauchy's strain tensor. In cylindrical coordinates, Green's strain components, ε_{xx}, $\varepsilon_{\theta\theta}$ and $\gamma_{x\theta}$ are

$$\begin{aligned}
\varepsilon_{xx} &= \frac{\partial u_1}{\partial x} + \frac{1}{2}\Big[\Big(\frac{\partial u_1}{\partial x}\Big)^2 + \Big(\frac{\partial u_2}{\partial x}\Big)^2 + \Big(\frac{\partial u_3}{\partial x}\Big)^2\Big] \\
\varepsilon_{\theta\theta} &= \frac{1}{\rho_r}\Big(\frac{\partial u_2}{\partial \theta} + u_3\Big) + \frac{1}{2\rho_r^2}\Big[\Big(\frac{\partial u_1}{\partial \theta}\Big)^2 + \Big(\frac{\partial u_3}{\partial \theta} - u_2\Big)^2 + \Big(\frac{\partial u_2}{\partial \theta} + u_3\Big)^2\Big] \\
\gamma_{x\theta} &= \Big(\frac{\partial u_1}{\rho_r \partial \theta} + \frac{\partial u_2}{\partial x}\Big) + \frac{1}{\rho_r}\Big[\Big(\frac{\partial u_1}{\partial x}\frac{\partial u_1}{\partial \theta}\Big) + \frac{\partial u_2}{\partial x}\Big(\frac{\partial u_2}{\partial \theta} + u_3\Big) + \frac{\partial u_3}{\partial x}\Big(\frac{\partial u_3}{\partial \theta} - u_2\Big)\Big]
\end{aligned} \tag{2.2}$$

where $\rho_r = R + z$. Substituting Eqs. (2.2) into Eqs. (2.1), the strain components are rewritten and abbreviated as

$$\varepsilon_{xx} = \varepsilon_{x,0} + zk_x \qquad \varepsilon_{\theta\theta} = \varepsilon_{\theta,0} + zk_\theta \qquad \gamma_{x\theta} = \gamma_{x\theta,0} + zk_{x\theta} \tag{2.3}$$

where $\varepsilon_{x,0}$, $\varepsilon_{\theta,0}$ and $\gamma_{x\theta,0}$ are corresponding strain components of the middle surface, while k_x, k_θ and $k_{x\theta}$ are changes of curvature and torsion of the middle surface. The shell theories distinguish from each other by the expression Θ_1 and Θ_2 in Eqs. (2.1) based on different deformation assumptions. In Donnell's shell theory, $\Theta_1 = \partial w/\partial x$, $\Theta_2 = \partial w/R\partial\theta$, and the variations of the middle surface in Eqs. (2.3) are

$$\begin{aligned}
\varepsilon_{x,0} &= \frac{\partial u}{\partial x} + \frac{1}{2}\Big(\frac{\partial w}{\partial x}\Big)^2 \qquad \varepsilon_{\theta,0} = \frac{\partial v}{R\partial\theta} + \frac{w}{R} + \frac{1}{2}\Big(\frac{\partial w}{R\partial\theta}\Big)^2 \\
\gamma_{x\theta,0} &= \frac{\partial u}{R\partial\theta} + \frac{\partial v}{\partial x} + \frac{\partial w}{\partial x}\frac{\partial w}{R\partial\theta}
\end{aligned} \tag{2.4}$$

and

$$k_x = -\frac{\partial^2 w}{\partial x^2} \qquad k_\theta = -\frac{\partial^2 w}{R^2 \partial \theta^2} \qquad k_{x\theta} = -2\frac{\partial^2 w}{R\partial x \partial \theta} \tag{2.5}$$

In the cylindrical coordinate system, the equations of motion with respect to the original configuration are (Kumar *et al.*, 2015)

$$\begin{aligned}
&\frac{\partial T_{xx}}{\partial x} + \frac{\partial T_{\theta x}}{\rho_r \partial \theta} + \frac{\partial T_{zx}}{\partial z} + \frac{T_{zx}}{\rho_r} + X = 0 \\
&\frac{\partial T_{x\theta}}{\partial x} + \frac{\partial T_{\theta\theta}}{\rho_r \partial \theta} + \frac{\partial T_{z\theta}}{\partial z} + \frac{T_{z\theta} + T_{\theta z}}{\rho_r} + Y = 0 \\
&\frac{\partial T_{xz}}{\partial x} + \frac{\partial T_{\theta z}}{\rho_r \partial \theta} + \frac{\partial T_{zz}}{\partial z} + \frac{T_{zz} - T_{\theta\theta}}{\rho_r} + Z = 0
\end{aligned} \tag{2.6}$$

where X, Y and Z are the sum of the body force and inertia force along x, θ, z directions, respectively. T_{ij} $(i, j = x, \theta, z)$ are the components of the first Piola-Kirchhoff (1st P-K) stress tensor, which can be expressed in terms of the symmetric second Piola-Kirchhoff (2nd P-K) stresses σ_{ij} by the relation

$$T_{ij} = \sum_{k=1}^{3} \sigma_{ik} \frac{\partial a_j}{\partial x_k} \tag{2.7}$$

where $x_1 = x$, $x_2 = R\theta$ and $x_3 = z$. $a_i = x_i + u_i$, $(i = 1, 2, 3)$ is the coordinate of a generic point inside the deformed shell. Here, $(i = 1, 2, 3)$ corresponds to the direction (x, θ, z), respectively. With the help of Eq. (2.7), the equations of motion can be expressed in terms of the 2nd P-K stress. Then, integrating the new equations of motion through thickness of the shell leads to the force equilibrium equations as

$$\begin{aligned}
&\frac{\partial N_x}{\partial x} + \frac{\partial N_{x\theta}}{R\partial \theta} - ch\frac{\partial u(x,\theta,t)}{\partial t} - \rho h \frac{\partial^2 u(x,\theta,t)}{\partial t^2} = 0 \\
&\frac{\partial N_\theta}{R\partial \theta} + \frac{\partial N_{x\theta}}{\partial x} + \frac{Q_\theta}{R} - ch\frac{\partial v(x,\theta,t)}{\partial t} - \rho h \frac{\partial^2 v(x,\theta,t)}{\partial t^2} = 0 \\
&\frac{\partial Q_x}{\partial x} + \frac{\partial Q_\theta}{R\partial \theta} + N_x \frac{\partial^2 w(x,\theta,t)}{\partial x^2} + N_{x\theta} \frac{\partial^2 w(x,\theta,t)}{R\partial x \partial \theta} + N_{\theta x} \frac{\partial^2 w(x,\theta,t)}{R\partial x \partial \theta} \\
&\quad + N_\theta \frac{\partial^2 w(x,\theta,t)}{R^2 \partial \theta^2} - \frac{N_\theta}{R} + \Big(\frac{\partial N_x}{\partial x} + \frac{\partial N_{\theta x}}{R\partial \theta}\Big)\frac{\partial w(x,\theta,t)}{\partial x} \\
&\quad + \Big(\frac{\partial N_{x\theta}}{\partial x} + \frac{\partial N_\theta}{R\partial \theta}\Big)\frac{\partial w(x,\theta,t)}{R\partial \theta} - ch\frac{\partial w(x,\theta,t)}{\partial t} - \rho h \frac{\partial^2 w(x,\theta,t)}{\partial t^2} + P = 0
\end{aligned} \tag{2.8}$$

Multiplying the first two equations of motion by z and integrating them through thickness, the moment equilibrium equations are obtained

$$\frac{\partial M_x}{\partial x} + \frac{\partial M_{\theta x}}{R\partial \theta} - Q_x = 0 \qquad \frac{\partial M_{x\theta}}{\partial x} + \frac{\partial M_\theta}{R\partial \theta} - Q_\theta = 0 \tag{2.9}$$

where

$$N_x = \int_{-h/2}^{h/2} \sigma_{xx}\Big(1 + \frac{z}{R}\Big)\, dz \qquad N_\theta = \int_{-h/2}^{h/2} \sigma_{\theta\theta}\, dz$$

$$
\begin{aligned}
N_{x\theta} &= \int_{-h/2}^{h/2} \sigma_{x\theta}\Big(1+\frac{z}{R}\Big)\,dz \qquad & N_{\theta x} &= \int_{-h/2}^{h/2} \sigma_{\theta x}\,dz \\
Q_x &= \int_{-h/2}^{h/2} \sigma_{xz}\Big(1+\frac{z}{R}\Big)\,dz \qquad & Q_\theta &= \int_{-h/2}^{h/2} \sigma_{\theta z}\,dz \\
M_x &= \int_{-h/2}^{h/2} \sigma_{xx}\Big(1+\frac{z}{R}\Big)z\,dz \qquad & M_\theta &= \int_{-h/2}^{h/2} \sigma_{\theta\theta} z\,dz \\
M_{x\theta} &= \int_{-h/2}^{h/2} \sigma_{x\theta}\Big(1+\frac{z}{R}\Big)z\,dz \qquad & M_{\theta x} &= \int_{-h/2}^{h/2} \sigma_{\theta x} z\,dz
\end{aligned}
\tag{2.10}
$$

where ρ is the material density, and c is the equivalently viscous damping coefficient of the material. P can be regarded as the external loading along the radial direction. External loadings in other directions are not considered.

In addition, the constitutive relation for linearly elastic plane stress problems is

$$
\sigma_{xx} = \frac{E}{1-\mu^2}(\varepsilon_{xx}+\mu\varepsilon_{\theta\theta}) \qquad \sigma_{\theta\theta} = \frac{E}{1-\mu^2}(\varepsilon_{\theta\theta}+\mu\varepsilon_{xx}) \qquad \sigma_{x\theta} = \frac{E}{2(1+\mu)}\gamma_{x\theta} \tag{2.11}
$$

where E is Young's modulus of the material, and μ is Poisson's ratio.

3. Governing equations for infinitely long cylindrical shells

For infinitely long shells, changes of the quantities along the axial direction as well as the axial displacement are regarded as zero. Additionally, viscous damping of the material is ignored. Therefore, Eqs. $(2.8)_1$ and $(2.9)_1$ are naturally satisfied based on these two assumptions, whereas Eqs. $(2.8)_2$ and $(2.8)_3$ are reduced to

$$
\begin{aligned}
&\frac{\partial N_\theta}{R\partial\theta} + \frac{1}{R}\frac{\partial M_\theta}{R\partial\theta} - \rho h\frac{\partial^2 v(x,\theta,t)}{\partial t^2} = 0 \\
&\frac{\partial^2 M_\theta}{R^2\partial\theta^2} - N_\theta\Big(\frac{1}{R}+k_\theta\Big) + \frac{\partial N_\theta}{R\partial\theta}\frac{\partial w(x,\theta,t)}{R\partial\theta} - \rho h\frac{\partial^2 w(x,\theta,t)}{\partial t^2} + P = 0
\end{aligned}
\tag{3.1}
$$

Substituting Eqs. (2.3) and (2.11) into Eq. (2.10) gives the expressions of N_θ and M_θ as

$$
N_\theta = \frac{Eh}{1-\mu^2}\varepsilon_{\theta,0} \qquad M_\theta = \frac{Eh^3}{12(1-\mu^2)}k_\theta \tag{3.2}
$$

The middle surface strain $\varepsilon_{\theta,0}$ and curvature change k_θ based on Donnell's theory are given in Eqs. (2.4) and (2.5).

However, it is known that Donnell's shell theory breaks down for non-shallow, long cylindrical shells experiencing large deformations, which is revealed in the expression of curvature change (Xue *et al.*, 2013). According to Donnell's theory, though some predominant nonlinear terms are retained, the curvature changes are expressed by linear functions of w. For radial displacements exceeding thickness of the shell, the change of curvature due to radius reduction can be obvious and should be comprised of two parts. Firstly, the change of curvature could be caused by shell radius variation, and can be rewritten as

$$
k'_\theta = \frac{1}{R+w} - \frac{1}{R} = -\frac{w}{R(R+w)} \tag{3.3}
$$

Secondly, bending deformation of the shell wall also contributes to the change pf curvature. Considering curvatures of the middle surface resulted from bending in the deformed and undeformed configurations, and rewriting the expressions of the curvature in terms of the radial displacement and its derivatives, leads to the change of curvature as

$$k_\theta'' = \frac{-\partial^2 w}{R^2\partial\theta^2}\Big[1+\Big(\frac{\partial w}{R\partial\theta}\Big)^2\Big]^{-3/2} \tag{3.4}$$

Therefore, for the buckling problem in this paper, the change of curvature k_θ defined in Eq. (2.5) can be replaced by

$$\widetilde{k}_\theta = k_\theta' + k_\theta'' = -\frac{w}{R(R+w)} - \frac{\partial^2 w}{R^2\partial\theta^2}\Big[1+\Big(\frac{\partial w}{R\partial\theta}\Big)^2\Big]^{-3/2} \tag{3.5}$$

By substituting the change of curvature in Eq. (3.5) and the middle surface strain $\varepsilon_{\theta,0}$ in Eq. (2.4) into Eqs. (3.1) and (3.2), the governing equations can be obtained in terms of middle surface displacements. The ultimate expressions are omitted here for conciseness. These equations can degenerate into those used in (Lindberg and Florence, 1987) by omitting the term $(\partial w/R\partial\theta)^2$. And the reduced equation of motion in the circumferential direction is

$$\frac{\partial^2 M_\theta}{R^2\partial\theta^2} - N_\theta\Big(\frac{1}{R}+k_{\theta L}\Big) - \rho h\frac{\partial^2 w(x,\theta,t)}{\partial t^2} + P = 0 \tag{3.6}$$

where N_θ and M_θ are defined in Eqs. (3.2). $\varepsilon_{\theta,0}$ in Eq. $(3.2)_1$ is rewritten as w/R and k_θ in Eq. $(3.1)_2$ is replaced by $k_{\theta L} = w/R^2 - \partial^2 w/R^2\partial\theta^2$.

Moreover, in order to quantitatively describe the buckling degree of cylindrical shells at a certain time during the buckling procedure, a new parameter is defined as

$$c_0 = \frac{1}{\pi r_0^2}\int_0^{2\pi} |r_0^2 - r_1^2|\, d\theta \tag{3.7}$$

which means the ratio of area surrounded by the buckled shell shape and the corresponding deformed circular line without buckling to the circular area. r_1 in Eq. (3.7) denotes radius of the buckled cylindrical shell, r_0 is the corresponding radius without the occurrence of buckling.

4. Solution procedure and validation

4.1. Solution procedure

The finite difference method (FDM) is employed to solve the partial differential equations. The scheme of central difference is applied to deal with the derivatives of displacements with respect to coordinates as

$$\begin{aligned}
&\Big(\frac{\partial f}{\partial\theta}\Big)_m = \frac{f_{m+1}-f_{m-1}}{2\Delta\theta} \qquad \Big(\frac{\partial^2 f}{\partial\theta^2}\Big)_m = \frac{f_{m+1}-2f_m+f_{m-1}}{(\Delta\theta)^2}\\
&\Big(\frac{\partial^3 f}{\partial\theta^3}\Big)_m = \frac{(f_{m+2}-f_{m-2})-2(f_{m+1}-f_{m-1})}{2(\Delta\theta)^3}\\
&\Big(\frac{\partial^4 f}{\partial\theta^4}\Big)_m = \frac{(f_{m+2}-f_{m-2})-4(f_{m+1}+f_{m-1})+6f_m}{(\Delta\theta)^4}
\end{aligned} \tag{4.1}$$

where f refers to displacement variations, $\Delta\theta$ is the grid size, and m is the number of an element. As for the partial derivative with respect to time, the following forward difference method is used

$$\Big(\frac{\partial^2 f}{\partial t^2}\Big)^n = \frac{1}{\Delta t}\Big[\Big(\frac{\partial f}{\partial t}\Big)^{n+1} - \Big(\frac{\partial f}{\partial t}\Big)^n\Big] \tag{4.2}$$

where Δt is the time step, and n is the step number. The displacement can be obtained by integrating Eq. (4.2) as

$$f^{n+1} = f^n + \Delta t\Big(\frac{\partial f}{\partial t}\Big)^{n+1} \tag{4.3}$$

Besides, the condition of periodicity of the cylindrical shell needs to be considered, namely

$$f(\theta) = f(\theta + 2\pi) \tag{4.4}$$

4.2. Validation

In order to validate the presented shell-buckling model, a cylindrical shell with $R = 48.5\,\text{mm}$ and $h = 1.5\,\text{mm}$ is taken as an example. The shell is subjected to a particularly non-uniform impact pressure on the opposite side to the shell outer surface. This pressure easily causes a relatively large radial displacement and strain and makes the effects of the added nonlinear terms in the presented model significant. The initial displacement and velocity of the shell are zero. The shell is made of steel. Without loss of generality, the shell is assumed to deform elastically. The impact pressure profile is illustrated in Fig. 2, and can be mathematically expressed as

$$P(\theta, t) = \begin{cases} P_0 \mathrm{e}^{-7t/t_0} \sin(4\theta) & \theta \in \left[0, \frac{\pi}{4}\right] \wedge \left[\pi, \frac{5\pi}{4}\right] \\ 0 & \text{otherwise} \end{cases} \tag{4.5}$$

in which P_0 is the loading magnitude and t_0 represents the total calculation time. The range $[0, \pi/4] \wedge [\pi, 5\pi/4]$ can be regarded as the loaded region of the shell. $P_0 = 400\,\text{MPa}$ and $t_0 = 100\,\mu\text{s}$ are adopted in this paper for numerical calculations.

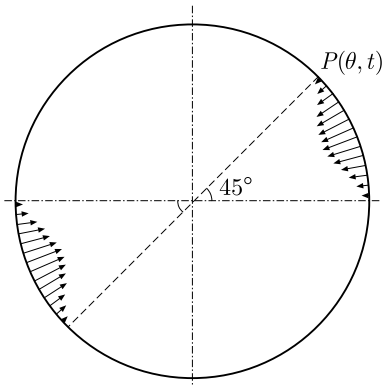

Fig. 2. Pressure profile applied on the cylindrical shell

To show the accuracy and efficiency of the presented model, the radial displacements distributed along the circumferential direction at the instant of $t = 100\,\mu\text{s}$ are displayed in Fig. 3. It should be mentioned that the results from the FE model without particular assumptions on the deformation mechanism are thought to be more accurate, whereas the assumptions are made in both analytical models. The red curve is calculated by a commercial FEM software in a three-dimensional configuration. The FEM model is processed by Abaqus/Explicit with 4-node doubly curved general-purpose shell elements. 72000 elements are used in total. This model adopts assumption (H2) in this work, but the effect of large deformation to the equilibrium position of the structure is considered in the FEM model. The other two curves are calculated by the model presented in this paper and the model by Lindberg and Florence (1987), respectively. It is clear that the results of the presented model agrees well with those of FEM, while the model by Lindberg and Florence (1987), shown by the blue dash line, deviates from FEM apparently.

Both the FEM and current models give an inward movement of middle points in the loaded regions, while the movement of the middle points predicted by Lindberg and Florence (1987) is outward. Thus, the presented model is more credible than that by Lindberg and Florence (1987). Therefore, the presented model is able to deal with transient impact problems of thin-walled cylindrical shells undergoing large displacements.

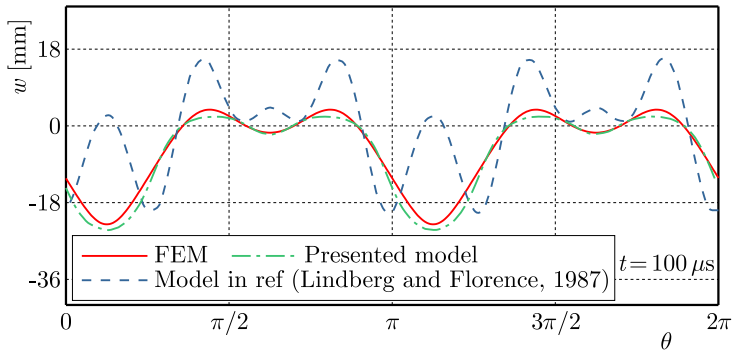

Fig. 3. Radial displacements at 100 μs of different models

5. Shell buckling under randomly radial impact pressures

In this Section, the dynamic buckling behavior of the thin-walled cylindrical shell under radial impact pressures randomly distributed in the circumferential direction is investigated. Explosive devices, like shaped-charge weapons and oil well perforators, are usually subjected to impact pressures that have significantly radial components over 100 MPa, and metal shells always deform plastically. Thus, a constitutive equation of plasticity should be used instead of the elastic model in Eqs. (2.11). The widely used Johnson-Cook constitutive model without the temperature effect is chosen in the following analysis and expressed as

$$\sigma = (A + B\varepsilon^n)\Big(1 + C\ln\frac{\dot{\varepsilon}}{\dot{\varepsilon}_0}\Big) \tag{5.1}$$

where the reference strain rate $\dot{\varepsilon}_0$ is taken as $1.0\,\mathrm{s}^{-1}$. A, B, n and C are coefficients depending on the material. For simplicity, the tangent modulus, defined as $E_t = d\sigma/d\varepsilon$, is adopted to replace Young's modulus in Eqs. (2.11) and updated in every numerical time step to simulate the plastic behavior using the constitutive equation.

Naturally, uniform impact pressures are prone to be influenced by randomly environmental factors leading to nonuniformity of the pressures. Suppose that the impact pressure distributes in the form of white noise as

$$P(\theta, t) = P'(t)\Big[1 + \sum_{n=1}^{N} \gamma_n \cos(n\theta + \varphi_n)\Big] \tag{5.2}$$

in which N is the term number of the Fourier series. The parameters γ_n and φ_n denote the disturbance magnitude and random phase angle, respectively. Subsequently, the effect of random characteristic, material property and structural size on the dynamic buckling behavior of the shell are investigated. The shell examples taken in the following analysis are listed in Table 1.

5.1. Effect of random characteristics of pressure

Three groups of pressure parameters are chosen to study the effect of random characteristics on the buckling behavior of the shell. Figure 4 shows radial pressure distributions at the initial

Table 1. Shell cases with different materials and sizes (Zhang *et al.*, 2015)

Case No.	1	2	3	4	5
Material	4043 Steel	7075-T6 Al	7075-T6 Al	7075-T6 Al	OFHC COPPER
ρ [kg/m^3]	7830	2700	2700	2700	8960
E [GPa]	200	86	86	86	124
μ	0.29	0.3	0.3	0.3	0.34
R [mm]	40	40	40	40	40
h [mm]	1.5	1.5	2	2.5	1.5
A [MPa]	792	473	473	473	90
B [MPa]	510	210	210	210	292
n	0.26	0.38	0.38	0.38	0.31
C	0.014	0.033	0.033	0.033	0.025

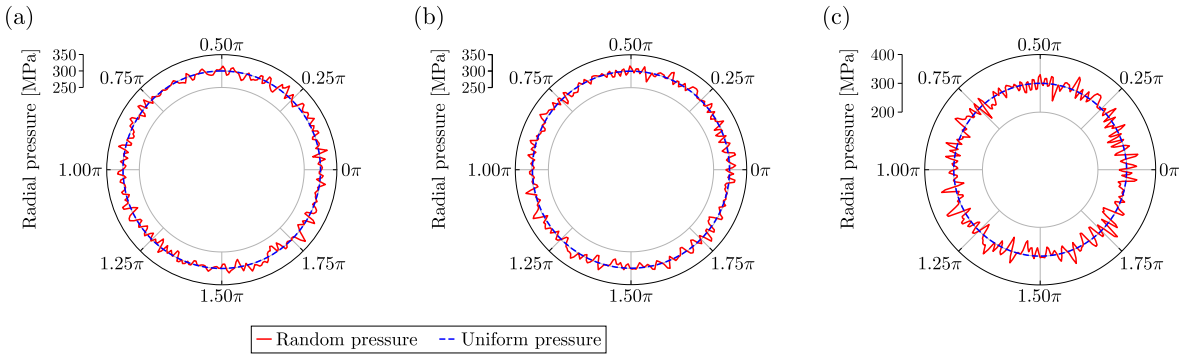

Fig. 4. Initial pressure distributions: (a) $\gamma_n = 0.005$, random phase I; (b) $\gamma_n = 0.005$, random phase II; (c) $\gamma_n = 0.01$, random phase II

time of three cases, in which $P'(t) = 300\,\text{MPa}$ and $N = 100$. The solid red line and dash blue line represent the pressure with white noise along the circumferential direction and the uniform pressure, respectively.

The parameters γ_n and φ_n vary from one case to another. The pressures in Figs. 4a and 4b have the equal perturbation amplitude ($\gamma_n = 0.005$) but different phase angles. The perturbation amplitude of the pressure in Fig. 4c is twice of that in Fig. 4b ($\gamma_n = 0.01$), but sharing the equal phase angles. The pressures in Figs. 4a, 4b and 4c are simply called pressure (a), pressure (b) and pressure (c), hereafter.

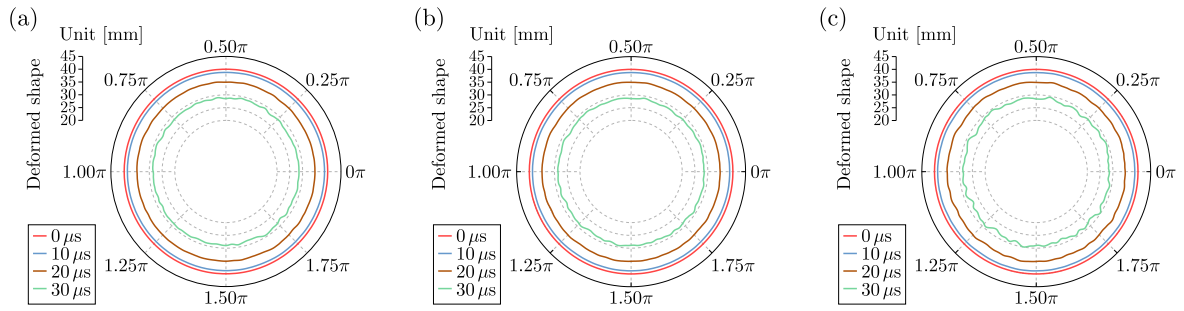

Fig. 5. Deformation evolution under: (a) pressure (a), (b) pressure (b), (c) pressure (c)

Under pressures shown in Fig. 4, deformation evolutions of cylindrical shell No. 1 in Table 1 are exhibited in Fig. 5. Taking Fig. 5a for instance, the wrinkled circles from the outside to inside represent the deformed shape of the cylindrical shell at different times. It is clear that the buckling degree is gradually magnified in a certain deformation profile with an increase of time,

which is visualized in Figs. 5b and 5c as well. In addition, the mean deformation values over the circumferential direction at an instant of 30 μs are almost the same for the three figures. The shell under pressures (a) and (b) shows the similar buckling degree, while the buckling in Fig. 5c is much severer than the former two. It is worth mentioning that a continuous circle deformation without buckling can be depicted for a uniform pressure $P = P'(t)$, which is omitted here for conciseness.

In order to show the buckling degree of the cylindrical shell under different pressures more clearly, Fig. 6 draws the evolution of c_0 defined in Eq. (3.7). It is clear that c_0 increases almost monotonously for the three non-uniform pressures, which means that the buckling degree is becoming stronger as the shell collapses. The values of c_0 for pressures (a) and (b) show almost no discrepancy, while c_0 for pressure (c) is much higher. This is consistent with the pressure characteristics, and the effectiveness of c_0 to describe the buckling degree quantitatively is justified. Furthermore, Fig. 6 tells us that the threshold value of c_0 can be used as the tolerance limit of shell buckling under non-uniform pressures.

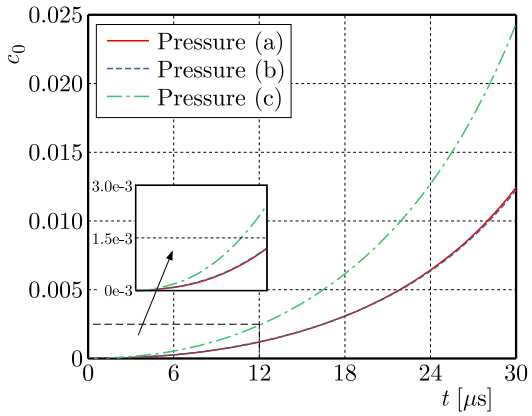

Fig. 6. c_0 versus time for different pressures

The crest number of the deformed cylindrical shell is sometimes concerned in the engineering. According to Fig. 5, the crest number calculated for the three pressures is around 26. And further analyses indicate that this number is dependent on the material property and the value of N in Eq. (5.2).

In summary, the magnitude of uniform pressure P' can remarkably influence the mean deformation value of the cylindrical shell, and the disturbance magnitude γ_n is responsible for the buckling degree. The random phase angle φ_n affects the distribution of pressure, thus it is responsible for the exact deformation contour of the cylindrical shell. The loading itself as well as perturbation do not always change for a particular engineering application. Hence, designing a suitable structure and choosing a proper material are the conventional measures to avoid buckling. This will be discussed in detail in the following sections.

5.2. Effect of material

In order to study the effect of materials on the dynamic buckling behavior, No. 1, 2 and 5 shells in Table 1 made of steel, aluminum and copper with the same size are taken into consideration. The loading parameters are set to be $P'(t) = 300$ MPa, $N = 100$, and $\gamma_n = 0.005$. The random phase angles are the same as those in Fig. 4b.

Figure 7a illustrates the radius of the cylindrical shell at $t = 20\,\mu$s, and Fig. 7b shows the evolution of c_0 over time. Under the same pressure condition, the radial displacement as well as the radius perturbation magnitude of the aluminum shell is larger than those of steel and copper shells. Among the three materials, the aluminum shell experiences the most violent

buckling deformation, which is revealed by the value of c_0 in Fig. 7b. At the time $t = 20\,\mu$s, c_0 of the aluminum shell is almost 10 times of that of steel and copper shells. The mean radius of the steel shell (35.0 mm) and copper shell (35.6 mm) are close to each other at $t = 20\,\mu$s. Besides, the buckling degrees of steel and copper shells show little difference. Such buckling of the aluminum shell in this case is sometimes catastrophic and cannot be accepted. Then, when the aluminum shell is used in such a situation, optimization of the size of the cylindrical shell might be needed.

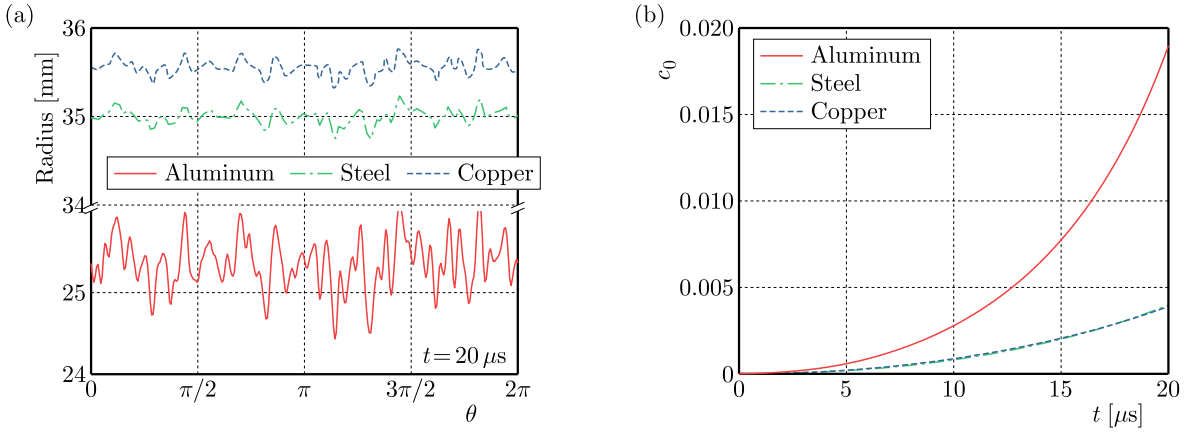

Fig. 7. (a) Radius of shells with different materials ($t = 20\,\mu$s), (b) c_0 versus time for different shell materials

5.3. Effect of shell thickness

In this Section, the effects of the shell thickness h on the buckling of cylindrical shells are investigated. The pressure is retained the same as that in Section 5.2. Shells No. 2-4 in Table 1 are taken for calculation in this Section.

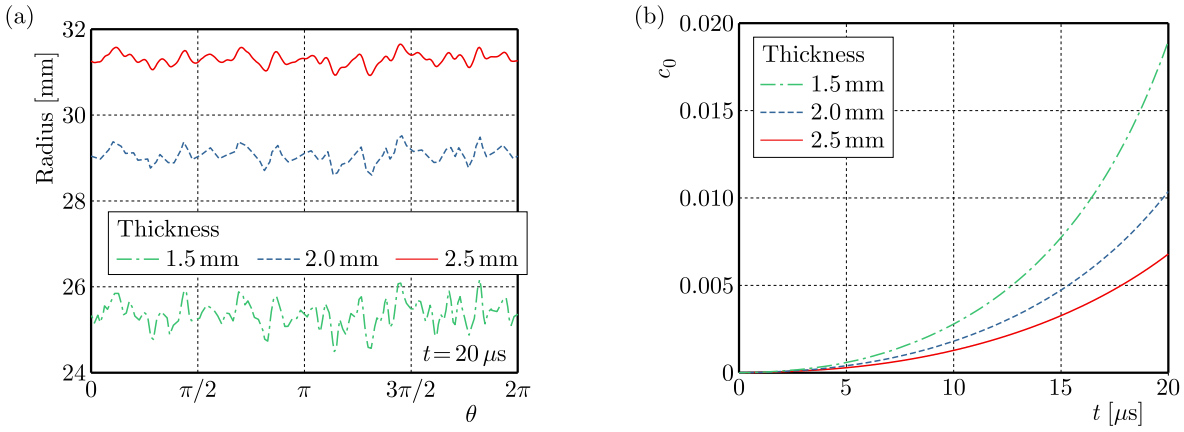

Fig. 8. (a) Radius of shells with different thickness, (b) c_0 versus time for shells with different thickness

Figure 8a shows results for the radius of aluminum shells with different h. At the instant of $t = 20\,\mu$s, the mean radial displacement increases with the reduction of h, leading to an decrease in the radius. Meanwhile, the perturbation magnitude is relatively larger for a thinner cylindrical shell. The buckling degree parameter c_0, as expected, increases during the deformation process regardless of the wall thickness, as revealed in Fig. 8b. And the value of c_0 is higher when the shell is thinner. The crest numbers of the three shells are 31, 23 and 18 for the wall thickness of 1.5 mm, 2 mm and 2.5 mm, respectively. The effect of thickness on the crest number has also been confirmed by Lindberg and Florence (1987).

6. Conclusion

By considering the nonlinear terms in the geometrical equation of the cylindrical shell and maintaining the curvature variation due to a significant change of the shell radius, a buckling model is proposed to study large deformation behavior of the shell under radial impact pressures randomly distributing in the circumferential direction. Green's strain tensor and the 1st P-K stress tensor are employed to describe the large deformation, and a new parameter is introduced to quantitatively judge the buckling degree of the shell. The following conclusions can be drawn from the numerical analyses:

- The bucking model proposed in this paper can accurately describe the large deformation behavior of the shell under non-uniform pressures.
- The buckling shape of the shell after deformation is contributed by the magnitude of the uniform pressure, the magnitude of disturbance and the angle phase of random disturbance. A more uniform pressure distribution produces a more circular shape after deformation.
- The buckling behavior of the shell is dependent on the material properties remarkably. Aluminum shells buckle more easily compared with steel and copper ones under the same pressure condition.
- The buckling degree can be effectively described by the defined parameter c_0 which increases with reduction of the shell wall thickness.

Acknowledgements

This work was partially supported by the National Natural Science Foundation of China (Grant Nos. U2141246 and 11702137).

References

1. Amabili M., 2008, *Nonlinear Vibrations and Stability of Shells and Plates*, Cambridge University Press, New York
2. Amabili M., Païdoussis M.P., 2003, Review of studies on geometrically nonlinear vibrations and dynamics of circular cylindrical shells and panels, with and without fluid-structure interaction, *Applied Mechanics Reviews*, **56**, 349-381
3. An H., Zhou L., Wei X., An W., 2016, Nonlinear analysis of dynamic stability for the thin cylindrical shells of supercavitating vehicles, *Advances in Mechanical Engineering*, **9**, 1-15
4. Ben-Haim Y., 1993, Convex models of uncertainty in radial pulse buckling of shells, *Transactions of the ASME. Journal of Applied Mechanics*, **60**, 683-688
5. Bykov A.I., Dolotenko M.I., 2015, An MC-1 cascade magnetocumulative generator of multi-megagauss magnetic fields – ideas and their realization, *Instruments and Experimental Techniques*, **58**, 531-538
6. Darabi M., Ganesan R., 2016, Non-linear dynamic instability analysis of laminated composite cylindrical shells subjected to periodic axial loads, *Composite Structures*, **147**, 168-184
7. Elishakoff I., 2000, Uncertain buckling: Its past, present and future, *International Journal of Solids and Structures*, **37**, 6869-6889
8. Farid J., 2012, *Importance of Perforation Process and its Techniques*, Dalhousie University, Nova Scotia
9. Gu W., Tang W., Liu T., 1996, Dynamic pulse buckling of cylindrical shells subjected to external impulsive loading, *Journal of Pressure Vessel Technology*, **118**, 33-37
10. Hutchinson J., 1965, Axial buckling of pressurized imperfect cylindrical shells, *AIAA Journal*, **3**, 1461-1466

11. Hutchinson J.W., 2016, Buckling of spherical shells revisited, *Proceedings of the Royal Society A-Mathematical Physical and Engineering Sciences*, **472**

12. Jones N., Okawa D.M., 1976, Dynamic plastic buckling of rings and cylindrical shells, *Nuclear Engineering and Design*, **37**, 125-147

13. Karagiozova D., Alves M., 2008, Dynamic elastic-plastic buckling of structural elements: A review, *Applied Mechanics Reviews*, **61**, 040803

14. Kumar A., Das S., Wahi P., 2011, Dynamic buckling of thin-walled cylindrical shells subjected to fluctuating radial loads, *21st International Conference on Structural Mechanics in Reactor Technology*

15. Kumar A., Lal Das S., Wahi P., 2015, Instabilities of thin circular cylindrical shells under radial loading, *International Journal of Mechanical Sciences*, **104**, 174-189

16. Kundalwal S.I., Shingare K.B., 2020, Electromechanical response of thin shell laminated with flexoelectric composite layer, *Thin-Walled Structures*, **157**, 107138

17. Lindberg H.E., 1992a, An evaluation of convex modeling for multimode dynamic buckling, *Transactions of the ASME. Journal of Applied Mechanics*, **59**, 929-936

18. Lindberg H.E., 1992b, Convex models for uncertain imperfection control in multimode dynamic buckling, *Transactions of the ASME. Journal of Applied Mechanics*, **59**, 937-945

19. Lindberg H.E., Florence A.L., 1987, *Dynamic Pulse Buckling Theory and Experiment*, Martinus Nijhoff Publishers, Dordrecht

20. Sahu S.K., Datta P.K., 2007, Research advances in the dynamic stability behavior of plates and shells: 1987-2005-Part I: Conservative systems, *Applied Mechanics Reviews*, **60**, 65-75

21. Saran S., Ayisit O., Yavuz M.S., 2013, Experimental investigations on aluminum shaped charge liners, *Procedia Engineering*, **58**, 479-486

22. Suresh Kumar R., Kundalwal S.I., Ray M.C., 2017, Control of large amplitude vibrations of doubly curved sandwich shells composed of fuzzy fiber reinforced composite facings, *Aerospace Science and Technology*, **70**, 10-28

23. Teng J.G., 1996, Buckling of thin shells: Recent advances and trends, *Applied Mechanics Reviews*, **49**, 263-274

24. Wei Z.G., Batra R.C., 2006, Dynamic buckling of thin thermoviscoplastic cylindrical shell under radial impulsive loading, *Thin-Walled Structures*, **44**, 1109-1117

25. Xu X., Ma Y., Lim C.W., Chu H., 2006, Dynamic buckling of cylindrical shells subject to an axial impact in a symplectic system, *International Journal of Solids and Structures*, **43**, 3905-3919

26. Xue J., Yuan D., Han F., Liu R., 2013, An extension of Karman-Donnell's theory for non--shallow, long cylindrical shells undergoing large deflection, *European Journal of Mechanics – A/Solids*, **37**, 329-335

27. Zhang D., Shangguan Q., Xie C., Liu F., 2015, A modified Johnson-Cook model of dynamic tensile behaviors for 7075-T6 aluminum alloy, *Journal of Alloys and Compounds*, **619**, 186-194

Manuscript received June 20, 2023; accepted for print July 28, 2023

JOURNAL OF THEORETICAL AND APPLIED MECHANICS
61, 4, pp. 783-791, Warsaw 2023
https://doi.org/10.15632/jtam-pl/171544x

THE EFFECT OF GRAPHITE FLAKE DIAMETER ON THE RESISTANCE TO THERMAL SHOCK, MICROSTRUCTURE AND MECHANICAL PROPERTIES OF SILICON CARBIDE NANOMATERIALS

Mohammed H. Mahmood
Department of Projects, University of Anbar, Iraq
e-mail: mohammed.hussein@uoanbar.iq

Wekar M. Khalaf
Mechanical Engineering Department, University of Anbar, Iraq
e-mail: wekar@uoanbar.edu.iq

Kafel Azeez
Renewable Energy Research Center, University of Anbar, Iraq
e-mail: kafelazeez1966@uoanbar.edu.iq (corresponding author)

To ascertain the impact of graphite flake diameter on the microstructure and mechanical properties as well as resistance to thermal shock, graphite flakes of various diameters have been added to zirconium dibromide (ZrB_2) 20 vol.% nano-silicon carbide (SiC) 20 vol.% graphite ($ZS_{np}G$) ceramics. The objective of this study is to investigate the effect of graphite flake diameter on silicon carbide nanomaterials. The study aims to identify a strategy for achieving high comprehensive performance of ZrB_2-based ceramics incorporating graphite for future research on ultra-high temperature ceramics (UHTCs). The dispersion of measurements has been conducted by combining a solid powder with ethanol at various mass fractions. The results demonstrated that, while no changing fracture toughness considerably, the relative density and flexural strength of $ZS_{np}G$ ceramics initially increased and then declined with graphite diameter increasing. The micro-crack length reduction due to residual thermal stress, appearance of silicon carbide nanoparticles within granulation, and management of graphite distribution all contributed significantly to the improvement of flexural strength $ZS_{np}G$ ceramics. According to the computed thermal shock parameters, $ZS_{np}G$ ceramics fracture propagation was constrained by graphite with a larger starting diameter and prevented with a finer starting diameter.

Keywords: graphite, flake diameter, thermal shock, microstructure

1. Introduction

Ultra-high temperature ceramics (UHTCs) are a family of materials made of nitrides, carbides and boron compounds of transition alloys. In applications, zirconium-based (ZrB_2) UHTCs are used in missile propulsion, recyclable atmospheric re-entry vehicles and thermoplastics. They have low density, high melting point ($> 2500^\circ C$) and resistance to chemical corrosion. One may find them employed for safety measures in hypersonic spacecraft (Xiang *et al.*, 2015; Gautam and Mohan, 2015; Wang *et al.*, 2009a; Guo, 2009).

By adding small sized silicon carbide nanoparticles (SiC_{np}), which are intragranular nano-structures, zirconium dibromide mechanical characteristics and resistance to oxidation can be greatly enhanced (Han *et al.*, 2009; Chamberlain *et al.*, 2006; Zhu *et al.*, 2007; Guo *et al.*, 2009). This method can not get over their inherent brittleness and resistance to thermal shock, which prevents them from using in harsh environments (Yang *et al.*, 2011). To address these

shortcomings, one approach that included addition of a larger phase into ceramics with ZrB_2 has been adopted (Liu *et al.*, 2010).

The use of graphite can increase reliability of brittle materials because it can stop fracture growth and release residual stress (Guo *et al.*, 2008; Liu *et al.*, 2009a). The aircraft industry has substantially increased the use of natural graphite flakes. The graphite flakes controlled ceramics ZrB_2-SiC (ZS) has been found to substantially increase thermal shock resistance while maintaining acceptable levels of oxidation resistance as reported in the available literature (Liu *et al.*, 2009b; Yang *et al.*, 2009; Hou *et al.*, 2013). Because graphite flakes in ZrB_2-SiC-graphite (ZSG) ceramics behave as defects, adding the graphite considerably reduces flexural of strength ZS ceramics.

In addition, the decrease in flexural strength take also place because graphite weakens bonding and reduces ceramics capacity to transfer load (Iao *et al.*, 2014). Therefore, it is necessary to research the impact of diameter of graphite on thermal and mechanical characteristics as well as the enhancement of flexural strength of ZrB_2-based ceramics.

The recent research has concentrated on carbon fiber reinforced ZrB_2-based ceramics because, when compared to other reinforcements, the carbon fiber offers more benefits in improving fracture toughness (Calabrese *et al.*, 2018; Zamora *et al.*, 2012) and has a high potential in significantly increasing the resistance to thermal shock.

High sintering temperature, on the other hand, causes substantial deterioration of carbon fibers in modified ZrB_2-based ceramics, impeding research on such materials. As a result, techniques to control carbon fiber degradation are essential in the production of carbon fiber reinforced ZrB_2-based ceramics. Conventional steps include decreasing the processing time, using carbon coated fibers and reducing the melting point (Zhang *et al.*, 2008). For carbon fiber reinforced ZrB_2-based ceramics, spark plasma sintering (SPS) may be advantageous because it combines the effects of rapid heating, powder cleaning of the surface, and fast consolidation of powders to theoretical density (Mishra and Pathak, 2008). Because nanosized particles have a much higher sintering occupation than micrometer powders, they are used as the base material in the conventional method of lowering the sintering temperature of ZrB_2 (Lee *et al.*, 2021).

It is important to study the effect of mechanical properties and diameter of graphite flakes on the microstructure and resistance to thermal shock of silicon carbide nanomaterials in order to achieve highly comprehensive performance of ZrB_2-based ceramics for future research on extremely-high temperature ceramics (UHTCs). This research intends to find a solution by investigating the effect of graphite diameter on ZrB_2-based ceramics. The goal of this work is to pave the way for future studies of UHTCs by outlining a plan to improve the performance of ZrB_2-based ceramics in a wide variety of applications.

2. Methods and materials

2.1. Classification

The powder as received was mixed with ethanol at various powder mass ratios to create suspensions for all measurements. PEI dosage was administered on a dry weight basis (dwb%). The pre-mixed solution with the content desired suspension was added to powder mixtures of 20% graphite and 20% nano-SiC addition to ZrB_2 with varying diameters (designated as $ZS_{np}G_1$, $ZS_{np}G_2$, and $ZS_{np}G_3$). The premixed solution has been then deflocculated ultrasonically (JYD-801, Jiatuanda Technology Co. Ltd, Shenzhen, China) at an output power. The various powder mixtures were vacuum hot pressed for 1 hour at 1750°C under a tensile stress load of 30 MPa using an implicitly heated graphite die lined with BN-coated graphene sheets after drying in a related evaporator.

2.2. Preparation

The solid particles were mixed with ethanol at different powder mass percentages to create suspensions for all measurements. Doses of PEI were reported in terms of dwb% of the powder. To achieve an appropriate dispersant concentration, a premixed solution was added to powder combinations of ZrB_2 plus 20% nano-SiC and 20% graphite with varying diameters (designated $ZS_{np}G_1$, $ZS_{np}G_2$, and $ZS_{np}G_3$), which were then ultrasonically deflocculated using a JYD-801 from Jiatuanda Technology Co.

2.3. Materials

In this study, zirconium diboride (ZrB_2), 20% nano silicon carbide (SiC), and 20% graphite flakes of different sizes were utilized. Suspensions were made by combining the powder as obtained with ethanol at varying powder mass percentages, and the PEI dose was represented as a mean dry weight percentage of the powder basis (dwb%). After being ultrasonically extracted from the human body, powder mixtures of ZrB_2 containing 20% nanoSiC and 20% graphite (named $ZS_{np}G_1$, $ZS_{np}G_2$, and $ZS_{np}G_3$) were treated with the premixed solution that had the requisite dispersant concentration.

2.4. Characterization

Microstructure, mechanical properties and thermal shock resistance of graphite-containing ZrB_2-based ceramics were studied as a function of flake diameter in this study. X-ray diffraction (XRD), scanning electron microscopy (SEM), energy dispersive spectroscopy (EDS) and transmission electron microscopy (TEM) were all used to evaluate the materials. We tested flexural strength and Vickers hardness of the samples to get a sense of their mechanical qualities. The ability of samples to withstand a sudden temperature drop was measured by quenching them with cold water.

3. Discussion of results

3.1. Tests characteristics

SEM images of $ZS_{np}G$ ceramic reveal where the materials have been fractured. In this study, the microstructure features and mechanical properties of the ceramics were examined using these micrographs.

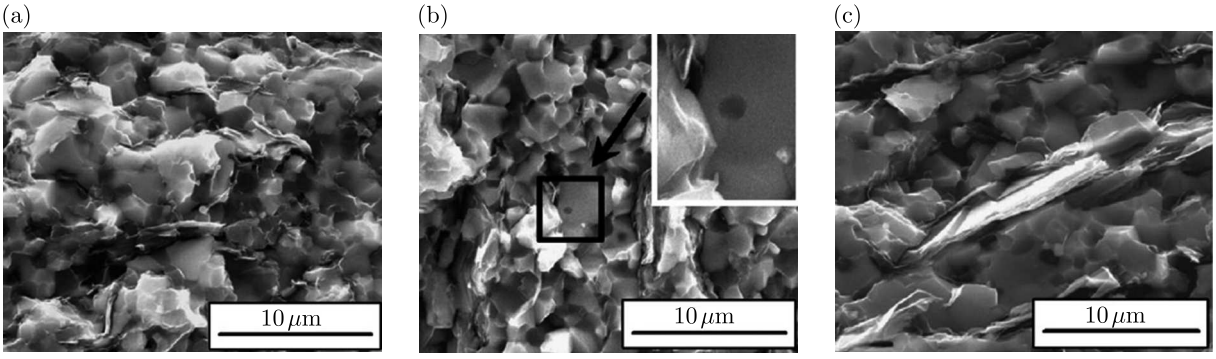

Fig. 1. Micrograph SEM of $ZS_{np}G$ ceramic fracture surfaces

Standard scanning electron micrographs (SEM) of $ZS_{np}G$ ceramic fracture surfaces are shown in Fig. 1. Nano-SiC particles may be seen within individual ZrB_2 grains in high-magnification

SEM images (Fig. 1b, arrow). Natural graphite flakes in $ZS_{np}G$ ceramics possessed basic planes perpendicular to the hot pressing direction, and the flakes diameters on fracture surfaces were similar to those found in raw graphite. When the graphite diameter was increased to 20 μm, the relative density of $ZS_{np}G$ ceramics dropped down to 98.7%. Due to the increased sintering driving force (Lv *et al.*, 2006), fine ZrB_2, ZrC, and SiC particles were produced in situ on the particle surface. A decrease in surface free energy increases density. Due to smaller contact area between graphite flakes and ceramic particles, sintering and driving forces were diminished when the graphite diameter was increased to 20 μm. The relative density of $ZS_{np}G$ ceramics was reduced as a result.

The conclusion is that the microstructure and mechanical characteristics of graphite-containing ZrB_2-based ceramics were significantly influenced by the diameter of graphite flakes. The study discovered that increasing the diameter of graphite flakes caused weaker bonding inside the $ZS_{np}G$ composite, which resulted in pits and microcracks reducing the flexural strength (Zhang *et al.*, 2009). Furthermore, a decrease in the relative density was observed when the diameter of graphite was increased to 20 μm. It was because there was less contact space between the graphite flakes and ceramic particles. $ZS_{np}G$ ceramics showed good thermal shock resistance, according to this investigation.

Adding graphite to the ceramics weakened it because weak interfaces occurred, which lowered flexural strength (Wang *et al.*, 2011). Thus, as in $ZS_{np}G_1$, the flexural strength was considerably reduced and the graphite dispersion capacity increased with lowered graphite diameter.

Table 1. $ZS_{np}G$ ceramics containing graphite flakes with different diameters and the resulting differences in mechanical characteristics and relative densities (Wang *et al.*, 2009b)

Materials	Fracture toughness [MPa·$\sqrt{\text{m}}$]	Young's modulus [GPa]	Flexural strength [MPa]	Relative density [%]
$ZS_{np}G_1$	4.31 ± 0.11	330.89 ± 19.43	451.93 ± 23.21	99.4
$ZS_{np}G_2$	4.54 ± 0.15	356.82 ± 24.64	523.06 ± 18.52	100
$ZS_{np}G_3$	4.06 ± 0.19	306.52 ± 27.96	405.58 ± 19.63	98.7

During the polishing process of $ZS_{np}G$ ceramics, a significant amount of graphite was pulled out from the composite, resulting in weaker bonding within the $ZS_{np}G$ composite. This was revealed by SEM micrographs of polished surfaces shown in Figs. 2 and 3. The diameter of pits caused by the removal of graphite grew along with the size of graphite crystals. During the flexural strength test, those holes acted as gaps causing stress concentration and a subsequent decrease in strength. Therefore, a considerable reduction in flexural strength in $ZS_{np}G_3$ might be because of a combination of microcracks and pits created by a considerable graphite pullout during polishing.

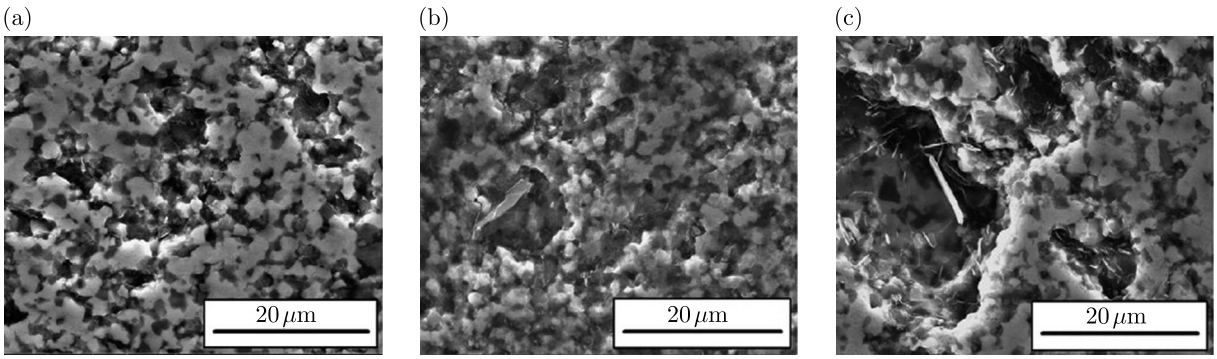

Fig. 2. Polished surfaces SEM micrographs for parallel specimens

The flexural strength of $ZS_{np}G$ ceramics cannot be solely based on the size of graphite. The flexural strength of $ZS_{np}G$ ceramics increased for diameters from 5 μm to 10 μm and then decreased from 10 μm to 20 μm, while fracture toughness did not change significantly. This was because adding the graphite to ceramics weakened it due to weak interfaces that occur, which lowered the flexural strength. However, increasing the diameter of graphite flakes could improve the mechanical properties up to a certain point by enhancing crack deflection and bridging mechanisms. Beyond this point, further increamente in graphite flake size led to weaker bonding within the composite and smaller flexural strength. Therefore, other factors such as microstructure characteristics and processing conditions also play a significant role in determining the mechanical properties of $ZS_{np}G$ ceramics (Zhang *et al.*, 2009).

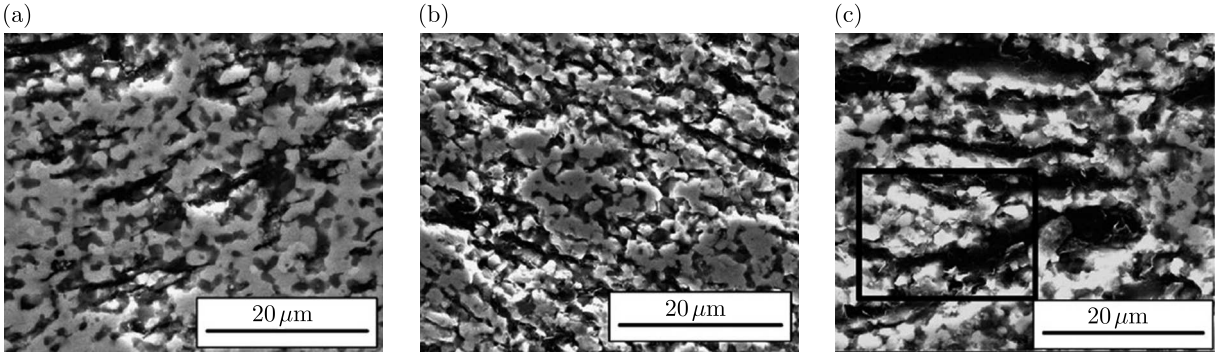

Fig. 3. SEM micrographs of polished surfaces

The perpendicular polished surfaces of $ZS_{np}G$ specimens with graphite of various sizes are depicted in micrographs in Fig. 3. In Figs. 3a and 3b, there were no discernible microcracks, but in Fig. 3c, a lengthy microcrack was discovered at the intersection of SiC and/or ZrB_2 and graphite. These properties demonstrated that the thermal residual stress and density of preexisting connecting cracks were also reduced as the graphite diameter decreased, which was consistent with subsequent studies on magnesium sulphate composites (Wang *et al.*, 2011). The source of longer cracks are the larger particles, while finer particles caused shorter break propagation distances from the particle. According to that theory, large-diameter graphite in $ZS_{np}G_3$ would result in microcracks formation, which was the primary cause of the decline in flexural strength and relative density (Liu *et al.*, 2010).

3.2. Thermal shock behavior

Figure 4 depicts the strength and stiffness of $ZS_{np}G$ ceramics after and before thermal shock at various temperatures. The modulus of elasticity of $ZS_{np}G_1$ and $ZS_{np}G_2$ ceramics was found to be greatly increased for a growth of the thermomechanical temperature difference up to 398°C. Thermal shock behavior of $ZS_{np}G$ ceramics was investigated by estimating the flexural strength drop caused by rapid quenching of test specimens from extremely high temperatures. The samples were heated in an electric resistance furnace for 15 minutes at a specific temperature before being placed in a 20°C water bath. After the thermal shock, all specimens were examined for preserved flexural strength. The study discovered that $ZS_{np}G$ ceramics have a good thermal shock resistance, which is important for materials used in high-temperature applications with fast temperature variations.

Statistically, the force of thermal shock is similar to the initial force. However, $ZS_{np}G_1$ and $ZS_{np}G_2$ ceramics showed a significant decrease in flexural strength when quenched from 400°C to 450°C. However, the dropping trend of flexural strength of $ZS_{np}G_3$ during water quenching varied from that of $ZS_{np}G_1$ and $ZS_{np}G_2$.

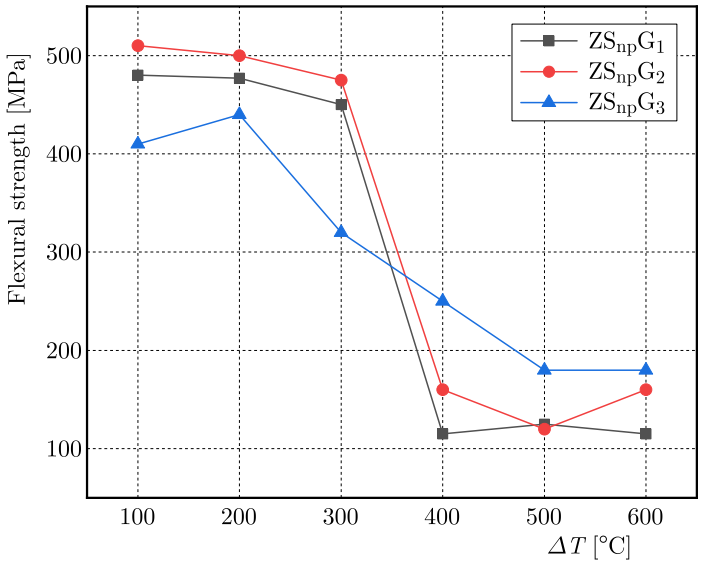

Fig. 4. The effect of temperature difference on retained strength

The researchers investigated the thermal shock response of $ZS_{np}G$ ceramics with graphite flakes of different diameters and concluded that the critical temperature differences did not suggest that they had the same thermal shock reaction. Therefore, it is important to consider other factors such as microstructure characteristics and processing conditions when evaluating the $ZS_{np}G$ ceramics thermal shock behavior.

Above $T = 350°C$, the $ZS_{np}G_3$ curve displayed a typical decrease in flexural strength owing to unstable fracture propagation that might occur occasionally in $ZS_{np}G_3$ ceramics. The considerable loss of flexural strength and lower starting temperature of that loss after water quenching revealed that the unstable fracture propagation may might occasionaly occur in $ZS_{np}G_3$ ceramics. This was because a higher thermal residual stress could be induced by a bigger diameter of graphite, which had been investigated before. The energy dissipation and deflection or pinning of a fracture occurred as it propagated through a field of residual thermal stress. Therefore, the response to thermal shock of $ZS_{np}G$ ceramics with graphite flakes of varying sizes was influenced by multiple factors such as microstructure characteristics, processing conditions and thermal residual stress induced by the graphite flakes (Mishra and Pathak, 2008).

As defined in ASTM C1525-04 (Lv *et al.*, 2006), the critical difference in temperature is determined by employing a linear regression among sites which initially reduced the average flexural strength of dampened rods to 32% as the mean material strength. All three critical temperatures found for $ZS_{np}G_1$, $ZS_{np}G_2$, and $ZS_{np}G_3$ were higher than 379°C recorded for the SiC ceramics containing 15% ZrB_2 (Lee *et al.*, 2021). Furthermore, the fact that both materials have the same critical temperature difference does not imply that they have the same response to thermal shock.

The trend of decreasing flexural strength of $ZS_{np}G_3$ after water quenching differed from that of $ZS_{np}G_1$ and $ZS_{np}G_2$ as the critical temperature differences did not imply that they had the same sensitivity to thermal shock. The study looked for a thermal shock response of $ZS_{np}G$ ceramics with varied sizes of graphite flakes and discovered that while $ZS_{np}G_1$, $ZS_{np}G_2$, and $ZS_{np}G_3$ had similar critical temperature differences, their decreasing patterns in flexural strength were different following water quenching. This was due to the fact that the microstructure features and processing circumstances of each ceramic differed, influencing their thermal shock response. As a result, numerous aspects must be considered when analyzing the thermal shock response of $ZS_{np}G$ ceramics with varied diameters of graphite flakes (Zhang *et al.*, 2008). The

fracture resistance thermal stress was calculated by multiplying the material strength σ, Young's modulus E, Poisson's ratio ν and coefficient of thermal expansion α.

The maximum temperature difference that can occur before cracks start to form is predicted by a thermal shock parameter R. It is evident that materials with significant strength and heat conductivity, as well as low values of thermal expansion and Young's modulus, can achieve a high resistance to fracture induction (Mishra and Pathak, 2008)

$$R = \frac{1-\nu}{E\alpha} \qquad R^{IV} = \frac{K_{IC}^2}{\sigma^2(1-\nu)} \tag{3.1}$$

where σ is the material strength, ν is Poisson's ratio and K_{IC} is toughness of fracture, respectively. R^{IV} determines resistance of the ceramics to catastrophic fracture propagation with the critical crucial temperature difference. In terms of the parameter R^{IV}, higher resistance to thermal shock is dependent on the ratio of Poisson's to toughness as well as lower strength of the material (Gautam and Mohan, 2015).

As can be seen in Fig. 4, the trend of impact of temperature difference on the retained strength curves for $ZS_{np}G_1$ and $ZS_{np}G_2$ is the same. The study searched for the thermal shock response of $ZS_{np}G$ ceramics with varied diameters of graphite flaked and discovered that the trend of retained strength vs. temperature difference curves for $ZS_{np}G_1$ and $ZS_{np}G_2$ is the same. Therefore, only the thermal shock parameter of $ZS_{np}G_2$ was used to compare with that of $ZS_{np}G_3$. However, it is important to note that although their trends were similar, the fracture initiation parameters were different, which affected the starting temperature of loss of flexural strength during thermal shock.

The coefficient of thermal expansion and Poisson's ratio of $ZS_{np}G$ were assumed to be of the same in order to ease computation since they are thought to have similar compositions. Therefore, the elevated R value can mostly be attributed to the exceptional flexural strength of $ZS_{np}G_2$. The computed crack propagation parameter R^{IV} of $ZS_{np}G_2$ was about 33% bigger than that of $ZS_{np}G_2$, showing that the propagation of cracks was impeded in $ZS_{np}G_3$ ceramics.

The moderate loss of flexural strength and lower ending temperature of strength reduction after water quenching suggested that unstable fracture propagation might occur occasionally in $ZS_{np}G_3$ ceramics (Fig. 4). A higher residual thermal stress could be induced by a bigger diameter of graphite, which had been investigated previously. The energy dissipation and deflection or pinning of a fracture occurred as it propagated through the field of residual thermal stress. As a graphite particle was driven during fracture propagation, interfacial friction between the graphite and other components was caused by the residual thermal stress. Meanwhile, at the edges of SiC particles, fracture deflection occurred, and considerable residual stresses during sliding and cracking used more energy of crack propagation (Liu *et al.*, 2010). This was due to the fact that the boundary of graphite flakes was a weak interlayer.

A little distinction may also be seen between $ZS_{np}G_1$ and $ZS_{np}G_2$ in terms of their thermal shock resistance parameters. In spite of this, $ZS_{np}G_1$ remained in the same mode of the thermal shock resistance as $ZS_{np}G_2$. The critical graphite size may be postulated if diameter of the graphite remains constant. It stays less than the essential diameter because the thermal shock behavior of $ZS_{np}G$ ceramics changes significantly if the graphite has a diameter larger than the critical one. This study examined the thermal shock response of $ZS_{np}G$ ceramics using graphite flakes of various sizes, and it was discovered that larger diameter flakes can stop cracks from spreading in $ZS_{np}G$ ceramics while smaller flakes can stop cracks from originating at all. In order to fully comprehend the fundamental process underlying those phenomena, additional investigation and theoretical study are required. Therefore, based on the experimental findings, a critical graphite size may be proposed, but additional research is required to completely understand its role.

4. Conclusions

The study undertaken investigates the response to thermal shock of $ZS_{np}G$ ceramics with graphite flakes of varying sizes, and the conclusions can be summarized as:

- The lower the residual thermal stress and pre-existing connecting contribution of fractures, the smaller graphite diameter.
- Longer cracks were induced by larger particles, while finer particles caused shorter break propagation lengths. As a result, a large-diameter graphite in $ZS_{np}G_3$ would produce microcracks, which was the principal source of decrease in bending strength and relative density. The presence of intragranular nano-sized SiC particles, regulation of graphite dispersion and shortening of microcrack length were all responsible for the increase in flexural strength.
- Bigger diameter graphite could slow the spread of cracks in $ZS_{np}G$ ceramics, whereas smaller diameter graphite were more effective at preventing crack initiation.
- Although $ZS_{np}G_1$, $ZS_{np}G_2$, and $ZS_{np}G_3$ had similar critical temperature differences, their decreasing trends in flexural strength were different during water quenching due to different microstructure characteristics and processing conditions.
- It is important to consider multiple factors when evaluating the thermal shock response of $ZS_{np}G$ ceramics with graphite flakes of varying sizes.

Overall, these findings suggest that controlling the graphite size and distribution can significantly impact the thermal shock behavior and mechanical properties of $ZS_{np}G$ ceramics.

References

1. Calabrese L., Brancato V., Palomba V.V., Frazzica A., Cabeza L.F., 2019, Magnesium sulphate-silicone foam composites for thermochemical energy storage: Assessment of dehydration behaviour and mechanical stability, *Solar Energy Materials and Solar Cells*, **200**, 109992
2. Chamberlain A.L., Fahrenholtz W.G., Hilmas G.E., 2006, Low-temperature densification of zirconium diboride ceramics by reactive hot pressing, *Journal of the American Ceramic Society*, **89**, 12, 3638-3645
3. Gautam G., Mohan A., 2015, Effect of ZrB_2 particles on the microstructure and mechanical properties of hybrid (ZrB_2+Al3Zr)/AA5052 insitu composites, *Journal of Alloys and Compounds*, **649**, 174-183
4. Guo S.Q., 2009, Densification of ZrB_2-based composites and their mechanical and physical properties: a review, *Journal of the European Ceramic Society*, **29**, 6, 995-1011
5. Guo S.Q., Yang J.M., Tanaka H., Kagawa Y., 2008, Effect of thermal exposure on strength of ZrB_2-based composites with nano-sized SiC particles, *Composites Science and Technology*, **68**, 14, 3033-3040
6. Guo W.M., Yang Z.G., Vleugels J., Zhang G.J., 2012, Effect of pressure loading cycle on spark plasma sintered ZrB_2-SiC-Yb_2O_3 ceramics, *Ceramics International*, **38**, 6, 5293-5297
7. Han W., Li G., Zhang X., Han J., 2009, Effect of AlN as sintering aid on hot-pressed ZrB_2-SiC ceramic composite, *Journal of Alloys and Compounds*, **471**, 1-2, 488-491
8. Hou Y., Hu P., Zhang X., Gui K., 2013, Effects of graphite flake diameter on mechanical properties and thermal shock behavior of ZrB_2-nanoSiC-graphite ceramics, *International Journal of Refractory Metals and Hard Materials*, **41**, 133-137
9. Lee J.Y., Nagalingam A.P., Yeo S.H., 2021, A review on the state-of-the-art of surface finishing processes and related ISO/ASTM standards for metal additive manufactured components, *Virtual and Physical Prototyping*, **16**, 1, 68-96

10. Liu Q., Han W., Han, J., 2010, Influence of SiCnp content on the microstructure and mechanical properties of ZrB_2-SiC nanocomposite, *Scripta Materialia*, **63**, 6, 581-584

11. Liu Q., Han W., Hu P., 2009a, Microstructure and mechanical properties of ZrB_2-SiC nanocomposite ceramic, *Scripta Materialia*, **61**, 7, 690-692

12. Liu Q., Han W., Zhang X., Wang S., Han J., 2009b, Microstructure and mechanical properties of ZrB_2-SiC composites, *Materials Letters*, **63**, 15, 1323-1325

13. Lv Y., Wen G., Lei T.Q., 2006, Tribological behavior of W2B5 particulate reinforced carbon matrix composites, *Materials Letters*, **60**, 4, 541-545

14. Mishra S.K., Pathak L.C., 2008, Effect of carbon and titanium carbide on sintering behaviour of zirconium diboride, *Journal of Alloys and Compounds*, **465**, 1-2, 547-555

15. Wang Y., Liang J., Han W., Zhang X., 2009, Mechanical properties and thermal shock behavior of hot-pressed ZrB_2-SiC-AlN composites, *Journal of Alloys and Compounds*, **475**, 1-2, 762-765

16. Wang Z., Wang S., Zhang X., Hu P., Han W., Hong C., 2009, Effect of graphite flake on microstructure as well as mechanical properties and thermal shock resistance of ZrB_2-SiC matrix ultrahigh temperature ceramics, *Journal of Alloys and Compounds*, **484**, 1-2,390-394

17. Wang Z., Wu Z., Shi G., 2011, Fabrication, mechanical properties and thermal shock resistance of a ZrB_2-graphite ceramic, *International Journal of Refractory Metals and Hard Materials*, **29**, 3, 351-355

18. Xiang L., Cheng L., Shi L., Yin X., Zhang L., 2015, Mechanical and ablation properties of laminated ZrB_2-SiC/BN ceramics, *Journal of Alloys and Compounds*, **638**, 261-266

19. Xiao K., Guo Q., Liu Z., Zhao S., Zhao, Y., 2014, Influence of fiber coating thickness on microstructure and mechanical properties of carbon fiber-reinforced zirconium diboride based composites, *Ceramics International*, **40**, 1, 1539-1544

20. Yang F., Zhang X., Han J., Du S., 2008, Mechanical properties of short carbon fiber reinforced ZrB_2-SiC ceramic matrix composites, *Materials Letters*, **62**, 17-18, 2925-2927

21. Yang H., Zhang L., Guo X., Zhu X., Fu X., 2011, Pressureless sintering of silicon carbide ceramics containing zirconium diboride, *Ceramics International*, **37**, 6, 2031-2035

22. Zamora V., Ortiz A.L., Guiberteau F., Nygren M., 2012, Crystal-size dependence of the spark-plasma-sintering kinetics of ZrB_2 ultra-high-temperature ceramics, *Journal of the European Ceramic Society*, **32**, 2, 271-276

23. Zhang X., Xu L., Du S., Liu C., Han J., Han W., 2008, Spark plasma sintering and hot pressing of ZrB_2-SiCW ultra-high temperature ceramics, *Journal of Alloys and Compounds*, **466**, 1-2, 241-245

24. Zhang X.H., Wang Z., Hu P., Han W.B., Hong C.Q., 2009, Mechanical properties and thermal shock resistance of ZrB_2-SiC ceramic toughened with graphite flake and SiC whiskers, *Scripta Materialia*, **61**, 8, 809-812

25. Zhu S., Fahrenholtz W.G., Hilmas G.E., 2007, Influence of silicon carbide particle size on the microstructure and mechanical properties of zirconium diboride-silicon carbide ceramics, *Journal of the European Ceramic Society*, **27**, 4, 2077-2083

Manuscript received May 4, 2023; accepted for print July 31, 2023

JOURNAL OF THEORETICAL AND APPLIED MECHANICS
61, 4, pp. 793-805, Warsaw 2023
https://doi.org/10.15632/jtam-pl/171748

PARAMETRIZATION OF THE MAIN ROTOR AND WORKING ENVIRONMENT FOR DIFFERENT FLIGHT CONDITIONS – COMPUTATIONAL FLUID DYNAMICS ANALYSIS AS AN APPLICATION FOR MULTIDISCIPLINARY OPTIMIZATION

Jakub Kocjan

Military University of Technology, Doctoral School, Warsaw, Poland

e-mail: jakub.kocjan@wat.edu.pl (corresponding author)

Stanisław Kachel, Robert Rogólski

Military University of Technology, Faculty of Mechatronics, Armament and Aerospace, Warsaw, Poland

e-mail: stanislaw.kachel@wat.edu.pl; robert.rogolski@wat.edu.pl

The paper shows a method of aerodynamic modelling of the whole rotor and exemplary results obtained from complex analyses. The analytical basis of rotor aerodynamics for different phases of the helicopter flight is shown. The analytical calculations are provided to model a single blade motion according to its azimuth angle and to validate the obtained results. The parametric design method is shown to be applied for different blade planform shapes and various section airfoils. The Computational Fluid Dynamics (CFD) fluid domain for the flow around the blade is also prepared using a parametric method. The parametric graphic script is developed to create the flow domain for a one-blade simulation or for a complete n-bladed rotor effect. The obtained blade model with enclosure is implemented into CFD environment. The method for fluid mesh preparation and the way of defining its properties are given. The simulation is carried out as transient for the n-bladed rotor. In this simulation, various flight conditions are taken into account. Real rotary motion of the blades is simulated with artificially enforced mesh motion. The obtained numerical results are compared then with analytical assumptions. The simulation findings which are the inputs for further analysis are shown with graphical representations. As an output of the research, new options for main rotor optimization are developed. The usage of combined parametric modelling confirmed with aerodynamic analysis for different flight conditions is shown in the work as a new perspective for design optimization of the main rotor.

Keywords: helicopter, main rotor, rotor blade, geometric modelling, computational fluid dynamics (CFD)

1. Introduction

The Russian invasion on Ukraine revised the usage of helicopters on modern battlefield. The need of preparing constructions that are capable to provide better features for comprehensive military operations is observed more than in any other conflict in XXI's century. As a consequence, a lot of countries are improving existing structures and searching for brand new solutions of VTOL vehicles (Oh *et al.*, 2021). Therefore, also in Polish Military University of Technology, a development of rotorcraft design methods is being conducted as an activity included in a complex research program which is aimed at finding new approaches and design solutions for needs of structural or aeroelastic optimization. This work is a second part of the recalled research program. The first one was focused on preparing a parametric blade model and its analytical and CFD validation for further analysis. The research were preceded with comparative

analysis of commonly used helicopter configurations. The results of evaluation and proposals for construction improvements were published in (Kachel *et al.*, 2021).

The parametrization of the blade provides a less time-consuming solution for the preliminary design phase. The advantages of parametric blade modeling were demonstrated in numerous publications including (Sagimbayev *et al.*, 2021; Ma *et al.*, 2021). What is more in this stage of the study, the fluid enclosures for CFD analysis are also parametrized and generated by the prepared program. The usage of parametric models to fulfill the required features of shape and structure is shown in (Lim, 2018; Allen *et al.*, 2021) for airfoil design, (Tixadou, 2021; Grebenikov *et al.*, 2021) for strength design and (Bailly *et al.*, 2019) for aerodynamics. Some model tasks from the above works defined with parametrization declared both for aerodynamic shape, blade structure and fluid domain are highly advanced numerical problems. Solving such problems generally demands applying Fluid Structure Interactions (FSI) techniques, which gives optional results varied due to different design configurations. Simulations of the rotor aerodynamic and aeroelastic effects, taking into account sensitivity analysis due to key design parameters, significantly support the decision-making process in relation to the selection of optimal utility variants.

In the research described here, for preparation parametric models and fluid enclosures, some specific programming language was used. Examples of parametrization in the modelling using GRIP language were shown in (Ryazanov, 2016; Shabliy and Dmitrieva, 2014; Grabowik *et al.*, 2015). Open GRIP (Graphic Interactive Programming) available in Siemens NX CAD environment is a language that provides a possibility to create an external solid body or internal structure geometry of any airframe part. Virtual elements are generated with the use of commands and parameters defined with a specific programming code. The GRIP language is dedicated for research processes, because it grants an option for inertia properties of the generated model. The obtained model features can be used for aerodynamic or strength analyses carried out in further stages of the simulations. The logical conditions that are enclosed in the program code can be used to prepare loops which will provide a possibility of strength calculation with fitting the best dimensions. As an output, a geometry generator is prepared with initial optimization functions. Other main rotor optimization studies with focusing on aerodynamic optimization were presented in (Stalewski, 2017a,b; Xie *et al.*, 2017; Stalewski and Zalewski, 2019; Okumuş *et al.*, 2022) while optimization procedure for best flight performance was shown in (Slavik *et al.*, 2029).

The aim of the research presented herein is to analyze the aerodynamic rotor model in different flight conditions. The new approach is to provide geometry with enclosures prepared to be applied into CFD environment, where different flight conditions with real main rotor motion could be evaluated and compared. One of the examples of CFD usage for strength analysis was presented in (Spyropoulos *et al.*, 2021). There are some main research institutes that are focused on main rotor optimization problems, ONERA French Aerospace Lab and DLR German Aerospace Center for instance. They published several methods of solving the optimization problem using CFD methods (Goerke *et al.*, 2012; Wilke, 2021; Jain, 2022). However, there were no parametrization of the rotor blade shape, position and entire fluid domains simultaneously for given flight conditions, which is the main goal of this research in order to provide a comprehensive tool for future combined optimization solutions.

As it was mentioned above, the solutions for the optimization process which are being developed in the mentioned research program, started with evaluating the blade and assessing the methods for further analysis. The preliminary results from the initial stage of investigations were published in (Kocjan *et al.*, 2022). In this research, geometry of the existing rotor was taken as an example for evaluating the proposed solution. The GRIP program code for the modeling was developed by adding the option for enclosures preparation and expand possibilities to enter more parameters of the main rotor by end-user. The dimensions of enclosures are adequate to rotor dimensions.

The prepared model will be a basis for fluid dynamics computation using Ansys Fluent. The parameters of main rotor movement will be calculated from analytic formulae. The value of collective pitch control and a change of cyclic control are calculated with the use of a MATLAB code. Then the calculated values are inputs for CAD model generation and then for CFD motion simulation. Furtherly, the mesh for numerical simulation is generated with the Fluent meshing tool. The mesh size decreases as it approaches the blade surface. The inflation model is also applied. In the research, a poly-hexcore mesh was used. The prepared mesh is configured for calculation using sliding mesh options. The mesh motion is described with outcomes of analytical calculations, which were earlier prepared. During the studies, the mesh size was adapted to obtain best results within a reasonable time. The results were compared with the assumptions. The lift and drag values were used to evaluate the model and to check if the parametrized rotor model with air domains is applicable to CFD environment and if the obtained numerical results, especially pressure distributions, are reasonable and eventually acceptable. To the best of co-authors' knowledge, similar research merging the proposed methods for the helicopter main rotor design and main rotor optimization operation has not been performed so far.

This paper is organized in a specifically intended way. The research methods are described in Sections 2 and 3, where the mathematical model, which is the basis for parametric programming, is defined. In Section 3, the parametric programming is described. The mesh properties and simulation setup are presented in Section 4. The results and evaluation of the method is discussed in Section 5. The research methods and outputs, with application to next phases of the program are concluded in Section 6.

2. Analytical model for parametrization

2.1. Mathematical model

The conditions of operation of the main rotor are complex and impose on a designer a necessity to check all of the working aspects. Before performing, an optimization loop for parametrization of main rotor features must be introduced.

The first data to be introduced are blade parameters. To obtain required operational capabilities, the blades construction requires to take into consideration both geometric and aerodynamic characteristics. The flow periodic changes, flexibility of blades and conditions of operation in the presence of a strong centrifugal force imply a relationship between pressure loads and deformations of the material. The blades were well parametrized in the previous step of the research (Kocjan *et al.*, 2022), the deformations are going to be considered in the further phases.

In the presented studies, the conditions of the n-bladed main rotor operation are analyzed and transformed as input parameters for geometry generation and numerical CFD simulation. To prepare a rotor model which is ready to be implemented into Ansys Fluent, in accordance with (Johnson, 1994; Bramwell *et al.*, 2001), pitch angles should be calculated for the main rotor trim conditions. The trim of the rotor is calculated from the thrust, pitching moment for lateral and longitudinal movement

$$\theta(\psi) = \theta_0 - A_1 \cos\psi - B_1 \sin\psi \tag{2.1}$$

where the angles are calculated for different flight conditions. The helicopter speed is given in calculation as a dimensionless speed ratio. To find the longitudinal cycling pitch angle, the first step is to calculate the H-force coefficient in the disc plane

$$h_{cD} = \frac{1}{4}\mu\delta \tag{2.2}$$

As a result, the disc incidence can be calculated as follows

$$\alpha_D = -\frac{1}{w_c}\Big(\frac{1}{2}\mu^2 d_0 + h_{cD}\Big) \tag{2.3}$$

where d_0 is the fuselage drag ratio and w_c is the weight coefficient. Now the mean inflow ratio relative to the disc plane can be obtained in the following way

$$\lambda_D = (\mu\alpha)_D - \lambda_i \tag{2.4}$$

The next step for the rotor trim is to calculate the collective pitch angle which will be used for GRIP program to prepare the main rotor geometry installed for designated flight conditions. The collective pitch is calculated from the main rotor thrust expression

$$t_{cd} = \frac{a}{4}\left(\frac{2}{3}\theta_0\frac{1-\mu^2+\frac{9\mu^4}{4}}{1+\frac{3\mu^2}{2}} + \lambda_D\frac{1-\frac{\mu^2}{2}}{1+\frac{3\mu^2}{2}}\right) \tag{2.5}$$

Further, in order to obtain the longitudinal cycling pitch angle, it is crucial to calculate the flapping coefficient

$$a_1 = \frac{2\mu\Big(\frac{4\theta_0}{3} + \lambda_D\Big)}{1+\frac{3\mu^2}{2}} \tag{2.6}$$

Therefore, the B_1 angle (with the assumptions for a change of the center of gravity – h and f) is ready to be calculated

$$B_1 = \frac{a_1 + C_{mf} + h_{cD}h - w_c f}{w_c + C_{ms}} \tag{2.7}$$

where C_{mf} is the pitching moment coefficient for fuselage and C_{ms} is the pitching moment coefficient due to hinge offset. Then, to get the lateral cyclic pitch angle, the lateral flapping coefficient should be given with the following expression

$$b_1 = \frac{\frac{4}{3}(\mu a_0 + 1.1v^2\lambda_i)}{1+\frac{\mu^2}{2}} \tag{2.8}$$

In consequence, the lateral cyclic pitch angle can be written as

$$A_1 = -b_1 - \frac{w_c f + \frac{T_t}{W}t_c h_t}{t_c h + C_{ms}} \tag{2.9}$$

At the end of analytical consideration, for the main rotor evaluation, its drag force is needed and it can be calculated from the expression

$$D = \frac{P}{V} + X \tag{2.10}$$

where P is the power required for the evaluated flight conditions, X is a force acting in the longitudinal direction. The X-force can be estimated with the formula

$$X = -T\sin\alpha_D - H_D\cos\alpha_D$$

2.2. Analytical calculations for preparing the simulation

All calculation formulae described above were all prepared in MATLAB software. The outputs of calculations are a basis for geometry generation in GRIP program and then for model configurations applicable in Ansys Fluent.

It starts with the input parameters of the designed blade and flight conditions. The blade planform is defined with a specific polynomial function. Next, the rotor solidity factor is calculated as an integral. Using MATLAB functions required for the collective pitch are possible to be established. The weight coefficient, fuselage drag ratio, inflow velocity and disc incidence are computed. After that, the inflow ratio relative to the disc plane can be processed. The program in the further step is solving equation (2.5) to obtain the collective pitch value. Next stage of the calculations is to estimate the flapping coefficients. The pitching moment coefficient is assessed at the subsequent step. With the flapping and pitching moment coefficient, the B_1 angle is ready to be computed. After obtaining the first angle, the second is calculated similar to the first using the equations mentioned above. The MATLAB source code used for all described calculations is shown in Fig. 1.

The calculated collective pitch is modelled in CAD geometry. The collective pitch angles are a basis for the rotor cyclic pitch movement modelled then in Ansys Fluent.

```
a1DtG=rad2deg(a1)

hcd2=1/4*u*del+a*lamd/4*(1/2*a1-u*tet0)

alfd2=-(0.5*u^2*d0*cos(tc)+hcd2)/wc-tc
ud2=u*cos(alfd2)
lamd2=ud2*alfd2-lami

a0=y/8*(tet0*(1-19*u^2/18+3*u^4/2)/(1+3*u^2/2)+4/3*lamd2*(1-u^2/2)/(1+3*u^2/2))
dtf=(1-sin(alfd2)/(1+sin(alfd2)))
b1=4*((u*a0+1.1*dtf^(1/2)*lami)/3)/(1+u^2/2)
qc=del*(1+3*u^2)/8-lamd2*wc-u*hcd

Cms=b*Mb*xg*e/(2*Solid*A*R)
B1=a1+(Cmf+hcd2*h-wc*f)/(wc*h+Cms)
B1=simplify(B1)
axis=simplify(a1-B1)
B1=rad2deg(B1(1,1))
B1=simplify(B1)


 H=hcd2*ro*A*om^2*R^2*Solid
 P=qc*ro*A*om^3*R^3*Solid

 X=-W*sin(alfd2)-H*cos(alfd2)
D=P\V+X
D=simplify(D)

alfd2=simplify(alfd2)
a1=simplify(a1)
axis=simplify(rad2deg(a1)-B1)

alfHT=simplify(D/W+H/W)
alfHT=simplify(rad2deg(alfHT))


Q=qc*ro*Solid*A*om^2*R^3



%%mass=@(x) Mb.*(x/(0.79*R)-0.21/0.79)        % mass function
%%Inert=@(x) mass(x).*x.^2
```

Fig. 1. Example of MATLAB numerical code for preliminary calculations

3. Parametric model for simulation process

The main goal of this research is to obtain a new approach for main rotor blade modelling, which will be implemented into the main rotor optimization loop. The goal is achieved using Open

GRIP code, which is implemented into Siemens NX. The program was taken from the first stage of the studies and improved. The program algorithm is shown in Fig. 2.

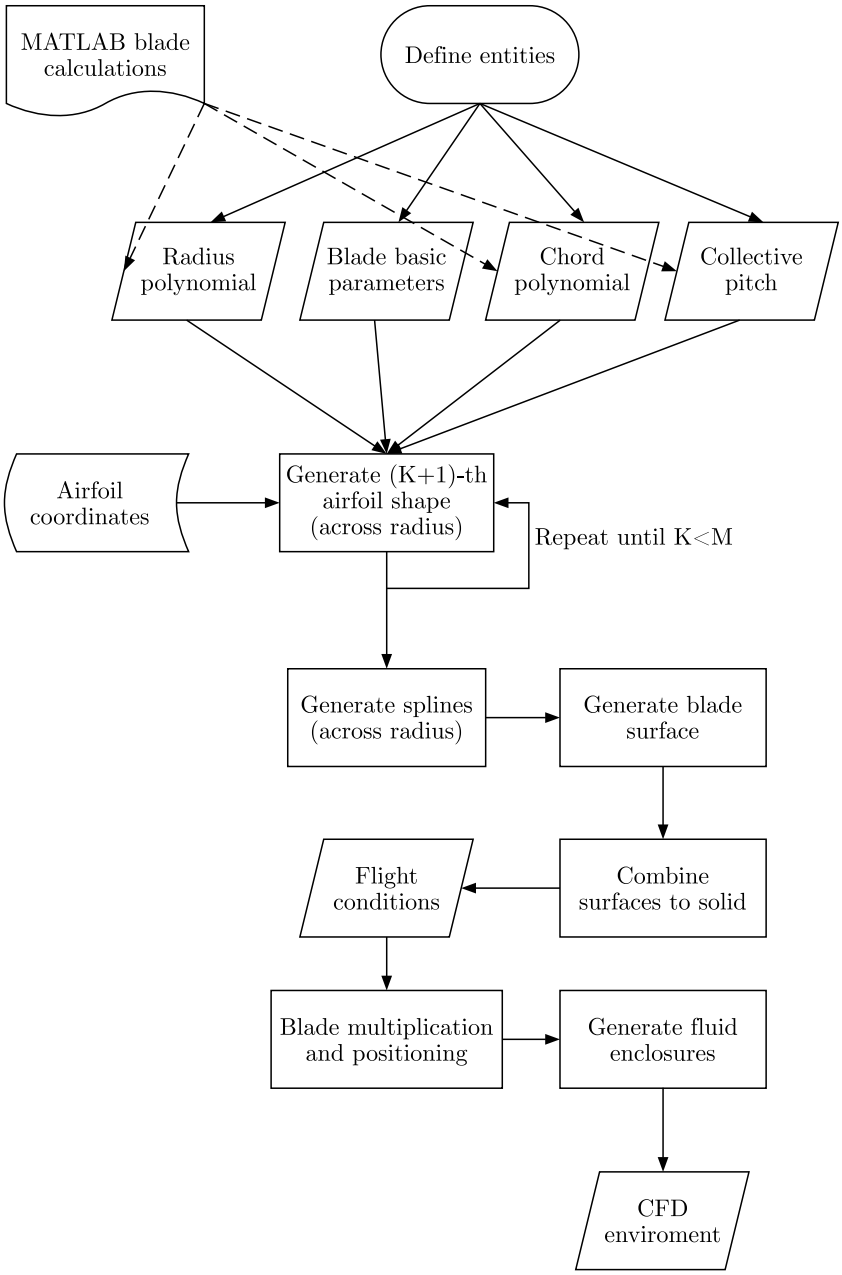

Fig. 2. Enhanced algorithm for generating parametric geometry model

The geometry of the model is parametrized in the program using all main rotor geometrical dimensions. The user is able to enter the blade basic parameters into a popup input window. The first parameters are the number of blades, rotor radius and blade chord. The airfoil is generated from the text file with coordinates, so the user can prepare the blade for any chosen airfoil geometry. The next stage of parametrization is to enter the polynomial coefficient for blade twist and blade chord, so the blade chord and twist can change along the span. With the prepared solution, the blade shape can be freely changed with accordance to analytically calculated values. The windows with applets for introducing control parameters are shown in Figure 5. The shape generation is based on inbuilt GRIP commands for the line and splines,

which provides the desired shape. The number of sections to create the geometry can also be chosen. An example of generating the blade geometry is shown in Fig. 3.

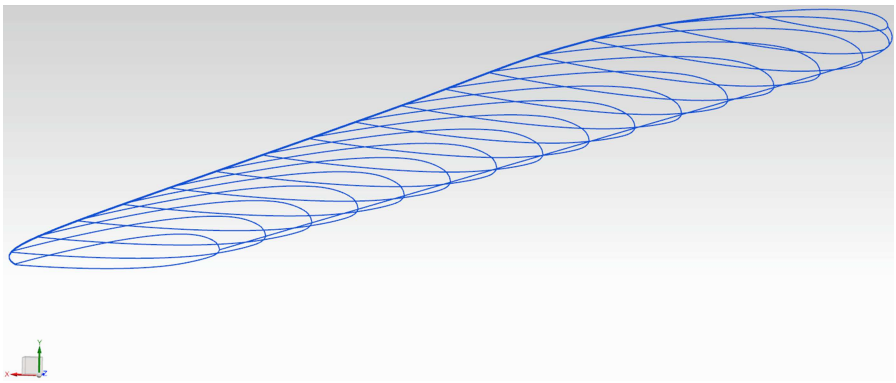

Fig. 3. Blade parametrisation

The second stage of parametrization is the n-bladed rotor. The blades are positioned with the angles that were trimmed analytically. Each blade is positioned at a different angle in accordance to their initial azimuthal position in simulation.

The next phase is generation of fluid enclosures for multi-moving mesh simulation. In the code, the volumes of fluid domains are programmed proportionally to the rotor dimensions. The domains are generated as follows: the main air enclosure as a cuboid for forward flight and as a cylinder for hover, rotor enclosure as a cylinder with each blade havig its own cylinder domain. The space geometry of applicable enclosure variants is presented in Fig. 4. The selectable flight conditions – forward flight or hovering are possible to be chosen by the user.

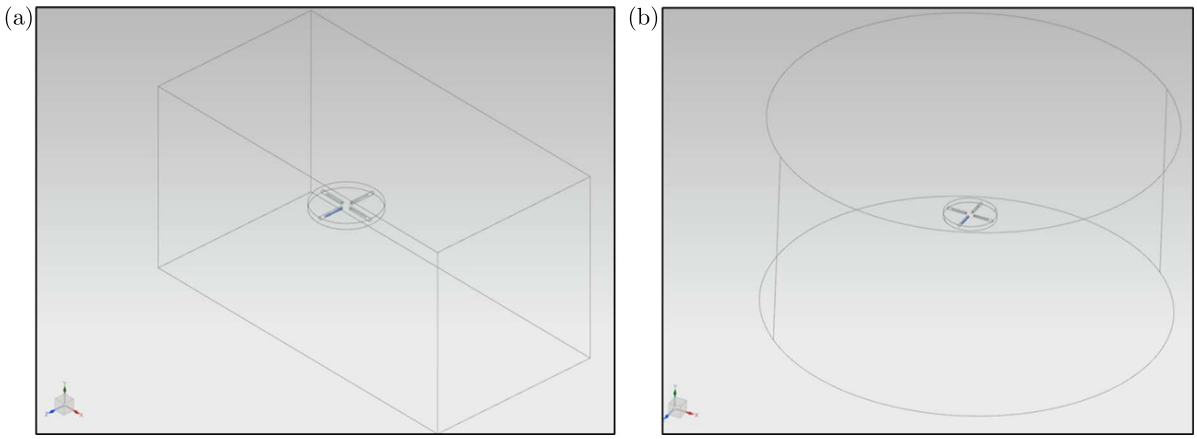

Fig. 4. Fluid domains: (a) for forward flight, (b) for hovering flight

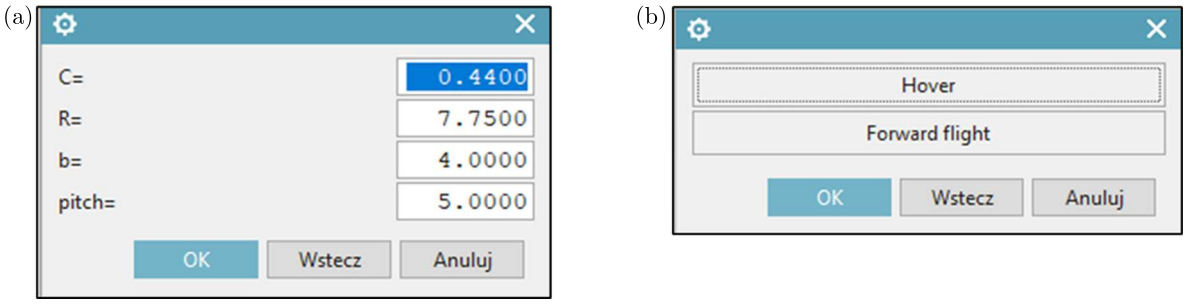

Fig. 5. User input options: (a) blade parameters, (b) flight conditions

The ready to simulation geometry is generated in few seconds, so the designer can prepare different models for CFD analysis in a short time.

4. Mesh and simulation properties

The model for CFD simulations was prepared in Ansys Fluent. The generated geometry with fluid domains was imported into the mentioned environment. To generate the fluid mesh of finite volume elements, the Fluent Mesher was used. It was chosen because of the future automatization of the process. This software provides a full path of activities that are necessary to generate the ready-to-use mesh. Body sizing, face sizing and inflation options were used to prepare a correct simulation. The boundary layer was generated using the aspect ratio options. The air enclosure size was calculated from the rotor dimensions. The ratios chosen to obtain correct domains were defined in the following way: X for the air enclosure, Y for the rotor enclosure and Z for the blade enclosures. The maximum size of a single volume element was set as 5000 mm, the elements on the blade were set to a value of 10 cm spanwise and chordwise. The inflation was set for 15 layers with 80 aspect ratio. The $y+$ value was established at an average value of 300, which gave the boundary layer a wall function. The mesh was generated as a poly-hexcore mesh and consisted of approximately 10^6 elements (depending on the model). An example of the prepared mesh is shown in Fig. 6.

Fig. 6. Polyhexcore mesh of fluid volume elements

The domains were named adequate to their destinations. The velocity inlet for the forward flight was set as a pressure far-field – velocity inlet, and the end of the cuboid was provided as a pressure outlet. The pressure far-field – velocity inlet option in Ansys Fluent provides a possibility to set the inlet velocity direction and magnitude with the vector coordinates. The contact regions were named to identify the internal connection between the domains in the preparing of the solution. K-ω SST viscosity model was chosen for the simulation, because it is recommended for solving CFD rotor tasks. The viscosity model results with the $y+$ for wall function boundary layer treatment were checked whether it gave satisfying results without extending calculation, what would be for more complex boundary layer simulations. The time step for transient simulation was set at 0.001 s. The convergence for each time step was settled for continuity at 10^{-5} with 100 iterations. The fluid domain with declared boundary conditions and the rotor model inside is presented in Fig. 7.

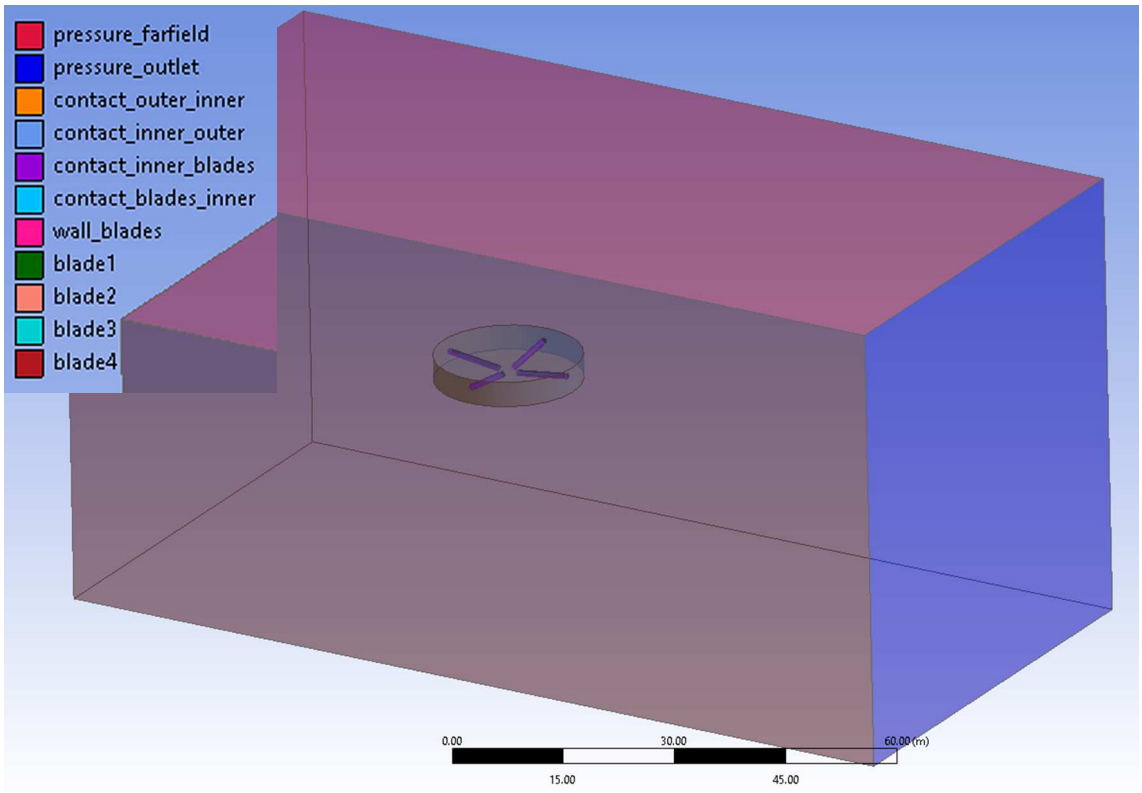

Fig. 7. The fluid domain with boundary conditions and the rotor model enclosure defined for the CFD process

5. Results

As a basis for CFD calculations, the rotor geometry of the rotorcraft W-3 Sokol was taken. The parameters of the helicopter are: radius – 7.85 m, chord – 0.44 m, rotational speed – 255 rpm, weight 6400 kg. The lift force should be adequate to the aircraft weight and the drag force is calculated from analytical assumptions. The first cut calculation was made for the existing rotor dimensions and features. The rotor position and movement were calculated in MATLAB program described in Section 2.2. For evaluation of the method, various rotor dimensions and flight parameters were used. The angles for the preparation of simulation are shown in Table 1.

Table 1. Calculated angles for simulation

Case No.	Collective [deg]	B_1 [deg]	A_1 [deg]	Tip path angle [deg]
1	11.12	3.46	−3.72	10.75
2	11.52	5.26	−4.87	10.71
3	8.31	2.52	−3.45	7.44
4	9.85	5.48	−5.48	7.43
5	9.48	3.10	−4.38	7.83

The calculated results are presented in Table 2. It shows that the assumptions which were made for the movement simulation and calculations are correct. The values of basic rotor forces are similar to those calculated, the average difference between the results and analytical calculations is at 4%. The comparison is made with analytical calculations of the drag force and

helicopter weight. The lift force that is required for flight of the helicopter is generated adequately to the needs.

Table 2. Simulation results

Case No.	Analytical assumptions					CFD simulation	
	Weight	MR radius [m]	Blade chord [m]	Flight speed [km/h]	Drag [N]	Lift [N]	Drag [N]
1	62784	7.85	0.3	100	1276	61706	1256
2	62784	7.85	0.3	150	2870	63708.25	2982
3	62784	7.85	0.44	100	1276	61537	1139
4	62784	7.85	0.44	200	5098	62625	5132
5	62784	7	0.6	100	1276	66850	1295

In consequence, working conditions of rotor blades can be evaluated using the obtained results. The major finding, that will be used in optimization loop (which will be aimed at mass reduction of the blades and stiffness improvement), is the pressure distribution. Examples of pressure distributions are shown in Fig. 8.

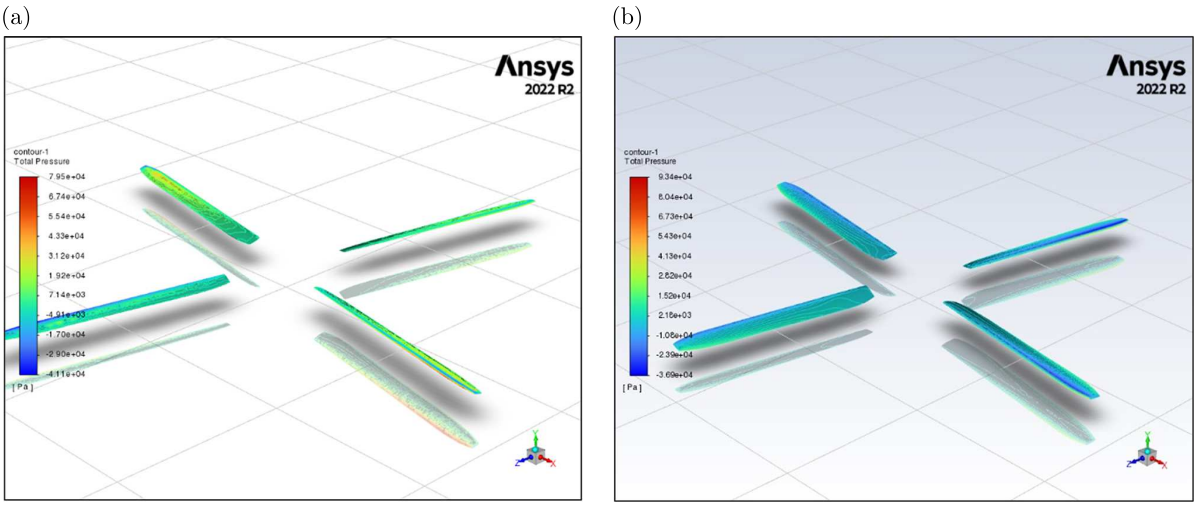

Fig. 8. Pressure distribution: (a) case 1, (b) case 2

The pressure distribution for the calculated flight case enables determination of the load acting on rotor blade surfaces during their rotary movement. Different flight conditions and different blade geometry can be evaluated by the designer. To obtain these results with application of the proposed method, 6 to 8 hours is needed, where 15 minutes is 3D model preparation, 45 min to 2 h is mesh and simulation preparation, the rest is Fluent processing time (which is also depending on mesh parameters).

The proposed way of model preparation and calculation of simulation parameters provides information about the influence of parametrisation on the obtained dimensions. The required drag and lift are the same for different flight parameters, however the angles of rotor disc and blade pitch positions are changing depending on blades dimensions. With CFD simulation, the proposed modelling was proved to be correct and applicable to next steps of rotor optimisation.

6. Conclusions

As it is described at the beginning of this paper, this research is a part of the program aimed at finding new solutions for rotorcraft structures design using optimization methods. This is a

next step for preparing a full rotor model which will be optimized to obtain the best mass and stiffness characteristics.

It is confirmed that developing the rotor model with fluid enclosures, using parametric modelling, provides a versatile tool to quickly prepare different rotor geometries for CFD analysis. The code properties provide a possibility to prepare correct fluid domains. The enclosures are generated proportionally to rotor dimensions. The Open GRIP syntax Boolean options, to cut out the volumes from wider areas, enables an exact model preparation, which is ready to be analyzed using dedicated software. The model compatibility problem with software did not occur during the calculations. Using the parametric modeling significantly reduced the time of simulation preparation for different geometries and flight conditions.

The CFD analysis confirmed the expected results. The mathematical model of the rotor movement led to similar forces that were inputs for analytical calculations. The generated domains and models were easily configured for mesh simulation. The interior contacts for mesh interaction during simulation of motion were correctly corresponding with the indented contact regions.

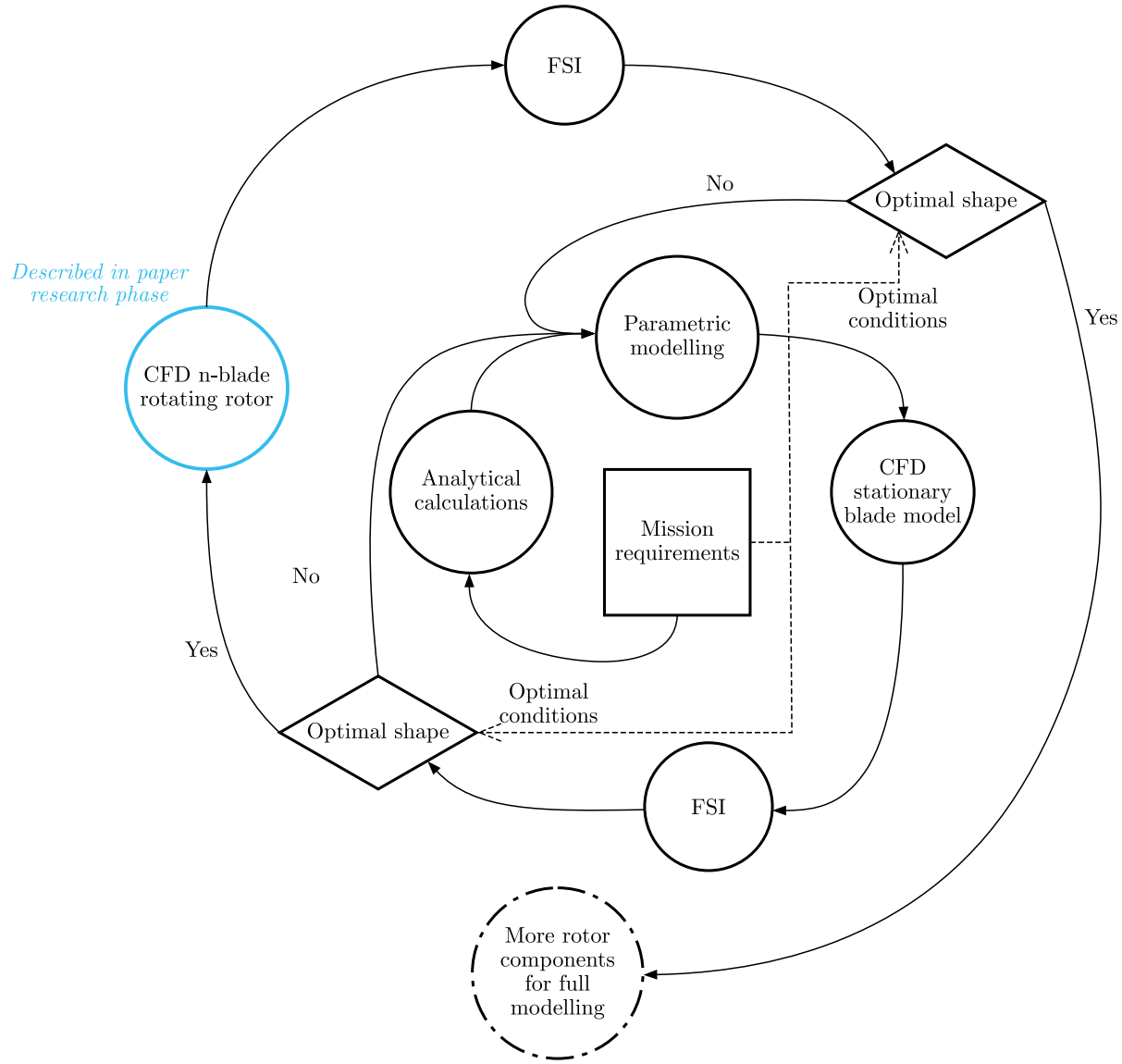

Fig. 9. Design spiral for rotor optimization

The simulation results showed that the model was correctly prepared. However, providing all required conditions to replicate the working environment of the real rotor, the simulation of the rotor movement and a change of pitch angles was time and memory consuming. But in fact it is a necessary condition to obtain correct results.

The studies shows a new way of preparing and conducting main rotor CFD simulations using a parametric approach. The parametric modelling reduces the total time of simulations. The results obtained showed the working conditions of the main rotor blades in terms of pressures, velocity or turbulence. The outputs can now be combined in Ansys with FEM analysis and calculated simultaneously using the FSI procedure.

The advantage of the procedure is fidelity of the simulation. This kind of simulations provides high fidelity results, that can be used to evaluate parameters of prepared blades such us the shape and strength structure. This will be a next phase of the proposed optimization loop. The application of the studies described in this paper is only a one of many activities included in the optimization procedure illustrated with the so called design spiral. It is shown in Fig. 9.

Acknowledgement

The methods and results presented in this paper have been obtained during research works conducted within a university research project entitled "Methods of optimal design of aircraft to improve its structural and aerodynamic properties". It was financed by the Military University of Technology (Warsaw, Poland), in in 2022 and 2023, under the university research project UGB-782/2022 and UGB-819/2023.

Data Availability Statement

Program code is available at: https://github.com/jakubkocjan/parametricrotordesign (accessed on 30 November 2022).

The work and its results were presented during the conference "Mechanika w Lotnictwie, ML-XX 2022".

References

1. Allen L.D., Lim J.W., Haehnel R.B., Dettwiller I.D., 2021, *Rotor Blade Design Framework for Airfoil Shape Optimization with Performance Considerations*, Engineer Research and Development Center
2. Bailly J., Bailly D., Didier B., 2019, Multifidelity aerodynamic optimization of a helicopter rotor blade, *AIAA Journal*, **57**, 8, 3132-3144
3. Bramwell A.R.S., Done G., David B., 2011, *Bramwell's Helicopter Dynamic*, Butterworth-Heinemann, Linacre House, Jordan Hill, Oxford
4. Grabowik C., Kalinowski K., Kempa W., Paprocka I., 2015, A method of computer aided design with self-generative models in NX Siemens environment, *IOP Conference Series: Materials Science and Engineering*, **95**, 1
5. Grebrnikov A.G., *et al.*, 2021, Analysis of design and technological features of the main rotor blades of heavy transport helicopters, *Open Information and Computer Integrated Technologies*, **93**
6. Goerke D., Le Denmat A.L., Schmidt T., Kocian F., Nicke S., 2012, Aerodynamic and mechanical optimization of CF/PEEK blades of a counter rotating fan, *Proceedings of the ASME Turbo Expo*, **7**, Parts A and B
7. Jain R., 2022, Computational fluid dynamics transition models validation for rotors in unsteady flow conditions, *Journal of Aircraft*, **59**, 4
8. Johnson W., 1994, *Helicopter Theory*, Dover Publications, New York
9. Kachel S., Rogólski R., Kocjan J., 2021, Review of modern helicopter constructions and an outline of rotorcraft design parameters, *Problems of Mechatronics Armament Aviation Safety Engineering*, **12**, 3

10. Kocjan J., Kachel S., Rogólski R., 2022, Helicopter main rotor blade parametric design for a preliminary aerodynamic analysis supported by CFD or panel method, *Materials*, **15**, 12

11. Lim J.W., 2018, Application of parametric airfoil design for rotor performance improvement, *44th European Rotorcraft Forum 2018, ERF 2018*, **1**

12. Ma L., Zhao Q., Zhang K., Zhang X., Zhao M., 2021, Aeroelastic analysis and structural parametric design of composite rotor blade, *Chinese Journal of Aeronautics*, **34**, 1

13. Oh S., Park D., Ji H.M., 2021, Development of preliminary conceptual design/comprehensive analysis programs for next generation rotorcraft, *Journal of the Korean Society for Aeronautical and Space Sciences*, **49**, 1

14. Okumuş O., Senipek M., Ezertas A., 2022, Multi-objective multi-fidelity aerodynamic optimization of helicopter rotor, *AIAA SCITECH 2022 Forum*

15. Ryazanov A.I., 2016, Automated 3D modeling of working turbine blades, *Russian Engineering Research*, **36**, 9

16. Sagimbayev S., Kylyshbek Y., Batay S., Zhao Y., Fok S., Lee T.S., 2021, 3D multidisciplinary automated design optimization toolbox for wind turbine blades, *Processes*, **9**, 4

17. Shabliy L.S., Dmitrieva I.B., 2014, Conversion of the blade geometrical data from points cloud to the parametric format for optimization problems, *ARPN Journal of Engineering and Applied Sciences*, **9**, 10

18. Slavik S., Klesa J., Brabec J., 2020, Propeller selection by means of pareto-optimal sets applied to flight performance, *Aerospace*, **7**, 3

19. Spyropoulos N., Papadakis G., Prospathopoulos J.M., Riziotis V.A., 2021, Investigating the level of fidelity of an actuator line model in predicting loads and deflections of rotating blades under uniform free-stream flow, *Applied Sciences*, **11**, 24

20. Stalewski W., 2017a, Design and optimisation of main rotor for ultralight helicopter, *Journal of KONES Powertrain and Transport*, **24**, 4

21. Stalewski W., 2017b, *Design and aerodynamic optimization of rotorcraft* (in Polish), Warsaw

22. Stalewski W., Zalewski W., 2019, Aerodynamic design and optimisation of main rotors for light rotorcrafts, *45th European Rotorcraft Forum 2019, ERF 2019*, **1**

23. Tixadou E., 2021, Optimisation of the structure of A helicopter blade in view of reducing cabin vibration, *Proceedings of the 47th European Rotorcraft Forum*, Google Scholar

24. Wilke G., 2021, Quieter and Greener rotorcraft: concurrent aerodynamic and acoustic optimization, *CEAS Aeronautical Journal*, **12**, 3

25. Xie J., Xie Z., Zhou M., Qiu J., 2017, Multidisciplinary aerodynamic design of a rotor blade for an optimum rotor speed helicopter, *Applied Sciences*, **7**, 6

Manuscript received April 24, 2023; accepted for print August 3, 2023

JOURNAL OF THEORETICAL AND APPLIED MECHANICS
61, 4, pp. 807-818, Warsaw 2023
https://doi.org/10.15632/jtam-pl/172571

INFLUENCE OF THE SHAPE OF THE COPPER COMPONENT ON MECHANICAL PROPERTIES OF THE FRICTION MATERIAL USED IN DISC BRAKES

Andrzej Borawski

Bialystok University of Technology, Faculty of Mechanical Engineering, Bialystok, Poland

e-mail: a.borawski@pb.edu.pl

Brakes are an important safety feature of vehicles. The materials of which the friction elements are made pose some risk to the environment. This can be a case during manufacture, operation and disposal. Any step to improve the ecology deserves thorough examination and possible introduction into production. For this reason, it has been decided to investigate whether it is possible to replace aramid with another material that is already present in its composition. The choice fell on copper, which was used in prepared samples in the form of both powder and fibers.

Keywords: friction materials, composite, mechanical strength, material properties

1. Introduction

Automobiles are extremely popular these days. Most households own one or more vehicles. It is estimated that the number of vehicles on our planet will increase to over 2 trillion by 2030. In addition, today's cars are characterized by much better performance. The combination of the above two factors can lead to dangerous situations on the road. Therefore, it is extremely important that vehicles are equipped with effective braking systems. The health or even lives of many road users may very often depend on their correct operation. The high level of today's scientific workshop provides the opportunity to develop solutions that can meet the restrictive requirements.

The most popular and widely used solution since the first horse-drawn carriages has been friction brakes (Eriksson, 2000). Then, as now, these brakes are a kind of converter of kinetic energy of motion into thermal energy (Kukutschová *et al.*, 2010). Such a solution, despite obvious advantages, unfortunately has its disadvantages. One of the biggest is the amount of heat generated during emergency braking, especially in vehicles with high weight (Kuciej *et al.*, 2020). For this reason, friction materials must have suitable properties that allow them to operate at such high temperatures, but also to dissipate the heat quickly enough to prevent overheating of the brake fluid, for example (Ertan and Yavuz, 2010). In addition, the friction materials used in vehicle brakes should be weather-resistant and pose as little risk to the environment as possible during manufacturing, operation, and recycling (Singaravelu *et al.*, 2019).

The friction layer of the brake pad is usually a composite material with different compositions depending on the manufacturer. There are several thousands materials as the basis for the components used, of which 10-20 are selected for a single product (Nagesh *et al.*, 2014). Like any composite, the pad must contain a reinforcement. Currently, this role is most often played by aramid, and sometimes by carbon or glass fibers. Unfortunately, as described in a previous work (Borawski, 2023), their production is associated with particular hazards for humans and the environment.

One of the most important pad materials is copper. It is a multifunctional and almost indispensable component of friction materials (Österle *et al.*, 2010). It does not only ensure structural integrity, but also significantly improves dissipation of frictional heat. Thanks to these properties, copper significantly reduces the risk of fading at high temperatures (Kumar and Bijwe, 2011). A major problem is the fact that copper, so necessary in friction materials, becomes one of the components of wear products released into the environment as a result of friction and rubbing. Unfortunately, as numerous studies have shown, it is a serious pathogen, especially for aquatic organisms, but also for humans, where it can cause severe multi-organ diseases (Azizishirazi *et al.*, 2013). For this reason, regulations have been introduced to limit the percentage content of this element in friction materials from 2025 (Hjortenkrans *et al.*, 2007). Therefore, numerous researchers have attempted to replace copper with organic fibers (Matejka *et al.*, 2013; Yun *et al.*, 2010), solid lubricants (Lee *et al.*, 2010), and various types of metals (Martínez *et al.*, 2014). However, the test results showed that none of the proposed materials was a fully satisfactory alternative to copper.

Considering the above fact, which is almost related to the necessity of using copper in brake pads, it was decided to test if copper could take over the role of aramid, i.e., serve as reinforcement in addition to its basic function. For this purpose, geometry of copper particles must be changed from spherical to fibrous. From a literature survey, the shape and size of the particles can have the following effects in the course of the friction process (Sellami *et al.*, 2020; Wojciechowski *et al.*, 2013; Kumar and Bijwe, 2011):

- the finer the copper particles, the better the lubrication properties and thus the lower coefficient of friction and greater resistance to abrasive wear;
- an irregular shape or sharp edges increase the value of the coefficient of friction;
- a higher copper concentration improves the lubricity and thermal conductivity of the final product.

In the previous works, it was shown that the shape of the copper could indeed affect the COF. Using fibers instead of round particles and removing aramid increased the coefficient of friction by about 13% (Borawski, 2023). The purpose of this work is to examine how the above change in the reinforcement method affects mechanical properties of the composite friction material.

It is considered that the most important mechanical properties of friction materials are hardness, density, compressive and shear strength, water and oil absorption, friction and wear resistance (Akíncíoğlu *et al.*, 2021). Literature review has shown that researchers more often focus on tribological than mechanical properties, which are equally important from an operational point of view. Wannik *et al.* (2012) studied samples produced with an addition of boron. The research results, such as hardness, porosity, and specific gravity, were compared to results for a commercial material. The bootstrap method was used to analyze the results. Bahari *et al.* (2012) investigated the hardness and wear resistance of friction materials with the addition of rice husk dust (RHD) at a concentration of 10% and 30%. The obtained results showed that RHD, especially at a concentration of 30%, had a positive effect on the hardness of the proposed prototype material. Comprehensive material studies were conducted by Parandaman *et al.* (2015). They focused on tensile, bending strength and additionally friction and wear tests. In their study, they prepared four groups of samples with different coconut fiber contents: 0%-15% by volume (5% increments). They also used a variable compression pressure (10-60 tons). It was found that the coconut fiber content of 5% and 10% gave the best flexural and compressive strength. A classical strength measuring machine was used for the tests. Gai *et al.* (2022) addressed a similar issue. The subject of their study was also four groups of samples, but they were cut from commercially available brake pads. The tests included determination of bending resistance, hardness, coefficient of friction and abrasion resistance. X-ray and scanning microscopy

tests were also conducted. The researchers found that the composition of the material had a significant impact on the results of the tests performed. Accordingly, a higher carbon content had a positive effect on the mechanical strength of the friction material. They also found a coupling between hardness and wear rate. Mutlu *et al.* (2015) studied mechanical properties of the material samples he produced. Candlenut and coconut shells, which are rare in this role, were present in the composition. Their total content varied between 40% and 60%. The rest consisted of iron powder, carbon, resin and pineapple leaf fibers. The components were crushed with a mill and then pressurized in a hydraulic press. The semi-finished products were subjected to a pressure of 15 kPa and then heated at 100°C. Water absorption, hardness and tribological properties were tested on the finished samples. A chemical composition analysis was also performed using the EDS method. Again, a correlation between hardness and wear resistance was confirmed. The high content of plant-derived additives proposed by the researchers also improved resistance to water absorption. The mechanical properties of friction materials made of basalt were studied by Gai *et al.* (2022). It served as a filler. The other constituents were selected from the conventional range, i.e. resin as the matrix, glass fiber as the reinforcement, and bronze and cast iron as friction modifiers. The authors determined mechanical properties such as compressive strength, hardness, tensile strength and water absorption, among others. They found that the addition of basalt had positive effects, including an increase in the compressive strength or coefficient of friction compared to conventional materials. The tensile strength and thermal conductivity were even better than those of ceramic-based friction materials.

Based on this analysis, it was decided to conduct compression, bending, tensile strength tests and to measure the hardness and water absorption of water, brake fluid and oil. In authors opinion, these are the most important mechanical properties of composite friction materials, the values of which should be at a certain level.

2. Materials and methods

Each of the above studies required a different test, often performed at a different stand. Most of the tests were destructive, so individual samples were required. These were prepared according to the proportions given in Table 1. Component mixtures were measured using a Steinberg SBS--LW-300A balance. The materials were then mixed in a custom-built device using an additive technology (Fig. 1). The device was thoroughly cleaned and dried after each use. The final mixtures were poured in a mold and then placed in a hydraulic press and loaded with a force of $100 \cdot 10^3$ N for about 12 hours. After the load was removed, the samples were annealed at 60°C for 48 h. After this time, the molds were removed and the surfaces of the samples were ground to give them the desired shape, dimension and surface roughness.

Table 1. Composition of the prepared samples

Component	Contents [%]			
	S1	S2	S3	S4
CuZn20	12	12	12	12
Cu	25	25	25	25
S355 Steel	7	7	7	7
Aramid	12	8	4	0
Resin	17	17	17	17
Graphite	5	5	5	5
Fly ash	18	22	26	30
EN-GJS-400-12	4	4	4	4

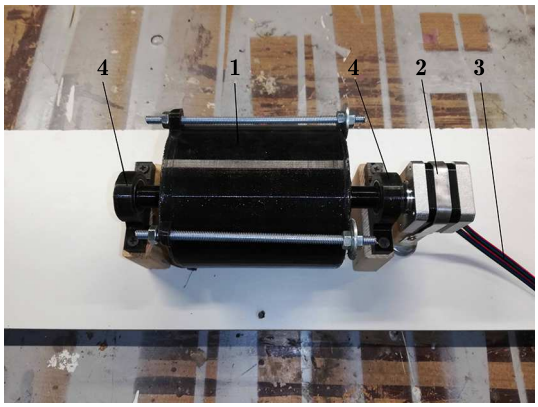

Fig. 1. Mixing of sample components: 1 – mixing unit, 2 – stepper motor, 3 – driver connection, 4 – bearing

2.1. Static compression test

The latest standard ISO 6310 provides for different test variants. They can be performed at both low and high temperatures. The test methods have also been divided into pneumatic (method A) and hydraulic (method B), depending on the type of a braking system. A maximum compression speed of 15 mm/min is also specified. The limit pressure is 10 MPa or 16 MPa – depending on the intended use of the material. This compressive strength test was performed using the Instron 8502 device (Fig. 2), which meets the requirements of the Standard. To maximize accuracy, the input parameters of the test were set as follows: feed rate 0.1 mm/s, measurement frequency 100 Hz. The samples prepared for this test were cylindrical, had a diameter of 20 mm and a height of 25 mm (Fig. 3).

Fig. 2. Compressive strength test

2.2. Static bend test

The brake pads are subjected to a small amount of bending under real conditions. It results only from the fact that the pad working on the inner side of the brake disk is pressed only in the central part, and the movement of the outer pad causes pressure to the caliper on the opposite

Fig. 3. Samples tested in compression test

edges. The fact that the friction material is mounted on a steel support plate further reduces the effects of bending versus compression and stretching on potential damage. Nevertheless, bending does occur, therefore it was considered reasonable to perform a static bending test to obtain a more complete picture of the mechanical properties of the proposed material.

The Instron 8502 apparatus was used for the tests. The technical standard BN 0601-12-1 suggests that the bending tests should be performed with a three-point support – two lower fixed supports, and the upper one movable. The maximum feed rate of the breaking mandrel was set at 5 mm/min. A prerequisite for correctness of the test is that the cracks occur at a distance of no more than 10 mm from the load application. Therefore, to maximize quality of the results, the speed was set to 0.05 mm/s (3 mm/min). The recording frequency was set to 100 Hz as before. Rectangular samples with dimensions of 12 mm×12 mm×90 mm were used in the study (Fig. 4). According to the Standard, the distance between the supports was 75 mm and the load was applied centrally (Fig. 5).

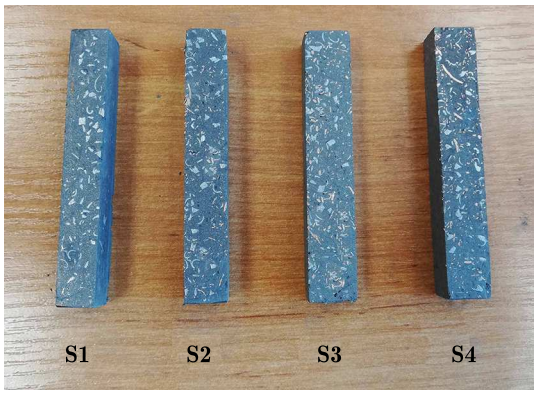

Fig. 4. Samples made for bending tests

Fig. 5. Bending resistance test

2.3. Static tensile test

The basis for this type of test is the standard ISO 6892-1:2019. The test described therein is simple and consists of uniaxial stretching of a material sample. The prerequisite for correct performance is the use of self-centering holders that ensure the required stress state. The above Standard recommends that the stress increase rate in the sample be between 2 MPa/s and 20 MPa/s.

In this case, Instron 8502 was also used with special holders that allow the centering of the sample (Fig. 6). The input parameters for the test were assumed to be a feed rate of 0.05 mm/s and a maximum displacement of 50 mm. This ensured the correct stress increase rate.

The samples used in the test were the same as in the bending test – rectangular with dimensions 12 mm×12 mm×90 mm.

Fig. 6. Tensile strength test

2.4. Hardness measurement

The hardness of the prepared samples was measured ten times at randomly selected points for each sample. This was necessary because the composite material was generally not homogeneous. The tests were carried out with the PRL 610 hardness tester (Fig. 7).

The final test result was the arithmetic mean. The standard deviation for each measurement was calculated according to the following formula

$$s = \sqrt{\frac{1}{n-1}\sum_{i=1}^{n}(x_i - \overline{x})^2} \tag{2.1}$$

where: s – standard deviation, n – number of measurements, x_i – result of the i-th measurement, $\overline{x}$ – arithmetic mean of the results for a given sample.

Fig. 7. Hardness tester PRL 610

2.5. Measurement of water, brake fluid and oil absorption

This parameter is extremely important, as the properties of the friction material can change when saturated with a liquid. The most influential substances here are oils (which can reduce the coefficient of friction) and brake fluids (whose corrosive properties can reduce structural integration of the composite material). Absorption is closely related to porosity. Some manufacturers deliberately design the friction material to be highly absorbent, which they believe improves heat dissipation from the friction junction (Gai *et al.*, 2022). According to the applicable Standard, i.e. ISO-6314, cylindrical samples (diameter 1″, height 20 mm) immersed in liquids and left for 7 days were tested. These fluids were water, common 5W30 viscosity grade motor oil and DOT4 brake fluid. Each sample was thoroughly cleaned and weighed prior to testing using a Steinberg SBS-LW-300A precision balance and then measured with a micrometer. After testing, the surface of the samples was dried with paper towels, then weighed and measured again. Based on this data, the water absorption could be determined.

3. Results and discussion

The results of the strength tests are presented in Fig. 8-10. The static compression test showed that all samples submitted for testing had similar strength. Sample S3 had a slight advantage over the others, withstanding stresses of nearly 79.6 MPa.

The results obtained in the tensile and bending tests turned out to be extremely interesting and surprising. When samples with a high aramid content (S1 and S2) were bent, clear fiber breaks could be seen. These materials resemble brittle materials in their properties. Changing copper geometry from powder (S1) to fiber (S2) increased the allowable stresses by almost 50%. The most favorable sample was S3, which exhibited properties similar to a plastic due to the

small amount of aramid and long copper fibers. This sample showed a stress limit of just over 80.7 MPa. The worst performing sample was the one in which the aramid was completely replaced by copper fibers – a much more ductile metal. As a result, S4 composite lost a significant amount of its strength, for which the reinforcement was responsible. The maximum stress is only 26 MPa, which is just under 30% of the value achieved by S3 sample.

During the tensile test, S3 sample also proved to be the strongest, reaching the allowable stress of 9.2 MPa. Samples with a higher content of aramid and copper in the form of shorter fibers (S2) and powder (S1) turned out to be weaker, but reaching the limit stresses took more time. All samples containing aramid (S1-S3) showed clear characteristics of brittle materials. The last sample (S4), where aramid was completely replaced by copper fibers, behaved like a typical plastic material. The stress buildup was much slower, and there was no clear fracture boundary. The cause for such behavior should be sought in the properties of copper.

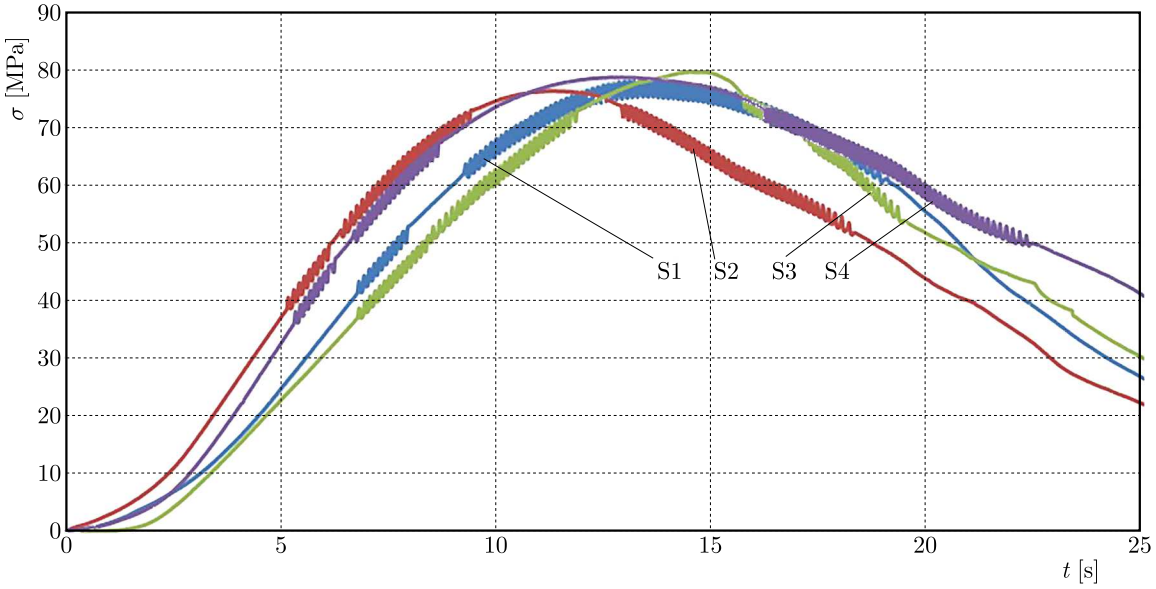

Fig. 8. Static compression test

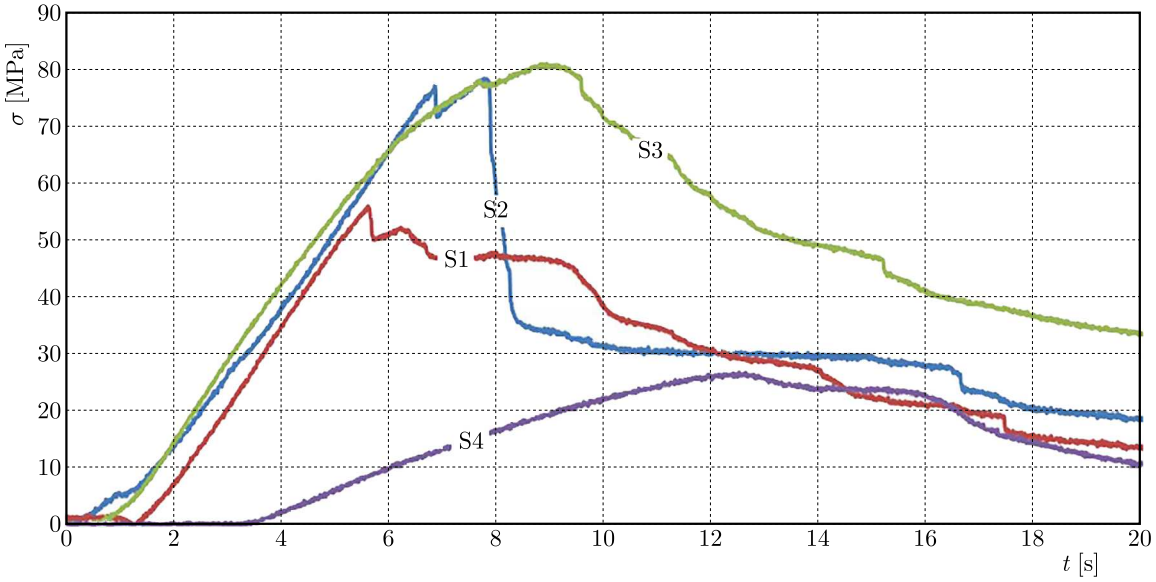

Fig. 9. Static bend test

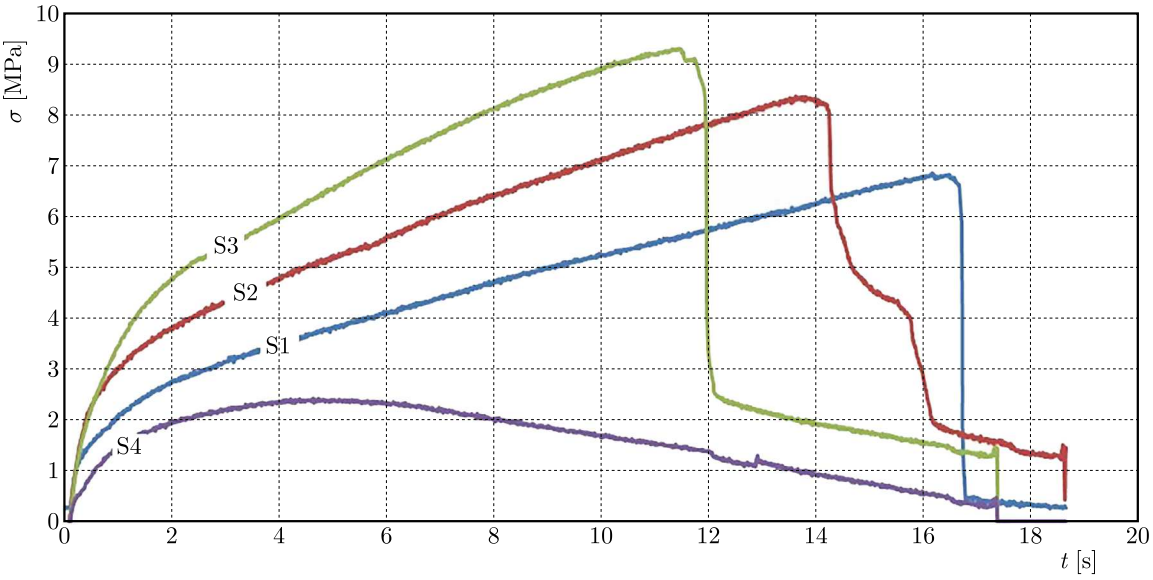

Fig. 10. Static tensile test

The results of the hardness test are shown in Fig. 11. This parameter is closely related to mechanical strength. It determines the resistance to plastic deformation, penetration, scratching or frictional wear. The measurements showed that the values for samples S1-S3 were similar. Taking into account the standard deviation, whose high value results from the fact that the object of study is a composite material, it can be assumed that the samples of these three groups have the same hardness. The results for sample S4, taking into account the standard deviation, are within the above range, but the average value here is the lowest. A clear reflection is visible in the strength tests described above.

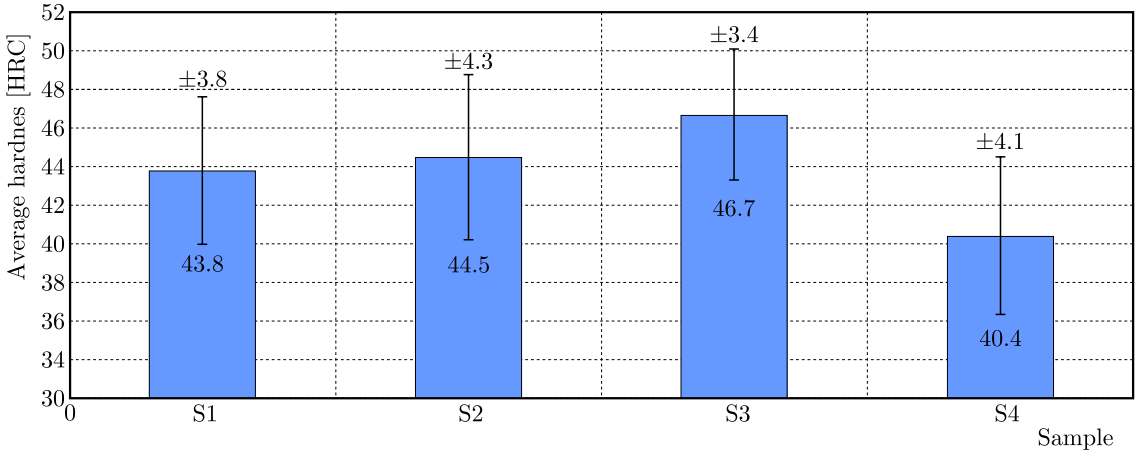

Fig. 11. Hardness test results

The results of the fluid absorption tests are shown in Table 2. After the measurements were completed, the liquid on the surface of each sample was wiped off before it was calcified. The final absorbance value was calculated using the following equation

$$A = \frac{M_f - M_i}{M_i} \cdot 100\% \tag{3.1}$$

where: A – absorption, M_f – mass of the sample after immersion in liquid, M_i – initial mass.

The above values show that all samples are characterized by similar, low absorption. Slight variations are due to random factors in the production process.

Table 2. Results of liquid absorption tests

Substance	Sample	M_i [g]	M_f [g]	Mass gain [g]	A [%]
Water	S1	30.269	30.404	0.135	0.445
	S2	30.771	30.960	0.189	0.615
	S3	31.604	31.719	0.115	0.364
	S4	31.743	31.947	0.204	0.644
5w30 oil	S1	30.762	30.873	0.111	0.362
	S2	31.637	31.853	0.216	0.683
	S3	31.204	31.356	0.152	0.486
	S4	31.097	31.247	0.150	0.481
Water	S1	30.576	30.777	0.201	0.659
	S2	31.215	31.334	0.119	0.380
	S3	31.261	31.386	0.125	0.399
	S4	31.369	31.539	0.170	0.542

4. Summary

This paper presents the results of tests of the mechanical properties of composite materials. These prototype materials were developed with the intention of being used in braking systems. The prepared samples differed in the type of reinforcement. It has been found that:

- the best strength properties and the highest hardness are obtained when a significant part of the aramid reinforcement is replaced by a copper one with moderate fibre length (sample group S3),
- the type of reinforcement used has no effect on the absorption of water, oil and brake fluids,
- the complete absence of a conventional reinforcement with the properties of a brittle material leads to a significant reduction in the mechanical properties of the composite friction material, making it more plastic.

Summing up, it is possible to reduce the aramid content and thus the environmental impact generated during the manufacturing process, while improving the mechanical properties of the composite. This can be achieved by changing the geometry of copper particles from powder to fibre.

Acknowledgments

The research was carried out as a part of work No. WZ/WM-IIM/5/2023 at the Białystok University of Technology and financed from the research subsidy provided by the Ministry of Science and Higher Education.

References

1. Akíncíoğlu G., Akíncíoğlu S., Öktem H., Uygur I., 2021, Brake pad performance characteristic assessment methods, *International Journal of Automotive Science and Technology*, **5**, 1, 67-78
2. Azizishirazi A., Dew W.A., Forsyth H.L., Pyle G.G., 2013, Olfactory recovery of wild yellow perch from metal contaminated lakes, *Ecotoxicology and Environmental Safety*, **88**, 42-47
3. Bahari S.A., Isa K.H., Kassim M.A., Mohamed Z., Othman E.A., 2012, Investigation on hardness and impact resistance of automotive brake pad composed with rice husk dust, *AIP Conference Proceedings*, **1455**, 155–161

4. Borawski A., 2023, Study of the influence of the copper component's shape on the properties of the friction material used in brakes – Part one, *Tribological Properties, Materials*, **16**, 2, 749

5. Eriksson M., 2000, *Friction and Contact Phenomena of Disc Brakes Related to Squeal*, Citeseer, Pensylvania

6. Ertan R., Yavuz N., 2010, An experimental study on the effects of manufacturing parameters on the tribological properties of brake lining materials, *Wear*, **268**, 11-12, 1524-1532

7. Gai P.F., Adisa A.B., Aje T., Bawa M.A., 2022, Physico-mechanical properties of basalt-based brake pad as alternative to ceramics brake pad, *Saudi Journal of Engineering and Technology*, **7**, 1, 16-33

8. Hjortenkrans D.S.T., Bergbäck B.G., Häggerud A.V., 2007, Metal emissions from brake linings and tires: Case studies of Stockholm, Sweden 1995/1998 and 2005, *Environmental Science and Technology*, **41**, 15, 5224-5230

9. Kuciej M., Grzes P., Wasilewski P., 2020, A comparison of 3D and 2D FE frictional heating models for long and variable applications of railway tread brake, *Materials*, **13**, 21, 4846

10. Kukutschová J., Roubček V., Mašláň M., Jančk D., Slovák V., Malachová K., 2010, Wear performance and wear debris of semimetallic automotive brake materials, *Wear*, **268**, 1- 2, 86-93

11. Kumar M., Bijwe J., 2011, Non-asbestos organic (NAO) friction composites: Role of copper; its shape and amount, *Wear*, **270**, 3-4, 269-280

12. Lee P.W., Leist J., Filip P., 2010, Use of hexagonal boron nitride in automotive friction materials, *SAE Technical Paper*, **2010-01-1676**, 1-12

13. Matějka V., Fu Z., Kukutschová J., Qi S., Jiang S., Zhang X., Yun R., Vaculík M., Heliová M., Lu Y., 2013, Jute fibers and powderized hazelnut shells as natural fillers in non-asbestos organic non-metallic friction composites, *Materials and Design*, **51**, 847-853

14. Martínez A.M,. Echeberria J., Loreto D., Antonio Z., Rampin M., Ilaria J., 2014, Development of copper-free low steel brake pads for light vehicles, *Proceedings of Eurobrake*, **EB2014--DF-002**, 1-9

15. Mutlu I., Sugöz I., Keskin A., 2015, The effects of porosity in friction performance of brake pad using waste tire dust, *Polmeros*, **25**, 5

16. Nagesh S.N., Siddaraju C., Prakash S.V., Ramesh M. R., 2014, Characterization of brake pads by variation in composition of friction materials, *Procedia Materials Science*, **5**, 295-302

17. Österle W., Prietzel C., Kloss H., Dmitriev A.I., 2010, On the role of copper in brake friction materials, *Tribology International*, **43**, 12, 2317-2326

18. Parandaman P., Jayaraman M., Ramasamy K.K., Premkumar M., 2015, Mechanical performance of coir and glass fibre reinforced hybrid composite materials for automotive brake pad, *International Journal of Applied Engineering Research*, **10**, 32, 23981-23988

19. Sellami A., Hentati N., Kchaou M., Chowdhury M. A., Elleuch, R., 2020, Effect of size and shape of copper alloys particles on the mechanical and tribological behavior of friction materials, *Mechanics and Industry*, **21**, 613, 1-13

20. Singaravelu D.L., Ragh R., Vijay R., Manoharan S., Kchaou M., 2019, Development and performance evaluation of eco-friendly crab shell powder based brake pads for automotive applications, *International Journal of Automotive and Mechanical Engineering*, **16**, 2, 6502-6523

21. Wannik W.B., Ayob A.F.M., Samion S., Masjuki H.H., Fadhi Fadhi Ahmad M., 2012, The effect of boron friction modifier on the performance of brake pads, *International Journal of Mechanical and Materials Engineering*, **7**, 1, 31-35

22. Wojciechowski A., Gołowicz A., Michalski R., 2013, Influence of the form of copper in the friction material of disc brakes on the coefficient of friction and wear in rig tests, *Archiwum Motoryzacji*, **62**, 77–88

23. Yun R., Filip P., Lu Y., 2010, Performance and evaluation of eco-friendly brake friction materials, *Tribology International*, **43**, 11, 2010-2019

Manuscript received June 30, 2023; accepted for print August 16, 2023

JOURNAL OF THEORETICAL AND APPLIED MECHANICS
61, 4, pp. 819-831, Warsaw 2023
https://doi.org/10.15632/jtam-pl/172966

APPLICATION OF THE FOREST CLASSIFIER METHOD FOR DESCRIPTION OF MOVEMENTS OF AN OSCILLATOR FORCED BY A STOCHASTIC SERIES OF IMPULSES

Marek Sulewski, Agnieszka Ozga
AGH University of Krakow, Faculty of Mechanic Engineering and Robotics, Krakow, Poland
e-mail: sulewski@agh.edu.pl; aozga@agh.edu.pl

The article discusses the analysis of motion of an oscillator forced by a sequence of stochastic impulses with the use of decision tree algorithms and a random forest classifier. The aim of this paper is to verify the accuracy of distinguishing distributions in the desired time period and to check whether the length of the time interval affects the accuracy of data classification. Moreover, the statistical parameters directly influencing classification of distributions are presented. The analysis has been performed in Python environment, the data were obtained in computer simulation. The results of classification for two classification algorithms with regard to two divisions of the test and training set sizes are presented. In case of the decision tree classifier, it has been observed that for each time interval this algorithm classifies the data achieving a high level of accuracy, but for the purpose of data classification for each time period it selects different statistics, which makes it impossible to unequivocally determine which statistic influences the recognition of distribution. In case of the random forest classification algorithm, the importance and influence of the parameters on the distribution between the three distributions are the same both in 5-minute and 10-minute intervals. The differences between significance of the parameters depending on length of the interval are not significant.

Keywords: machine learning, random forest classifier, stochastic series of impulses

1. Introduction

The theory of random dynamical systems is an interdisciplinary domain (Sobczyk, 1983; Iwankiewicz and Kotulski, 2009; Zembaty, 2009; Socha and Soong, 1991; Liu *et al.*, 2023; Banks *et al.*, 2023). It is applied in mechanics (Litak *et al.*, 2008; Bozzoni *et al.*, 2011; Hračov and Náprstek, 2017; Weber *et al.*, 2021; Smolnicki *et al.*, 2013; Rączka *et al.*, 2013) where, like in the present paper, the idea of research refers to non-deterministic mechanics. The state of a system observed at any given moment does not univocally determine the states of the system at consecutive moments, which issues from the random character of stimulaton. It is worth mentioning that in Poland the studies on random dynamic systems flourished in the third quarter of the 20th century (Piszczek, 1982; Skalmierski and Tylikowski, 1972) when, by means of a complex mathematical apparatus, a series of stochastic equations describing various kinds of dynamic mechanical systems have been determined. Having reached a certain level of knowledge, the studies have not been continued.

The research on systems forced by a random series of impulses also started in the second half of the 20th century (Roberts, 1966, 1972; Roberts and Spanos, 2003) and have been continued ever since. The first attempts at verification of properties of a stochastic model by means of simulation methods were presented by Professor Iwankiewicz (Iwankiewicz, 1993). The research was also conducted by (Mazur-Śniady and Śniady, 1986; Jabłoński and Ozga, 2008) in Poland.

By introducing machine learning into the analysis of dynamic mechanical systems, we are starting the next level of research. In this original approach, thousands of samples have been analyzed for different parameters of random forcing in order to examine usefulness of developed algorithms.

In this study, the developed algorithms are aimed at solving an inverse problem, namely recognition of the distribution of size of impulses forcing vibrations of an oscillator. Although there exists a mathematical model that allows one to calculate the impulse distributions, its applicability, however, is limited. Thus, other solutions of this problem are searched for, and this stage of research is described in this paper.

2. Mathematical model of an oscillator forced by a random series of impulses

The random forest classifier discussed in this paper was carried out for a one-dimensional physical system (Jabłoński and Ozga, 2013) the state of which was described by random variable $x(t)$. The equation of vibrations of an oscillator with damping was presented in a dimensionless form

$$\frac{d^2x}{dt^2} + 2b\frac{dx}{dt} + a^2x = f(t) \tag{2.1}$$

At this stage of research into the possibility of recognizing random distributions of excitation impulses, it is difficult to assess whether the oscillator will be in the form of a mechanical or electronic system. Since the value of $x(t)$ is accepted as dimensionless, consequently, the units occurring with coefficients a, b, and $f(t)$ are referred to time only.

The $f(t)$ is a series of random impulses with random strength η_i occurring at random instants of time t_i

$$f(t) = \sum_{t_i<t} \eta_i \delta(t - t_i) \tag{2.2}$$

where $\delta(t - t_i)$ – Dirac distribution.

The time intervals between impulses $\tau_i = (t_i - t_{i-1})$ are independent continuous random variables for which the function of probability density assumes the form of an exponential function

$$t(\tau) = \begin{cases} \lambda \mathrm{e}^{-\lambda\tau} & \text{for} \quad \tau \geqslant 0 \\ 0 & \text{for} \quad \tau < 0 \end{cases} \tag{2.3}$$

where the constant λ is the impulse occurrence frequency.

For the random variable described by Eq. (2.3), the mean distance between impulses is $1/\lambda$ s, standard deviation also amounts to $1/\lambda$ s, while the median interval between impulses equals $\ln 2/\lambda$.

The values of the η_i impulse are independent discrete random variables with a finite expected value. When intervals between the impulses and strength of the impulses are independent random variables, then the solution of this problem for zero initial conditions is

$$x(t) = \frac{1}{c} \sum_{0<t_i<t} \eta_i \mathrm{e}^{-b(t-t_i)} \sin[c(t - t_i)] \tag{2.4}$$

where $c = \sqrt{a^2 - b^2}$.

The article examines $\overline{m}_i(t)$ – estimators of the k-th stochastic raw moments of the random variable $x(t)$ calculated using the equation

$$\overline{m}_k = \frac{1}{t/h} \sum_{n<t/h} x^k(nh) \tag{2.5}$$

where h is the period of sampling, t is time.

3. Designing of experimental studies using the qualitative method of analysis

Studies on the stochastic model described by Eqs. (2.1)-(2.5) should be appropriately designed so that step changes do not occur in the computed ordinary moments some time after the start. Earlier analyses have shown (Jabłoński and Ozga, 2010, 2012; Ozga, 2019) that oscillators with strong damping should be used, and that impulses should occur frequently enough for values of estimators of ordinary moments calculated from Eq. (2.5) to change to the least extent. The rate of the oscillator own vibrations should be selected appropriately for the impulse occurrence frequency λ. The last step consists in checking whether the value of random impulses is sufficient to force vibrations of the oscillator.

The research is carried out in order to solve the inverse problem, namely to discern the distribution of impulses forcing vibrations of an oscillator at a shortest possible period of time. There is an infinite number of possible cases for which simulation or experimental studies could be developed. Taking into account previous experiences as well as the time necessary to generate one trial, and applying the principle that simple systems will allow for clear presentation of the solution of the research problem, the authors selected an oscillator with damping $b = 10$ and the frequency of vibrations $c = 20$ for $\lambda = 10$ and $h = 10^{-3}$ (Fig. 1). In the presented simulation investigations, vibrations of the oscillator evoke three distributions Φ_i of the pseudo-random variable η_i

1. Φ_1 : $p(\eta_1 = 80) = 0.5$ $p(\eta_2 = 70) = 0.5$
2. Φ_2 : $p(\eta_1 = 130) = 0.5$ $p(\eta_2 = 20) = 0.5$
3. Φ_3 : $p(\eta_1 = 140) = 0.5$ $p(\eta_2 = 10) = 0.5$

The parameters of the distributions were selected so that:

- the expected value of the distributions forcing vibrations in all three cases was the same and amounted to 75,
- the distribution Φ_1 was characterized by two impulses η_1 and η_2 of a similar force influencing the oscillator,
- the distributions Φ_2 and Φ_3 were characterized by two events of different forces of the impact. The value of η_1 symbolizes an impulse of a great force of impact while the value of η_2 an impulse of a little force of impact on the oscillator,
- the differences in statistics (Table 1) of the three discrete random variables are distributed as follows: between Φ_1 and the remaining distributions, the differences are significant. The parameters of the distributions Φ_2 and Φ_3 are similar.

Table 1. Parameters of distributions of the random variables Φ_i

Distribution	Parameter		
	Φ_1	Φ_2	Φ_3
Expected value	75	75	75
Standard deviation	5	55	65
Changeability coefficient	0.0667	0.7383	0.8667
Second raw moment	5 650	8 650	9 850

Figure 1 represents execution of a single movement $x(t)$ and the raw moments computed on the basis of this single execution. Thanks to strong damping occurring in the system at a certain time after the start (see Fig. 1 after 500 s), subsequent impulses do not cause step changes at the computed moments. Distributions were selected so that the mean value was the same in all three cases, hence the estimators of the first ordinary raw moment have similar values after

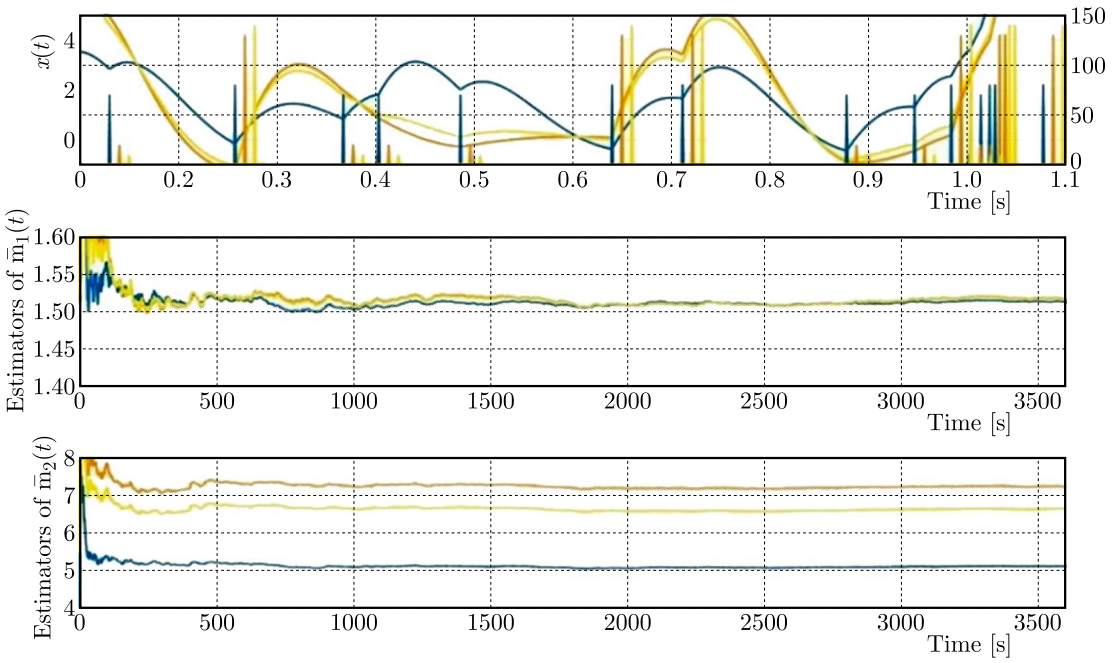

Fig. 1. The movements $x(t)$ of vibrations of an oscillator forced by a random series of impulses for one second; below the first stochastic raw moment and the second one computed on the basis of $x(t)$ for 900 s

1800 s. Stochastic raw moments of the second order (and subsequent orders) are different. It should be emphasized, however, that the presented results were obtained in the simulation that was organized in a specific way. In all three cases, the impulses worked at the same random time, and, what is more, if the strongest impulse was randomly chosen in the first distribution, the impulses selected in the second and third distributions were also the strongest ones. Similarly, the same pertains to the weakest impulses.

It should be taken into account that there exists an infinite number of possible movements, and the possibility of differentiating between the distributions when impulses occur at different random times and have different random values should be checked. In order to visualize this problem, thousand samples were generated for each of the discussed distributions. As it has already been mentioned, it is the estimators of the second raw moments computed on the basis of moments (2.5) that are used in the analysis. Calculations include all values of $x(t)$ since the very beginning till the moment when the values are recorded in the file. Movement (2.4) and moments (2.5) were determined with the sampling frequency of 10^3 s, and the values of moments were saved in the file every second. The analyzed time series of the second order raw moments were presented as tunnels (Fig. 2) covering all recorded samples. The tunnel was created by determining the maximum and minimum values of each of the thousand samples separately for each second. The mean value of all the calculated estimators was also computed.

Visualization of the research in the form of tunnels shows that for the second moment the samples generated for the distribution Φ_1 differ significantly from the others. In further analysis, this distribution will act as a control group, and the research questions will concern the Φ_2 and Φ_3 distributions.

Based on the second diagram, we can also state that we have to do with three time-dependent phenomena. During the start, up to the 600th second, the distributions Φ_2 and Φ_3 are distinguishable in approximately 50% of cases. Between the 600th and 1800th second, the number of samples in which time series have similar statistical parameters decreases. After the 1800th second all three distributions are distinguishable. The time at which the tunnels formed from

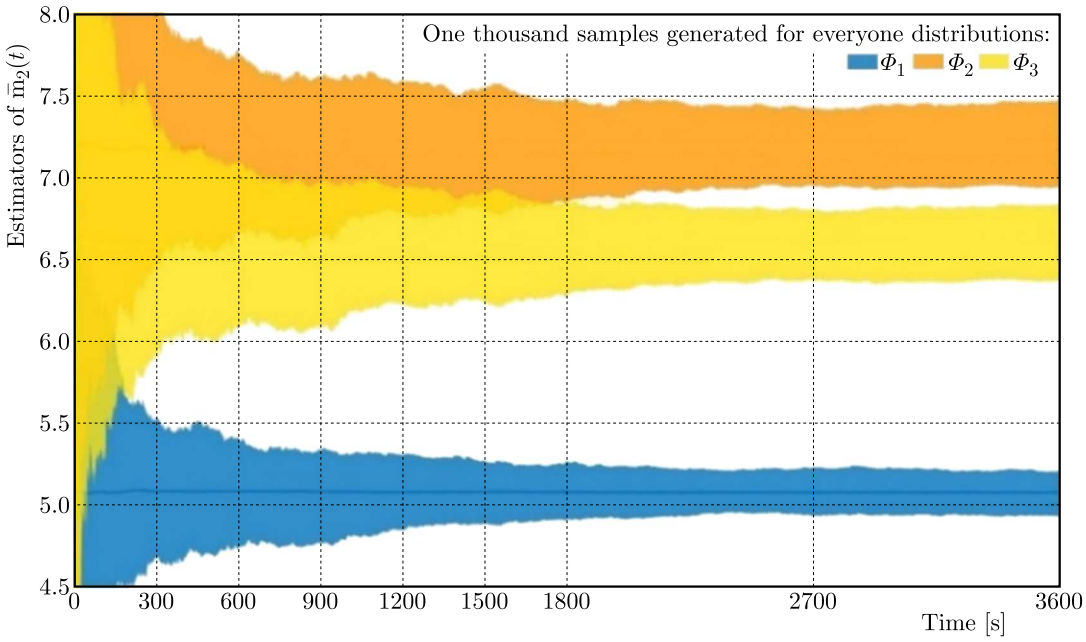

Fig. 2. The second stochastic raw moment calculated from the location $x(t)$ for a thousand different samples presented as tunnels

the generated samples for two similar distributions split up is an approximated value – this is how the samples were randomly distributed. It should be expected, however, that the time series of the subsequent samples will split up within an approximated time interval. These initial exploratory investigations allow for posing two research questions:

1. How precise differentiation of the distributions Φ_2 and Φ_3 before the 1800th second is possible?
2. Does the duration of the analyzed time interval influence the accuracy of classification using the decision tree algorithm and random forest classifier?

In order to answer the research questions posed above, further exploratory investigations should be carried out. It is necessary to check the distributions for single samples in two intervals from 600th second to 2000th one and after 2000th second, presenting the values that occur in the time series in the form of a frequency distribution. The conducted analysis shows that depending on the time interval, statistical parameters describing discrete distributions are different – they differ in the mean value, dominant, variance, etc. All distributions represented in Fig. 3 are multimodal.

On the basis of Fig. 3 it can be assumed that for any several minutes, the long interval starting after the 1800th second, no matter whether we take its mean value, median or dominant, all three distributions will be distinguishable. We can take into consideration either all three statistical parameters or just one of them. Before the 1800th second, the situation is more complicated, hence it seems necessary to use supervised learning algorithms to discern the distributions which force vibrations on the basis of analysis of one sample. Moreover, neither the parameters that could be used for classification of the distribution nor the length of the time interval that should be taken into consideration are known. From the point of view of its application in engineering designs, the sooner we know what distribution we are to deal with, the better. Therefore, nine time intervals presented in Fig. 4 were assigned for further analysis. The intervals are five minutes long while the length of the time intervals with even indices is ten minutes.

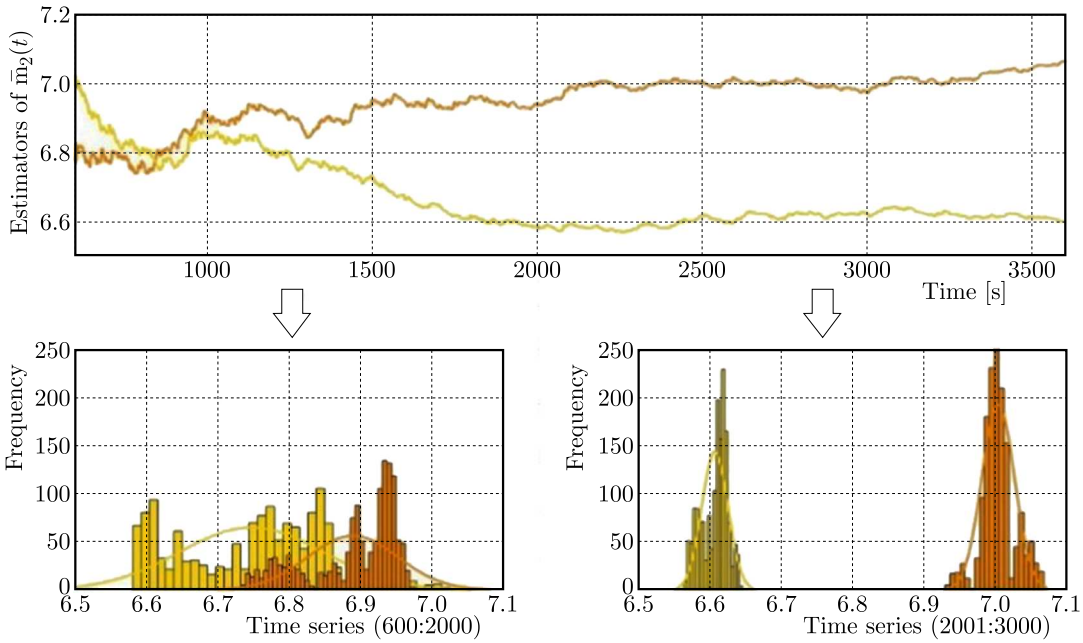

Fig. 3. Distribution of the second raw stochastic moment calculated from the location $x(t)$ for two samples generated from Φ_2 and Φ_3 distributions

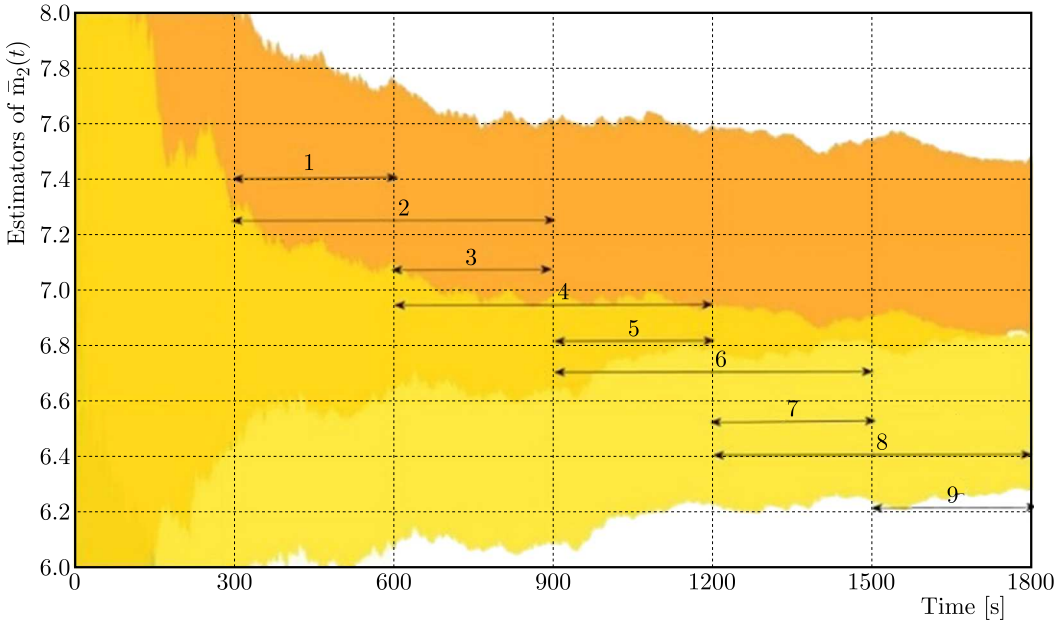

Fig. 4. Time intervals selected for further analysis, represented as tunnels composed from 1000 samples

We will answer the research questions using the following supervised machine learning algorithms. They are the decision tree classifier and the random forest classifier, later described as DTC and RFC, respectively. Along with the indicated time intervals, an analysis was performed using the previously prepared code. At least about 300 impulses were randomly selected during five-minute time intervals, which for the exponential distribution given by Eq. (2.3) allowed one to obtain the λ imposed in the simulations with an accuracy of 0.1%. The tests carried out for shorter values of the time interval indicated the obtaining of less accurate classification results than those presented in the next Section.

4. Data analysis using the decision tree classifier and random forest classifier algorithms

Machine learning (ML) algorithms find patterns, information links in data sets, and then help making decisions and forecasts based on shared data. Out of the logistic regression, elements like naive Bayes, k-nearest neighbors, decision tree, random forest and support vector machine algorithms have been considered. The decision tree classifier and random forest tree algorithms (Szeliga, 2019) have been chosen.

The first one is a decision tree classifier which is a supervised learning algorithm that is dedicated for classification problems. It is a solution which works as a flow chart. It divides the data points into a finite number of categories. This algorithm automatically selects the variables that differentiate the variable the most.

The second one is a random forest algorithm. It is an expansion of the decision tree classifier. First, it builds multiple decision trees based on training data. Then it matches the new data from the test set to one of the trees as a random forest. It averages the data to combine it with the closest random tree on the data scale. The random forest models are useful because they solve the decision tree algorithm problem of unnecessarily forcing data points within a category.

4.1. Determination of the most important statistical parameters describing the time series of the second raw moment estimators

The analysis started with the calculation of basic statistical parameters (Bąk *et al.*, 2020) such as amplitude, one percent above the standard deviation, minimum, mean, and maximum value, maximum slope, percent close to the median, median, median absolute deviation, skewness, standard deviation and weighted mean. Statistical parameters have been defined for the second raw moment, separately for each of the considered samples. Using the same algorithm, the influence of a given parameter on the classification of distributions for two-time intervals was determined (Fig. 5).

Using machine learning methods, it was possible to determine basic statistics that make it possible to recognize the distribution. Figure 5 shows these statistics for nine time periods. In addition, a parallel classification was devised for divisions of the training and test sets in ratios 30/70 and 50/50. The proposed division of the test and training sets results from the typical division in the 30/70 ratio (Szeliga, 2019). One thousand trials is used in the classification. To obtain as many test cases as possible in the area belonging to both tunnels (Fig. 4), the division of 50/50 was also made.

Focusing on Fig. 5, it should be noted that there is a problem with determining the basic statistics that allow one to distinguish the distributions. For odd (300 s) and even (600 s) intervals using the DTC algorithm, each time interval shown in Fig. 5 (marked as TP_x, where x is the next time interval) is described by different statistics. Moreover, it should be observed that the significance of the statistics changes for each time period. For this reason, this algorithm is not suitable for this type of analysis.

A similar verification was conducted for the same intervals with the use of a random tree classifier (Fig. 6).

From this analysis (Fig. 6), it can be seen that in the case of the intervals with a duration of 300 s, the standard deviation (24%), skewness (20%), amplitude (15%) and median absolute deviation (11%) have the highest impact on classification. The minimum value (1%) and the maximum slope (1%) have the lowest impact.

DTC for 30/70									
	TP_1	TP_2	TP_3	TP_4	TP_5	TP_6	TP_7	TP_8	TP_9
Amplitude		0.03		0.01					
Maximum slope		0.45				0.48			
Maximum									
Mean					0.37				
Median	0.34	0.09							
Median absolute deviation	0.65	0.01		0.50		0.02		0.51	
Minimum									
Percent beyond 1 std					0.63				
Percent close to median									
Skew			0.49	0.49		0.48		0.49	
Std		0.42	0.51			0.01	1		1
Weighted average						0.01			

DTC for 50/50									
	TP_1	TP_2	TP_3	TP_4	TP_5	TP_6	TP_7	TP_8	TP_9
Amplitude		0.27	0.51				0.51		0.51
Maximum slope									
Maximum	0.04			0.57					
Mean	0.30								
Median	0.10				0.75				
Median absolute deviation					0.05	0.50			
Minimum	0.03	0.65				0,01			
Percent beyond 1 std		0.07						1	
Percent close to median	0.02								
Skew 0.42		0.49	0.43	0.20	0.49				
Std	0.10						0.49		0.49
Weighted average									

Fig. 5. Representation of basic statistics determined for the second raw moments using DTC algorithms for the indicated time intervals considering division of the harvest in the proportion of 30/70 and 50/50

RFC for 30/70									
	TP_1	TP_2	TP_3	TP_4	TP_5	TP_6	TP_7	TP_8	TP_9
Amplitude	0.15	0.11	0.15	0.11	0.15	0.11	0.15	0.11	0.15
Maximum slope	0.01	0.07	0.01	0.074	0.01	0.07	0.01	0.07	0.01
Maximum	0.09	0.04	0.09	0.04	0.09	0.04	0.09	0.04	0.09
Mean									
Median	0.05	0.07	0.05	0.07	0.05	0.07	0.05	0.07	0.05
Median absolute deviation	0.11	0.15	0.11	0.15	0.11	0.15	0.11	0.15	0.11
Minimum	0.01	0.02	0.01	0.02	0.01	0.02	0.01	0.02	0.01
Percent beyond 1 std	0.10	0.05	0.10	0.05	0.10	0.05	0.10	0.05	0.10
Percent close to median									
Skew	0.20	0.29	0.20	0.29	0.20	0.29	0.20	0.29	0.20
Std	0.24	0.19	0.24	0.19	0.24	0.19	0.24	0.19	0.24
Weighted average	0.03		0.03		0.03		0.03		0.03

Fig. 6. Representation of basic statistics for the second raw moments determined using RFC algorithms for the indicated time intervals considering division of the harvest in the proportion of 30/70

In terms of the 600 s time intervals, the largest percentage was for skewness (29%), standard deviation (19%) and median absolute deviation (15%). The smallest share was that of the minimum value (2%). Additionally, in the case of RFCs, the percent close to median and mean

value is not included in the classification. The statistics presented in Fig. 6 are the same for both divisions. The importance and influence of the parameters on the distribution between the three distributions is the same both in the 5-minute and 10-minute intervals. The differences between the significance of the parameters depending on the length of the interval are not significant.

Since in particular time intervals, the statistical parameters responsible for the classification do not change only in the case of random forest algorithms, only these algorithms will be used for the research presented in the following Sections of this article.

4.2. Definition of the best RFC parameters

For the time series generated during simulation tests, the selection of hyperparameters was performed using the *grid_search* function.

Hyperparameters are the parameters that cannot be learned directly from estimators. It is recommended to search the hyperparameter space for the indicated time intervals to obtain the best cross-validation result. It allows one to find the best parameter values for a given estimator and the parameters which can be used to define the classification algorithm. Definition of these parameters reduces the time of the classification process.

In the case of DTC algorithms from the attributes like splitter, max depth, min samples split, min samples leaf, max features, max leaf nodes, class weight, we decided to define max depth, min samples leaf, min samples split and splitter. The max depth attribute defines the maximum depth of the tree. The min samples leaf attribute signifies the minimum number of the samples required to be at a leaf node. This parameter may affect the smoothing of the model. The min samples split determines the minimum number of samples that is required for internal division in the case of classification.

In the case of RFC algorithms, we need to mention the n estimators, criterion, max depth, min samples split, min samples leaf, max features, max leaf nodes, random state, verbose, max samples parameters. For the analysis we choose the following parameters: n estimators, that is the number of trees in the random forest classifier algorithm, and max depth attribute.

4.3. Evaluation of the classification algorithms

In the first step, classification of the downloaded data was conducted and classifier evaluation measures, such as precision, recall, f1-score and support, were determined.

The precision measure is responsible for recognizing a class, for example which part positively predicted elements are of all those marked as a part of this register.

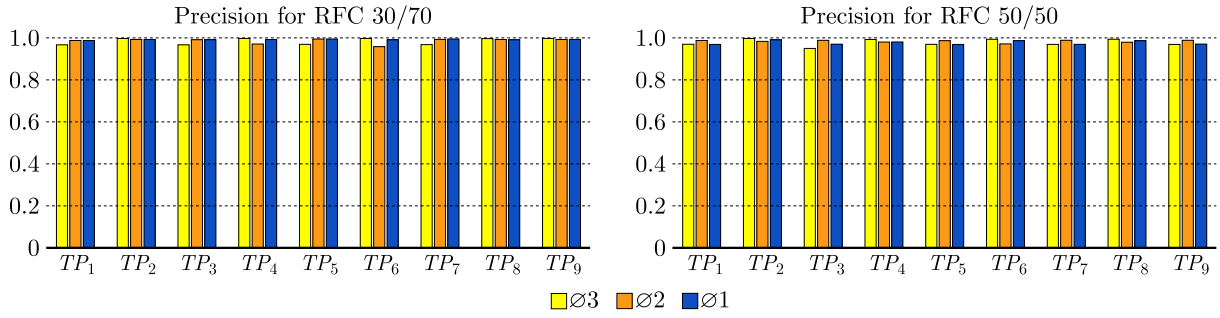

Fig. 7. Precision parameter for RFC for two splits

Figure 7 shows the precision parameter for nine-time intervals for two divisions 30/70 and 50/50 (test set/training set). It should be noted how this parameter changes depending on the recognized distribution. In the case of division, where there is 70% of the training set, we can see that for all time intervals the precision is 100% for the first distribution, which in the case

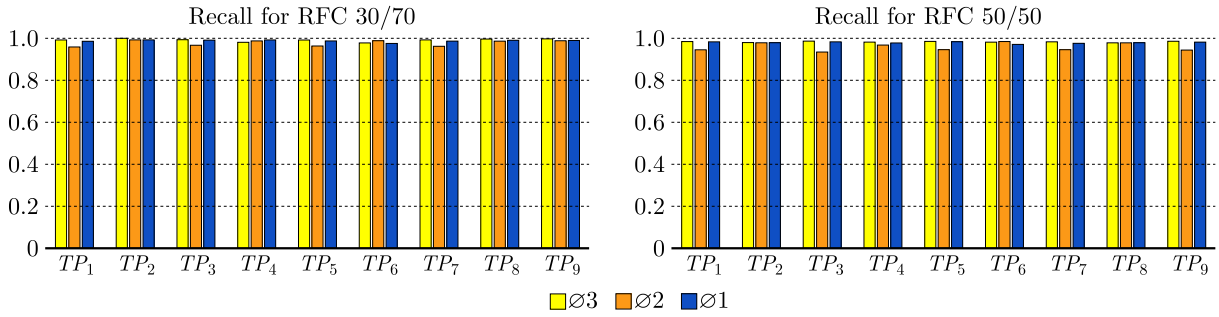

Fig. 8. Recall parameter for RFC for two splits

of these specifically analyzed data may be a determinant of proper operation of the algorithm (Fig. 8). There are slight differences when the test set is 50%. The level is between 98% and 100%, which means that the test set in the case of these variables should have more than five hundred samples. Expected difficulties exist with the second and third distributions. The precision in the case of the 30/70 division only for the 8th and 9th time interval is flawless for all three distributions. In the case of the 50/50 division, it was not possible to obtain 100% precision in the rare of the analyzed time intervals.

The next parameter was recall. This parameter called in some publications sensitivity or true positive rate informs how many elements from a given class have been correctly recognized.

The recall on the tested splits was also on high level. We can see that in the case of the 30/70 split, the first and third to seventh time periods did not reach the 100% recall level for the three distributions. Only for the eighth and ninth time periods was the 100% recall level reached.

For the 50/50 split, no time intervals except the eighth one, achieved the 100% recall level.

The last parameter is an F_1-score determined according to equation

$$F_1 = 2\frac{\text{precision} \cdot \text{recall}}{\text{precision} + \text{recall}} \tag{4.1}$$

In statistical rating of classification, it is a harmonic mean of the precision and recall. Figure 9 presents the F_1-score for nine time periods for 30/70 and 50/50 splits.

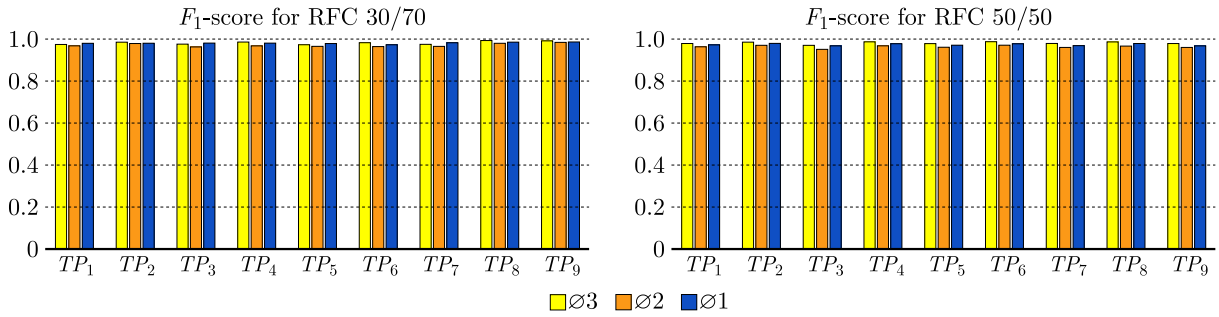

Fig. 9. F_1-score parameter for RFC for two splits

All these tree parameters allow us to evaluate the RFC for the mentioned time periods.

4.4. Summary of the classification algorithms in nine time periods

Figure 10 shows the accuracy of the RFCs on the test and training sets when their split is 30/70 and 50/50, respectively, for the three distributions. It should be emphasized that for this analysis, the search for the best hyper parameters was conducted in order to classify the appropriate class in the best possible way. The accuracy of classification using RFCs on training sets for all time intervals and both division is 100%.

RFC for 30/70									
	TP_1	TP_2	TP_3	TP_4	TP_5	TP_6	TP_7	TP_8	TP_9
Accuracy using DTC on training set	1	1	1	1	1	1	1	1	1
Accuracy using DTC on test set	0.989	1	0.989	0.994	0.989	0.989	0.989	1	1

RFC for 50/50									
	TP_1	TP_2	TP_3	TP_4	TP_5	TP_6	TP_7	TP_8	TP_9
Accuracy using DTC on training set	1	1	1	1	1	1	1	1	1
Accuracy using DTC on test set	0.987	0.987	0.980	0.999	0.987	0.993	0.987	0.997	0.987

Fig. 10. Representation of accuracy on training and the test set for second raw moments using RFC algorithms for the indicated time intervals considering division of the harvest in the proportion of 30/70 and 50/50

Accuracy for 30% of the test set ranged from 98.9% to 100%. For a 50% of the test set, the accuracy ranged from 98% to 100%.

5. Conclusion

After the analysis of the distributions of the second raw stochastic moments for the indicated nine time intervals, using the algorithm of random decision trees and the random forest classifier, the second algorithm was selected for further work based on the achieved results. It can be concluded that the algorithm RFC allows for recognition of distributions and determination of statistical parameters, which have the highest impact on distinguishing distributions.

When answering the question how it is possible to precisely differentiate the distributions Φ_2 and Φ_3 before 1800 s, it should be noted that high precision was achieved in fitting the data to a given distribution. For the RFC classifier, for the case where a 30% test set was considered, for 5-minute intervals an average of 100% for Φ_1, 100% for Φ_2 and 97% for Φ_3 was achieved. In the case of 10-minute intervals, 100% was achieved for Φ_1 and Φ_3 and 98.5% for Φ_2. Thus, the differences in the precision of classification depending on the length of the intervals are not significant.

Based on the results obtained for the decision trees algorithm, it should be stated that it is not suitable for the analysis of this type of technical problems because despite the positive results of the classifier operation, the share of individual statistics and their significance changes with each time interval.

Acknowledgement

The article was financed by a research subsidy number: 16.16.130.942 and project No 10.16.130.79990.

References

1. Banks D.M., Bekker J.C., Vermeulen H.J., 2023, Parameter estimation of a distribution transformer model using pseudo-random impulse sequence perturbation, *31st Southern African Universities Power Engineering Conference, SAUPEC*, 1-6
2. Bąk I., Markowicz I., Mojsiewicz M. Wawrzyniak K., 2020, Mathematical statistics. Examples and problems (in Polish), *Statystyka matematyczna. Przykłady i zadania*, CeDeWu Sp. z o.o., Warszawa
3. Bozzoni F., Corigliano M., Lai C.G., Salazar W., Scandella L., Zuccolo E., Latchman J., Lynch L., Robertson R., 2011, Probabilistic seismic hazard assessment at the Eastern Caribbean Islands, *Bulletin of the Seismological Society of America*, **111**, 5

4. Fenner M.E., 2020, *Machine Learning with Python for Everyone*, Addison Wisley Data

5. Hračov S., Náprstek J., 2017, Approximate complex eigensolution of proportionally damped linear systems supplemented with a passive damper, *Procedia Engineering*, **199**, 1677-1682

6. Iwankiewicz R., 1993, Stochastic methods in problems of dynamical systems subjected to a random series of impulses (in Polish), [In:] *Metody Stochastyczne w Zagadnieniach Układów Dynamicznych Poddanych Losowym Seriom Impulsów*, Prace Naukowe Instytutu Materiałoznawstwa i Mechaniki Technicznej Politechniki Wrocławskiej, Wrocław

7. Iwankiewicz R., Kotulski Z., 2009, *Stochastic Methods in Mechanics: Status and Challenges*, IPPT PAN, Warszawa

8. Jabłoński M., Ozga A., 2008, Statistical characteristics of vibrations of a string forced by stochastic forces, *Mechanics*, **27**, 1, 1-7

9. Jabłoński M., Ozga A., 2010, Distribution of stochastic impulses acting on an oscillator as a function of its motion, *Acta Physica Polonica A*, **118**, 74-77

10. Jabłoński M., Ozga A., 2012, Determining the distribution of values of stochastic impulses acting on a discrete system in relation to their intensity, *Acta Physica Polonica A*, **121**, A174-A178

11. Jabłoński M., Ozga A., 2013, *Distribution of Random Pulses Acting on a Vibrating System as a Function of its Motion*, AGH University Press, Krakow

12. Litak G., Borowiec M., Friswell M. I., Szabelski K., 2008, Chaotic vibration of a quarter-car model excited by the road surface profile, *Communications in Nonlinear Science and Numerical Simulation*, **13**, 7, 1373-1383

13. Liu Y., Xu J., Lu J., Gui W., 2023, Stability of stochastic time-delay systems involving delayed impulses, *Automatica*, **152**, 110955

14. Mazur-Śniady K., Śniady P., 1986, Dynamic response of linear structures to random streams of arbitrary impulses in time and space, *Journal of Sound and Vibration*, **110**, 1, 59-68

15. Ozga A., 2019, Determining the distribution of stochastic impulses in linear discrete dynamical systems (in Polish), AGH University Press, 130-136, ISBN: 978-83-7464-997-1

16. Piszczek K., 1982, *Stochastic Methods in the Theory of Mechanical Vibrations* (in Polish), PWN, Warszawa

17. Rączka W., Konieczny J., Sibielak M., 2013, Laboratory tests of shape memory alloy wires, *Solid State Phenomena*, **199**, 365-370

18. Roberts J.B., 1966, On the response of a simple oscillator to random impulses, *Journal of Sound and Vibration*, **4**, 1, 51-61

19. Roberts J.B., 1972, System response to random impulses, *Journal of Sound and Vibration*, **24**, 1, 23-34

20. Roberts J.B., Spanos P.D., 2003, *Random Vibration and Statistical Linearization*, New York Dover Publication

21. Skalmierski B., Tylikowski A., 1972, *Stochastic Processes in Dynamics* (in Polish), PWN, Warszawa

22. Smolnicki T., Stańco M., Pietrusiak D., 2013, Distribution of loads in the large size bearing – problems of identification, *Tehnički Vjesnik*, **20**, 5, 831-836

23. Sobczyk K., 1983, Stochastic methods in mechanics: state and development trends (in Polish), *Mechanika Teoretyczna i Stosowana*, **21**, 4, 557-564

24. Socha L., Soong T.T., 1991, Linearization in analysis of nonlinear stochastic systems, *Applied Mechanics Reviews*, **44**, 10

25. Szeliga M., 2019, *Practical Machine Learning* (in Polish), PWN SA, Warszawa

26. Tylikowski A., 1982, Vibrations of a harmonic oscillator caused by a series of random collisions (in Polish), *Prace Instytutu Podstaw Budowy Maszyn PW*, **13**, 101-112

27. Weber H., Kaczmarczyk S., Iwankiewicz R., 2021, Non-linear response of cable-mass-spring system in high-rise buildings under stochastic seismic cxcitation, *Materials*, **14**, 22, 6858

28. Zembaty Z., 2009, Tutorial on surface rotations from wave passage effects: stochastic spectral approach, *Bulletin of the Seismological Society of America*, **99**, 2B, 1040-1049

Manuscript received October 27, 2022; accepted for print August 25, 2023

JOURNAL OF THEORETICAL AND APPLIED MECHANICS
61, 4, pp. 833-845, Warsaw 2023
https://doi.org/10.15632/jtam-pl/173036

THREE-DIMENSIONAL MODELLING AND PARAMETER IDENTIFICATION OF THE SEATED HUMAN BODY EXPOSED TO RANDOM VIBRATION

Igor Maciejewski, Andrzej Błażejewski, Sebastian Pecolt, Tomasz Krzyzynski, Piotr Zaporski

Koszalin University of Technology, Department of Mechatronics and Automation, Koszalin, Poland
e-mail: igor.maciejewski@tu.koszalin.pl; andrzej.blazejewski@tu.koszalin.pl; sebastian.pecolt@tu.koszalin.pl; tomasz.krzyzynski@tu.koszalin.pl; piotr.zaporski@tu.koszalin.pl

The paper deals with the modelling and parameter identification of the human body in a sitting posture. The advantage of this paper is to announce a simplified, but also a reliable three-mass model representing dynamic behaviour of the main human body parts, i.e. pelvis, torso and head. Their equivalent masses are interconnected by classical mechanical constraints in the form of springs and dampers. The stiffness and damping coefficients are identified by means of an original optimisation procedure that is used to minimise the error between measurement and simulation results. The model is proposed to be used for simulation studies of vibration-induced effects on the human body as well as for defining a specific vibration-isolation properties of automotive seat suspension systems with minimal computing cost and time.

Keywords: bio-mechanical model, human body, vibration exposure

1. Introduction

Bio-mechanical modelling began to develop in the 1970s. Its aim is to replicate the conduct of the human body within a simplified way. Bio-mechanical models can be employed to witness the behaviour of the system in various conditions under the impact of external forces, which enables one to carry out kinetic and dynamic analysis. The main development of bio-mechanical modelling has began in medicine, rehabilitation and sport. At present, bio-mechanical models are widely utilised to predict human interactions with mechanical systems. Computer models of the human body are gaining increasing popularity due to the potential for developing more complicated models that allow study of a given problem on a much larger scale in a much shorter time.

The simplest models, that have been and still are used in study on the system dynamics, are uniaxial models. Despite their simple structure, such systems consist of numerous components and sections along with non-linear properties. Simple uniaxial models are often used to simulate only a selected part of the body in which a single movement direction is dominant. One of the initial bio-mechanical simulations employed for jumping and landing was crafted in the 1980s. The representation portrays the model as a single-axis setup comprised of two masses linked by springs and dampers (Fritz, 1981).

The next stages of development of bio-mechanical models are complex single-axis models for examining the movement of the human physique during diverse undertakings, e.g. contact of the foot against the ground or a three-mass depiction of a seated subject. Two-dimensional models (Liu and Qin, 2020, 2021), with up to several degrees of freedom are additionally employed for investigating kinematics of the human physique. They are used in various sport disciplines

to study specific movements (Maciejewski *et al.*, 2022), for which only individual parts of the human body are modelled. They are also used to carry out analyses covering the entire human body. Such models typically consist of rigid bodies with continuous or discrete weight allocation, frequently regarded as rigid constituents. The advanced programmes enabling analysis of the behaviour of the human model are based on mathematical analysis, are additionally supported by visualization and offer numerous kinematic and dynamic alternatives. They facilitate the construction and simulation of spatial configurations with numerous degrees of liberty. A good illustration is the BoB Biomechanics (Shippen and May, 2016; Mihcin *et al.*, 2019) environment working with MATLAB®.

There are many models that are not directly based on bio-mechanics, which are called virtual computer models (Zhao *et al.*, 2021). A bio-mechanical system like a black box with a specific number of inputs can represent the human interaction and body response outputs. These models do not directly mirror human bio-mechanics, but concentrate on bodily reactions. They are extensively employed in sports (Glowiński *et al.*, 2018), rehabilitation (Glowinski *et al.*, 2017a, 2019), medicine for analysing motion kinematics (Głowiński *et al.*, 2015, 2017b). A lot of research into reducing vibration of seat suspension systems employs bio-mechanical representations of the human physique in a seated stance. Some researchers present complex 3D models with many degrees of freedom (Zheng *et al.*, 2011). Unfortunately, the literature lacks bio-mechanical models of humans that describe human vibration in various directions, even when the input vibration is generated solely along one axis.

Creating a credible human spatial model is not an easy task. In addition to the anthropometric data of the human regarding its individual masses and structural dimensions of the body parts (Chandler *et al.*, 1975), the parameters describing visco-elastic connections (stiffness and damping coefficients) between particular masses are required. The vast majority of these parameters can be identified by using different optimisation techniques. In (Desai *et al.*, 2018), the authors present a 2D multi-body model featuring 20 degrees of freedom (DOF) formulated for a seated subject, with model parameters fine-tuned through the utilisation of a genetic algorithm (GA). The empirical information are achieved from the existing literature (Mandapuram *et al.*, 2011), wherein the biodynamic response to an uncorrelated biaxial vibration is assessed. The impacts of palm support, lumbar cushioning, and vibration intensity on the interplay between the body and the seat and backrest are delineated through the utilisation of the apparent mass concept. The model developed by the authors can replicate the observed seat-to-head transmissibility responses (STHT) of the human physique.

A dependable representation of the human physique enables one to develop the seat suspension system in relation to its vibration isolation characteristics that can improve overall driving comfort of the drivers. There are many studies describing the significance of safeguarding the operator from vertical vibrations experienced in the seat suspension (Stein *et al.*, 2008; Adam and Jalil, 2017), but only a little work is reported on reducing the horizontal vibration (Sun and Jing, 2016; Sun *et al.*, 2015; Maciejewski *et al.*, 2017; Maciejewski and Krzyzynski, 2020). For instance. in the paper (Kim *et al.*, 2005), the authors constructed a bio-mechanical representation of the human physique for evaluating vibrations while in a seated posture. In their work, the model comprises multiple concentrated masses interconnected by linear springs and dampers.

The continuous exposure of the human physique to low-frequency vibration (below 20 Hz) may affect human well-being and comfort. Experimental study of the biodynamic responses of the human physique can aid in comprehending the impacts of vibrations on drivers and as a result to enhance the suspension control strategy. For this purpose, many control methods are employed for enhancement of the operator comfort through semi-active (Maciejewski *et al.*, 2019) and active seat suspension systems (Maciejewski *et al.*, 2022). The aim of this paper is to put forth a bio-mechanical representation of the human physique while seated, which can be

used for simulation studies of the effects of vibration on the drivers and to determine vibration isolation characteristics of automotive seat suspension systems.

2. Physical and mathematical model

A methodology for developing the human model includes the following assumptions. The authors of this paper adopt a strategy aimed at building a minimal model, i.e. as simple as possible and thus computationally efficient. Furthermore, the reliability of this model should be experimentally verified under laboratory conditions. First of all, the physical model of the human body is determined to represent the seated human in a position typical for driving a car, working machine or other motor vehicle (Fig. 1). At this point, it is also decided on the type of coordinate system in which the model is located.

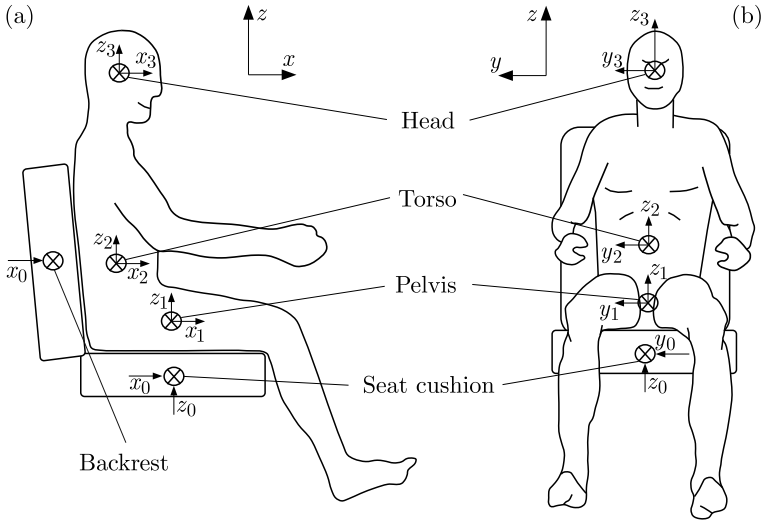

Fig. 1. Posture of the seated human body in a vehicle: (a) side view, (b) front view

In order to simplify the problem formulation and its numerical solution, the three-mass model is considered to represent the human pelvis, torso and head (Fig. 1). Assessing the layout of the human body in the driver's position, Fig. 1 shows two places of the input vibration, e.g. transmitted by the backrest and seat cushion. It is assumed that the driver is mainly influenced by forces transmitted through the seat. The forces acting on the feet and generated by the steering wheel are not taken into account because they are insignificant for the whole-body vibration (WBV) exposure.

2.1. Physical model

Assuming that each mass is a rigid body with finite dimensions (Fig. 2), the anatomical connections between individual parts of the human body are represented by spring-damper systems. Their dynamic properties are defined by appropriate values of the stiffness $k_{i(i-1)j}$ and damping $d_{i(i-1)j}$ coefficients. The indices next to the coefficients indicate the numbers of bodies $i = 1, 2, 3$ between which these systems are placed as well as the direction $j = x, y, z$ in which the spring and damping forces are considered. Due to asymmetrical configuration of the bio-mechanical model, the angular motion of bodies around particular axes is provided and the corresponding torsional stiffness and damping follow from visco-elastic properties of the applied connections. In this model, the locations of the centres of individual bodies are important (symbol *otimes* in Fig. 2), at which kinematic values, i.e. displacements, velocities

and accelerations, are determined. These are linear quantities measured along the xyz coordinate system together with angular quantities θ, φ, ψ that are described around each axis.

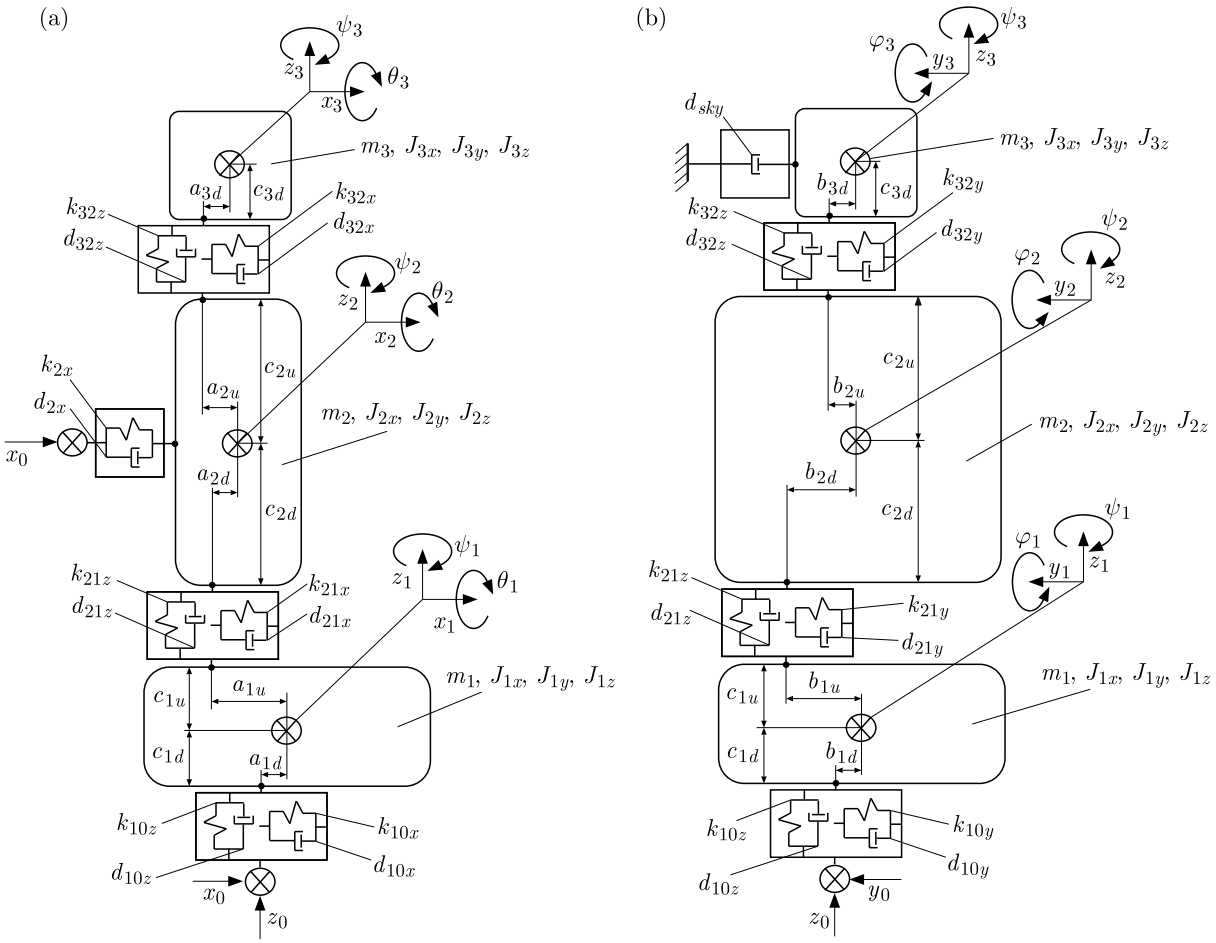

Fig. 2. Physical model of the seated human body: (a) side view, (b) front view

An important feature of aforementioned model is the location of the spring-damper systems in relation to the mass centres. This makes it possible to simulate the behaviour of human body parts, such as head (mass No. 3 in Fig. 2) or torso (mass No. 2 in Fig. 2), whose centres of mass are in fact not aligned (symmetrised) with and pelvis (mass No. 1 in Fig. 2). Possible locations for mounting the visco-elastic elements are defined by their corresponding dimensions, i.e. a_{id} and a_{iu}, b_{id} and b_{iu}, c_{id} and c_{iu}, where the number $i = 1, 2, 3$ represents the selected human body part. The another indexes indicate the mounting position of a given mass, i.e. the indexes u and d mean the upper and lower fixation points, respectively. The physical model presented in this paper (Fig. 2) allows one to develop its mathematical description for the purpose of simulating mechanical reactions of the seated human body to vibration.

2.2. Mathematical model

The mathematical model takes into account linear and angular movements of individual bodies (displacements x_i, y_i, z_i and angles of rotation $\theta_i, \varphi_i, \psi_i$) that are determined in local coordinate systems with the orgines in the centres of each mass (Fig. 3). In this model, the input vibration is transferred through spring-damper elements that are connected at the bottom and top of particular bodies, and these visco-elastic elements generate reaction forces around each axes, i.e. the bottom forces $F_{i(i-1)x}$, $F_{i(i-1)y}$, $F_{i(i-1)z}$ and the top forces $F_{(i+1)ix}$, $F_{(i+1)iy}$, $F_{(i+1)iz}$.

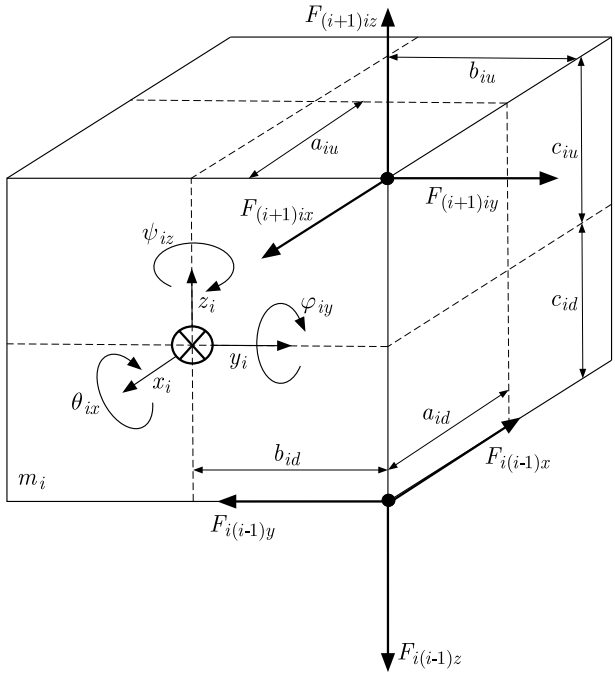

Fig. 3. Forces transferred through spring-damper elements in the local coordinate system of an individual mass

The following equations describe linear motion of particular bodies in different directions

$$\begin{aligned} &m_i\ddot{x}_i = F_{i(i-1)x} + F_{(i+1)ix} + F_{2x} \qquad m_i\ddot{y}_i = F_{i(i-1)y} + F_{(i+1)iy} + F_{sky} \\ &m_i\ddot{z}_i = F_{i(i-1)z} + F_{(i+1)iz} \qquad i = 1,2,3 \end{aligned} \tag{2.1}$$

where: m_i is mass of individual bodies ($i = 1,2,3$), $\ddot{x}_i$, $\ddot{y}_i$, $\ddot{z}_i$ are linear accelerations measured along particular axes, F_{2x} is the reaction force of the seat backrest (acting only in the longitudinal x-direction on the torso), F_{sky} is the active force stabilising the human head in the lateral y-direction.

The bottom and top forces connecting individual bodies of the human body model are determined as follows:

— along the x-axis

$$\begin{aligned} F_{i(i-1)x} &= d_{i(i-1)x}[-(\dot{x}_i - \dot{x}_{(i-1)}) - b_{id}(\dot{\psi}_i - \dot{\psi}_{(i-1)}) - c_{id}(\dot{\varphi}_i - \dot{\varphi}_{(i-1)})] + \ldots \\ &\quad + k_{i(i-1)x}[-(x_i - x_{(i-1)}) - b_{id}(\psi_i - \psi_{(i-1)}) - c_{id}(\varphi_i - \varphi_{(i-1)})] \\ F_{(i+1)ix} &= d_{(i+1)ix}[(\dot{x}_{(i+1)} - \dot{x}_i) - b_{iu}(\dot{\psi}_{(i+1)} - \dot{\psi}_i) + c_{iu}(\dot{\varphi}_{(i+1)} - \dot{\varphi}_i)] + \ldots \\ &\quad + k_{(i+1)ix}[(x_{(i+1)} - x_i) - b_{iu}(\psi_{(i+1)} - \psi_i) + c_{iu}(\varphi_{(i+1)} - \varphi_i)] \end{aligned} \tag{2.2}$$

— along the y-axis

$$\begin{aligned} F_{i(i-1)y} &= d_{i(i-1)y}[-(\dot{y}_i - \dot{y}_{(i-1)}) + a_{id}(\dot{\psi}_i - \dot{\psi}_{(i-1)}) + c_{id}(\dot{\theta}_i - \dot{\theta}_{(i-1)})] + \ldots \\ &\quad + k_{i(i-1)y}[-(y_i - y_{(i-1)}) + a_{id}(\psi_i - \psi_{(i-1)}) + c_{id}(\theta_i - \theta_{(i-1)})] \\ F_{(i+1)iy} &= d_{(i+1)iy}[(\dot{y}_{(i+1)} - \dot{y}_i) + a_{iu}(\dot{\psi}_{(i+1)} - \dot{\psi}_i) - c_{iu}(\dot{\theta}_{(i+1)} - \dot{\theta}_i)] + \ldots \\ &\quad + k_{(i+1)iy}[(y_{(i+1)} - y_i) + a_{iu}(\psi_{(i+1)} - \psi_i) - c_{iu}(\theta_{(i+1)} - \theta_i)] \end{aligned} \tag{2.3}$$

— along the z-axis

$$\begin{aligned} F_{i(i-1)z} &= d_{i(i-1)z}[-(\dot{z}_i - \dot{z}_{(i-1)}) - a_{id}(\dot{\varphi}_i - \dot{\varphi}_{(i-1)}) + b_{id}(\dot{\theta}_i - \dot{\theta}_{(i-1)})] + \dots \\ &\quad + k_{i(i-1)z}[-(z_i - z_{(i-1)}) - a_{id}(\varphi_i - \varphi_{(i-1)}) + b_{id}(\theta_i - \theta_{(i-1)})] \\ F_{(i+1)iz} &= d_{(i+1)iz}[(\dot{z}_{(i+1)} - \dot{z}_i) - a_{iu}(\dot{\varphi}_{(i+1)} - \dot{\varphi}_i) + b_{iu}(\dot{\theta}_{(i+1)} - \dot{\theta}_i)] + \dots \\ &\quad + k_{(i+1)iz}[(z_{(i+1)} - z_i) - a_{iu}(\varphi_{(i+1)} - \varphi_i) + b_{iu}(\theta_{(i+1)} - \theta_i)] \end{aligned} \tag{2.4}$$

where $d_{i(i-1)j}$, $d_{(i+1)ij}$ and $k_{i(i-1)z}$, $k_{(i+1)iz}$ are the damping and stiffness coefficients which represent visco-elastic connections between neighbouring bodies ($i = 1, 2, 3$) in the specific direction $j = x, y, z$ of the vibration exposure, a_{id}, a_{iu}, b_{id}, b_{iu}, c_{id}, c_{iu} are the distances defining fixations of the lower (index u) and upper (index d) visco-elastic elements to particular bodies. The above equations (Eqs. (2.2)-(2.4)) take into account the linear displacements of individual masses as well as their possible rotations around each axis. Assuming relatively small torsional movements, the angular displacements are approximated by corresponding values of the angles θ_i, φ_i and ψ_i.

The force F_{2x} representing contact of the human body with the seat backrest as well as the active force F_{sky} stabilising the head are defined in the following way

$$F_{2x} = -d_{2x}(\dot{x}_2 - \dot{x}_0) - k_{2x}(x_2 - x_0) \qquad F_{sky} = -d_{sky}\dot{y}_3 \tag{2.5}$$

where d_{2x}, k_{2x} are the damping and stiffness coefficients of the backrest, d_{sky} is the sky-hook damping ratio that reproduce the human action against vibration.

The next set of equations describe the angular motion of particular bodies around particular axes

$$\begin{aligned} J_{ix}\ddot{\theta}_i &= -F_{i(i-1)y}c_{id} - F_{i(i-1)z}b_{id} - F_{(i+1)iy}c_{iu} + F_{(i+1)iz}b_{iu} \\ J_{iy}\ddot{\varphi}_i &= F_{i(i-1)x}c_{id} + F_{i(i-1)z}a_{id} + F_{(i+1)ix}c_{iu} - F_{(i+1)iz}a_{iu} \qquad i = 1, 2, 3 \\ J_{iz}\ddot{\psi}_i &= F_{i(i-1)x}b_{id} - F_{i(i-1)y}a_{id} - F_{(i+1)ix}b_{iu} + F_{(i+1)iy}a_{iu} \end{aligned} \tag{2.6}$$

where J_{ix}, J_{iy} and J_{iz} are mass moments of inertia for individual body segments ($i = 1, 2, 3$) that are defined around each axis of the Cartesian coordinate system.

3. Measurement and data processing

The experimental set-up for measuring the body motion under vibration in various directions is shown in Fig. 4. The vibration shaker is used to generate random oscillatory motion along three orthogonal directions, i.e. longitudinal x-direction (Fig. 4a), lateral y-direction (Fig. 4b) and vertical z-direction (Fig. 4c). Three-directional accelerometers are mounted to individual human body parts such as pelvis, torso and head. Additionally, the fourth accelerometer is utilised to measure the input vibration source of the shaker providing random vibration with a frequency between 0.5 Hz and 12.5 Hz. The data obtained from accelerators are recorded by a PC-based data acquisition system with the sampling time of 1 ms.

The originally measured acceleration signals are reduced to the sampling frequency of 200 Hz by averaging of every 5 samples and then converted into frequency-domain data. For each signal, the power spectral density (PSD) is computed by employing Welch's method (Stoica and Moses, 2005) with a Hamming window applied to 50% overlapping the segments of the measurement data. The length of each data segment corresponds to the time period of 10.24 s that allows one to achieve a frequency resolution of 97.66 mHz. Based on such prepared frequency-domain data, the vibration transmissibility of particular human body parts are calculated as follows

$$T_{ij}(2\pi f) = \frac{\sqrt{\mathrm{PSD}_{ij}(2\pi f)}}{\sqrt{\mathrm{PSD}_{0j}(2\pi f)}} \qquad i = 1, 2, 3 \qquad j = x, y, z \tag{3.1}$$

Fig. 4. Experimental set-up for measuring body motion exposed to vibration in different directions: (a) longitudinal x-direction, (b) lateral y-direction, (c) vertical z-direction

where $\mathrm{PSD}_{ij}(2\pi f)$ is the power spectral density of the selected human body part (pelvis $i = 1$, torso $i = 2$ and head $i = 3$), $\mathrm{PSD}_{i0}(2\pi f)$ is the power spectral density of the base vibration that is measured along a specific axis of the vibration transfer (the longitudinal axis $j = x$, lateral axis $j = y$ and vertical axis $j = z$), f is the frequency in Hz.

A scalar transmissibility function (Eq. (3.1)) is therefore estimated via PSD as a ratio between two measured signals, i.e. the base vibration and vibration of the selected human body part. If a magnitude of the transmissibility function is below 1, then the desired vibration reduction is achieved. Otherwise, the unwanted amplification of a vibration magnitude is observed due to resonances of the human body parts and organs.

4. Identification of model parameters

The identification of model parameters is conducted by minimising the root mean square error (RMSE) of the transmissibility function determined above. Such a procedure is realised in the following way

$$\mathrm{RMSE} = \sum_{i=1}^{3} \sum_{j=x}^{z} \sqrt{\frac{1}{N} \sum_{n=1}^{N} [T_{ij}(2\pi f_n) - \widehat{T}_{ij}(2\pi f_n)]^2} \qquad \begin{matrix} i = 1,2,3 \\ j = x,y,z \end{matrix} \tag{4.1}$$

where T_{ij} and $\widehat{T}_{ij}$ are magnitudes of the simulated and measured transmissibility functions, respectively, that correspond to the frequency vector f_n of N-elements. The proposed identification method accepts fitting of more than one transmissibility function evaluated for individual human body parts ($i = 1,2,3$) and along various directions ($j = x,y,z$) of the vibration transmission.

Assuming the averaged masses m_1, m_2 and m_3 of the particular human body parts (Chandler *et al.*, 1975) as well as their mass moments of inertia J_{1j}, J_{2j} and J_{3j} around different axes ($j = x,y,z$ – see Appendix), the objective function to be minimised is defined as follows

$$\min_{d_{i(i-1)j}, k_{i(i-1)j}, d_{2x}, k_{2x}, d_{sky}} \mathrm{RMSE}(d_{i(i-1)j}, k_{i(i-1)j}, d_{2x}, k_{2x}, d_{sky}) \qquad \begin{matrix} i = 1,2,3 \\ j = x,y,z \end{matrix} \tag{4.2}$$

where $d_{i(i-1)j}$ and $k_{i(i-1)j}$ are the damping and stiffness coefficients determining visco-elastic interactions between individual masses of the bio-mechanical model, d_{2x} and k_{2x} are the damping and stiffness coefficients representing the transmission of fore-aft vibration through the seat backrest (only in the longitudinal x-direction), d_{sky} is the damping coefficient describing active stabilisation of the head due to the human body's ability to absorb vibrational energy (only in the lateral y-direction). The block diagram for identification of the unknown model parameters is presented in Fig. 5.

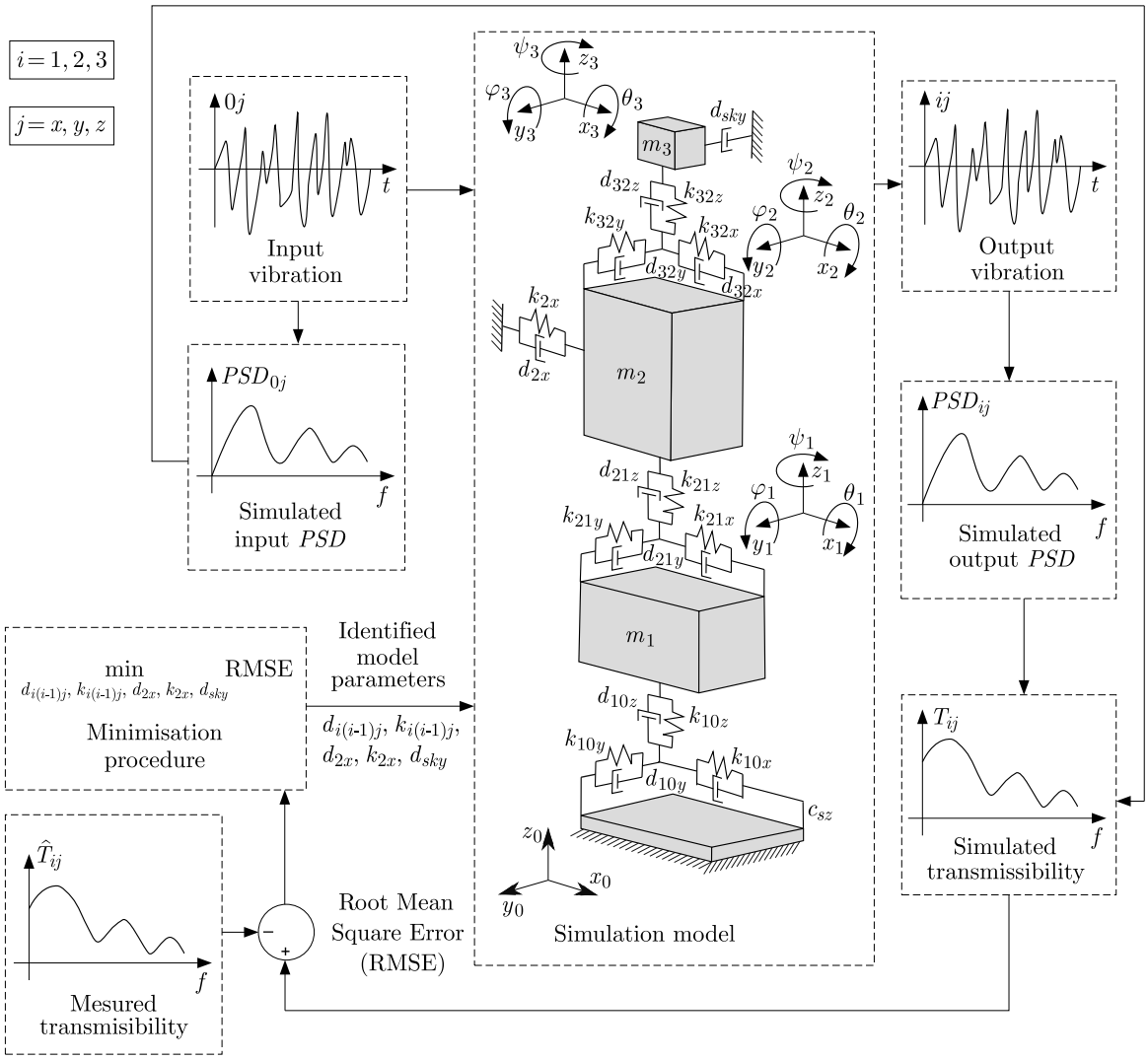

Fig. 5. Block diagram for identification of the unknown model parameters

For the reason of finding a minimum of the objective function (Eq. (4.2)) of several variables, the gradient method is utilised. Such a method is implemented in the MATLAB® environment and can be employed for searching an optimal configuration of the unknown damping and stiffness coefficients that have a significant influence on the model output. The initial estimate of these parameters plays an important role in minimising the error between the simulation and measurement results, therefore the proposed optimisation procedure is repeated many times by using a large number of random starting points. The optimal model parameters that conform to a global minimum of the RMSE are shown in Table 1. As follows from this table, if the stiffness and damping coefficients are equal to zero along some axis (x, y or z) then the vibration transmission of a model does not occur for these directions. The obtained results are strictly connected with a specific geometrical configuration of the bio-mechanical model that depends on the complete set of its dimensions such as a_{id}, a_{iu}, b_{id}, b_{iu} and c_{id}, c_{iu} $(i = 1, 2, 3)$ – see Appendix.

5. Simulation and experimental results

The bio-mechanical model discussed within the framework of this paper is investigated by means of a numerical simulation and an experimental research under laboratory conditions. The male subject of 90 kg is employed for measurements of the seated human body exposed to whole-body

Table 1. Identified model parameters for different directions of the input vibration

Parameter	Input vibration			Unit
	along x-axis	along y-axis	along z-axis	
d_{10x}	23.58	0	6711	Ns/m
k_{10x}	27507	0	10.13	N/m
d_{10y}	0	24069	0	Ns/m
k_{10y}	0	171570	0	N/m
d_{10z}	10000	0	1525	Ns/m
k_{10z}	82931	0	14222	N/m
d_{21x}	38.13	0	1.04	Ns/m
k_{21x}	27646	0	16094	N/m
d_{21y}	0	10	0	Ns/m
k_{21y}	0	8522	0	N/m
d_{21z}	2619	0	1266	Ns/m
k_{21z}	6126	0	66258	N/m
d_{32x}	50	0	85.65	Ns/m
k_{32x}	3418	0	16860	N/m
d_{32y}	0	2487	0	Ns/m
k_{32y}	0	63442	0	N/m
d_{32z}	2404	0	1325	Ns/m
k_{32z}	500	0	24584	N/m
d_{2x}	10	0	1684	Ns/m
k_{2x}	8045	0	62046	N/m
d_{sky}	0	35.51	0	Ns/m

vibration. The laboratory examination of the human dynamics are executed according to the International Standard ISO-7096 (2000) that rigorously defines the person posture on a seat as well as experimental instrumentation of the test rig (Fig. 4). The signals acquired from 3D linear accelerometers measuring acceleration of the input vibration together with accelerations of the particular human body parts (pelvis, torso and head) are used for further analysis. Based on these signals, the transmissibility functions (Eq. (3.1)) are evaluated and compared with the results obtained by computer simulation in the studied frequency range of 0.5 Hz to 12.5 Hz (Fig. 6).

As shown in Fig. 6, the proposed model demonstrates good agreement with the measurement results. The bio-dynamic response of the seated human body is captured in various directions of the vibration influence even if the input vibration is generated along a single axis (vibration generated along the longitudinal x-direction – Fig. 6a,b and vibration generated along the vertical z-direction – Fig. 6d,e). Exception to this rule is observed when vibration is generated along the lateral y-direction – Fig. 6c. Due to system symmetry around the z-axis, only the lateral vibration response of both simulation model and human subject is shown. Note that other geometrical configurations of the bio-mechanical model can produce its dynamic response along various axes (x, y and/or z) of the three-dimensional coordinate system.

Considering the system configuration depicted in Appendix , the transmissibility functions for the input vibration applied in the x-direction are illustrated in Fig. 6a,b. There is a significant increase of the vibration that are transferred from the human pelvis to the head (through the torso) in both directions of the vibration transmission, i.e. from the x-direction to x-direction (Fig. 6a) and also from the x-direction to z-direction (Fig. 6b). In turn, an application of the input vibration in the y-direction (Fig. 6c) results in a different dynamic response of the vibrating system. The torso points out high magnitudes of vibration at low frequencies and the

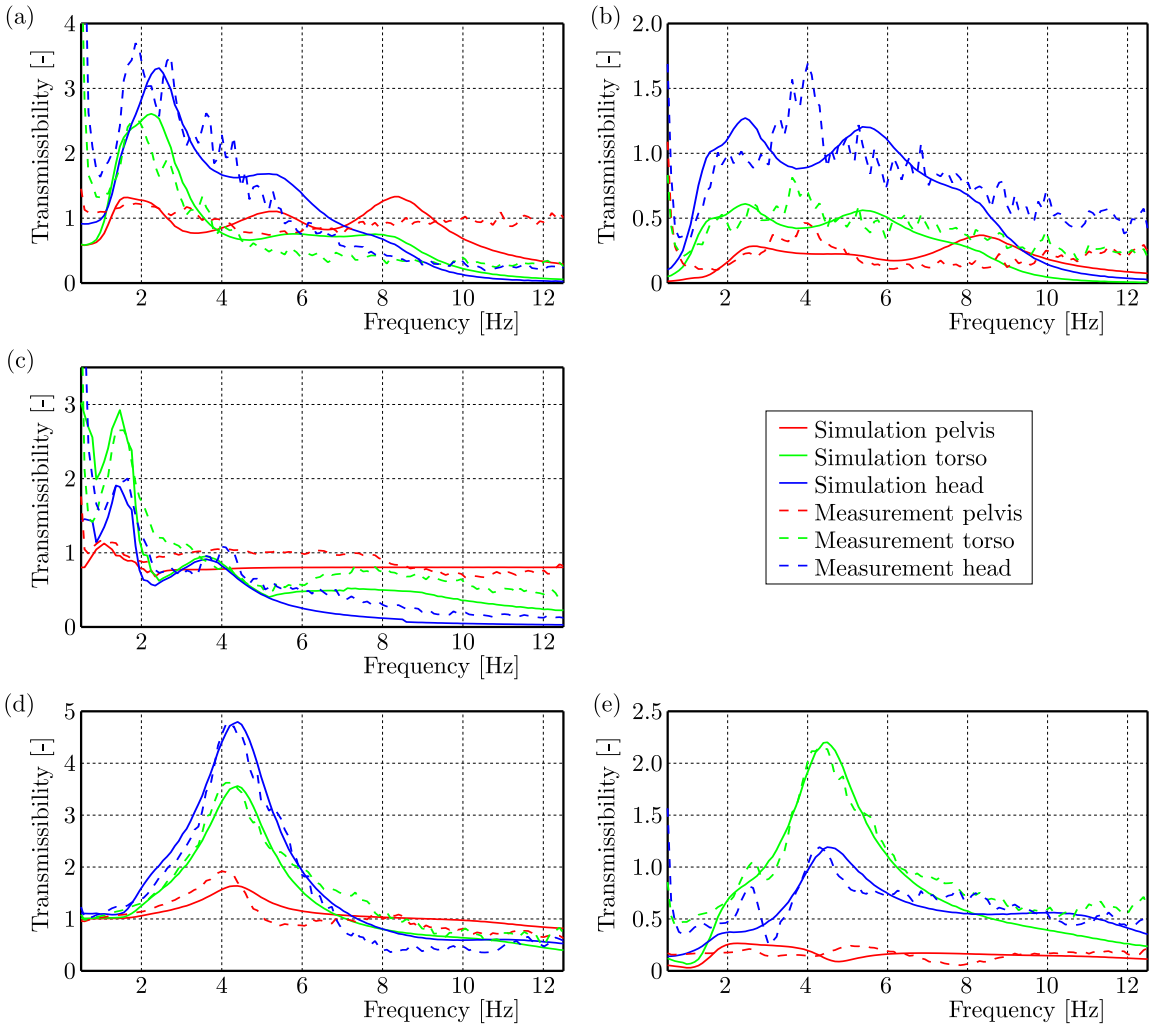

Fig. 6. Transmissibility functions of the human body obtained for different directions of the vibration exposure from: (a) x-direction to x-direction, (b) x-direction to z-direction, (c) y-direction to y-direction, (d) z-direction to z-direction, (e) z-direction to x-direction

Table 2. RMS accelerations of different human body parts obtained by means of computer simulation and laboratory measurement

Output vibration	Human body part	Input vibration					
		along x-direction		along y-direction		along z-direction	
		RMS acceleration [m/s^2]					
		simulation	experiment	simulation	experiment	simulation	experiment
x-direction	Pelvis	1.488	1.451	0	0.149	0.354	0.333
	Torso	1.607	1.555	0	0.112	1.387	1.412
	Head	2.449	2.544	0	0.170	0.846	0.883
y-direction	Pelvis	0	0.189	1.289	1.370	0	0.182
	Torso	0	0.163	1.429	1.410	0	0.151
	Head	0	0.161	1.151	1.241	0	0.194
z-direction	Pelvis	0.354	0.311	0	0.169	1.528	1.468
	Torso	0.529	0.561	0	0.137	2.377	2.403
	Head	1.042	1.148	0	0.175	2.852	2.796

head vibration is actively reduced by the human due to enlarged postural control. Subsequently, the vibration input in the z-direction (Fig. 6d,e) leads to an increase in vibration transmission by individual parts of the human body, i.e. from the pelvis through the torso to the head, but this phenomenon is observed only along the vertical axis (Fig. 6d). Similarly to the previous direction of excitation, the human head shows lower magnitudes while vibration is transferred from the vertical z-direction to the longitudinal x-direction (Fig. 6e).

The presented results well represent the dependence of human sensitivity to vibration in terms of frequency. According to ISO-2631 (1997), the most dangerous range of frequencies for horizontal vibration is between 0.5 Hz and 3 Hz (Figs. 6a and 6c) and for vertical vibration, the frequency ranges from 4 Hz to 8 Hz (Fig. 6d), because several body eigenfrequencies of the seated human are included within these scopes. The root mean square (RMS) accelerations of different human body parts, which are obtained by means of computer simulation and laboratory measurement, are listed in Table 2. Notice that the simulated RMS accelerations equal to $0\,\mathrm{m/s^2}$ mean that no vibration transmission across the selected axes is obtained. Even then the measured RMS accelerations have low values as a result of the measurement noise.

6. Conclusions

In the paper, a simplified model of the human body is proposed and investigated by means of experimental tests under laboratory conditions. The presented model reproduces the dynamic spatial response of a seated human subject to harmful vibration even if the model input is selected as a single-axis excitation. The application of such a model leads to better prediction of human reactions to the whole-body vibration than in commonly used uniaxial models. The input vibration energy is transferred via the human body in various directions simultaneously, which results in a reduction of vibration amplitudes measured along the axis compliant with the excitation direction. As follows from the results shown in this paper, the recommended model is helpful for explaining and predicting human behaviour in a vibrational environment and can be satisfactorily used for simulation purposes of the seating dynamics. A developed simulation model of the human body will be combined with the seat suspension system in further research. The passive and active suspension systems of various mechanical structures will be investigated in order to decrease the harmful influence of mechanical vibrations on humans.

Appendix – Constant model parameters of the seated human body

Parameter	Value	Unit
Masses of individual body parts		
Pelvis (m_1)	25.18	kg
Torso (m_2)	46.77	kg
Head (m_3)	8.04	kg
Mass moments of inertia around different axes		
Pelvis around longitudinal axis (J_{1x})	0.3659	$\mathrm{kg{\cdot}m^2}$
Pelvis around lateral axis (J_{1y})	0.6650	$\mathrm{kg{\cdot}m^2}$
Pelvis around vertical axis (J_{1z})	0.9705	$\mathrm{kg{\cdot}m^2}$
Torso around longitudinal axis (J_{2x})	1.412	$\mathrm{kg{\cdot}m^2}$
Torso around lateral axis (J_{2y})	1.032	$\mathrm{kg{\cdot}m^2}$
Torso around vertical axis (J_{2z})	0.867	$\mathrm{kg{\cdot}m^2}$
Head around longitudinal axis (J_{3x})	0.0871	$\mathrm{kg{\cdot}m^2}$
Head around lateral axis (J_{3y})	0.1020	$\mathrm{kg{\cdot}m^2}$

Head around vertical axis (J_{3z})	0.0687	kg·m^2
Dimensions for mounting visco-elastic elements		
Pelvis along longitudinal axis – lower fixation (a_{1d})	0	m
Pelvis along lateral axis – lower fixation (b_{1d})	0	m
Pelvis along vertical axis – lower fixation (c_{1d})	0.06	m
Pelvis along longitudinal axis – upper fixation (a_{1u})	−0.15	m
Pelvis along lateral axis – upper fixation (b_{1u})	0	m
Pelvis along vertical axis – upper fixation (c_{1u})	0.06	m
Torso along longitudinal axis – lower fixation (a_{2d})	0	m
Torso along lateral axis – lower fixation (b_{2d})	0	m
Torso along vertical axis – lower fixation (c_{2d})	0.225	m
Torso along longitudinal axis – upper fixation (a_{2u})	−0.025	m
Torso along lateral axis – upper fixation (b_{2u})	0	m
Torso along vertical axis – upper fixation (c_{2u})	0.225	m
Head along longitudinal axis – lower fixation (a_{3d})	−0.045	m
Head along lateral axis – lower fixation (b_{3d})	0	m
Head along vertical axis – lower fixation (c_{3d})	0.15	m

Acknowledgements

We would like to thank Isringhausen GmbH and Co. KG for the assistance in the experimental research.

References

1. Adam S.A., Jalil N.A.A., 2017, Vertical suspension seat transmissibility and SEAT values for seated person exposed to whole-body vibration in agricultural tractor – preliminary study, *Procedia Engineering*, **170**, 435-442
2. Chandler R.F., Clauser C.E, McConville J.T., Reynolds H.M., 1975 *Investigation of Inertial Properties of the Human Body*, U.S. Department of Transportation within the Project: Seat Design, Driver Comfort, and the Automotive Package, Washington
3. Desai R., Guha A., Seshu P., 2018, Multibody biomechanical modelling of human body response to direct and cross axis vibration, *Procedia Computer Science*, **133**, 494-501
4. Fritz M., 19981, Analyse der vertikalen Auflagenkraft bei unterschiedlichen Sprüngen anhand von gemessenen und simulierten Kraftkurven, *Leistungssport*, **11**, 1, 74-78
5. Głowiński S., Blażejewski A., Królikowski T., Knitter R., 2019, Gait recognition: a challenging task for MEMS signal identification, *Sustainable Design and Manufacturing*, **155**, 473-483
6. Glowinski S., Blazejewski A., Krzyzynski T., 2017a, Human gait feature detection using inertial sensors wavelets, *Wearable Robotics: Challenges and Trends – Part of the Biosystems and Biorobotics*, **16**, 397-401
7. Glowinski S., Blazejewski A., Krzyzynski T., 2017b, Inertial sensors and wavelets analysis as a tool for pathological gait identification, *Innovations in Biomedical Engineering – Part of the Advances in Intelligent Systems and Computing*, **526**, 106-114
8. Głowiński S., Blażejewski A., Krzyżyński T., 2018, Body part accelerations evaluation for chosen techniques in martial arts, *Advances in Intelligent Systems and Computing*, **623**, 235-243
9. Głowiński S., Krzyżyński T., Pecolt S., Maciejewski I., 2015, Design of motion trajectory of an arm exoskeleton, *Archive of Applied Mechanics*, **85**, 75-87

10. International Organization for Standardization ISO 2631, 1997, *Mechanical Vibration and Shock – Evolution of Human Exposure to Whole Body Vibration*, Geneva
11. International Organization for Standardization ISO 7096, 2000, *Earth-Moving Machinery – Laboratory Evaluation of Operator Seat Vibration*, Geneva
12. Kim T.H., Kim Y.T., Yoon Y.S., 2005, Development of a biomechanical model of the human body in a sitting posture with vibration transmissibility in the vertical direction, *International Journal of Industrial Ergonomics*, **35**, 9, 817-829
13. Liu C., Qiu Y., 2020, Localised apparent masses over the interface between a seated human body and a soft seat during vertical whole-body vibration, *Journal of Biomechanics*, **109**, ID 109887, 1-12
14. Liu C., Qiu Y., 2021, Mechanism associated with the effect of backrest inclination on biodynamic responses of the human body sitting on a rigid seat exposed to vertical vibration, *Journal of Sound and Vibration*, **510**, ID 116299, 1-22
15. Maciejewski I., Blazejewski A., Pecolt S., Krzyzynski T., 2022, A sliding mode control strategy for active horizontal seat suspension under realistic input vibration, *Journal of Vibration and Control*, **29**, 11-12, 2539-2551
16. Maciejewski I., Krzyzynski T., 2020, Global sensitivity analysis in optimisation of the vibration reduction systems, *AIP Conference Proceedings*, **2239**, 020028
17. Maciejewski I., Krzyzynski T., Meyer L., Meyer H., 2017, Shaping the vibro-isolation properties of horizontal seat suspension, *Journal of Low Frequency Noise, Vibration and Active Control*, **36**, 3, 203-213
18. Maciejewski I., Krzyżyński T., Pecolt S., Chamera S., 2019, Semi-active vibration control of horizontal seat suspension by using magneto-rheological damper, *Journal of Theoretical and Applied Mechanics*, **57**, 2, 411-420
19. Mandapuram S., Rakheja S., Marcotte P., Boileau P.E., 2011, Analyses of biodynamic responses of seated occupants to uncorrelated fore-aft and vertical whole-body vibration, *Journal of Sound and Vibration*, **330**, 16, 4064-4079
20. Mihcin S., Kose H., Cizmeciogullari S., Ciklacandir S., Kocak M., Tosun A., Akan A., 2019, Investigation of wearable motion capture system towards biomechanical modelling, *IEEE International Symposium on Medical Measurements and Applications*, 1-5
21. Shippen J., May B., 2016, BoB – biomechanics in MATLAB, *Proceedings of the 11th International Conference BIOMDLORE*,
22. Stein G.J., Mčka P., Gunston T.P., Badura S., 2008, Modelling and simulation of locomotive driver's seat vertical suspension vibration isolation system, *International Journal of Industrial Ergonomics*, **38**, 5-6, 384-395
23. Stoica P., Moses R., 2005, *Spectral Analysis of Signals*, Prentice Hall, New Yersey
24. Sun X., Jing X., 2016, A nonlinear vibration isolator achieving high-static-low dynamic stiffness and tunable anti-resonance frequency band, *Mechanical Systems and Signal Processing*, **80**, 166-188
25. Sun S., Yang J., Deng H., Du H., Li W.H., Nakano M., 2015, Horizontal vibration reduction of a seat suspension using negative changing stiffness magnetorheological elastomer isolators, *International Journal of Vehicle Design*, **68**, 104-118
26. Zhao Y., Alashmori M., Bi F., Wang X., 2021, Parameter identification and robust vibration control of a truck driver's seat system using multi-objective optimization and genetic algorithm, *Applied Acoustics*, **173**, ID 107697, 1-13
27. Zheng G., Qiu, Y., Griffin M.J., 2011, An analytic model of the in-line and cross-axis apparent mass of the seated human body exposed to vertical vibration with and without a backrest, *Journal of Sound and Vibration*, **330**, 26, 6509-6525

Manuscript received August 28, 2023; accepted for print September 22, 2023

JOURNAL OF THEORETICAL AND APPLIED MECHANICS
61, 4, pp. 847-856, Warsaw 2023
https://doi.org/10.15632/jtam-pl/172875

EULER-LAGRANGE EQUATIONS AND NOETHER'S THEOREM OF A MULTI-SCALE MECHANO-ELECTROPHYSIOLOGICAL COUPLING MODEL OF NEURON MEMBRANE DYNAMICS

Peng Wang

School of Civil Engineering and Architecture, University of Jinan, Jinan, Shangdong, P.R. China
e-mail: cea_wangp@ujn.edu.cn; sdpengwang@163.com

Noether's theorem is applied into a multi-scale mechano-electrophysiological coupling model of neuron membrane dynamics. The Euler-Lagrange equations in generalized coordinates of this model are deduced by the nonconservative Hamilton principle. The Noether symmetry criterion and conserved quantities based on the Lie point transformation group are given. The influence of external non-potential forces and material parameters on the forms of Noether conserved quantities is detailed discussed, which indicates that the conserved quantities are very depending on the loading rate and mechanical parameters of the membrane.

Keywords: Noether symmetry, conserved quantities, Hamilton principle, mechno-electrophysiological coupling, axon

1. Introduction

Symmetry and first integrals are two fundamental structures of ordinary differential equations (ODE), which can reduce the order of ODE and even can give solutions to ODE (Bluman and Anco, 2002). Since Noether revealed the relation between symmetry and conserved quantity, Noether's theorem (Noether, 1918) has been extended to many fields. Kosmann-Schwarzbach and Schwarzbach (2011) gave a comprehensive review of Noether's theorem, such as theorem for discrete equations in mathematics (Dorodnitsyn, 2001; Hydon and Mansfield, 2011; Peng, 2017; Mansfield *et al.* , 2019; Peng and Hydon, 2022), physics (Wang, 2011, 2012; Wang and Zhu, 2011), mechanics and engineering (Mei, 1993, 2004; Zhang and Chen, 2018; Zhang, 2022). Noether's symmetry always can refer to conserved quantities, it is also called variational symmetry (Peng and Hydon, 2022). Besides Noether's symmetry, there are Lie's symmetry (Olver, 1986; Chen *et al.*, 2005), Mei symmetry (Mei, 2000; Fang *et al.*, 2007; Wang and Xue, 2016; Luo *et al.*, 2018) and other symmetries (Wang, 2018).

Recently, a new model of an axon membrane that is a multi-scale memchano--electrophysiological coupling model (Drapaca, 2015) has been proposed to understand the propagation of an action potential. Though there are different viewpoints on origin of the action potential, this new model may bridge a simple way to compare micro-mechanical parameters with experiments directly, which may be helpful in clinic applications. However, differential equations describe those models as nonlinear and multi-scale, which is not easy to solve out. Symmetry analysis based on Lie's group is a powerful tool in reduction of nonlinear differential equations and getting exact solutions (Olver, 1986). However, to our knowledge, Noether's symmetry has not been introduced into this problem.

In this paper, we will applied Noether's theorem into this model, and give Noether's symmetry criterion and conserved quantities.

The construction of this paper is as following. In Section 2, we will generalize the model in (Drapaca, 2015) and give a generalized Lagrange equation of the axon dynamics. Because the

author (Drapaca, 2015) supposes that the capacitor of the membrane is constant, and uses the classical Hodgkin-Huxley equation to replace the equations of dynamics describing the mechano--transduction of ionic channel activation and inactivation, so that the results cannot reflect the mechanical information of subcellular structure affecting the action potential, in fact returning into the voltage active ionic channels scenario again. Furthermore, the author supposed no external forces acting on the system, all the process is triggered by the input electric current. So, in this part we will modified the model to be able to study a more general case, which considerd parameters of the subcellular and non-potential forces model and suppose both mechanical factors or voltage factors that can activate ionic gate control. Then we will deduce the Euler--Lagrange equation. In Section 3, Noether's symmetry and conserved quantities of the neural dynamics are studied. The criterion of Noether's symmetry and the expression form of conserved quantities are given. In Section 4, we will specifically discuss the deduced conserved quantities on various conditions. The final Section concludes the paper.

2. The Euler-Lagrange equations of neural membrane dynamics

2.1. A review of the model

As we know, the membrane of an axon consists of a phospholipid bilayer with an embedded channel protein. The propagation of electric signals in the neuron system is by producing action potential accompanied with an ion channel open or shut. The action potential can induce deformation of the neuron membrane, whereas the inverse deformation of the neuron membrane can also induce the action potential, so it is a coupling process. Modelling the axon as

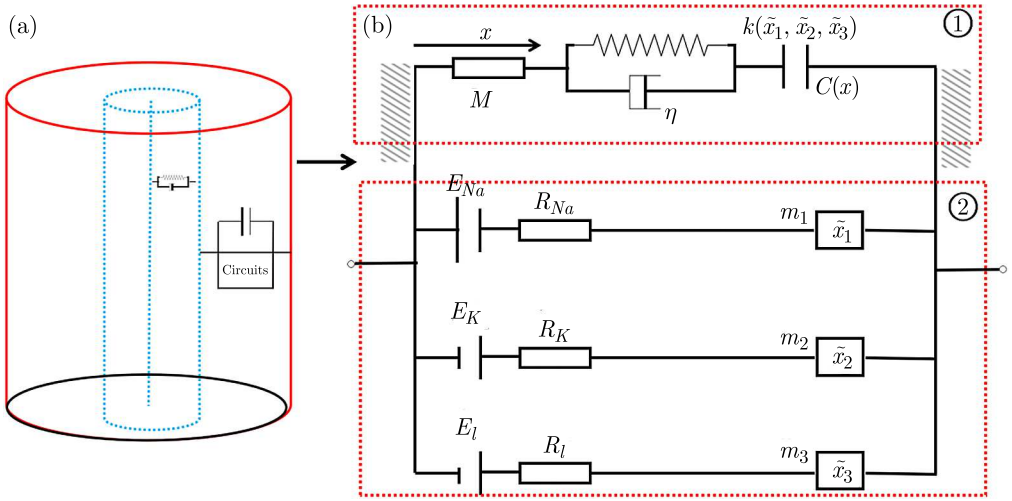

Fig. 1. The schematic of an axon (a) and mechano-electrical coupling of the axon membrane (b). The axon is an axi-symmetric homogeneous circular cylinder with intracellular space filled with axoplasm (light blue), and the outer layer is the membrane space between blue and red. By symmetry and homogeneity of the column, we study half of the axon. In cellular scale, we model the intracellular space as a viscoelastic material by the Kelvin model connects with the axon capacitor (the dotted box ①), where $(k\widetilde{x}_1, \widetilde{x}_2, \widetilde{x}_3)$ is relative to the response of cytoskeleton, where $(\widetilde{x}_1, \widetilde{x}_2, \widetilde{x}_3)$ is relative motion of the cytoskeleton with different ionic channels, x is displacement of the membrane. Mechanical motion or electrical stimuli can trigger the circuit. In the subcellular scale, the ionic exchange obeys the classic Hodgkin-Huxley equations (dotted box ②), but add mechanotransduction channel action that is motion of the channel protein $(\widetilde{x}_1, \widetilde{x}_2, \widetilde{x}_3)$

an axi-symmetric cylinder with intracellular space and outer membrane and supposing the axon is homogenous, we can use a linear visco-elastic Kelvin-Voigt model to formulate the macro-

-mechanical process and Hodgkin-Huxley model to describe the electric process. The coupling process is unified through capacitance and membrane displacement, see Fig. 1.

The axon can be considered as an axisymmetric cylinder with a circular cross section, so we can study a half axon by symmetry. We can express the macro-mechanical kinetic energy as $T = 0.5M\dot{x}^2$, where M denotes half constant mass of the neuron of the constant cross-sectional area A and $x(t)$ is the macroscopic (cell level) displacement of the membrane depending on time, because the movement of the membrane affects the axon capacitor, which consequently induces depolarization electric current of the axon membrane. The macro mechanical potential energy is $V = -0.5kx(t)^2$. The mechanical dissipation function (work of the viscous force) $\psi_m = 0.5\eta\dot{x}^2$, where η is the viscosity coefficient. The micro relative kinetic energy of cytoskeleton structures or ionic gate control movement is $T^* = 0.5(m_1\dot{x}_1^2 + m_2\dot{x}_2^2 + m_3\dot{x}_3^2)$, where $x_1(t)$, $x_2(t)$ and $x_3(t)$ are time-dependent micro displacements of the cytoskeleton regulating activations of Na^+ and K^+ channels and, respectively, the inactivation of Na^+ channel, and varying with the deformation of the neuron membrane or conduction of the action potential, and m_1, m_2, m_3 are constant masses of mechno-sensitive channel proteins or lipid rafts. Here, the explanation T^* and components therein, is different from electrical kinetic energy in (Drapaca, 2015), but instead as the kinetic energy of the cytoskeleton from the point of view of mechanotransduction in intracellular. The electric energy of capacitor is $W_e = 0.5e_c^2/C(x)$, where $C(x)$ is capacitance of the membrane. The electric dissipation function is $\psi_e = 0.5R_{Na}\dot{e}_{Na}^2 + 0.5R_K\dot{e}_K^2 + 0.5R_l\dot{e}_l^2 + E_{Na}\dot{e}_{Na} + E_K\dot{e}_K + E_l\dot{e}_l$, where currents denote the transmembrane current induced by the membrane deformation or action potential.

2.2. The Lagrange equation of the model

Based on the conservation law of charge, we have holonomic constraint to the charge: $e_C - e_{Na} - e_K - e_l = 0$, so the number if degrees of freedom of the coupling system is seven. Introduce generalized coordinates to express universally the spatial and electrical variables q_s $(s = 1, \ldots, 4, 4+1, \ldots, 7)$, where $q_1 = x$, $q_2 = x_1$, $q_3 = x_2$, $q_4 = x_3$ and $q_5 = e_{Na}$, $q_6 = e_K$, $q_7 = e_l$. The Lagrangian of the neuronal axon membrane mechano-electrophysiological model is

$$L(t, q_s(t)\dot{q}_s(t)) = T + T^* - V - W_e \tag{2.1}$$

The virtual work of nonconservative generalized forces is

$$\delta W(t, q_s, \dot{q}_s) = -\Big(\frac{\partial(\psi_m + \psi_e)}{\partial\dot{q}_s} - Q_s\Big)\delta q_s \tag{2.2}$$

The Hamilton principle of the nonconservative mechano-electrophysiological system of the axon membrane is

$$\int_0^t (\delta L + \delta W)\, dt = 0 \tag{2.3}$$

By expanding the above equation, and using the communication relation $d\delta = \delta d$ which holds for holonomic constrained systems, and end points relations $\delta q(0) = 0$, $\delta q(t) = 0$, we can get mechano-electrophysiological coupling Euler-Lagrange equations of the axon membrane dynamics

$$\frac{d}{dt}\frac{\partial L}{\partial\dot{q}_s} - \frac{\partial L}{\partial q_s} + \frac{\partial\psi}{\partial\dot{q}_s} = Q_s \qquad s = 1, \ldots, 7 \tag{2.4}$$

where $\psi = \psi_m + \psi_e$. The coupling equations of motion describe the changes of ions between the outer and intercellular space and micro and macro deformation of the neuron membrane.

Take the very expression of Lagrangian L, Eq. (2.1), into Eq. (2.4), then we can obtain Euler-Lagrange differential equations the same as in (Drapaca, 2015)

$$M\ddot{x} + kx + \eta\dot{x} - \frac{1}{2}\frac{\partial C}{\partial x}\Big(\frac{q_C}{C}\Big)^2 = Q_1 \tag{2.5}$$

and

$$m_1\ddot{x}_1 + \frac{1}{2}\frac{\partial k}{\partial x_1} = Q_2 \qquad m_2\ddot{x}_2 + \frac{1}{2}\frac{\partial k}{\partial x_2} = Q_3 \qquad m_3\ddot{x}_3 + \frac{1}{2}\frac{\partial k}{\partial x_3} = Q_4 \tag{2.6}$$

and

$$R_{Na}\dot{e}_{Na} + E_{Na} = V \qquad R_K\dot{e}_K + E_K = V \qquad R_l\dot{e}_l + E_l = V \tag{2.7}$$

where $V = U_i = q_C/C$ is potential of the capacitor. Kirchoff's current law demands $\dot{q}_C = \dot{q}_{Na} + \dot{q}_K + \dot{q}_l$. Take Eqs. (2.7) into Kirchoff's current law, the well-known Hodgkin-Huxley equation of the membrane potential can be found

$$\frac{d}{dt}(CV) = I - \frac{1}{R_{Na}}(V - E_{Na}) - \frac{1}{R_K}(V - E_K) - \frac{1}{R_l}(V - E_l) \tag{2.8}$$

where I is the external stimulus current.

Remark 1. *(i) In Ref. (Drapaca, 2015), the author supposed external non-potential forces $Q_s = 0$, that is the coupling process is triggered all by electric current which is not accordance with other supposed mechanical signals which can also induce action potential (Heimburg and Jackson, 2005), so for an alternative in the present paper, we suppose that both of them can induce the action potential.*

(ii) At the some time, Drapaca uses the Hodgkin-Huxley equation to replace equations (2.6) which makes the parameters of m_1, m_2, m_3, k, E_{Na}, E_K, E_l, R_1, R_2, R_3 all depend on voltage V, which may reduce the model into Hodgkin's and Huxley's electric paradigm.

(iii) Though the parameters m_1, m_2, m_3, k, E_{Na}, E_K, E_l, R_1, R_2, R_3 are difficult to prescribe due to insufficient knowledge of neuronal mechanotransduction processes as Drapaca said in (Drapaca, 2015), we try to discuss their influences on the conserved quantities of the axon membrane in theory which may be useful for future experiment design.

In the following study we will treat the general cases by Noether's symmetry analysis.

3. Noether's symmetry and conserved quantities of the neuronal membrane dynamics

We introduce a one-parameter infinitesimal Lie point transformation group in space (t, q_s)

$$t^* = t + \varepsilon\xi_0(t, \mathbf{q}) \qquad q_s^* = q_s + \varepsilon\xi_s(t, \mathbf{q}) \qquad s = 1, \ldots, 7 \tag{3.1}$$

where ε is an infinitesimal parameter, $\xi_0(t, \mathbf{q})$, $\xi_s(t, \mathbf{q})$ are infinitesimal transformation generators. The infinitesimal generator vector

$$X^{(0)} = \frac{\partial}{\partial t}\xi_0(t, \mathbf{q}(t)) + \frac{\partial}{\partial q_s}\xi_s(t, \mathbf{q}(t)) \tag{3.2}$$

which is the operator for the infinitesimal generator of the one-parameter Lie group of transformations (3.1) in space $(t, \mathbf{q})$. The first prolongation of the infinitesimal generator vector is

$$X^{(1)} = X^{(0)} + \frac{\partial}{\partial \dot{q}_s}[\dot{\xi}_s(t, \mathbf{q}(t)) - \dot{\xi}_0(t, \mathbf{q}(t))\dot{q}_s(t)] \tag{3.3}$$

The second prolongation of the infinitesimal generator vector is

$$X^{(2)} = X^{(1)} + \frac{\partial}{\partial \dot{q}_s}[\ddot{\xi}_s(t, \mathbf{q}(t)) - 2\ddot{q}_s(t)\dot{\xi}_0(t, \mathbf{q}(t)) - \dot{q}_s(t)\ddot{\xi}_0(t, \mathbf{q}(t))] \tag{3.4}$$

which defines the first or second extended one-parameter Lie group of transformation in space $(t, \mathbf{q}, \dot{\mathbf{q}})$ or space $(t, \mathbf{q}, \dot{\mathbf{q}}, \ddot{\mathbf{q}})$ by partial derivatives, where $(\dot{\bullet})$ means the first derivative to t, $(\ddot{\bullet})$ means the second derivative to t.

The Hamilton action is

$$S(\gamma) = \int_{t_0}^{t_1} L(t, q_s, \dot{q}_s)\, dt \tag{3.5}$$

Under the infinitesimal transformation, the curve γ is transformed to curve γ^*. The corresponding Hamilton action is transformed to

$$S(\gamma^*) = \int_{t_0^*}^{t_1^*} L(t^*, q_s^*, \dot{q}_s^*)\, dt^* \tag{3.6}$$

The variation ΔS of the Hamilton action S is the main linear part of the difference $S(\gamma^* - S(\gamma))$ to the infinitesimal parameter ε, then we have

$$\Delta S = \int_{t_0}^{t_1} [\Delta L + L(\Delta t)^{\bullet}]\, dt \tag{3.7}$$

where Δ denotes anisochronous variation, and δ denotes isochronous variation. Expanding the above equation, we have

$$\Delta S = \int_{t_0}^{t_1} \Big(L\frac{d}{dt}\Delta t + \frac{\partial L}{\partial t}\Delta t + \frac{\partial L}{\partial q_s}\Delta q_s + \frac{\partial L}{\partial \dot{q}_s}\Delta \dot{q}_s \Big)\, dt \tag{3.8}$$

Replace the infinitesimal transformation Eq. (3.1) into Eq. (3.8), and use the relation $\delta q_s = \Delta q_s - \dot{q}_s \Delta t = \varepsilon(\xi_s - \dot{q}_s \xi_0)$, $\Delta \dot{q}_s = (\Delta q_s)^{\bullet} - \dot{q}_s(\Delta t)^{\bullet}$, then the following expression can be obtained

$$\Delta S = \int_{t_0}^{t_1} \Big\{ \frac{d}{dt}\Big[L\xi_0 + \frac{\partial L}{\partial \dot{q}_s}(\xi_s - \dot{q}_s\xi_0) \Big] + \Big(\frac{\partial L}{\partial q_s} - \frac{d}{dt}\frac{\partial L}{\partial \dot{q}_s} \Big)(\xi_s - \dot{q}_s\xi_0) \Big\}\, dt \tag{3.9}$$

Definition 1. If the variation of Hamilton action satisfies

$$\Delta S = 0 \tag{3.10}$$

infinitesimal transformation (3.1) is the Noether symmetrical transformation.

Based on Definition 1, we can get the Noether symmetry criterion.

Criterion 1. If the infinitesimal generators ξ_0, ξ_s satisfy

$$L\dot{\xi}_0 + X^1(L) = 0 \tag{3.11}$$

the transformation invariance is named Noether's symmetry, which is also called variational symmetry.

For Noether's symmetry, we can deduce the conserved quantities.

Theorem 1. For a Lagrangian system, if the generators $\xi_0(t, \mathbf{q})$, $\xi_s(s, \mathbf{q})$ of infinitesimal transformations is Noether's symmetry, there exist conserved quantities as

$$I_N = L\xi_0 + \frac{\partial L}{\partial \dot{q}_s}(\xi_s - \dot{q}_s\xi_0) = \text{ const} \tag{3.12}$$

which are called Noether conserved quantities. We can directly deduce this result from Eq. (3.9).

In fact, we can generalize the Noether symmetry to non-conservative dynamical systems.

Definition 2. If the Hamilton action is a generalized quasi-invariant under an infinitesimal transformation group, that is, the variation satisfies

$$\Delta S = -\int_{t_0}^{t_1} \Big[\frac{d}{dt}(\Delta G) + \Big(Q_s - \frac{\partial \psi}{\partial \dot{q}_s}\Big)\delta q_s\Big]\, dt \tag{3.13}$$

infinitesimal transformation (3.1) is a generalized quasi-symmetrical transformation, where $G(t, \mathbf{q}, \dot{\mathbf{q}})$ is a gauge function, and $(Q_s - \partial\psi/\partial\dot{q}_s)\delta q_s$ is the sum of virtual work of generalized non-conservative forces.

Based on Definition 2, we can get the generalized Noether symmetry criterion.

Criterion 2. If there exists a gauge function $G(t, \mathbf{q}, \dot{\mathbf{q}})$ making the infinitesimal generators ξ_0, ξ_s satisfy

$$L\dot{\xi}_0 + X^1(L) + \Big(Q_s - \frac{\partial \psi}{\partial \dot{q}_s}\Big)(\xi_s - \dot{q}_s\xi_0) + \dot{G}_N = 0 \tag{3.14}$$

the infinitesimal transformation is named a quasi-Noether symmetry.

The Noether symmetry always can lead to conserved quantities.

Theorem 2. For Lagrange equation Eq. (2.4) of the neuronal membrane dynamics, if the infinitesimal generators $\xi_0(t, \mathbf{q})$, $\xi_s(s, \mathbf{q})$ satisfy Criterion 2, the system has the following first integrals

$$I_N = L\xi_0 + \frac{\partial L}{\partial \dot{q}_s}(\xi_s - \dot{q}_s\xi_0) + G_N = \text{ const} \tag{3.15}$$

which are also Noether conserved quantities.

Proof: Expanding Definition 2, we have

$$\Delta S = \int_{t_0}^{t_1} \Big\{ \frac{d}{dt}\Big[L\xi_0 + \frac{\partial L}{\partial \dot{q}_s}(\xi_s - \dot{q}_s\xi_0)\Big] + \Big(\frac{\partial L}{\partial q_s} - \frac{d}{dt}\frac{\partial L}{\partial \dot{q}_s} - Q_s + \frac{\partial \psi}{\partial \dot{q}_s}\Big)(\xi_s - \dot{q}_s\xi_0)\Big\}\, dt = 0 \tag{3.16}$$

considering Eq. (2.4), we can get the results directly.

4. Noether's symmetry generators and conserved quantities

Take the exact form of Lagrangian L and dissipative function ψ into Noether identity Eq. (3.14), then we have

$$\begin{aligned}
&\xi_1\Big(-kq_1+\frac{V^2}{2}\frac{\partial C(q_1)}{\partial q_1}\Big)+M\dot{q}_1(\dot{\xi}_1-\dot{q}_1\dot{\xi}_0)+(Q_1-\eta\dot{q}_1)(\xi_1-\dot{q}_1\xi_0)-\xi_2\frac{1}{2}q_1^2\frac{\partial k}{\partial q_2}\\
&+m_2\dot{q}_2(\dot{\xi}_2-\dot{q}_2\dot{\xi}_0)+Q_2(\xi_2-\dot{q}_2\xi_0)-\xi_3\frac{1}{2}q_1^2\frac{\partial k}{\partial q_3}+m_3\dot{q}_3(\dot{\xi}_3-\dot{q}_3\dot{\xi}_0)\\
&+Q_3(\xi_3-\dot{q}_3\xi_0)-\xi_4\frac{1}{2}q_1^2\frac{\partial k}{\partial q_4}+m_4\dot{q}_4(\dot{\xi}_4-\dot{q}_4\dot{\xi}_0)+Q_4(\xi_4-\dot{q}_4\xi_0)\\
&+(Q_5-R_{Na}\dot{q}_5-E_{Na})(\xi_5-\dot{q}_5\xi_0)-\xi_5V+(Q_6-R_K\dot{q}_6-E_K)(\xi_6-\dot{q}_6\xi_0)-\xi_6V\\
&+(Q_7-R_l\dot{q}_8-E_l)(\xi_7-\dot{q}_7\xi_0)-\xi_7V+L\dot{\xi}_0+\dot{G}_N=0
\end{aligned}\tag{4.1}$$

Next, let us discuss the structures of Noether conserved quantities when the external nonpotential forces $Q_s\neq 0$ $(s=1,2,3,4)$. If $k=$ const and the total charges of the systems is invariant, we can get solutions

$$\xi_0=\pm1 \qquad \xi_1=\pm\dot{q}_1 \qquad \xi_2=\xi_3=\xi_4=0 \qquad \xi_i=\pm\dot{q}_s \quad (s=5,6,7) \tag{4.2}$$

$$\xi_0=\pm1 \qquad \xi_i=\pm\dot{q}_s \quad (s=1,2,3,4) \tag{4.3}$$

$$\xi_i=\pm\dot{q}_s \quad (s=5,6,7) \tag{4.4}$$

$$\xi_0=\xi_1=0 \qquad \xi_2=\xi_3=\xi_4=\pm1 \qquad \xi_5=\xi_6=\xi_7=0 \tag{4.5}$$

$$\xi_0=\xi_1=0 \qquad \xi_i=\pm\dot{q}_s \quad (s=2,3,4) \qquad \xi_5=\xi_6=\xi_7=0 \tag{4.6}$$

The corresponding Noether conserved quantities are

$$\begin{aligned}
&I_{N11}=\pm\Big(\frac{1}{2}m_2\dot{q}_2^2+\frac{1}{2}m_3\dot{q}_3^2+\frac{1}{2}m_4\dot{q}_4^2-W_q\Big) \qquad I_{N12}=0\\
&I_{N13}=\pm(m_2\dot{q}_2+m_3\dot{q}_3+m_4\dot{q}_4-Q_q) \qquad I_{N14}=-I_{N11}
\end{aligned}\tag{4.7}$$

Here, the composition of conserved quantities (4.7) depends on specific non-potential forces. W_q has several forms

$$\begin{aligned}
&Q_2=\ddot{q}_2 \qquad Q_3=\ddot{q}_3 \qquad Q_4=\ddot{q}_4 \qquad W_{q1}=\frac{1}{2}(\dot{q}_2^2+\dot{q}_3^2+\dot{q}_4^2)\\
&Q_2=\ddot{q}_3 \qquad Q_3=\ddot{q}_2 \qquad Q_4=\ddot{q}_4=0 \qquad W_{q2}=\dot{q}_2\dot{q}_3+\frac{1}{2}\dot{q}_4^2=0\\
&Q_2=\ddot{q}_4 \qquad Q_3=\ddot{q}_3=0 \qquad Q_4=\ddot{q}_2 \qquad W_{q3}=\dot{q}_2\dot{q}_4+\frac{1}{2}\dot{q}_3^2=0\\
&Q_2=\ddot{q}_2=0 \qquad Q_3=\ddot{q}_4 \qquad Q_4=\ddot{q}_3 \qquad W_{q4}=\dot{q}_3\dot{q}_4+\frac{1}{2}\dot{q}_2^2=0
\end{aligned}\tag{4.8}$$

and $Q_q=\dot{q}_2+\dot{q}_3+\dot{q}_4$ or a combination of $\dot{q}_s$ $(s=2,3,4)$. We point out that for solution (4.2)-(4.6), always holding $\xi_s-\dot{q}_s\xi_0=0$, the non-potential forces have no action on the Noether identities.

If $k=$ const , $C=$ const , we also have solutions (4.2)-(4.6), and the corresponding conserved quantities are

$$I_{N21}=I_{N11}\mp\frac{e_C^2}{2C} \qquad I_{N22}=-\frac{e_C^2}{2C} \qquad I_{N23}=I_{N13} \qquad I_{N24}=I_{N14} \tag{4.9}$$

We can get that for infinitesimal generators (4.5) and (4.6), the capacitance does not affect the conserved quantities.

If $k \neq$ const, $C =$ const, we have one solution (4.4), and the corresponding conserved quantities are $I_{N31} = -e_C^2/2C$. For $k \neq$ const, $C \neq$ const, we have one solution (4.4) with the trivial invariant $I_N = 0$.

There is a particular case $Q_1 = \eta\dot{q}_1$ in which the external non-potential force is synchronized with viscosity of the axon membrane material. Let us study the conserved quantities for this case. One solution of Noether's identity is

$$\xi_0 = \pm 1 \qquad \xi_1 = \xi_2 = \xi_3 = \xi_4 = 0 \qquad \xi_s = \pm\dot{q}_s \quad (s = 5, 6, 7) \tag{4.10}$$

The corresponding Noether conserved quantities are

$$I_N = \mp\Big(\frac{1}{2}M\dot{q}_1^2 + \frac{1}{2}kq_1^2 + \frac{e_C^2}{2C} + \frac{1}{2}m_2\dot{q}_2^2 + \frac{1}{2}m_3\dot{q}_3^2 + \frac{1}{2}m_4\dot{q}_4^2\Big) \tag{4.11}$$

Furthermore, if $k =$ const and the total charge of the system is invariant, we can get solutions (4.2) and (4,4) and corresponding conserved quantities with $I_{N61} = I_{N11}$, $I_{N62} = 0$, and other two solutions

$$\begin{aligned} &\xi_0 = \pm 1 \qquad \xi_1 = \mp\dot{q}_1 \qquad \xi_s = 0 \quad (s = 2, 3, 4) \qquad \xi_s = \pm\dot{q}_s \quad (s = 5, 6, 7) \\ &\xi_0 = \pm 1 \qquad \xi_1 = \mp\dot{q}_1 \qquad \xi_s = 0 \quad (s = 2, 3, 4) \qquad \xi_s = \pm\dot{q}_s \quad (s = 5, 6, 7) \end{aligned} \tag{4.12}$$

The corresponding Noether conserved quantities are

$$\begin{aligned} I_{N63} &= \mp\Big(M\dot{q}_1^2 + kq_1^2 + \frac{e_C^2}{C} + \frac{1}{2}m_2\dot{q}_2^2 + \frac{1}{2}m_3\dot{q}_3^2 + \frac{1}{2}m_4\dot{q}_4^2 - W_q\Big) \\ I_{N64} &= \pm\Big(\frac{1}{2}M\dot{q}_1^2 + \frac{1}{2}kq_1^2 + \frac{e_C^2}{2C}\Big) \end{aligned} \tag{4.13}$$

If $k =$ const, $C =$ const, we also have solutions (4.2)-(4.6) and (4.12), and the corresponding conserved quantities are $I_{N71} = I_{N21}$, $I_{N72} = I_{N22}$, $I_{N73} = I_{N13}$, $I_{N74} = I_{N14}$, and

$$\begin{aligned} I_{N75} &= \mp\Big(M\dot{q}_1^2 + kq_1^2 + \frac{e_C^2}{2C} + \frac{1}{2}m_2\dot{q}_2^2 + \frac{1}{2}m_3\dot{q}_3^2 + \frac{1}{2}m_4\dot{q}_4^2 - W_q\Big) \\ I_{N76} &= \pm\Big(\frac{1}{2}M\dot{q}_1^2 + \frac{1}{2}kq_1^2\Big) \end{aligned} \tag{4.14}$$

and other solutions and conserved quantities, for example,

$$\begin{aligned} &\xi_0 = 1 \qquad \xi_1 = -\dot{q}_1 \qquad \xi_s = \dot{q}_s \quad (s = 2, 3, 4, 5, 6, 7) \\ &\xi_0 = 1 \qquad \xi_s = -\dot{q}_s \quad (s = 1, 2, 3, 4) \qquad \xi_s = \dot{q}_s \quad (s = 5, 6, 7) \end{aligned} \tag{4.15}$$

The corresponding Noether conserved quantities are

$$\begin{aligned} I_{N77} &= -M\dot{q}_1^2 - kq_1^2 - \frac{e_C^2}{2C} \\ I_{N78} &= I_{N77} - m_2\dot{q}_2^2 - m_3\dot{q}_3^2 - m_4\dot{q}_4^2 + 2W_q \end{aligned} \tag{4.16}$$

In fact in (4.15), the generators ξ_s $(s = 2, 3, 4)$ have a few combination types.

If $k \neq$ const, $C =$ const, we have one solution (4.4), and the corresponding conserved quantities are $I_N = 0$. For $k \neq$ const, $C \neq$ const, we have one solution (4.4) with the trivial invariant $I_N = -e_C^2/2C$. For only $k =$ const, we have solutions (4.5) and (4.6) with corresponding conserved quantities as

$$\begin{aligned} I_{N81} &= -\frac{1}{2}\Big(M\dot{q}_1^2 + kq_1^2 + \frac{e_C^2}{2C} + m_2\dot{q}_2(\dot{q}_2 - 1) + m_3\dot{q}_3(\dot{q}_3 - 1) + m_4\dot{q}_4(\dot{q}_4 - 1) - W_q + Q_q\Big) \\ I_{N82} &= I_{N14} \end{aligned} \tag{4.17}$$

In this Section, we have discussed the effects of parameters k, C and non-potential forces Q_s on the forms of Noether conserved quantities.

Remark 2. *From the above calculation we can conclude that the Noether symmetry and Noether conserved quantities are strongly determined by non-potential forces and material parameters.*

5. Conclusion

Noether's theorem is applied in a multi-scale mechano-electrophysiological model of an axon membrane. Euler-Lagrange equations of the mechano-electrophysiological model of the neuron membrane are given through which one can deduce the classical H-H equation. Noether's symmetry criterion and Noether's conserved quantities are given under the Lie point transformations group. Through Noether criterion, we work out some solutions and give out the corresponding Noether's conserved quantities under different external stimuli. During calculation, we discovered that the Noether symmetry and Noether conserved quantities are strongly determined by non-potential forces and material parameters, which may be useful for an experiment design. As solving Noether's identities, we suppose that some material parameters are constants such as k, η, However the value of material parameters are difficult to determine, and they may be found by further stability analysis. As the axon membrane is an anisotropic diphasic soft material, the fractional derivative model (Drapaca, 2017) may be more suitable to describe its behavior, and we will analyze its Noether's symmetry in another paper.

Acknowledgments

This work was partly supported by National Natural Science Foundation of China Grant No. 12272148 and No. 11772141.

References

1. Bluman G.W., Anco S.C., 2002, *Symmetry and Integration Methods for Differential Equation*, Springer-Verlag, Berlin
2. Chen X.W., Li Y.M., Zhao Y.H., 2005, Lie symmetries, perturbation to symmetries and adiabatic invariants of Lagrange system, *Physics Letters A*, **337**, 274-278
3. Dorodnitsyn V., 2001, Noether-type theorems for difference equations, *Appllied Numerical Mathematics*, **39**, 307-321
4. Drapaca C.S., 2015, An electromechanical model of neuronal dynamics using Hamilton's principle, *Frontiers in Cellular Neuroscience*, **9**, 1-8
5. Drapaca C.S., 2017, Fractional calculus in neuronal electromechanics, *Journal of Mechanics of Materials and Structures*, **12**, 1, 35-55
6. Fang J.H., Ding N., Wang P., 2007, A new type of conserved quantity of Mei symmetry for Lagrange system, *Chinese Physics*, **16**, 887
7. Heimburg T., Jackson A.D., 2005, On soliton propagation in biomembranes and nerves, *Proceedings of the National Academy of Sciences*, **102**, 28, 9790-9795
8. Hydon P., Mansfield E., 2011, Extensions of Noether's second theorem: from continuous to discrete systems, *Proceedings of the Royal Society A: Mathematical, Physical and Engineering Sciences*, **467**, 3206-3221
9. Kosmann-Schwarzbach Y., Schwarzbach B.E., 2011, *The Noether Theorems: Invariance and Conservation Laws in the Twentieth Century*, Springer
10. Luo S.K., Yang M.J., Zhang Y.T., Dai Y., 2018, Basic theory of fractional Mei symmetrical perturbation and its applications, *Acta Mechanica*, **229**, 1833-1848

11. Mansfield E., Rojo-Echeburúa A., Hydon P., Peng L., 2019, Moving frames and Noether's finite difference conservation laws I, *Transactions of Mathematics and its Applications*, **3**

12. Mei F.X., 1993, Noether's theory of Birkhoffian systems, *Science in China, Serie A*, **36**, 12, 1456-1467

13. Mei F.X., 2000, Form invariance of Lagrange system, *Journal of Beijing Institute of Technology*, **9**, 120-124

14. Mei F.X., 2004, *Symmetries and Conserved Quantities of Constrained Mechanical Systems* (in Chinese), Beijing Institute of Technology Press, Beijing

15. Noether E., 1918, Invariante Variationsprobleme, *Nachr. Akad. Wiss. Göttingen, Mathematical Physic*, **2**, 235-257

16. Olver P.J., 1986, *Applications of Lie Groups to Differential Equations*, Springer, New York

17. Peng L., 2017, Symmetries, conservation laws, and Noether's theorem for differential-difference equations, *Studies in Applied Mathematics*, **139**, 457-502

18. Peng L., Hydon P., 2022, Transformations, symmetries and Noether theorems for differential-difference equations, *Proceedings of the Royal Society, A: Mathematical, Physical and Engineering Sciences*, **478**, 20210944

19. Wang P., 2011, Perturbation to Noether symmetry and Noether adiabatic invariants of discrete mechanico-electrical systems, *Chinese Physics Letters*, **28**, 040203-4

20. Wang P., 2012, Perturbation to symmetry and adiabatic invariants of discrete nonholonomic nonconservative mechanical system, *Nonlinear Dynamics*, **68**, 53-62

21. Wang P., 2018, Conformal invariance and conserved quantities of mechanical system with unilateral constraints, *Communications in Nonlinear Science and Numerical Simulation*, **59**, 463-471

22. Wang P., Xue Y., 2016, Conformal invariance of Mei symmetry and conserved quantities of Lagrange equation of thin elastic rod, *Nonlinear Dynamics*, **83**, 1815-1822

23. Wang P., Zhu H.J., 2011, Perturbation to symmetry and adiabatic invariants of general discrete holonomic dynamical systems, *Acta Physica Polonica A*, **119**, 298-303

24. Zhang Y., 2022, Nonshifted dynamics of constrained systems on time scales under Lagrange framework and its Noether's theorem, *Communications in Nonlinear Science and Numerical Simulation*, **108**, 106214

25. Zhang H.B., Chen H.B., 2018, Noether's theorem of Hamiltonian systems with generalized fractional derivative operators, *International Journal of Non-Linear Mechanics*, **107**, 34-41

Manuscript received August 29, 2022; accepted for print September 4, 2023

INFORMATION FOR AUTHORS

Journal of Theoretical and Applied Mechanics (***JTAM***) is devoted to all aspects of solid mechanics, fluid mechanics, thermodynamics and applied problems of structural mechanics, mechatronics, biomechanics and robotics. Both theoretical and experimental papers as well as survey papers can be proposed.

JTAM accepts full-text articles (max. 12 pages) as well as the short communications with all the requirements concerning standard publications, except a volume that is limited to 4 pages.

We accept articles in English only. The text of JTAM paper should not exceed 12 pages of standard format A4 (11-point type size, standard margins – 2.5 cm, single line spacing) including abstract, figures, tables and references.

The material for publication should be sent to the Editorial Office via electronic journal system: http://www.editorialsystem.com/jtam

Papers are accepted for publication after the review process. Blind review model is applied, which means that the reviewers' names are kept confidential to the authors. Reviewer(s) declare that there is no interpersonal relation with the author(s) that would affect the opinion and recommendation of the article for publication in JTAM. The final decision on paper acceptance belongs to the Editorial Board.

Starting from January 1, 2020, the Publisher of *Journal of Theoretical and Applied Mechanics* introduces a fee for published articles.

This applies only to papers submitted after this date and accepted by the Editorial Board for publication.

A payment of 500 EUR will be a condition for commencing the editorial procedure for upcoming articles.

After qualifying your paper for publication we will require LaTeX or TeX or Word document file and figures.

The best preferred form of figures are files obtained by making use of editorial environments employing vector graphics.

Requirements for paper preparation

Contents of the manuscripts should appear in the following order:

- Title of the paper.
- Authors' full name, affiliation and e-mail.
- Short abstract (maximum 100 words) and 3-5 key words (1 line).
- Article text (equations should be numbered separately in each section; each reference should be cited in the text by the last name(s) of the author(s) and the publication year).
- References (maximum 25) in alphabetical order.
- Titles of references originally published not in English, should be translated into English.

All the data should be reported in SI units.

Cena 40,00 zł (VAT 8%)

Contents